2005

Structural integrity and fatigue crack propagation life assessment of welded and weld-repaired structures

Mohammad Shah Alam
Louisiana State University and Agricultural and Mechanical College

STRUCTURAL INTEGRITY AND FATIGUE CRACK PROPAGATION LIFE ASSESSMENT OF WELDED AND WELD-REPAIRED STRUCTURES

A Dissertation

Submitted to the Graduate Faculty of the
Louisiana State University and
Agricultural and Mechanical College
in partial fulfillment of the
requirements for the degree of
Doctor of Philosophy

in

The Department of Mechanical Engineering

by
Mohammad Shah Alam
B.S., Bangladesh University of Engineering and Technology, 1993
M.S., South Dakota School of Mines and Technology, 2002
December, 2005

ACKNOWLEDGEMENTS

The author would like to express his deepest and most sincere gratitude to his supervisor Dr. M. A. Wahab, Associate Professor, Department of Mechanical Engineering, LSU for his continuous guidance, encouragement and sharing valuable time throughout the work. It is also much pleasure to acknowledge his untiring help by supplying supporting valuable references, information and financial support, without which this work could not have been completed.

The author would like to thank Dr. Su-Seng Pang, Dr. Michael M. Khonsari, Dr. Yitshak M. Ram of the Department of Mechanical Engineering, Dr. Ayman M. Okeil of the Department of Civil and Environmental Engineering and Dr. Annette S. Engel of the Department of Geology, Louisiana State University for serving as members in Graduate Advisory Committee and their valuable comments and suggestions, which have certainly improved the quality of this work. Special thanks extended to Dr. Samuel Ibekwe of the Department of Mechanical Engineering, Southern University, Baton Rouge for letting me use their Universal Testing Machine (MTS) facilities for various fatigue and fracture mechanics tests in this research.

The author is deeply indebted to his parents and other relatives for their encouragements and supports. The author also wishes to thank his colleagues and staffs of the Department of Mechanical Engineering for their sincere co-operation during this research work. Very special thanks go to my wife, Aysha Akter, who has sacrificed time and companionship to complete this work.

TABLE OF CONTENTS

ACKNOWLEDGEMENTS ii

LIST OF TABLES vi

LIST OF FIGURES vii

NOMENCLATURE xii

ABSTRACT xvi

CHAPTER 1 INTRODUCTION 1
1.1 General and Motivation of the Research 1
1.2 Required Activities for Assessing Structural Integrity 2
1.3 Example of Structural Integrity Assessment 3
1.3.1 Aircraft Structural Integrity 3
1.4 Objectives of This Research 4
1.5 Scope of Research Work 4

CHAPTER 2 LITERATURE REVIEW 9
2.1 Integrity Assessment 9
2.2 Fatigue Crack Growth and Propagation Life 11
2.3 Finite Element Simulation of Fatigue Crack Growth 14
2.4 Linear Elastic Fracture Mechanics and Stress Intensity Factor Calculations 16
2.5 Weld Residual Stress (WRS) and Its Effect on Fatigue Life 19
2.6 Approaches for Evaluation of Fatigue Crack Growth in Welded Joints 21
2.7 Fatigue Crack Growth in Welded Joints 23
2.8 Factors Affecting Fatigue Crack Growth in Welded Joints 25
2.8.1 Weld Geometry 25
2.8.2 Weld Defects and Weld Metallurgy 28
2.8.3 Materials and Welding Techniques 29
2.9 Distortion and Residual Stresses in Welding 29
2.10 Restraining Forces in Welding 31
2.11 Fatigue in Weld-Repaired Joints 34
2.12 Fractrographic Examination 39
2.13 Conclusions 40

CHAPTER 3 WELD AND WELD DEFECTS 43
3.1 Introduction 43
3.2 Weld Imperfections 44
3.3 Fatigue Crack Growth with Weld Defects 45
3.4 Finite Element Model 46
3.5 Model Dimensions 48
3.6 Materials and Material Properties 49
3.7 Results and Discussions 50
3.8 Validation of Predicted Results 54

3.9 Conclusions 56

CHAPTER 4 FATIGUE CRACK PROPAGATION LIFE OF WELDED STRUCTURES 57
4.1 Finite Element Modeling for Stress Intensity Factor Solutions 57
4.2 Assumption in Finite Element Model 58
4.3 Theory of Stress Field at the Crack Tip 58
4.4 Numerical Analysis: A New Approach for Fatigue Crack Growth Using Interface Element 62
4.4.1 Introduction 63
4.4.2 Traditional and New Approach 64
4.4.3 Theoretical Formulation 65
4.4.4 Interface Element and Its Properties 68
4.4.5 Equilibrium Equation of the System 70
4.4.6 Stiffness Matrix and Force Vector of Interface Element 71
4.4.7 FEM Simulation of Fatigue Crack Growth 72
4.4.8 Overall Methodology for Fatigue Life Calculation 74
4.4.9 Case Studies 75
4.4.9.1 Butt Welded Plate 75
4.4.9.1.1 Finite Element Model and Analysis 75
4.4.9.1.2 Results and Discussions 77
4.4.9.2 Welded Tubular Joints 81
4.4.9.2.1 Finite Element Model and Analysis 81
4.4.9.2.2 Results and Discussions 83
4.4.10 Traditional FEM Model for Fatigue Crack Propagation 90
4.4.11 Validation 91
4.4.12 Conclusions 93

CHAPTER 5 FINITE ELEMENT MODELING OF GAS METAL ARC WELDING (GMAW) 94
5.1 General 94
5.2 GMA Welding Process 95
5.3 Energy Equation 95
5.4 Model of Heat Input to the Work Piece 96
5.5 Surface Heat Losses 97
5.6 Finite Element Modeling of GMAW 98
5.7 Distortion and Residual Stress in Gas Metal Arc Welding 101
5.7.1 Finite Element Model and Analysis 102
5.7.2 Results and Discussions 103
5.7.3 Conclusions 109
5.8 Restraining Forces in Gas Metal Arc Welded Joint 109
5.8.1 Introduction 109
5.8.2 Mathematical Relation of Restraining Forces 110
5.8.3 Experimental Procedure 112
5.8.3.1 Design 112
5.8.3.2 Configuration 113
5.8.3.3 Instrumentation and Testing 115
5.8.3.4 Test Procedure 115

5.8.3.5 Welding Conditions 116
5.8.3.6 Edge Preparation 117
5.8.4 Experimental Results and Discussions 118
5.8.4.1 Side, End of Weld 118
5.8.4.2 Side, Start of Weld 122
5.8.4.3 Top, Start of Weld 124
5.8.5 Finite Element Model (FEM) and Analysis 126
5.8.6 FEM Results and Discussions 129
5.8.7 Conclusions 130

CHAPTER 6 FATIGUE IN WELD-REPAIRED JOINTS 131
6.1 Repair Techniques of Welded Joints 131
6.2 Weld Repair on Welded Joints with Crack 133
6.3 Fatigue Crack Failure Test Specimens 134
6.4 Fatigue Crack Failure Life Experiments 136
6.5 Comparison of Fatigue Crack Failure Life among Un-welded, Welded and Weld-Repaired Specimens. 137
6.6 Microscopic Examination and Micro-Characterization of Un-Welded, Welded and Weld-Repaired Joints 141
6.7 Conclusions 148

CHAPTER 7 CONCLUSIONS AND RECOMMENDATIONS FOR FUTURE WORK .. 149
7.1 Conclusions 149
7.2 Recommendations for Future Work 151

REFERENCES 152

APPENDIX A: LIST OF PUBLICATIONS FROM THIS RESEARCH 165

APPENDIX B: LIST OF ANSYS COMMAND 166

VITA 174

LIST OF TABLES

Table 3.1 Chemical composition of base and weld metals [Burk, 1978]. 49

Table 3.2 Mechanical properties of base, weld and heat-affected materials [Burk, 1978]..... 49

Table 5.1 Welding conditions for constant speed but varied heat input..... 117

Table 5.2 Welding conditions for constant heat input, varied speed..... 117

Table 5.3 Welding parameters..... 117

Table 6.1 Test parameters..... 137

Table 6.2 Test plan..... 137

LIST OF FIGURES

Figure 2.1 Typical fatigue crack growth rate curve [Anderson, 1995] 12

Figure 2.2 Typical longitudinal WRS distribution at butt weld [Wu, 2002] (a) mild steel (b) aluminum alloy (c) high alloy structure steel. 19

Figure 2.3 Crack opening displacement curve. 22

Figure 2.4 Weld geometry parameters at butt-weld joints 26

Figure 3.1 Different weld imperfections in a butt-joint [Maddox, 1994] 44

Figure 3.2 A 2-D schematic view of a single-V butt-joint with various weld imperfections. 48

Figure 3.3 Effect of weld imperfections on fatigue crack propagation life 50

Figure 3.4 The effect of residual stress, bending stress and dissimilar material properties in welded and un-welded base material 51

Figure 3.5 Effect of weld imperfections on fatigue crack propagation rate 51

Figure 3.6 Comparison of axial and bi-axial effect of a solidification crack and a circular porosity 53

Figure 3.7 The combined effects of both defects (solidification and porosity) under bi-axial loading when they interact each other. 53

Figure 3.8 Comparison of the results from FEM and empirical relations 54

Figure 3.9 Comparison of FEM and experimental results for solidification crack. 55

Figure 4.1 The three modes of loading that can be applied to a crack 58

Figure 4.2 Stress field at crack-tip [Anderson, 1995] 59

Figure 4.3 Stress normal to crack plane in mode-I loading 61

Figure 4.4 Interface element between crack faces 68

Figure 4.5 Interface element as a combination of non-linear truss and elastic-plastic elements. . 69

Figure 4.6 (a) Mechanical properties of interface (non-linear truss) element (b) Mechanical properties of elastic-plastic continuum 69

Figure 4.7 A schematic views of truss elements connected between two surfaces of two mild steel plates. 73

Figure 4.8 A 2-D FEM model of butt-welded plate 76

Figure 4.9 A typical constant amplitude axial cyclic load 76

Figure 4.10 Variation of fatigue crack growth rate with range of stress intensity factor 78

Figure 4.11 Variation of fatigue life with range of stress intensity factor 78

Figure 4.12 Variation of crack opening displacement with crack length 79

Figure 4.13 Variation of strain near crack-tip and crack-tip opening displacement (COD) with crack-tip stress 80

Figure 4.14 A schematic view of T- joint offshore structure under cyclic loading 81

Figure 4.15 (a) A 2-D FEM model of a tubular welded joint (compressive pressure load at the outer surface) 82

Figure 4.15 (b) A 2-D FEM model of a tubular welded joint (compressive pressure load at intermediate location between 45 and 90 degrees) 82

Figure 4.15 (c) Denser mesh at the crack-tip 83

Figure 4.16 Fatigue crack growth rate with the range of stress intensity factor 84

Figure 4.17 Variation of fatigue life with range of stress intensity factor 85

Figure 4.18 Variation of crack-tip opening displacement (COD) with crack-tip stress 86

Figure 4.19 Variation of strain at crack-tip with crack-tip stress. 86

Figure 4.20 Fatigue crack growth rate with the range of stress intensity factor (for case b) 87

Figure 4.21 Variation of fatigue life with range of stress intensity factor (case b) 88

Figure 4.22 Variation of crack-tip opening displacement (COD) with crack tip stress (case b) 88

Figure 4.23 Variation of strain at crack-tip with crack tip-stress (case b) 89

Figure 4.24 Traditional FEM model for fatigue crack propagation of a center cracked plate 90

Figure 4.25 Comparison of fatigue crack propagation life from new and traditional FEM model 91

Figure 4.26 Comparison of prediction and experimental results [Burk, 1978] 92

Figure 5.1 Gas metal arc welding process 94

Figure 5.2 A symmetric 3-D FEM model (254 x 25 x 6 mm) of figure 5.1 after distortion 103

Figure 5.3 Temperature distribution after 60 sec at a distance of 10 mm from centre of weld.. 104

Figure 5.4 Angular distortion with included angle 104

Figure 5.5 Longitudinal and transverse distortion..... 105

Figure 5.6 Residual stress over included angle in longitudinal and transverse direction 105

Figure 5.7 Residual stresses over distance in longitudinal and transverse direction 106

Figure 5.8 Isothermal line of the heat-affected-zone (727 ^{o}C) 107

Figure 5.9 Isothermal lines of fused zone (1480 ^{o}C) 108

Figure 5.10 A simple elastic-plastic model of welding 110

Figure 5.11 Thermal history of plastic strain..... 111

Figure 5.12 Equivalent loads of inherent strain 112

Figure 5.13 CAD drawing of the jig 113

Figure 5.14 Photo of the jig 114

Figure 5.15 Position of load cell for side of plate, end of weld..... 116

Figure 5.16 Variation of restraining forces with weld speed..... 118

Figure 5.17 Variation of restraining forces with distance (1 kN = 224.81 $lb_{f,}$) 119

Figure 5.18 Variation of restraining forces with heat input (1kJ = 0.95 Btu) 120

Figure 5.19 Detail of force rise while welding (1kJ = 0.95 Btu)..... 121

Figure 5.20 Force relaxation over time..... 121

Figure 5.21 Heat input and slope of force vs. time graph..... 122

Figure 5.22 Variation of restraining forces with speed (1 kN = 224.81 lb_f)..... 123

Figure 5.23 Variation of restraining force with heat input (1 kN = 224.81 lb_f)..... 123

Figure 5.24 Variation of restraining force with weld speed (1 kN = 224.81 lb_f)..... 125

Figure 5.25 Variation of restraining forces with heat input..... 125

Figure 5.26 A 3-D FEM weld model (symmetric part only) with mesh and boundary condition (500x100x10 mm)..... 127

Figure 5.27 Finite element model showing moving heat flux 128

Figure 5.28 Restraining force found from ANSYS post processing for side, start position with weld speed 300mm/min and heat put 1kJ/mm..... 129

Figure 5.29 Comparison of predictions with experimental result (weld speed 400 mm/sec, heat input 1 kJ/mm) 130

Figure 6.1 Weld design for single side weld repair (all dimensions in mm)..... 134

Figure 6.2 Fatigue crack test specimen geometry-un-welded and weld-repaired specimens..... 135

Figure 6.3 Fatigue crack test specimen for welded specimens (-pro)..... 135

Figure 6.4 Fatigue crack test specimen for single side weld-repaired specimens 136

Figure 6.5 Variation of failure life with range of stress of un-welded, welded and weld-repaired joints at stress ratio 0.1..... 138

Figure 6.6 Variation of failure life with range of stress of un-welded, welded and weld-repaired joints at stress ratio 0.2..... 138

Figure 6.7 Variation of failure life with range of stress of un-welded, welded and weld-repaired joints at stress ratio 0.3..... 139

Figure 6.8 Failure life with range of stress of un-welded joints at various stress ratios..... 140

Figure 6.9 Failure life versus range of stress of welded joints at various stress ratios..... 140

Figure 6.10 Failure life versus range of stress of weld-repaired joints at various stress ratios .. 141

Figure 6.11 SEM photograph of fracture surface of failed un-welded specimen (tested at stress ratio = 0.2, stress range = 80, MPa, frequency = 0.5 Hz) 143

Figure 6.12 SEM photograph of fracture surface of failed un-welded specimen (tested at stress ratio = 0.2, stress range = 100 MPa, frequency = 0.5 Hz) 143

Figure 6.13 SEM photograph of fracture surface of failed un-welded specimen (tested at stress ratio = 0.2, stress range = 92 MPa, frequency = 0.5 Hz) 144

Figure 6.14 SEM photograph of fracture surface of failed welded specimen (tested at stress ratio = 0.2, stress range = 48 MPa, frequency = 0.5 Hz) 144

Figure 6.15 SEM photograph of fracture surface of failed welded specimen (tested at stress ratio = 0.2, stress range= 48 MPa, frequency = 0.5 Hz) 145

Figure 6.16 SEM photograph of fracture surface of failed welded specimen (tested at stress ratio = 0.2, stress range = 48 MPa, frequency = 0.5 Hz) 145

Figure 6.17 SEM photograph of fracture surface of failed welded specimen (tested at stress ratio = 0.2, stress range = 40 MPa, frequency = 0.5 Hz) 146

Figure 6.18 SEM photograph of fracture surface of failed welded specimen (tested at stress ratio = 0.2, stress range = 24 MPa, frequency = 0.5 Hz) 146

Figure 6.19 SEM photograph of fracture surface of failed weld-repaired specimen (tested at stress ratio = 0.2, stress range = 24 MPa, frequency = 0.5 Hz) 147

Figure 6.20 SEM photograph of fracture surface of failed weld-repaired specimen (tested at stress ratio = 0.2, stress range = 40 MPa, frequency = 0.5 Hz) 147

NOMENCLATURE

Roman Notations	Meaning
a	half crack length for a central crack, constant
a_f	final crack length
a_o	initial crack length
B	breadth, width of plate
c	a constant
C	material dependent constant
C_p	specific heat
d	diameter of wire
D	diameter of nozzle
da /dN	crack growth rate (crack length per cycle)
E	modulus of elasticity
f	load vector, restraining force
h_t	tangent modulus
I	current
H	welding height/ reinforcement, natural convective heat transfer coefficient
h_g	force convective heat transfer coefficient
HAZ	heat-affected zone
k	stiffness matrix, thermal conductivity
K	stress intensity factor (MPa√m)
K_c	fracture toughness

K_{crit}	critical stress intensity factor
K_I	mode I stress intensity factor
K_{II}	mode II stress intensity factor
K_{III}	mode III stress intensity factor
K_{max}	maximum stress intensity factor
K_{min}	minimum stress intensity factor
K_{open}	crack opening stress intensity factor
K_s	spring stiffness
K_t	theoretical stress concentration factor
ΔK	range of stress intensity factor
ΔK_{th}	range of threshold stress intensity factor
L	length, latent heat of fusion
m	material dependent constant
m (x, a)	weight function
N	number of cycles
n	shape parameter
N_i	shape function
N_p	fatigue crack propagation life
Pr	Prandtl number
Q	heat input
r	distance from crack tip
R	stress ratio
R_e	Reynolds number
R_t	weld toe root radius

r_o	scale parameter
r_p	plastic zone radius
S	nominal stress
S_p	weld toe peak stress
S_{ys}	yield stress (same as σ_y)
t	thickness of plate
T_o	ambient temperature
T_s	solidus temperature
T_g	droplet temperature
T_L	liquidus temperature
ΔT	temperature interval of phase change
u	crack opening displacement
U	strain energy
v	weld speed
v_f	feed speed of wire
V	voltage
u_o	nodal displacement
U_s	interface energy during crack propagation
W	potential of external load
w	welding width
w_i	nodal displacement normal to the surface
Y	a constant
S	surface area
ΔS	range of stress

Greek Notations

Π	total energy
α	toe angle
δ	crack opening displacement
ε	strain
ϕ	Lennard-Jones surface potential
γ	surface energy per unit area
η	natural (local) coordinate, efficiency of welding
κ	a coefficient, constant
μ	shear modulus
ν	Poisson's ratio
θ	angle in radian
ρ	density
σ	nominal stress (local)
σ_{cr}	critical bonding strength
σ_y	yield stress (same as S_{ys})
σ_{open}	crack opening stress
ξ	natural (local) coordinate

ABSTRACT

Structural integrity is the science and technology of the margin between safety and disaster. Proper evaluation of the structural integrity and fatigue life of any structure (aircraft, ship, railways, bridges, gas and oil transmission pipelines, etc.) is important to ensure the public safety, environmental protection, and economical consideration. Catastrophic failure of any structure can be avoided if structural integrity is assessed and necessary precaution is taken appropriately.

Structural integrity includes tasks in many areas, such as structural analysis, failure analysis, nondestructive testing, corrosion, fatigue and creep analysis, metallurgy and materials, fracture mechanics, fatigue life assessment, welding metallurgy, development of repairing technologies, structural monitoring and instrumentation etc. In this research fatigue life assessment of welded and weld-repaired joints is studied both in numerically and experimentally.

A new approach for the simulation of fatigue crack growth in two elastic materials has been developed and specifically, the concept has been applied to butt-welded joint in a straight plate and in tubular joints. In the proposed method, the formation of new surface is represented by an interface element based on the interface potential energy. This method overcomes the limitation of crack growth at an artificial rate of one element length per cycle. In this method the crack propagates only when the applied load reaches the critical bonding strength. The predicted results compares well with experimental results.

The Gas Metal Arc welding processes has been simulated to predict post-weld distortion, residual stresses and development of restraining forces in a butt-welded joint. The effect of welding defects and bi-axial interaction of a circular porosity and a solidification crack on fatigue crack propagation life of butt-welded joints has also been investigated.

After a weld has been repaired, the specimen was tested in a universal testing machine in order to determine fatigue crack propagation life. The fatigue crack propagation life of weld-repaired specimens was compared to un-welded and as-welded specimens. At the end of fatigue test, samples were cut from the fracture surfaces of typical welded and weld-repaired specimens and are examined under Scanning Electron Microscope (SEM) and characteristics features from these micrographs are explained.

CHAPTER 1 INTRODUCTION

1.1 General and Motivation of the Research

Structural integrity (SI) has been defined as the science and technology of the margin between safety and disaster [James, 1998]. Proper evaluation of the structural integrity and remaining life of structures (aircraft, ship, railways, pressure vessel, gas and oil transmission pipelines etc.) is important to ensure the public safety, environmental protection, and the economical consideration for building new structures and maintaining and rehabilitate existing structures. In recent years, significant improvements have been made in the development of structural analysis methods.

Structural integrity of large engineering structures presents a unique challenge in the production of safe and cost-effective means of analysis, inspection and rehabilitation. Many existing structures are ageing and the development of new technologies and new methodologies for structural analysis are crucial for their sustainability. In the last two decades there has been a dramatic shift in the maintenance philosophy of large structure [James, 1998]. Economic pressure has forced to extend the service lives of these structures beyond the design life. Life extension of these large structures has become a major growth sector in the related industries.

Structural integrity includes all aspects of structural integrity in industrial components and equipment, including:

- Structural analysis
- Failure analysis
- Nondestructive testing
- Corrosion
- Fatigue and creep analysis

- Metallurgy and materials
- Fracture mechanics
- Fatigue assessment
- Welding metallurgy
- Structural monitoring and instrumentation
- Software development for life time assessment

1.2 Required Activities for Assessing Structural Integrity

Activities for assessing structural integrity depend on type of structures. Following activities are a general guideline for assessment of structural integrity.

- Design audits for the verification of integrity and early identification of potential problems.
- Identification of potential degradation and failure mechanisms.
- Analysis of the effects of design modifications on the integrity of structures.
- Analysis of the effects of changes in operating conditions or loads on the integrity of structures.
- Specification and assessment of repair schemes for equipment with damage.
- Determination of fatigue life. This covers a range of material types (including metals, polymers and composites) and stress states.
- Determination of critical defect sizes and remaining life for structures with defects.
- Assessment of inspection results to accurately characterize defects that are to be used in making a structural assessment.
- Specification of maintenance/inspection programs aimed at cost effective management of risk.
- Application of probabilistic approaches to structural integrity assessment.

- Application of numerical methods for simulation of mechanical and thermal state of structures under different loading conditions (e.g. Finite element modeling)
- Failure assessment of detected defects applying fracture mechanics principles
- Life-time estimation of structures and components
- Development of repairing technologies
- Development of expert systems
- Design of additional instrumentation of mechanical material testing equipment, implementation and development of software for test controlling and analysis

1.3 Example of Structural Integrity Assessment

1.3.1 Aircraft Structural Integrity

Many aircraft fleets around the world are being operated beyond their intended service life span and in environments more severe than their airframes were originally designed to accommodate [James, 1998]. This condition has increased demands on structural reliability requirements for aging military and commercial aircraft. Following typical works are needed for the assessment of structural integrity of aircraft**:**

- Structural design, analysis, and modification
- Parts drawings for fabrication and installation
- External loads development
- Stress analysis of welded components, such as engine mounting, brackets etc.
- Aircraft usage monitoring
- Maneuver and stress spectra development
- Vibration and static/dynamic fatigue testing
- Component and full-scale damage tolerance testing
- Damage tolerance and economic life assessment

- Structural and metallurgical failure analysis
- Nondestructive inspection development and application
- Structural condition inspection
- Life extension for aircraft
- Advanced aerospace materials studies, development, and application

1.4 Objectives of This Research

The following aspects of structural integrity of welded structures are the objectives of this research:

1. Determination of fatigue crack propagation life of welded and weld repaired structures (both numerically and experimentally).
2. Determination of bi-axial interaction of two defects on fatigue crack propagation life.
3. Application of numerical methods for simulation of mechanical and thermal state of welded joints (e.g. Finite Element modeling of gas metal arc welding) and the study of the consequences of welding (distortion, residual stress, restraining force, etc.)
4. Assessment of suitable repair techniques for welded joints with damage/ crack.
5. Fractographic examination of failure surfaces by Scanning Electron Microscope (SEM).

1.5 Scope of Research Work

A major survey on "Industrial practices related to design to avoid fatigue in pressure equipment" was organized and distributed in October 2000 to European pressure equipment organizations [Tailor, 2002]. A majority (58%) of respondents indicated experience of fatigue related problems in pressure equipment. These were mainly cracks or leaks. The consequences of the individual cases were not analyzed in detail. However, it was clear that all of these failures registered in that survey would require at least repair work or replacement of the damaged component. The risk of very costly loss of

production capacity is evident. Many of the equipment there contain high temperature media. Even a small leakage may lead to a risk of personal injury. The risk for personal injury is highest for catastrophic failure. Avoidance of this type of failure is extremely important.

As aircraft become older and accumulate more flight hours, the tendency they have to develop corrosion problems, fatigue cracking, overload cracking, etc. increases. This problem was never more evident than after an incident involving Aloha Airlines Flight 243 [Avram, 2001]. During the flight, part of the fuselage ripped off, causing the death of a female flight attendant. The cause was linked to stress corrosion cracking caused by the aircraft's flight environment and high number of flight hours. As a direct result of this tragedy, the U.S. government established the National Aging Aircraft Research Program under the direction of the Federal Aviation Administration (FAA) and the Airframe Structural Integrity Program under the direction of the National Aeronautics and Space Administration (NASA) [Conley, 1999]. The Air Force, aware of its aging aircraft fleet, established its own Aging Aircraft Program.

There are three basic ways to address aging aircraft problems as they arise: 1) aircraft replacement, 2) part replacement, 3) part repair [Conley, 1999]. The first, aircraft replacement, is not much of an option because of the high cost of modern day aircraft. Government budget cuts and the demand for industry to make a profit create a need to continue to use current aircraft for as long as possible.

The second option, part replacement, can create many problems. For older aircraft, such as the KC-135 and B-52, parts can be very difficult to obtain because they may not be in production anymore. Parts may have to be specially manufactured, leading to very high costs and long waiting periods. Also, replacing an entire aircraft part, depending on how substantial it is, can take a very long time, creating problems with training and mission sortie rates, especially in the case of fleet-wide problems. The third option, part repair, is the easiest and cheapest way to address the

problem. By focusing on fixing individual part damage, as opposed to replacing the entire part or airframe, the time and money needed to get the airframe up and running again is reduced.

It has been reported [Ghose et al., 1995] that inspections by the US Coast Guard have found fatigue cracks to be responsible for major structural damage in 65-100% of their vessels. A related report on Marine Structural Integrity Programs [Beg, 1992] points out that fatigue damage in highly stressed details initiates at the intersection of structural elements and discontinuities such as openings and welds. Due to complicated service environments and stress conditions on the structure elements of these vessels, welded components can be subjected to high periodic fatigue loads, which may finally lead to early fatigue failure. In addition, when cracks occur in the vicinity of welded structures, weld repairs are frequently considered for crack repair, in most cases, to extend service life [Beg,1992]. It is necessary to know and be able to assess whether, and to what extent, weld repair processes can improve fatigue life of cracked welded structures.

From the design point of view, fatigue properties of welded structures, such as crack growth rate data (da/dN) and fatigue strength curves (S-N data), should be determined accurately so that the fatigue life of the welded structure can be accurately evaluated. Several fatigue crack growth data for welded joints are available but very few data are available for weld repaired joints.

In this study the fatigue crack propagation life of welded and weld-repaired joints has been investigated both numerically and experimentally. In numerical analysis, a new approach for the simulation of fatigue crack growth in two dissimilar elastic materials has been developed; specifically, the concept has been applied to a butt-welded joint. In this method, the formation of new surface is represented by an interface element based on the interface potential energy. This method overcomes the limitation of crack growth at a rate of one element length per cycle. In this method the crack propagates only when the applied load reaches the critical bonding strength. In experimental analysis, the fatigue failure life is determined using universal material testing

machine (MTS). Various factors such as stress level, frequency, stress ratio, etc. of fatigue crack propagation life have also been investigated.

In welded structures, the presence of weld imperfections such as slag inclusions at welds toes, undercut, residual stresses, lack of penetration, misalignment, etc., effectively reduce the fatigue crack propagation life of the structures. Welded structures experience both axial and biaxial fatigue load and also have residual stress developed during welding which affect the fatigue life. In fatigue process, the interaction between a surface crack (solidification) and an embedded crack (porosity) may normally happen. Fitness-for-purpose is now widely accepted as the most rational basis for the assessment of weld imperfections, such that an imperfection would need to be repaired only if its presence is harmful to the integrity of the structure [Maddox, 1994]. To justify the integrity of welded structures, it is necessary to estimate the fatigue life of a welded joint containing the imperfections and to compare it with the required life. Therefore, this study makes an attempt to find the effect of welding defects and bi-axial interaction of a circular porosity and a solidification crack on fatigue crack propagation life of butt-welded joints.

The welding processes have been extensively used for the fabrication of various structures ranging from bridges and machinery to all kinds of sea-going vessels to nuclear reactors and space vehicle. This is because of the numerous advantages welding process offer compared to other fabrication techniques, such as: excellent mechanical properties of the welded joints, air and water tightness, and good joining efficiency. At the same time, however, welding creates various problems (distortion, residual stress, etc.) of its own that have to be solved. In the past these problems have been tackled through expensive experimental investigation. Fortunately, since the advent of the computer, a new tool (simulation) becomes available which could give solutions to many of the welding problems. In this study it is tried to develop a numerical model capable of the process simulation of the Gas Metal Arc Welding (GMAW) operation and measure the residual

stresses, distortion and restraining forces in plates while welding. The predicted results were compared with experimental results and reasonably good agreements were found.

Because weld-repair may led to loss of mechanical properties, microstructure change in HAZ and redistribution of weld residual stresses in weldments, the fatigue crack growth behavior can vary significantly compared to welded structures. At present, the effects of weld repair techniques on the variation of fatigue crack growth behavior still remain unclear, although these effects are critical for fatigue life evaluation of weld repaired structures. In order to evaluate the improvement in fatigue life of weld-repaired structures, fatigue crack propagation data should be determined first. Unfortunately at this time very limited work has been reported in this field. Therefore, some weld repaired techniques of Al-6061 flat plates butt-welded joints were investigated experimentally in this research. After weld repaired, the specimen were tested in MTS universal testing machine in order to determine fatigue crack propagation life. The fatigue crack propagation life of weld-repaired specimens was compared to un-welded and welded specimens.

The use of fractography in failure analysis is well established [James, 1992] and the type of information that can be gained from deductive reasoning supported by fractographic examination. It is often the case that fractographic evidence is crucial in correctly identifying the sequence of events in a failure, and in proving, beyond reasonable doubt, a particular scenario to be the most feasible. This applies equally to many cases involving polymers [James, 1999] or ceramics, as well as to metals. In this study fractographic examination of the failure surfaces of the un-welded, welded and weld repaired specimen were conducted. At the end of fatigue test, samples were cut from the fracture surfaces of typical un-welded, welded and weld repaired specimens and examined with Scanning Electronic Microscope (SEM). Fatigue crack initiation, stable propagation and fast growth areas of un-welded, welded and weld-repaired specimens were scanned and characteristics features were determined.

CHAPTER 2 LITERATURE REVIEW

2.1 Integrity Assessment

In recent years, with the development of powerful computing facilities, Finite Element (FE) analysis methods have been applied to the simulation of structural behavior using commercial FE software packages. However, for general usage, especially in routine structural integrity assessments, the simplified state-of-art methods are much more popular than full step-by-step elastic-plastic analysis methods.

The Linear Matching Method (LMM) has been developed recently for the integrity assessment for the high temperature response of structures [Chen and Ponter, 2003]. A complex 3-D tube plate in a typical AGR superheater header was analyzed by Chen and Ponter [2005(1)] for the shakedown limit, reverse plasticity and ratchet limit based upon the LMM. Both the perfectly plastic model and the cyclic hardening model were adopted for the evaluation of the plastic strain range. Comparisons of LMM results with other results by ABAQUS step-by-step inelastic analyses for several material models were given. Further cyclic creep-reverse plasticity analyses were presented in [Chen and Ponter, 2005(2)].

For the evaluation of the high temperature response of structures, British Energy Generation Ltd (BEGL)'s R5 integrity assessment procedure has been widely used in the last decades [Ainsworth, 2003]. However, the calculations in R5 were based largely on reference stress techniques, elastic solutions and simplified shakedown solutions. The R5 integrity assessment for cyclic plastic and creep behavior of structures can often be over conservative, as they are based on simplified numerical methods and 'expert knowledge' in structural mechanics and materials science.

Structural integrity assessment of the containment structure of a pressurized heavy water nuclear reactor using impact echo technique was carried out by Anish et al. [2002]. Impact-echo testing has been carried out for assessment of the structural integrity of the ring beam of a pressurized heavy water nuclear reactor (PHWR). In order to develop the test procedure for carrying out impact echo testing, mock up calibration blocks were made. The detection ability of the impact echo system has also been established in terms of the depth and the lateral dimension of the detectable flaw for the ring beam under consideration. Based on the optimized test parameters identified with the help of the studies carried out on the mock up blocks, impact echo testing was carried out on the ring beam of the reactor containment structure, for assessing its structural integrity.

Mikael [2000] investigated structural integrity from a fracture mechanics point of view. The emphasis in his work was on rate effects of fracture toughness but all investigations deal with phenomena or problems within the frame work of non-linear fracture mechanics. Three-point bend and compact tension specimens taken from beam sections of modern and older ordinary C-Mn structural steels were tested at intermediate loading rates at room temperature and -30 °C. The experimental work, except the loading rates used, was performed according to ASTM E-813. The fracture toughness of C-Mn structural steels depends strongly on the loading rate, and decreases rapidly with increasing loading rate at and just above the maximum prescribed in ASTM-E813. A path independent integral expression for the crack extension force of a two- dimensional circular arc crack was presented. The integral expression, which consists of a contour and an area integral, was derived from the principle of virtual work. It was implemented into a FEM post processing program and the crack extension force was calculated for a circular arc crack in a linear elastic material. Comparison with exact solutions for the effective elastic stress intensity factor shows acceptable accuracy for the numerical procedure used.

2.2 Fatigue Crack Growth and Propagation Life

The literature on fatigue crack propagation of welded structure has been reviewed in comprehensive details by Wu [2002]. Wu measured the crack growth rate during constant amplitude fatigue testing on un-welded, as-welded and weld repaired specimens of 5083-H321 aluminum alloy. A 3-D finite element analysis was conducted to determine the stress intensity factors for different lengths of crack taking into account the three-dimensional nature of the weld profile. The effects of crack closure due to weld residual stresses were evaluated by taking measurements of the crack opening displacements and utilized to determine the effective stress intensity factors for each condition. It was found that crack growth rates in welded plates are of the same order of magnitude as those of parent material when effective stress intensity factors were applied. However weld repaired plates exhibit higher crack growth rates compared to those un-welded plates.

Bell and Vosikovsky [1992] conducted research work on the fatigue crack initiation and propagation behavior for multiple cracks in welded T-joints for offshore structures. They showed that many semi-elliptical cracks initiate along the weld toe and progressively coalesce as they divided into fewer large cracks. It was also noted that crack coalescence accounted for a significant portion of the propagation life. Ferrica and Branco [1990] investigated the effects of weld geometry factors on the fatigue properties of cruciform and T-weld joints. The results showed that the thickness of main plate and the radius of weld-toe are the most important factors for the fatigue properties of welded joints. A method for the determination of weight functions relevant to welded joints and subsequent calculations of stress intensity factors was proposed by Niu and Glinka [1987]. The weight function for edge cracks emanating from the weld toe in a T-butt welded joint has been derived by using the Petroski- Achenback crack opening displacement function. The weight function makes it possible to study efficiently the effect of weld profile

parameters, such as the weld toe radius and weld angle, on stress intensity factors corresponding to different stress systems. They found that the local weld geometric parameters affect the stress intensity factors more than the local stress fields in the weld toe neighborhood. It has been found from experience that most common failures of engineering structures such as welded components are associated with fatigue crack growth caused by cyclic loading. Engineering analysis of fatigue crack growth is frequently required for structural design, such as in Damage Tolerance Design (DTD), and residual life prediction when an unexpected fatigue crack is found in a component of engineering structure. For analysis, the fatigue life of welded structures can be divided into two parts: (1) crack initiation phase, and propagation phase. Fatigue crack propagation behavior is typically described in terms of crack growth rate or crack length extension per cycle of loading (da/dN) plotted against the stress intensity factor (SIF) range (ΔK) or the change in SIF from the maximum to the minimum load (Fig. 2.1).

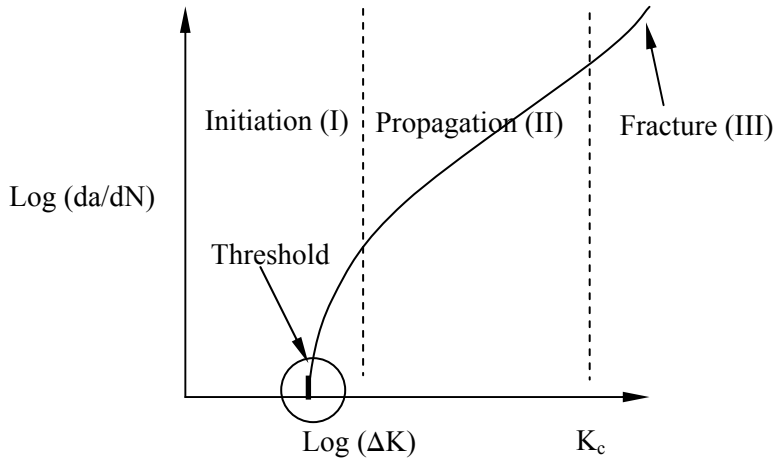

Figure 2.1 Typical fatigue crack growth rate curve [Anderson, 1995]

The central portion of the crack growth curve (propagation II) is linear in the log-log scale. Linear Elastic Fracture Mechanics (LEFM) condition essentially deals with crack propagation in this region, which is commonly described by the crack growth equation proposed by Paris and Erdogan [1963] , and popularly known as the Paris law, as given below:

$$da/dN = C(\Delta K)^m \tag{2.1}$$

where C and m are material dependent constants, and (ΔK) is the range of stress intensity factor (SIF). It should be noted that Paris law only represents the linear phase (region II) of the crack growth curve. As the stress intensity factor range increases approaching its critical value of fracture toughness (K_c), the fatigue cracks growth becomes much faster than that predicted by Paris law. Forman [1967] proposed the following relationship for describing region II and III together:

$$da/dN = \frac{C(\Delta K)^m}{(1-R)K_c - \Delta K} \tag{2.2}$$

where R is the stress ratio**,** equal to $\sigma_{min}/\sigma_{max}$**.**

Note that the above relationship accounts for stress ratio, R effects, while Paris law assumes that da/dN depends only on ΔK. Based on the above relationship, fatigue crack propagation life can be predicted by integrating both sides of these functions if a suitable SIF solution is obtained. Since weld geometry conditions may differ in various weld joints, traditional empirical relations become invalid in some cases and new models may have to be created for local stress distribution and accurate stress intensity factor calculation. In line with the traditional da/dN testing approach, nearly all the present da/dN data for welded joints were obtained by using bead removed specimens, for which classical two-dimensional solutions for stress intensity factors become applicable. It has been reported by Sanders and Lawrence [1977] that welded components with bead removed have different characteristics in fatigue crack growth compared with as-welded components because of the redistribution of welding defects and weld residual stress (WRS). In most practical engineering application, removing weld beads thoroughly is impossible or uneconomical especially for heavy welded structures such as those employed on offshore drilling platforms. Using da/dN data obtained from bead removed specimens for fatigue design or fatigue life prediction on as-welded joints may lead to erroneous conclusions. Therefore determination of

accurate stress intensity factor solutions for the correct weld geometry conditions is of practical significance structural design and fatigue life evaluation of welded structures.

2.3 Finite Element Simulation of Fatigue Crack Growth

Many earlier researchers used numerical approaches for fatigue crack propagation. In this regard, the works of Newman and Harry [1975], Newman [1977], Chermahini et al. [1988] and McClung and Sehitoglu [1989] are remarkable. A general trend of the numerical approach in this field for the past 25 years can be inferred from those references. Originally, a crack tip node–release scheme was suggested by Newman [1977], in which a change in the boundary condition was characterized for a crack growth. This was achieved by changing the stiffness of the spring elements connected to boundary nodes of a finite element mesh. Before Newman's work, investigators changed boundary conditions of the crack tip node directly to obtain a free or fixed node. When the crack tip is free, the crack advances by an element length. The approach Newman used to change boundary conditions was to connect two springs to each boundary node [Newman, 1977]. To get a free node, the spring stiffness in terms of modulus of elasticity was set equal to zero, and for the fixed ones it was assigned an extremely large value (about 10^8 GPa) which represents a rigid boundary condition. McClung and Sehitoglu [1989] have also investigated fatigue crack closure by the finite element method. Their model for the elastic-plastic finite element simulation of fatigue crack growth used a crack closure concept. They followed the node-release scheme at the maximum load and assumed that the crack propagates one element length per cycle. Wu and Ellyin [1996] studied fatigue crack closure using an elastic-plastic finite element model. They followed an extension of Newman's node- release scheme. They used a truss element instead of a spring element and released one node after each cycle of fatigue load.

Recently, the cohesive element approach has been broadly used in crack propagation simulations. Cohesive elements originate from the concept of cohesive zone, firstly introduced by

Dugdale [1960] and Barrenblatt [1962]. The implementation of cohesive zone into numerical analysis takes the form of cohesive elements, which explicitly simulate crack process zone. The work of Xu and Needleman [1994, 1995, 1996] demonstrated successful use of the cohesive-element technique in 2-D cases. In a cohesive element, the material separation process is described by the cohesive law, which defines the relation between crack surface traction and surface opening displacement. Xu and Needleman have used initial elastic and then exponentially decaying cohesive law (the Smith-Ferrante law). Camacho and Ortiz [1996, 1997] have proposed a simple, initial rigid and linear decaying cohesive law. The work of Pandolfi et al. [1999, 2000], and Ruiz et al. [2000, 2001] successfully implemented Camacho and Ortiz's cohesive model into 3-D analysis in a range of applications. Other recent numerical investigations using cohesive elements study the effect of the microstructure on the dynamic failure process [Zhai and Zhou, 2000, Zavallieri and Espinosa 2001], the three dimensional fracture of ductile metallic composite [Zhou, Molinari and Li, 2004], and the stochastic tensile failure of brittle ceramics [Zhou and Molinari, 2004]. Murakawa et al. [2000,2000,1999] use the concept of the interface element for the strength analysis of a joint between dissimilar materials. They also used it for the calculation of the strength of peeling of a bonded elastic strip and the fracture strength of a centre cracked plate under static load [Murakawa et al., 2000]. They further used it for simulation of hot cracking, push-out test of fibers in matrix, ductile tearing and dynamic crack propagation under pulse load and pre-stress condition [Murakawa et al., 1999]. They have not applied repeated cyclic load for fatigue crack propagation. Nguyen et al. [2001] investigated the use of cohesive theories of fracture, in conjunction with the explicit resolution of the near-tip plastic fields and the enforcement of closure as a contact constraint, for the purpose of fatigue life prediction. In their finite element model the crack advances by shifting the near-tip mesh continuously. After every

remeshing, the displacements, stresses, plastic deformations and effective plastic strains are transferred from the old to the new mesh.

This study is similar to cohesive model but in this model the element bonding strength, surface energy are used to set the criterion of crack propagation. Further the technique used in the finite element model is different from other models. It should be pointed out that the past use of finite element analyses had certain shortcomings and recent versions have been tremendous improvements and have removed many of these limitations. For example, to avoid numerical instability, schemes such as releasing the crack tip node at the bottom of a loading cycle were adopted in certain studies, e.g. [Wu and Ellyin, 1996]. They have not considered element bonding stress and surface energy, which are associated with crack formation and extension. They also did not consider the material properties change during cyclic loads. They applied symmetric boundary conditions at the crack plane and also assumed that the crack can propagate only in symmetric planes. In this study, a crack can propagate in both symmetric and anti-symmetric planes about the applied load.

2.4 Linear Elastic Fracture Mechanics and Stress Intensity Factor Calculations

It has been known that fatigue performance of welded structure is dependent upon local effects, such as local stress field, defect conditions and material properties. Since the defect conditions of welded structures are in most cases so severe that the crack initiation phase can be neglected, linear elastic fracture mechanics (LEFM) principles can be used to evaluate the fatigue crack growth behavior and thus, to predict fatigue life of welded structures. In order to appropriately assess fatigue crack growth process in welded joints it is necessary to obtain accurate results for stress intensity factor solutions in the crack propagation phase. Generally the stress intensity factor for a crack in a welded joint depends on the global geometry of the joint which include the weld profile, crack geometry, residual stress conditions and the type of loading.

Therefore, the calculation of the stress intensity factor, even for simple types of weldments, requires detailed analysis of the several geometric parameters and loading systems. The two approaches that have mostly been used till now for assessing stress intensity factors for crack in weldments are weight function method and the finite element method (FEM).

The numerical approach is based on basic weight functions applied for stress intensity factor calculation:

$$K = \int_0^a \sigma(x) m(x, a) dx \tag{2.3}$$

The stress distribution, σ(x) can be calculated by FE method. Weight function m(x, a) have been derived by Bueckner [1970] and Newman and Raju [1986] for 2-D and 3-D model edge crack and surface semi-elliptical crack in finite thickness plate, respectively. Concerned about the effects of weld profile geometry factors on local stress intensity factor evaluation, Niu and Glinka [1987] developed weight functions for 2-D models with edge and surface semi-elliptical cracks in flat plates and plates with corners. Although the derived functions exhibited validity against available literature data it is still an approximation method because the 3-D nature of weld geometry is ignored. Based on the Buckner's weight function, Nguyen and Wahab [1995] created a semi elliptical crack model for the stress intensity factor calculation on butt weld joints considering all weld geometry parameters. Using this model and Paris law, fatigue life of butt weld structures can be estimated. As a numerical approach, weight function methods require huge calculations, which is time consuming and inconvenient for practical engineering applications.

The applications of the finite element methods to determine crack tip stress field has developed rapidly in recent years. The method has great versatility: it enables the analysis of complicated engineering geometry and three-dimensional problems. It also permits the use of elastic-plastic elements to include crack tip plasticity. Basically, two different approaches can be followed in

employing finite element procedures to arrive at the required stress intensity factor. One approach is the direct method in which K follows from the stress field or from the displacement field around the tip of fatigue cracks [Anderson, 1995]. Equation (2.4) describes the calculation process for determining Mode I stress intensity factor solutions using crack tip stress field (different modes of loading has been explained in chapter 4):

$$K_I = \lim_{r \to 0} [\sqrt{\sigma \pi r}]\text{; where r is the distance from the crack tip.} \quad (2.4)$$

The stress intensity factor can be inferred by plotting the quantity in square brackets against distance from the crack tip, and extrapolating to r tends to 0. Alternatively, K_I can be estimated from a similar extrapolation of crack opening displacement.

$$K_I = \frac{2\mu}{k+1} \lim_{r \to 0} [u\sqrt{\frac{2\pi}{r}}] \quad (2.5)$$

k = 3-4ν (plane strain)

k= (3-ν)/(1+ ν) (plane stress)

where u is the crack opening displacement, μ is the shear modulus and ν is the Poisson's ratio. Equation (2.5) tends to give more accurate estimates of K than equation (2.4) because nodal displacement can be inferred with higher degree precision than stresses.

The second approach for K calculation comprises some indirect methods in which K is determined via its relation with other quantities such as the compliance, the elastic energy [Glinka, 1979] or the J-integral [Rice, 1968].

By means of advanced FEM, it is possible to build a 3-D FE model [Charmahini et al., 1988] for accurate stress intensity factor calculation on welded joints. Bowness and Lee [1996] carried out a 3-D FE study of stress intensity factor solutions for semi-elliptical weld toe cracks in T-butt welded joints. The method of displacement extrapolation was chosen for associated stress intensity factor calculation under membrane and bending loads. Values for the weld toe magnification factor

(WTME) which is described as the ratio of the stress intensity factor for the T-butt welded plate to that for the flat plate were derived in terms of crack depth, crack length and basic plate thickness. WTMF values were found to decrease when cracks grow in depth and length.

2.5 Weld Residual Stress (WRS) and Its Effect on Fatigue Life

Weld residual stress (WRS) introduced by the welding process can come from the expansion and shrinkage of weldments during heating and cooling, misalignment and microstructure variation in weldments and Heat-Affected-Zone (HAZ). Residual stresses in weldments have two effects. Firstly, they produce distortion, and second, they can be the cause of premature failure especially in fatigue fracture under lower external cyclic loads [Weisman, 1976].

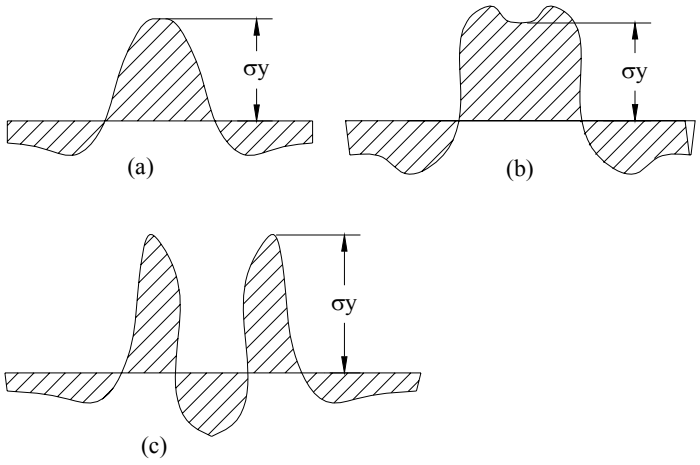

Figure 2.2 Typical longitudinal WRS distribution at butt weld [Wu, 2002]
(a) mild steel (b) Aluminum alloy (c) high alloy structure steel.

It has been confirmed by Bucci [1981] that WRS is quite large and will be tensile in the vicinity of the weld, where their magnitude is approximately equal to the yield strength of the weld metal, as shown in Figure 2.2. Some researchers confirmed that tensile residual stresses could significantly decrease the fatigue properties on welded joints. On the other hand, compressive stresses on the surface of weldments can significantly improve the fatigue strength of welded

structures. Itoh et al. [1989] studied the effect of residual stress on fatigue crack propagation rate in longitudinal welded residual stress field and found that the effect of crack growth rate in weld residual stress field could be evaluated in terms of the effective stress intensity range, based on the measurement of effective stress ratio and crack opening ratio. Kang et al. showed [1990] that the effective stress intensity factor and the effective stress ratio can be applied to predict fatigue crack growth rate in both tensile and compressive residual stress field by using base material's crack growth rate data with different stress ratio. Bucci [1981] investigated the effects of residual stress on fatigue crack growth measurement. He pointed out that during crack growth the crack opening load is required to offset compression at the crack tip caused by the superposition of clamping force attributed to the residual stress and crack closer.

Kosteas [1988], in a review of residual stress and its effect on the fatigue behavior of Al-5083 and Al-7020 welded components, reported that the magnitude of WRS reached up to the 0.2 times yield-limit in the HAZ for as-welded joints. He applied the hole drilling method with strain gauge rosettes to measure WRS in the position approx. 1.0 mm off the weld toe. Measurements at butt beam splices showed WRS values between 120 and 140 MPa.

Weld residual stresses have been known, after many years research, as one of the most critical factors, which can significantly influence the fatigue properties of welded joints. Many researchers [Ohji et al., 1987, Berkovis et al., 1998, Glinka, 1994, Weisman 1976, Radaj, 1992, Kosteas, 1988, Webster, 1992, Maddox, 1993] have reported on the basis of their experiments that the magnitude of the highest tensile residual stress may approach the yield strength of the parent material in some critical locations of weldments.

Nordmark et al. [1987] studied fatigue crack growth in CT specimens taken from the weld metal, heat affected zone (HAZ) and base metal of Al-5456-H117 of butt welded plate. Crack opening displacement measurements were taken during the fatigue crack growth tests so that the

effects of crack-opening loads and residual stress could be determined. On the basis of ΔK_{nom} the crack growth rates were investigated from the lowest to the highest in the heat affected zone, the base material and the Al-5456 welded metal respectively. However the use of Elbers's concept of effective stress intensity range, based on the measurement of crack opening loads, indicated that the crack propagation rates in the weld metal, HAZ and base metal were nearly equal. He finally concluded that the different fatigue crack growth rates measured for the three materials are the result of differences in the weld residual stresses.

2.6 Approaches for Evaluation of Fatigue Crack Growth in Welded Joints

For many years fatigue crack growth experiments have been carried out based on ASTM standard E-647, which is designed for normal uniform materials. Two types of specimens, compact tension (CT) and center crack tension (CCT) are recommended in this code for da/dN testing. Stress intensity factors are calculated in the form, $\Delta K = (K_{max} - K_{min})$ by empirical relations derived from finite element analysis. Although this method has been confirmed to give good results for normal uniform materials, it still needs to revise for determining fatigue crack propagation behavior in welded joints. Many researchers [Linda, 1990, Kang and Earmme, 1989, Nguyen and Wahab, 1995] have pointed out that, for welded joints, weld geometry factors and weld residual stress (WRS) can significantly affect the final crack growth data in the corresponding fatigue experiments. It has been confirmed by some researchers [Newman and Raju, 1986, Linda, 1990] that the acceptable methods for da/dN testing in welded joints are those replacing the normal stress intensity factor range, ΔK, by the effective stress intensity factor range, $\Delta K_{eff} = (K_{max} - K_{open})$, which accounts for the influence of crack closure and weld residual stress.

To obtain effective stress intensity factors in the presence of weld residual stress field, crack opening load, $\sigma_{open,}$ has to be determined. The σ_{open} can be estimated by analyzing the fatigue

loads crack opening displacement (COD) curve (fig. 2.3), which can be traced during fatigue crack propagation using COD gauges.

Several different approaches have been employed by investigators [Flec, 1984, Donald, 1988] for the determination of the crack opening load point $\sigma_{open,}$ including the lowest tangent point of the upper slope, the intersection of the tangents of two slopes, a compliance differential method, and a point of predefined deviation from the upper slope.

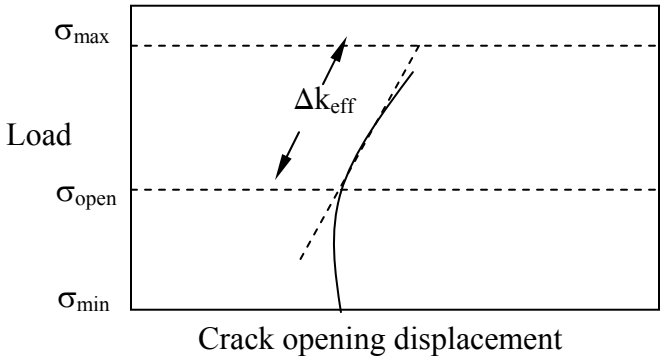

Figure 2.3 Load versus Crack opening displacement curve.

Donald [1988] developed constant and automatic method for global crack closure evaluation using predefined slope deviation. The approach compares each slope segment with the linear region of the load-displacement curve and computes the percents change in slope. He identified the slope segments corresponding to a deviation (offset) of greater than 1, 2, 4, 6 and 16 % from the linear region of the compliance curve. Applying this approach he obtained an excellent agreement between ΔK_{nom} at high stress ratios, wherein the crack closure is small and ΔK_{eff} at lower stress ratios, where the crack opening stress can be much higher than the minimum applied stress. However, in the near threshold regime, this agreement breaks down. As a result, the closure level corresponding to a 2 % change in the load displacement trace is suggested for determining ΔK_{eff} above near threshold regime.

2.7 Fatigue Crack Growth in Welded Joints

Considering fatigue crack growth in welded joints, the percentage of the crack propagation phase in the total fatigue life is very much dependent on the quality of the weld comprising weld geometry, initial defects in the weld, weld residual stresses and local stress conditions. Since welding defects can frequently exist in the vicinity of weldments, local stress concentrations around discontinuities and weld defects are fairly common. These crack-like defects begin to grow almost immediately when subjected to external cyclic fatigue loads, so that, for welded joints, the total fatigue life is mainly dominated by the crack propagation phase. Murthy et al. [1994] investigated the fatigue crack initiation and propagation behaviors of welded steel tubular structures. The results obtained indicated that the crack growth life was 75% to 89 % of the total life for all the welded joints tested. It has been confirmed by other researchers [Kapadia, 1978, Masubuchi, 1980, Nagamoto et al., 1987] that tensile residual stress can significantly decrease the fatigue properties on welded joints. On the other hand, compressive stresses on the surface of weldments introduced by post-weld treatment can significantly improve the fatigue properties of welded structures. Previous investigations [Nguyen and Wahab, 1995, Chitoshi et al. 1986] have indicated that WRS also has significant effects on the fatigue crack initiation phase and the early stage of crack propagation. Itoh [1989] studied the effects of residual stress on fatigue crack growth rate in longitudinal welded residual stress of C-Mn-Si steel and austenitic stainless steel.

Nagamoto et al. [1987] studied fatigue crack growth behavior of Al-5083 base and MIG welded plates. It has been shown that the crack growth in the base material was faster than in the welded specimens. Other researchers [Maddox, 1974, Benoit et al., 1978, Davis and Czyryca, 1981] obtained similar results in investigation on un-welded plates and weldments of steel. However, these da/dN results cannot explain the lower fatigue limit for weldments than for unwelded plates indicated by conventional S-N curves. Linda [1990] investigated fatigue crack

growth behavior in butt weld joint of Al-5456-H116 aluminum alloy and ASTMA 710 steel. Crack closure levels were determined graphically using the upper tangent point, and non-subjectively by measuring the 2% deviation from the upper linear portion of P-COD traces. The experimental results showed that the da/dN curve, when using the effective stress intensity factor range, shifted to faster growth rates in welded plates compared to the base plate. Crack closure loads of up to 80 % of the maximum load were measured in both Aluminum and steel welded specimens. These closure levels were mainly created by the presence of weld residual stress (WRS). For stress relieved steel specimens, the fatigue growth rate shifted to rates equivalent to those of the base plates. It was concluded in the paper that applying effective stress intensity factor, taking into account of weld residual stress effects, results in more accurate estimations of fatigue life in welded joints.

Bucci [1981] investigated the effects of residual stress on fatigue crack growth measurement. The fatigue crack growth tests were conducted on residual stress relieved and non-stress-relieved aluminum alloys using the ASTM standard test method (ASTM E647-78T) [1995]. He pointed out that during crack growth the crack opening load is required to offset compression at the crack tip caused by the superposition of clamping force attributed to the residual stress in the bulk material and the forces caused by crack closure described by Elber [1970]. The residual stress influence of da/dN could, therefore, be evaluated using the concept of effective stress intensity factor, which assumes that propagation occurs only when the crack is completely open. He also found that the influence of residual stress leads to erroneous interpretation of fatigue crack growth rate measurements made in accordance with standard ASTM E-647.

Bell and Vosikovsky [1992] conducted research work on the fatigue crack initiation and propagation behavior for multiple cracks in welded T-joints for offshore structures. The observations in the experiments showed that many semi-elliptical cracks initiate along the weld toe

and progressively coalesce as they developed into fewer large cracks. It was also noted that crack coalescence accounted for a significant portion of the propagation life. Based on the experimental observations an empirical crack shape development equation was created to account for crack coalescence at the weld toe. This empirical relation was defined by the following function:

$$\frac{a}{c} = e^{-\kappa a} \tag{2.6}$$

where a and c denote crack dimension in surface and depth directions respectively. The coefficient κ is a function of stress level and welds toe geometry. For constant amplitude load the coefficient, κ, can be correlated with a single parameter, the weld toe peak stress, $S_{p,}$ which reflects the geometry and thickness effects. This power relation was given by:

$$\kappa = 2.09 \times 10^{-6} \times (S_p)^{1.95} \tag{2.7}$$

The weld toe peak stress, S_p, can be calculated by empirical relations for stress concentration on welded joints or by finite element analysis. It had been shown that using crack coalescence model and Paris law gave the most accurate prediction of fatigue life for these joints.

2.8 Factors Affecting Fatigue Crack Growth in Welded Joints

Although fatigue crack growth graphs are negative characteristics of materials, many factors have to be taken into account when fatigue crack growth data (curves) are to be measured or to be applied for fatigue life prediction, especially in welded joints. Some such factors are described below.

2.8.1 Weld Geometry

It has been known that fatigue crack growth behaviors of welded joints are highly dependent not only on the materials and load conditions but also on weld geometry such as weld toe angle (α), weld toe root radius R_t, plate thickness (t), width of the weld reinforcement (w) and height of reinforcement (h).

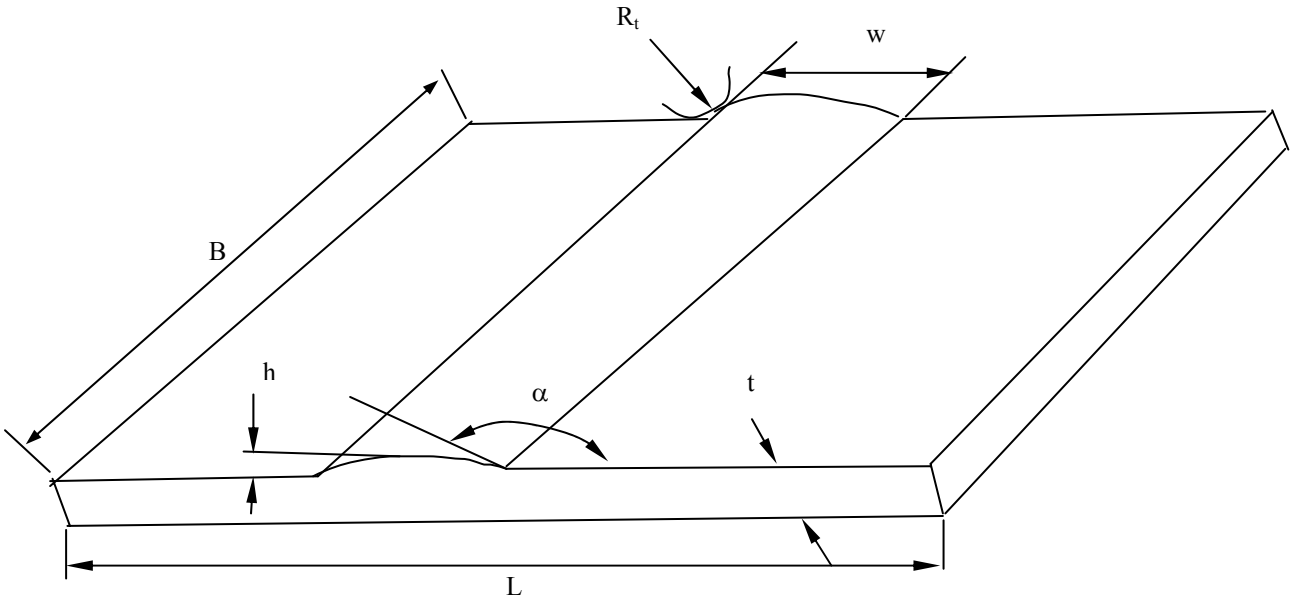

Figure 2.4 Weld geometry parameters at butt-weld joints

Ferrica and Branco [1990] investigated the effects of weld geometry factors on the fatigue properties of cruciform and T-weld joints. The results showed that the ratio of thickness of main plate and the radius of weld-toe (t/R_t) are the most important factors for the fatigue properties of welded joints. As the thickness of plates reduces, the fatigue strength and life will increase in the case of T and cruciform joints. These results have been confirmed by other researchers [Ohta et al., 1990, Bimalendu, 1993]. Sanders [1977] studied GMAW as welded butt welds in 25-30 mm AA5083-O, AA5083-H116, AA5456-H116 and AA5456-H117 Aluminum alloys. The investigations concluded that the angle at the toe of the reinforcement is the most critical factors in the determination of the fatigue life of as welded joints and actual maximum stress at the weld toe. Sanders [1977] and Lawrence et al. [1978] also reported that the removal of weld reinforcement may increased fatigue life, whether exposed to air or seawater, it care is taken to prevent surface defects during the bead-removal process. Niu and Glinka [1987] derived an empirical relation, accounting for the stress concentration K_t at weld toe, by finite element methods:

$$K_t = 1 + 0.512\alpha^{0.572}\left[\frac{t}{R_t}\right]^{0.469} \tag{2.8}$$

where α is the weld angle, t is the plate thickness and R_t is the weld toe radius.

Sanders and Gannon [1974] studied the effect of distributed porosity on the fatigue resistance of Al-5083-0 double V-groove butt weld joints. He reported that the welds with their reinforcement removed were more sensitive to porosity compared with the weld with reinforcement intact, although the former gave longer life than as welded joints when porosity level was lower. In other words, when a relatively higher level of weld inner-defects such as porosity, inclusions, lack of fusion and lack of penetration, exist in weldment, welds with bead reinforcement removed may exhibit shorter life than those of welds with bead on. This situation could be fairly true for weldments with a high level of weld inner-defects, for example weld repaired structures. Therefore the as-welded joints can exhibit different fatigue crack growth performance behavior compared to that of the weld with bead reinforcement intact, depending on the situation. Since most of the available fatigue crack growth data at the present time, have been obtained using specimens with weld bead reinforcement removed, this data can not represent the actual fatigue crack growth behavior in as-welded joints and will lead to erroneous prediction of fatigue life.

Nguyen and Wahab [1993] studied the effect of various weld geometry parameters on stress intensity factor and fatigue life of butt weld joints. They developed an analytical model to predict fatigue strength of welded joints subjected to co-influence effect of butt weld geometry parameters. They concluded that the value of stress intensity factor is strongly influenced by weld profile geometry factors such as weld toe radius, flank angle and plate thickness. The effect of plate thickness on stress intensity factor and fatigue strength is less significant compared to that of weld flank angle and the weld toe radius.

2.8.2 Weld Defects and Weld Metallurgy

Weld defects are those imperfections or discontinuities produced in the weldments because of the weld process, such as porosity, lack of penetration, slag inclusions, incomplete fusion, misalignment, undercut, weld profile etc. These weld defects can significantly influence local stress field in the vicinity of welds when the welded component is subjected to cyclic fatigue load. In most cases, weld defects lead to severe stress concentration and thus accelerate fatigue crack growth. Sanders and Lawrence [1977] studied the effects of lack of penetration (LOP) and lack of fusion (LOF) on the fatigue behavior of Al-5083-0 double-V groove butt welds. They concluded that LOP defects can seriously reduce the fatigue life of both types of weld, those with the reinforcement intact and those with the reinforcement removed. Less than full length, inclined LOF defects were generally less serious than LOP defects. Sanders also reported that the effects of internal discontinuities on fatigue performance of welds with reinforcements are minimal. The effect of weld reinforcement is so marked that only critical defects would affect the fatigue behavior and this is related to the loss of cross section area. Porosity only becomes a factor when the reinforcement is removed.

Weld toe cracks are often found in many important welded structures. The ability to assess the effects of these defects on fatigue life of the welded structures is therefore of practical significance. To carry out this assessment, it is necessary to have reliable stress intensity factor solutions. Existing stress intensity factor solutions are mostly derived from 2-D plane strain models containing edge cracks. However it has been recognized that fatigue cracks on the weld toe cannot be accurately represented by 2-D models because the effects of weld profile geometry are not taken into account. Some researches [Murthy et. al., 1994] have therefore been carried out using 3-D numerical modeling, which highlights the limitations of 2-D approach. Due to exceptional characteristics of the weld process, more factors, such as weld geometry, weld residual stresses

(WRS), metallurgical/microstructure changes and welding defects have to be taken into account when fatigue properties of welded structures are to be evaluated.

2.8.3 Materials and Welding Techniques

Chemical composition and condition of welding materials, including base metal and fillet material can directly affect fatigue crack growth rates of welded joints [Weisman, 1976]. Different materials have different mechanical properties and characteristics under cyclic loading. Phase change will occur in most kinds of steels when subjected to the welding process and residual stresses are introduced by these phase changes in areas like the weld toe and heat-affected zone. Generally these residual stresses tend to be tensile stress on hot spots and hence reduce the fatigue performance of welded joints. The magnitude of this influence is dependent on the type of material. However, in the case of austenite stainless steel and 5083 Aluminum alloys, no phase change occurs and hence no residual stresses due to phase change exist, although the latter may suffer substantial strength loss due to heating during the weld process. Different welding processes also have different effects on the fatigue properties of welded joints. Some welding methods such as submerged arc welding cause heavy heat input in the weld joints, producing higher thermal residual stresses. As mentioned previously, defects introduced during the weld process such as undercut, lack of fusion, lack of penetration, misalignment, porosity and poor profiles can also have significance influence on the fatigue properties of welded joints.

2.9 Distortion and Residual Stresses in Welding

The finite element modelling and simulation of welding has been extensively reviewed by Lindgren [2001]. He discussed the different aspects of finite element simulation of welding and also explained advantages and disadvantages of different techniques. Runnemalm [1999] also studied the finite element modelling and simulation of laser and gas metal welding. He used

adaptive meshing for three dimensional welding. He used quiet element approach and inactive element approach for modelling multi-pass welding.

Simulations where two-dimensional models are used still dominate the published work. This is partly due to the fact that they give useful results and partly due to the fact that three-dimensional simulations demand a large computing power if a good resolution is to be obtained. Michaleris at al. [1997] compared two-dimensional and three-dimensional models of a multi-pass butt-welded plate. They simulated the first pass with both models. The 2-D model had a larger fusion zone, despite a reduced heat input, and a larger zone with high tensile longitudinal stresses than the 3-D model. Michaleries and Debiccari [1997] transferred welding residual stresses obtained from a 2-D plane deformation model to a 3-D model of the structure in order to study weld-induced buckling. The first 3-D residual stress prediction of full weld appear to be by Lindgren and Karlsson [1988], who used shell elements when modelling a thin-walled pipe. Karlsson and Josefson [1990] modelled the same pipe using solid elements. The results from the different models were consistent. Nasstrom et al. [1992] made a first attempt to combine shell and solid elements in a model of weld. Gu and Goldak [1991] did the same but only for the thermal analysis. Dong et al. [1997] used shell elements in investigating the effects of wall thickness and welding speed on residual stresses of a pipe. They also implemented a layer activation/deactivation scheme in a composite shell element for simulating multi-pass welding [1997]. This was used in modelling a repair welds in a pipe [1998] and also for repair weld in panels [Dong et al., 1998 (1), Dong et al.1998 (2)]. Ravichandran et al. [1996] used a shell element to simulate the manufacturing of a T-beam by a one-pass fillet weld. They argued that the plane strain assumption is invalid for this case based on the results by Goldak et al. [1986]. Three-dimensional predictions of rotations and distortions in large welds were also performed by McDill et al. [1990], Tekriwal and Mazumder [1991]. Ueda et al. [1995] made three-dimensional simulations of a pipe-plate

joint. They studied the effect of the welding on the shape of holes and compared the use of instantaneous and moving heat sources around the circumference. Gu et al. [1997] used a 3-D model to investigate the out-of-plane deformation due to butt-welding of a plate where they account for gravity and different restraints.

The reviews by smith [1992] and Radaj [1992] include references to simulations performed up to 1992. The research in Japan is reviewed by Ueda et al. [1995] and Yurioka and Koseki [1997]. Simulation software used by different research groups are summarized by Dexter [1991]. Chandra [1985] reviews girth-butt welds in pipe somewhat; and more thorough review is given by Ravichandran [1997], who describes the use of finite element method for simulation welding of pipes. The research books published by Karlsson [1997], Masubuchi [1980], and Radaj [1992] had discussed useful information about welding simulation.

2.10 Restraining Forces in Welding

There have been significant amount of research on the measurement of residual stress and distortion. A significant contribution has been reported on the topics of residual stress and distortion by Koichi Masubuchi who compiled recent findings in book form in the international series on Material Science and Technology [Masubuchi, 1980]. These methods either measure free-distortion of an unrestrained plate or residual stress of a restrained plate after post weld cooling. Hideyuki Sunaga and Akitake Makinouchi [1998] developed method of modelling the drawbead effect as well as a method of estimating the restraining force as a function of the direction of drawbead line and geometry. They developed a specific apparatus to measure the drawbead force under a different clearance and different sheet sliding directions against the drawbead line. They also simulated the drawbead forming process to obtain a general understanding of the drawbead effect.

Jang and Lee [2003] proposed a method for predicting the welding deformation of large structures. The method uses both the inherent strain theory and the experimental results combined with the finite element method for accurate and efficient analysis. In the inherent strain theory, the residual plastic strain due to welding is defined as the inherent strain. Assuming the inherent strain is the initial strain, welding deformation can be easily calculated by elastic Finite Element analysis, omitting the complicated thermal elastic-plastic Finite Element analysis. Ueda and Ma [1995] described inherent strain for fillet joint by series function. Based on the series function, a simplified distribution pattern for inherent strains was derived. Jang and Seo [1996] estimated the inherent strain region and represented the inherent strain as a function of the mechanical melting temperature and the degree of restraint. The degree of restraint represents the level of resistance against the thermal deformation of the welding region. The degree of restraint of stiffened panel was determined from the analogy of the bar - spring model in the case of the simplified analysis model.

Murakawa et al. [1997] used a simplified analysis model to obtain the inherent strain. They represented the inherent strain as a function of the highest temperature and degree of restraint. However, this method has limitations in applying to complicated structures. Seo and Jang [1999] calculated the deformation of large structure using the unit loading method to obtain the degree of restraint. Tsai et al. [1999] studied the distortion mechanisms and the effect of welding sequence on panel distortion. In their study, distortion behaviors, including local plate bending and buckling as well as global girder bending, were investigated using the finite element method. It was found that buckling doesn't occur in structures with a skin-plate thickness of more than 1.6 mm unless the stiffening girder bends excessively. Warping is primarily caused by angular bending of the plate itself. The "Joint Rigidity Method (JRM)" was found to be effective in determining the optimum welding sequence for minimum panel warping.

For experimental weld ability studies taking into account predominantly the real structural effects on shrinkage restraint, the instrumented restraint cracking (IRC) test has been developed by Hoffmeister et al. [(Hoffmeister et al. 1987), (Hoffmeister and Harneshaug, 1987)]. The IRC test has the capability of continuous registration of the reaction forces and moments during welding and subsequent cooling. The test has extensively been applied to avoid cold cracking of linear welds and to investigate the effects of heat input as well as pre- and post heating on the reaction force and stress build up during cooling after welding of specifically restrained joints.

Britz and Hoffmeister [1987] investigated the effects of heat input and hydrogen- partial pressure of the TIG process without filler wire and of restraining conditions in the IRC (Instrumented Restraint Cracking) test on Hydrogen induced cracking for weld metals (StE 380, 15 NiCrMo, 10 6 (HY 80) and 12 Ni 19). In their study, the weld metals were fused from the roots of the plate materials exclusively. They found that the continuously measured combined nominal stresses transverse to the welds are strongly dependent on the transformation stress-release prior to cold cracking of the respective weld metals, and they also found that the higher restraint increases the nominal stresses. They found that the critical heat inputs for prevention of hydrogen weld metal cracking are increased with the given restraint conditions, hydrogen potentials, and carbon contents of the weld metal (12 Ni 19), revealing no fracture conditions. Potente et al. [2001] investigated the development of inherent stresses arising during welding by drilled-hole technique and finite element method. A rectangular plate and an actual rear car light geometry were investigated. In both cases there was a clear correlation between the inherent stresses induced and the welding parameters. In addition, by heating the parts prior to welding it was possible to reduce the level of inherent stresses in the component and this way it was possible to make a contribution towards the avoidance of stress cracking. Boellinghaus and Kannengiesser [2003] studied the effect of filler material selection and shrinkage restraint on strain build up in component welds.

They considered two cases, submerged-arc welded butt joints of structural steel plates and orbital TIG-welding of supermartensitic stainless steel tubular. They found that in both cases the forces and residual stresses transverse to the weld could significantly be reduced by selecting overmatching filler materials. Kannengieber et al. [2001] investigated the effect of weld metal strength and welding conditions on reaction forces and stress distribution of restrained components. In order to achieve a closer insight into the structural effects, component weld ability tests were performed by on-line monitoring of the reaction forces and moments. In particular, the effects of different values of the base material and weld metal strength on the reaction force and stress build up transverse to the welding direction were studied at a specific structural restraint. They found that the final reaction force and also the reaction stress level in the multilayer butt welds decreases with overmatch of the weld metal. Reaction forces and moments built up during welding and subsequent cooling were measured in a specifically designed large scale testing facility. Residual stresses were measured by the hole drilling technique after cooling of the specimens in the restrained as well as in the relieved condition.

2.11 Fatigue in Weld-Repaired Joints

In general, the success of the repair in weldments depends on the type of detail, the size and type of crack. Some experimental fatigue data from recent research on weld repair [Gibatein et al., 1987, Tubby, 1989, Haggensen and Slind, 1993] involving grinding combined with peening indicated that for shallow cracks the fatigue strength of the repaired weld can approach the strength of the unwelded plate. On the other hand, TIG dressing has been found, in some investigations [Miki and Takenouchi, 1989], to be more suitable for deep crack repairs than grinding. Nordmark et al. [1989] studied the advisability of repairing weld discontinuities in Al-5456-H116 transverse and longitudinal GMA butt joints. The investigations exhibited that weld repair of reinforcement-intact specimens reduced fatigue life by 40% to75 %, except when the weld reinforcement of the

repair was treated by grinding or by brush peeing. They also discovered in the experiments that reinforcement-intact repair welding of fatigue cracks was more effective for transverse joints than for longitudinal joints.

Nelson [1961] conducted the experiments on the effects of repeated repair welding on 5456H321 and 6061-T6 Aluminum. The specimens were welded and re-welded up to six times. He reported that the tensile properties across the welds were not significantly affected by the number of times the plates were re-welded. The width of the heat-affected zone (HAZ) was apparently not increased by the number of times of re-weld process. Weld repair, as an effective repair method, has been applied for crack repair in some parts of boats and commercial vehicles [Solsteel, 1993].

Various methods for repairing shallow surface cracks were discussed by Gurney [1979]. These techniques were investigated for the National Cooperative Highway Research Program [Fisher et al., 1979]. Techniques studied included grinding the weld toe, air-hammer peening, and gas-tungsten arc (GTA) re-melting the weld toe. These methods were applied to the ends of cover plates in full-scale welded girders in the laboratory and in the field. Weld toes were grounded in a very local region to remove small weld toe cracks. The cracks appeared as a fine line and the grinding was continued until the fine line was no longer visible without magnification. The results of these tests were mixed, and the technique was judged to be ineffective. Air-hammer peening of the local weld toe region was found to be a practical and reliable technique for repairing welds with cracks up to 3 mm deep and 50 mm long. Crack up to 4.5 mm deep can be repaired using the gas-tungsten arc re-melting procedure. Hole drilling, coring, or grinding are viable methods to remove entirely or blunt the tips of small through-thickness cracks.

A new low cost repair and strengthening method for steel offshore structures which offers potential savings in three areas: weight, installation and inspection requirements was presented by Williams and Ma [1993]. It out lines the evolution and development of the new patented technique

(the grouted stud/strap connection) from two existing and proven technologies, namely grouted pile-sleeve connections and stud friction welding. A testing program covering static strength and fatigue behavior of the connection was described which, on satisfactory completion, led to certifying authority approval of the new repair/strengthening method and associated design procedure.

The effects of repaired welding on tensile strength and fracture toughness of aged weldments of 18 Ni 250-grade maraging steel have been studied by Sinha et al. [1993]. It has established that aged weldments in the steel can be repaired and approximately 95% of the tensile strength of the initial welds could be achieved by post-repair aging treatment. They found that the repair had practically no effect on the fracture toughness of the weldments. The results have been discussed in terms of microstructural conditions in the various affected and unaffected zones of the initial weld.

Fatigue life of tubular joints in offshore steel structures under stochastic loading was studied by Agerskov and Ibso [1993). Fatigue test series with various types of stochastic loading that are realistic in relation to offshore structures have been carried through on both full-scale tubular joints and smaller welded test specimens. The test results obtained showed a significant difference in fatigue life, determined my Miner sum between constant amplitude and variable amplitude fatigue test.

A theoretical investigation of the effects of structural restraint, repair depth and wall thickness on the distribution of transverse residual stress at repaired welds in heavy-section plates and cylindrical structures was conducted using computer program by Leggatt [1991]. The applicability of the program was demonstrated by comparison with experimental measurements at a 28 mm deep repair weld in a 75-mm-thick carbon-manganese steel test panel. The computed stresses were in good agreement with the experimental results.

A study for the improvement of fatigue life of welded, weld repaired joints was conducted by Braid et al. [1997]. Improvements were gained by toe grinding, TIG dressing, shot peeing, and hammer peening. The core of the investigation was concerned with the fatigue strength of as-welded and weld-repaired longitudinal welds in T joints representative of stiffener in a ship with or with out hammer peening. The specimens were fabricated from 350 MPa grade structural steel and from 550 MPa steel. Both steels exhibited the same fatigue behavior in the as-welded conditions. The repair welding procedure used restored the fatigue strength to the original as-welded condition. Hammer peening improved the fatigue strength of the 550 MPa joints by 175% compared with the as welded condition.

Various types of repairs are discussed by Kelly and Dexter [1997] for fatigue cracks in marine structure, emphasizing the limited database on the fatigue performance of these repairs. Fatigue tests on full-scale welded beams showed that the original fatigues strength of various types of butt welds are all AWS category-D, regardless of the type of steel, whether they are two-sided or one-sided welds, with and without backing, and with and without the edges ground flush. Continued testing after vee- and weld repairs of the fatigue cracks indicate that vee- and weld repairs of through-thickness crack have the same fatigue strength as the original new butt welds, even after repairing the same location up to four times. The fatigue strength of weld access holes can also be nearly restored with repair welds of cracks.

A numerical study of a repair by flaw removal on a conventional welded joint was carried out by Rodriguez et al. [1998]. The repair profile was optimized with respect to the flaw and joint dimension in order to minimize the resulting stress concentration factor (SCF). Two dimensional (edge repair) and three dimensional (surface repair) finite element analyses were performed for the determination of SCF values and a graphical representation of results was presented. A relation between edge repair and surface repair was obtained. A study on underwater wet repair welding

and strength testing on pipe-patch joints was carried out by Wernicke and Pohl [1998]. The weldability and fatigue performance of pipe-patch connections were tested. The shape of the actual used repaired patch was optimized to the requirements of underwater wet welding at high tensile strength steels as BS4360 Gr 50 D. Steel materials in this grade showed problems in regard to high hydrogen susceptibility, and therefore cold cracking. The results of fatigue tests with as-welded and post-treated full-scale specimens were evaluated by means of the geometric stress approach. For ground welds, a longer life has been obtained in the tests. Especially hammer peening yields to a much more improved fatigue life due to high compressive residual stresses.

A new tensile testing technique for evaluating the overall effect of a repair weld on the strength of a welded joint was done by Rogers and Bynum [1998]. The new technique involves testing of "wide panel" tensile specimens which contain the full length of a repair weld within a longer initial weld, allowing the specimen to capture the combined effects of residual stresses, local strength degradation, and load distribution around a repair. The development of strains in the repair area of standard aluminum alloy specimens and new high-performance aluminum-lithium alloy specimens was observed and evaluated using photo-elastic material. The results of that evaluation showed an increased sensitivity to repair welding residual stresses in the aluminum-lithium alloy specimens.

Wu [2002] measured the fatigue crack growth rate during constant amplitude fatigue testing on un-welded, welded and weld-repaired specimens of Al-5083-H321 aluminum alloy. It was found that crack growth rates in welded plates were the same order of the magnitude as those of parent materials when effective stress intensity factors were applied. However weld repaired plates exhibited higher crack growth rates compared to those of un-welded and once-only welded plates.

Crack growth data of weld repaired structures under fatigue loads is necessary for the application of fracture mechanics methods to evaluate the effects of weld repair and calculate

residual life of weld repaired structures. Therefore, the investigation of fatigue crack growth behavior of weld-repaired structures is of significant importance.

2.12 Fractrographic Examination

A study on crashing aircraft was reported by James [1999]. A Piper PA36-375 Pawnee Brave crop duster aircraft suffered an accident during landing, in which the main landing gear collapsed. The aircraft had flown a total of some 4217 hours at the time of the accident, and had completed about 88 hours since a rebuild. The owner stated that during touchdown, he noticed something passing under the aircraft on the left side. The aircraft then collapsed onto its belly and slid to a halt, causing extensive damage. The failure had involved fracture of both lower saddle brackets and the two main attachment bolts, which allowed the landing gear legs to rotate round and collapse. The main landing gear was found on the runway some distance from the final position of the aircraft, while the right main leg was located beneath the aircraft. Each main landing gear leg is in the form of a one-piece steel leaf-spring strut, which is attached to the fuselage frame by an outboard saddle clamp assembly and a single inboard attachment bolt. The saddle clamp assembly comprises a pair of 'L' shaped clamp halves, fitted back-to-back with a corresponding pair of 'L' shaped plastic pads fitted inside the clamp halves. These prevent fretting contact between the saddle clamps and the spring blade, and assist in uniform spreading of the contact pressure.

Fractography examination of the landing gear and saddle components showed that failure was due to fracture of the lower saddle clamps at the change of section from the strap element to the bolt housing, coupled with fracture of the inboard attachment bolts. As is normally the case in aircraft failures, the fracture surfaces were inspected to see if any evidence of fatigue crack growth could be found. The bolt fracture surfaces showed the cup and cone appearance typical of ductile overload. Both of the lower saddle clamp brackets, however, showed clear evidence of fatigue

crack growth initiating from their upper surfaces. Significant corrosion damage was present on the fatigue regions, indicating that the cracks had been present in the components for some time.

Chowdhury et al. [1998] studied failure analysis of a weld repaired steam turbine casing using scanning electron microscope (SEM) equipped with the dispersive X-ray analysis (EDX) facility after 5 years of repair. The base metal, a low alloy ferrite steel with ferrite-pearlite structure, did not show any abnormality to indicate significant degradation. Fracture surface showed voids and micro-cracks. They concluded that the cracks might have initiated from the voids present in the weld region possibly by thermal fatigue mechanism. The propagation of cracks generated by thermal fatigue was facilitated by the formation of embrittled σ-phase at the austenite grain boundary and this ultimately led to an early failure of the casing.

Park [2004] studied fatigue failure surface of aluminum 2024-T-3 alloy using SEM. He found a gradual transition in failure mode from tensile mode (ductile) to brittle on the surface. He also found that a ductile failure mode is prominent as the crack grows trans-granularly through the materials.

2.13 Conclusions

Assessment of structural integrity is a useful tool to avoid catastrophic failure of any structures. Proper evaluation of fatigue crack propagation life is necessary for assessment of structural integrity. There are much works available in literature about fatigue crack growth. In finite element method, the cracks do not generally propagate with each cyclic load. Because materials do not remember load history during cyclic load, the properties of materials are not changed after cyclic load. Therefore, in traditional finite element methods, the crack tip mesh is redefined or the crack tip node is released in each cycle and the crack tip extends one element length per cycle when the applied stress reached the maximum level**.** But in reality, crack propagation is non-linear phenomenon and crack advance takes place in very small increments

over many cycles. To reduce this limitation, the interface element (a new approach) is used in this analysis. Basically in crack formation and extension, failure is the consequence of new surface formation accompanied by crack extension. The crack is formed when the applied stress exceeds the critical bonding strength of the material. The bonding strength decreases with cyclic load and progressively becomes weak. Finally the bond loses its strength and breaks; and cracks form and extend slowly. The total stiffness of the material decreases with the decreases of bonding strength. As the cyclic load continues, the stiffness decreases and the crack propagates slowly. Therefore, there is a close relationship between the bonding strength and crack propagation. Based on this idea, interface elements (nonlinear element) are used between the crack faces, which explicitly model the formation of new crack surfaces.

The effects of welding defects on fatigue life have been studied by many researchers. But study about the interaction between a surface crack and an embedded crack (porosity) under bi-axial loading has not been found in literature at this time. Therefore, an attempt is made to find the effect of welding defects and bi-axial interaction of a circular porosity and a solidification crack on fatigue crack propagation life of butt-welded joints.

Finite element analysis of manufacturing process such as welding is computationally demanding. Some numerical works about simulation of gas metal arc welding are available in literature. Some researchers used adaptive meshing technique, a mesh with a fine region that is moving with the heat source. This solution requires some kind of re-meshing capability. Some researchers used inactive element approach which requires the re-structuring of data each time the model is extended. The elements and nodes that corresponding to weld not laid are not included in the finite element model. All elements corresponding to welds to be laid are defined at the start of the analysis. Thus, their locations have to be defined on the original geometry. The user defines the cross-section of each weld pass and the code will find all elements with their center within this

polygon. There is one complication with this approach. All nodes have their initial locations specified by the user. The structure will deform as the analysis goes on and it is likely that nodes that are included in the model when all elements are activated will cause these elements to be too deformed. In this study, a quiet elements approach using birth and death option in Ansys is used. The welds that have not yet been laid, is included in the computational model. These elements are made passive at the start of analysis. These elements have temperature dependent material properties. As the analysis is started, the temperature increased and the material properties of these elements are changed. This approach is easy to implement in most finite element codes and it also allow the nodes in the interior of the passive elements to move with the structures. This approach has been used by other researcher [Runnemalm, 1999]. There are much works on weld distortions and residual stresses but very few works are available about restraining forces of weld. Therefore an effort for calculating restraining forces is made in this work.

From the available research, the effects of weld repair techniques on the variation of fatigue crack growth behavior still remain unclear although these effects are critical for fatigue life evaluation of weld repaired structures. In order to evaluate the improvement in fatigue life of weld-repaired structures, fatigue crack propagation data should be determined first. Unfortunately at this time limited works have been reported in this field. Therefore, some weld- repaired works will be performed in mild steel flat and curve plates butt-weld joints.

Few studies [Park, 2004, James, 1999, Chowdhury at al., 1998] are found about fractography examination of the failure surfaces of welded structures but works about weld repaired structures are rare. Therefore, at the end of fatigue test, samples will be cut from the fracture surfaces of typical un-welded, welded and weld repaired specimens and examined with Scanning Electronic Microscope (SEM).

CHAPTER 3 WELD AND WELD DEFECTS

3.1 Introduction

Early researches have generally established that the fatigue life comprises of two phases: crack initiation and crack propagation. In smooth specimens the crack initiation phase comprises of a considerable proportion of the total life. But for welded structures, the presence of weld imperfections such as slag inclusions at welds toes, undercut, residual stresses, lack of penetration, misalignment, etc., effectively reduce the initiation phase [Berkovis et al., 1998]. All welded joints contain small slag inclusion at the weld toe [Nordmark et al., 1987], which acts as pre-existing cracks and stress-raisers. Fatigue crack propagation commences from these inclusions very early in the life. The welded joints also contain "locked-in" tensile residual stresses that arise due to incompatible thermal strains caused by heating and cooling cycles of welding process, contribute to fatigue crack propagation life. Welded joints almost always result in stress concentration associated with weld geometry and the presence of welding defects. This local stress concentration influences the fatigue crack propagation. The results of a study [Murthy et al., 1994] indicated that crack propagation life was 75% to 89% of the total life for all types of welded joints tested. Hence, for welded joints, the entire life may be assumed to be dominated by fatigue crack propagation. The welded structures also experience bi-axial loading during service life. In fatigue process, the interaction between a surface crack and an embedded crack (porosity) may normally happen.

Fitness-for-purpose is now widely accepted as the most rational basis for the assessment of weld imperfections, such that an imperfection would need to be repaired only if its presence is harmful to the integrity of the structure [Maddox, 1994]. To justify the integrity of welded structures, it is necessary to estimate the fatigue life of welded joint containing the imperfections and to compare it with the required life. Therefore, this study makes an attempt to find the effect of

welding defects (some work has been published in [Wahab and Alam, 2004]) and bi-axial interaction of a circular porosity and a solidification crack on fatigue crack propagation life of butt-welded joints (some work has been published in [Wahab and Alam, 2003]).

3.2 Weld Imperfections

The major weld imperfections include porosity, lack of penetration, lack of fusion, slag inclusion, undercut, misalignment etc. [Maddox, 1994]. The size and frequency of imperfection depend on the welding process, weld procedure, geometry of weldment including ease of access for welding, and the care exercised in making the weld. These imperfections have different characteristics and, in most cases, are difficult and costly to detect and define nondestructively. The majority of fatigue cracks in welded structures originate at a weld toe or a weld termination rather than from internal imperfections.

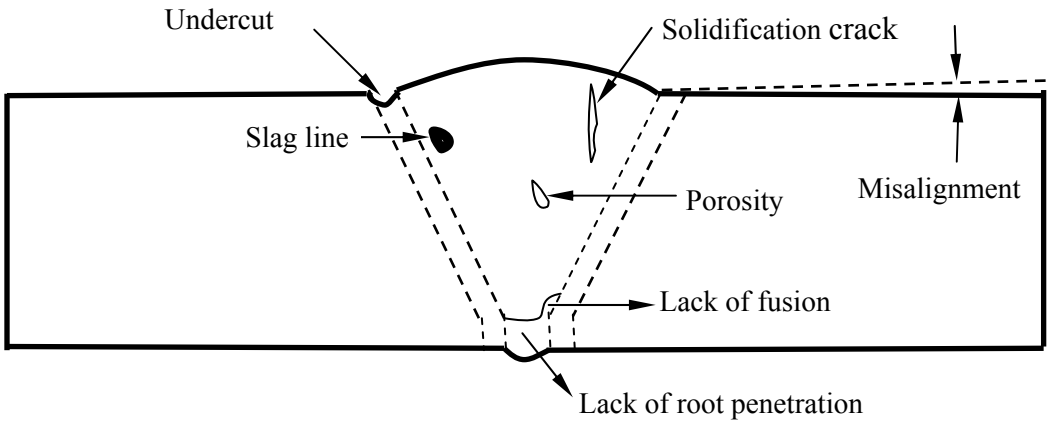

Figure 3.1 Different weld imperfections in a butt-joint [Maddox, 1994]

This behavior is attributed to the fact that for a given fatigue life, a much larger embedded imperfection can be tolerated than a surface imperfections [Barsom, 1994]. Different weld imperfections as described by Maddox [1994] are shown in Fig. 3.1. The welded joints also contain residual stresses that arise due to incompatible thermal strains caused by heating and cooling cycles of welding process and affect the fatigue crack propagation life.

It is mentioned earlier (section 2.5) that welding introduces a self-balancing residual stress system in and around the weld [Maddox, 1994]. Tensile residual stresses can reduce fatigue strength and fatigue life whereas surface compressive residual stress may increase the fatigue life. Tensile residual stresses are combined with the applied stresses to change the effective mean stress and hence the fatigue propagation life decreases.

3.3 Fatigue Crack Growth with Weld Defects

Fatigue crack growth rate is usually analyzed in terms of fracture mechanics by using relations involving stress intensity factor. The most accepted approach to the analysis of fatigue crack propagation by linear-elastic fracture mechanics is to use a semi-empirical power law, called Paris' law which has been explained in section 2.2 (equation 2.1. Paris' law only represents the linear phase of crack growth curve (region II in fig. 2.1)). Crack growth for the region II and III together is calculated using Forman equation (equation 2.2).

The number of cycles required to propagate a crack from an initial crack size a_o, to a final crack a_f, can be calculated by integrating the Forman equation (equation 2.2):

$$N_p = \int_{a_o}^{a_f} \frac{(1-R)K_c - \Delta K}{C(\Delta K)^m} \tag{3.1}$$

For 3-D model under bi-axial load (combined torsion and axial) the effective stress intensity factor is calculated according to following equation:

$$K_{effective} = \sqrt{K_I^2 + K_{II}^2 - \frac{K_{III}^2}{(1-\upsilon)}} \tag{3.2}$$

where, ν is Poisson's ratio and K_I, K_{II}, K_{III} are the stress intensity factors for mode I, II, III respectively (Different modes have been explained in Chapter 4).

The essential part of these calculations is to calculate the stress intensity range, ΔK. An equation of the form $\Delta K = Y\Delta\sigma\sqrt{\pi a}$ is usually assumed to relate the range of stress intensity

factor, with the nominal stress range, $\Delta\sigma$ and with the crack length, a; Y is a factor related to the specific geometry in question.

In order to appropriately assess fatigue crack propagation in welded joints it is necessary to obtain accurate results for stress intensity factor solution in the crack propagation phase. Generally the stress intensity factor for a crack in a welded joint depends on the global geometry of the joint, which include the weld profile, crack geometry, residual stress condition, the properties of HAZ material and the type of loading. Therefore, the calculation of the stress intensity factor, even for simple types of weldments, requires detailed analysis of several geometric parameters and loading systems. The two approaches that have mostly been used till now for assessing stress intensity factors for crack in weldments are the weight function method [Bueckner, 1970] and the finite element method (FEM).

The FEM enables the analysis of complicated weld geometry due to its great versatility. It is able to use elastic-plastic elements to include crack tip plasticity. In FEM the stress intensity factor can be calculated directly from the stress field or from the displacement field around the crack tip. In this study FEM has been used for calculation of stress intensity factor.

3.4 Finite Element Model

A 2-D finite element model of single-V butt-welded joints [Wahab and Alam, 2004] has been created by ANSYS 7.1 input file to study various weld imperfections such as solidification crack, undercut and porosity. It is already mentioned that the magnitude of the stress intensity factor at the tip of crack in the weld region is also affected by factors other than the weld geometry, such as the presence of residual stresses and the changes to the material properties in the heat affected zone. In this model, the combined influences of these factors have been studied and are included for final analysis. The properties are collected from available literatures [Burk, 1978 and Leggatt, 1991]. Cyclic axial and bending loads are applied in the model. The magnitude of axial load near

yield strength (280 MPa (40.610 ksi)) and the magnitude of bending stress are assumed approximately equal to 8 % of yield strength.

A crack- tip- node release scheme as suggested in [Newman, 1977], in which, a change in the boundary condition was characterized for a crack growth has been considered. Since 2-D model cannot represent torsional loading (the applied torque acts rotational rather than translational direction), a 3-D model [Alam and Wahab, 2003] has also been created to study bi-axial loading (torsion and cyclic axial). Since bending stress results from angular weld distortion, its effect has been incorporated into loading the model. In addition to axial and bending load, torsional shear load about 1% of yield strength are also applied in this model. For interaction of bi-axial crack configuration, the porosity is considered stationary and the solidification crack is moving toward the porosity.

In linear elastic problems, it has been found that the displacements near the crack tip (or crack front) vary as $1/\sqrt{r}$, where r is the distance from the crack tip. The stresses and strains are singular at the crack tip, varying as $1/\sqrt{r}$. To pick up the singularity in the strain, the crack faces should be coincident, and the elements around the crack tip (or crack front) should be quadratic, with the mid-side nodes placed at the quarter points.

Such elements are treated as singular elements [Ansys, 1999]. In this analysis, the singularity around the crack tip was removed by generating a radially growing mesh with singular elements at the crack tip. The triangular solid element was used for fracture analysis. For the convergence of the results, the element size was varied from coarse to fine and when the results were approximately constant that specific element size was selected and used throughout the analysis. The element size was reduced to less than 1/8th of the initial crack length near the crack tip to achieve appropriate accuracy of the results. A path around the crack tip was created and the stress

intensity factor was computed directly from the FEM model. Care was taken that the model size simulates a real weld joint in service condition.

3.5 Model Dimensions

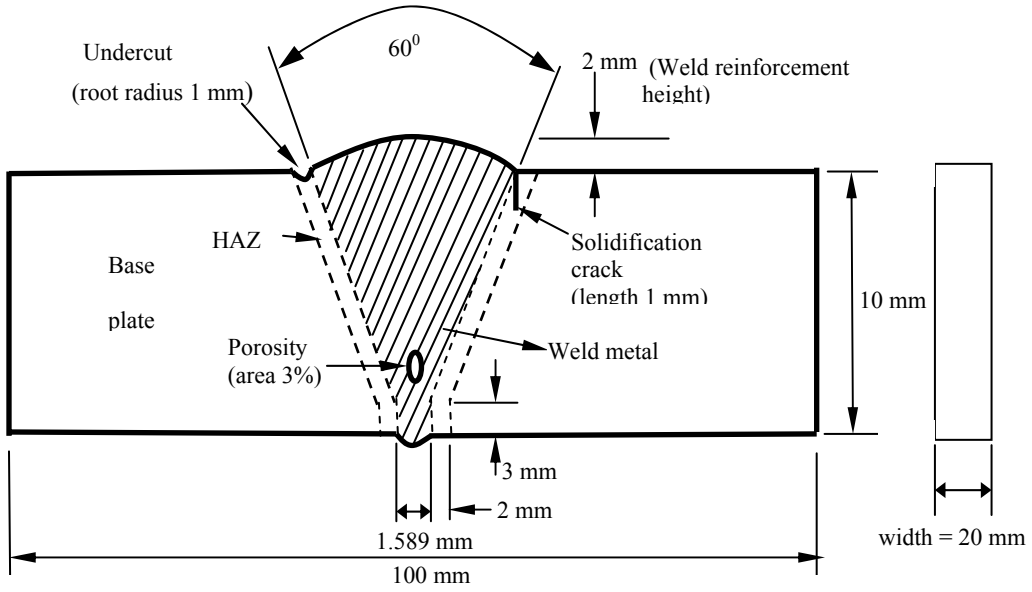

Figure 3.2 A 2-D schematic view of a single-V butt-joint with various weld imperfections.

The simulated weld model (Fig.3.2) was assumed according to the dimension of a single-V butt joint described in work by Giachino et al. [1973]. The plate size was 100 x 20 x 10 mm. The initial crack length for solidification crack was considered as 4.00 mm (0.2 of width) as recommended by ASTM - E647 [1995]. The undercut size is considered as 2 x 1 mm semi-elliptical crack as suggested by Harrison [1989]. The porosity area is generally expressed as percentage of area on radiograph and in this study 3% of welded area is considered which is within the range illustrated by Maddox [1993]. Fatigue strength depends on material and its properties and generally structural steel is more commonly used in welded structure.

3.6 Materials and Material Properties

Fatigue cracks in welded joints may propagate through three main regions – weld metal, HAZ and parent plate. The material considered in this analysis is carbon-manganese structural steel. The chemical compositions and mechanical properties of base, weld and HAZ metals are given in Table 3.1 and Table 3.2 [Burk, 1978] respectively.

Table 3.1 Chemical composition of base and weld metals [Burk, 1978].

Material	C	Mn	P	S	Si	Ni	Cr	Mo	Cu	Fe
ASTM A36	0.21	1.1	0.12	0.021	<0.10	<0.10	0.08	0.10	0.10	Bal.
Weld material (Electrode) E60S-3	0.09	1.0	0.017	0.024	0.50	--	--	--	--	Bal.

Table 3.2 Mechanical properties of base, weld and heat-affected materials [Burk, 1978].

Material	Modulus of elasticity, E (GPa)	0.2% offset Yield strength (MPa)	Ultimate tensile strength (MPa)
ASTM A36	207 (30000 ksi)	280 (40.6 ksi)	460 (66.7 ksi)
Weld material E60S-3	189 (27400 ksi)	580 (84 ksi)	710 (102.97 ksi)
A36 HAZ	189 (27400 ksi)	534 (77.45 ksi)	667 (96.74 ksi)

The Paris' crack growth rate constants for steel were assumed as: C = 3 $x10^{-11}$, m = 4 and suggested by other researchers [Harrison 1989], [Maddox, 1993]. The residual stress distribution was considered as normal distribution for longitudinal butt-welding [Glinka 1994], maximum tensile stress was at the centerline of weld and then slowly decreased. Then compressive stress slowly increased to a maximum value and then slowly decreased to zero.

3.7 Results and Discussions

The effect of weld imperfections (solidification crack, undercut and porosity) on fatigue crack propagation is shown in Fig. 3.3. In an ideal weld condition, it is assumed that there are no weld imperfections but an initial crack length (material defect) of 400 μm and the final crack length of 0.5 x plate thickness is considered. It is seen from the Fig. 3.3 that the fatigue crack propagation life decreases significantly with weld imperfections. The fatigue strength decreases about 55% for solidification crack, 45% for undercut and 18 % for porosity at life $2x10^6$ cycles.

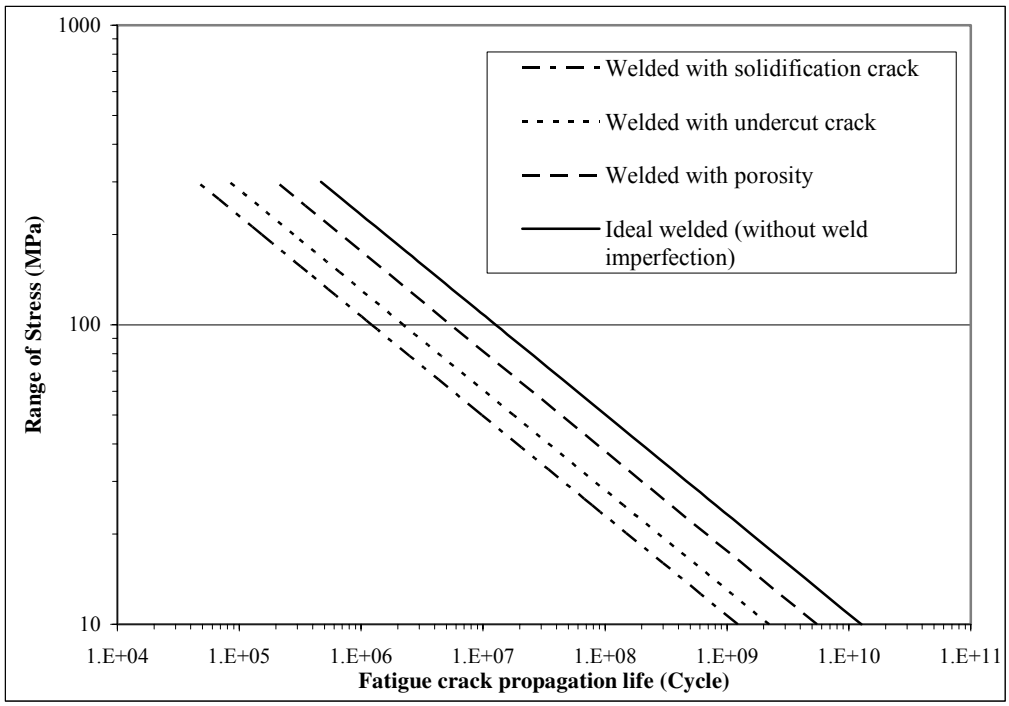

Figure 3.3 Effect of weld imperfections on fatigue crack propagation life

Comparing to porosity, the fatigue strength decrease about 45 % in surface solidification crack and 32% in undercut at life $2x10^6$ cycles. But the change greatly influenced by initial crack length. If lower initial crack length (<4 mm) would be considered, the change would be less.

The solidification crack is a surface crack and has sharp notch where stress concentration is greater than other two cases. Hence the effect of solidification crack is more pronounced than

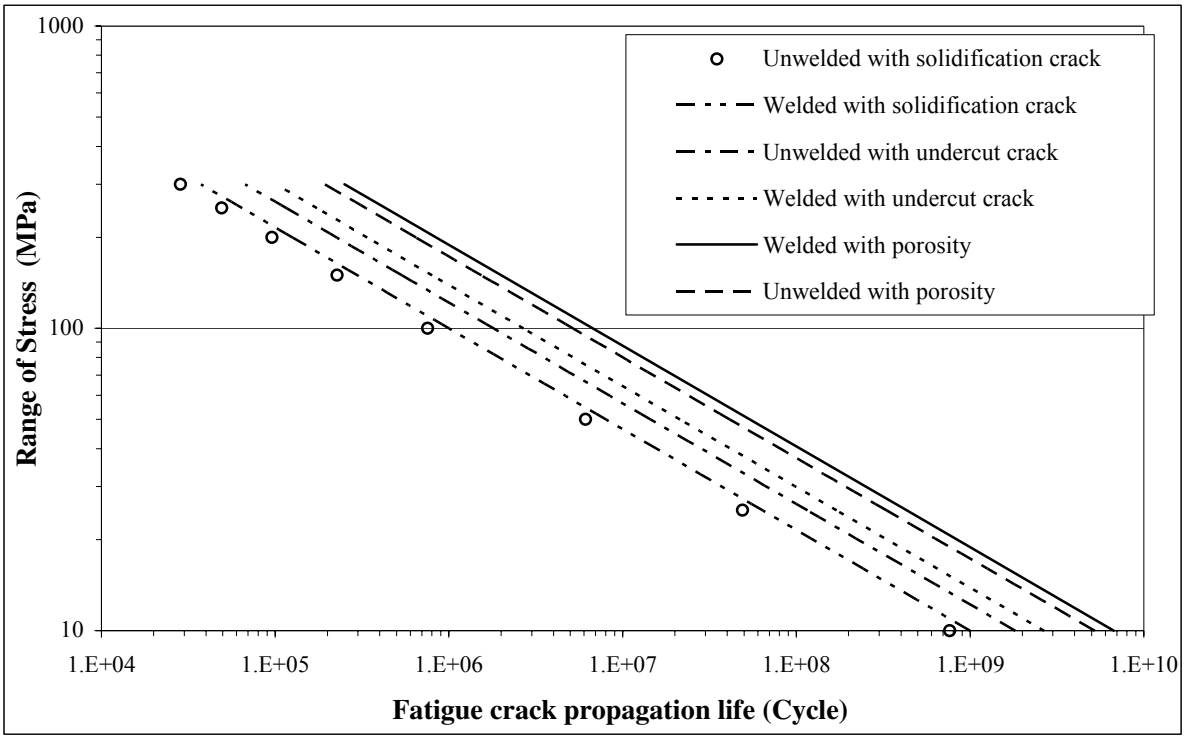

Figure 3.4 The effect of residual stress, bending stress and dissimilar material properties in welded and un-welded base material

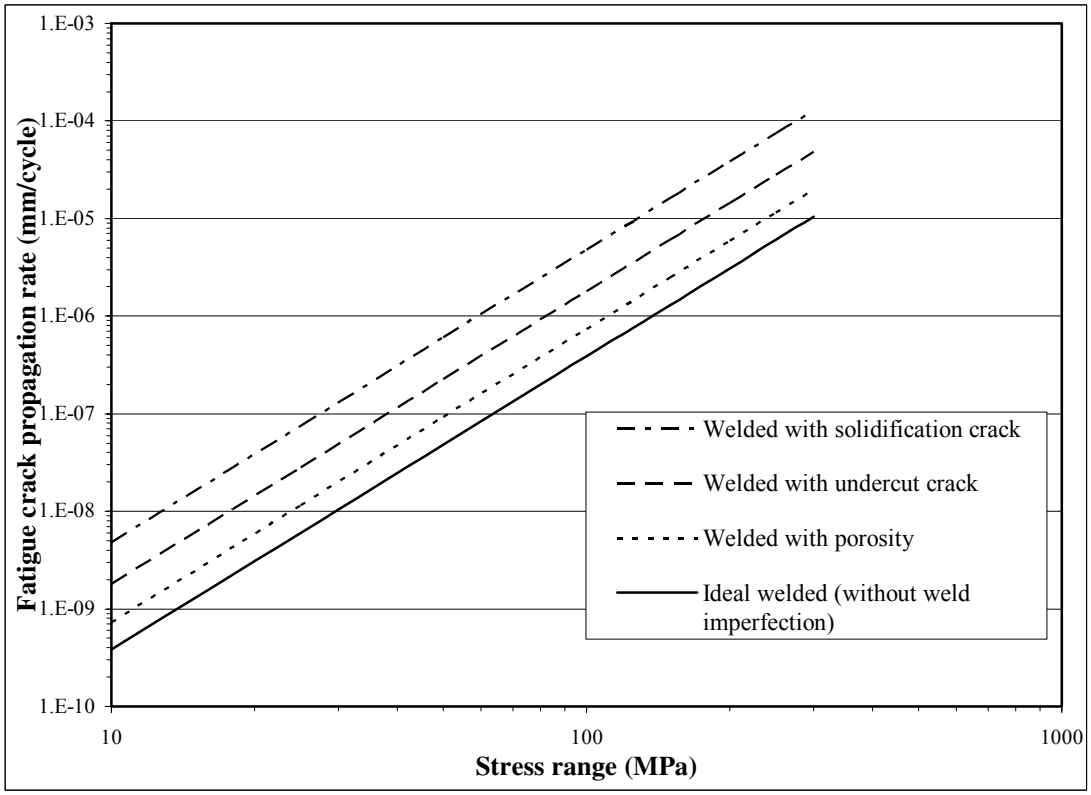

Figure 3.5 Effect of weld imperfections on fatigue crack propagation rate

undercut or porosity. Undercut is semi-circular surface crack having a large root radius and is associated less stress concentration comparing to solidification crack. Therefore its effect is less than solidification crack. In this study porosity is considered as an elliptical through thickness crack (2D model). Due to its shape and position, it accumulates less stress concentration comparing to other two cases and consequently it has less effect on fatigue crack propagation life. The effects of simulated weld (residual stress, bending stress and dissimilar material properties) on fatigue crack propagation are shown in Fig.3.4.

The simulated welds include the effect of residual and bending stress, and the effect of dissimilar material properties of base, weld and HAZ material. The un-welded cases are without the effects of residual and bending stresses and material is considered to be only base metal. It has been found that the fatigue strength decreases about 11.5 % for solidification crack, 10% for undercut and 9% for porosity at life $2x10^6$ cycle. The effect of various weld imperfections as discussed above on fatigue crack propagation rate is shown in Fig. 3.5. In general, weld imperfections increase the fatigue crack propagation rate and decrease the fatigue strength. For a particular propagation rate, 10^{-7} m/cycle, the fatigue strength decreases about 55% for solidification crack, 44% for undercut and 18% for porosity. Comparison of axial and bi-axial effect of a solidification crack and a circular porosity is shown in Fig. 3.6. At low axial cyclic loading, the effect of torsion is more than in high axial cyclic loading. At 10^6 cycles, the fatigue strength decreases about 12% due to torsional loading. Again the combined effect of two defects decreases fatigue strength about 9% at 10^6 cycles. The combined effects of both defects under bi-axial loading when they are approaching to interact are shown in Fig. 3.7. When they are approaching the fatigue life decreases but when they coincide, the life increases. When they interact, the sharpness of notch of solidification crack decreases due to presence of porosity and hence the fatigue life increases.

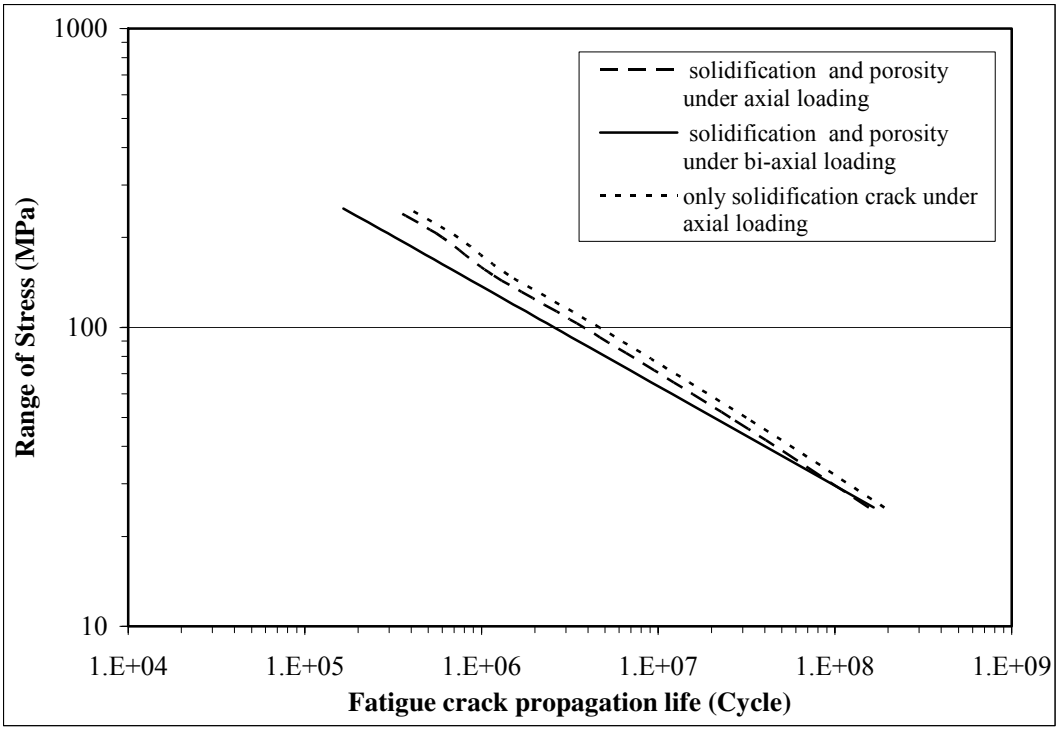

Figure 3.6 Comparison of axial and bi-axial effect of a solidification crack and a circular porosity

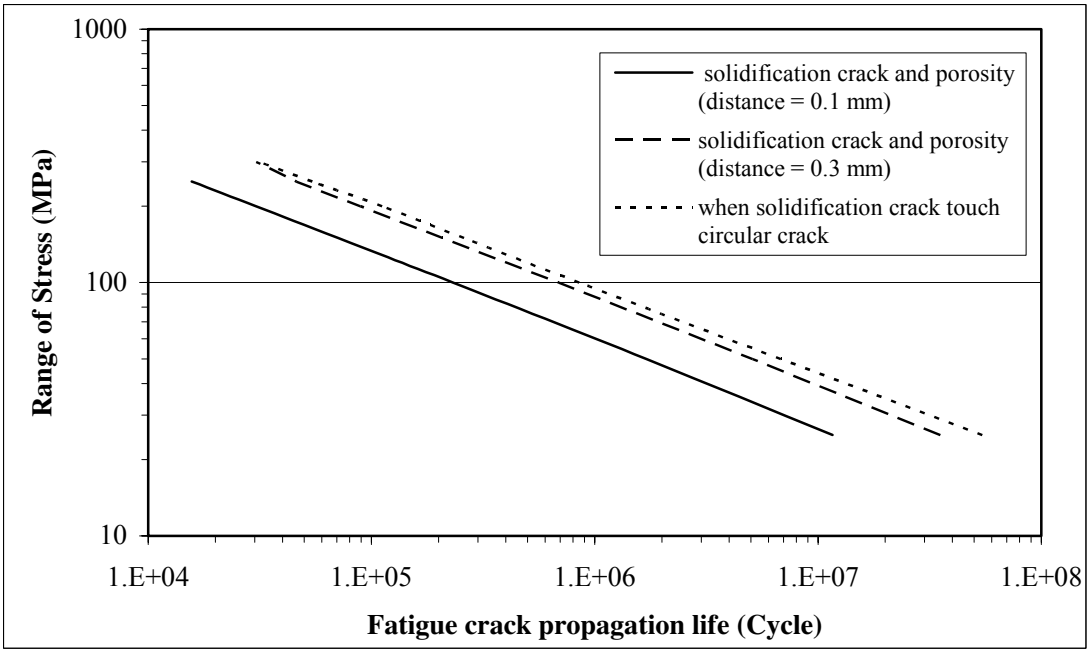

Figure 3.7 The combined effects of both defects (solidification and porosity) under bi-axial loading when they interact each other.

3.8 Validation of Predicted Results

For the validation of the prediction results, the range of stress intensity factor, ΔK, for the un-welded and welded specimens were calculated using the following empirical Eq.(3.3) shown below [Broek, 1982].

$$\Delta K = \Delta\sigma \sqrt{\pi a}\,[1.12 - 0.23(a/w) + 10.55(a/w)^2 - 21.72(a/w)^3 + 30.39(a/w)^4] \quad (3.3)$$

where $\Delta\sigma$ is the stress range, a crack length, w is the width of plate.

The results were also compared with that obtained using the following relations [Maddox, 1974].

$$\Delta K = \Delta\sigma\sqrt{\pi a}\sqrt{\sec\frac{\pi a}{2w}} \quad (3.4)$$

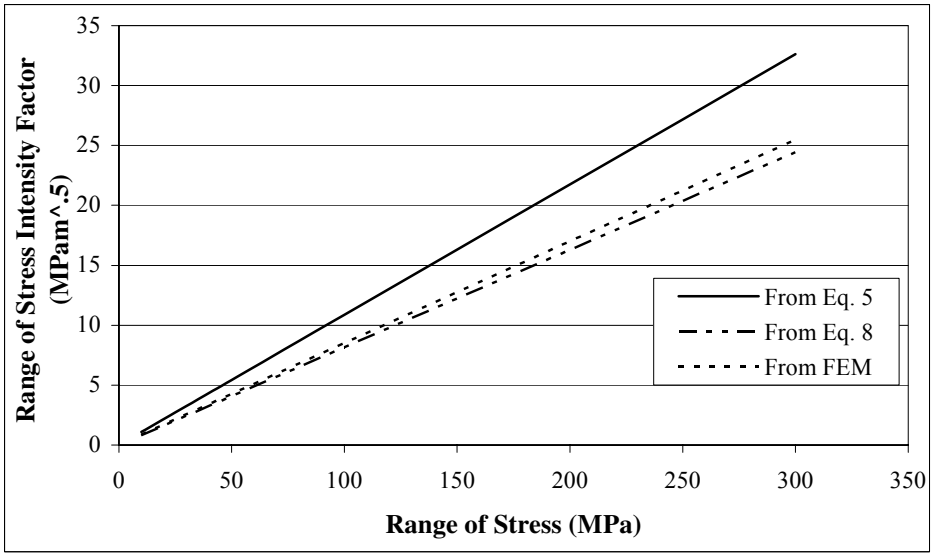

Figure 3.8 Comparison of the results from FEM and empirical relations

An additional correction for crack tip yielding was also considered and the plastic zone radius, r_p, was calculated as:

$$r_p = \frac{1}{2\pi}\left(\frac{\Delta K}{2\sigma_{ys}}\right)^2 \quad (3.5)$$

In Eq. (3.5) twice the uniaxial yield stress, σ_{ys}, was used because of reversed plastic flow at the crack tip that occurs under cyclic loading [Newman and Raju, 1986]. The resulting equation for ΔK was modified as :

$$\Delta K = \Delta\sigma\sqrt{\pi a}\sqrt{\sec\frac{\pi a}{2w}}\sqrt{1+\frac{1}{8}\left(\frac{\Delta K}{2\sigma_{ys}}\right)^2} \tag{3.6}$$

The comparisons of the results obtained are shown in Fig.3.8. From the comparisons, it can be seen that the results from FEM is close to the results obtained from equation (3.6) but vary linearly from equation (3.3). Equation (3.6) includes the effect of plastic zone correction and also includes the effect of yield stress and it compares well with experimental result [Maddox, 1974]. Equation (3.6) appears to be more realistic, and the results obtained in this study are within the acceptable range.

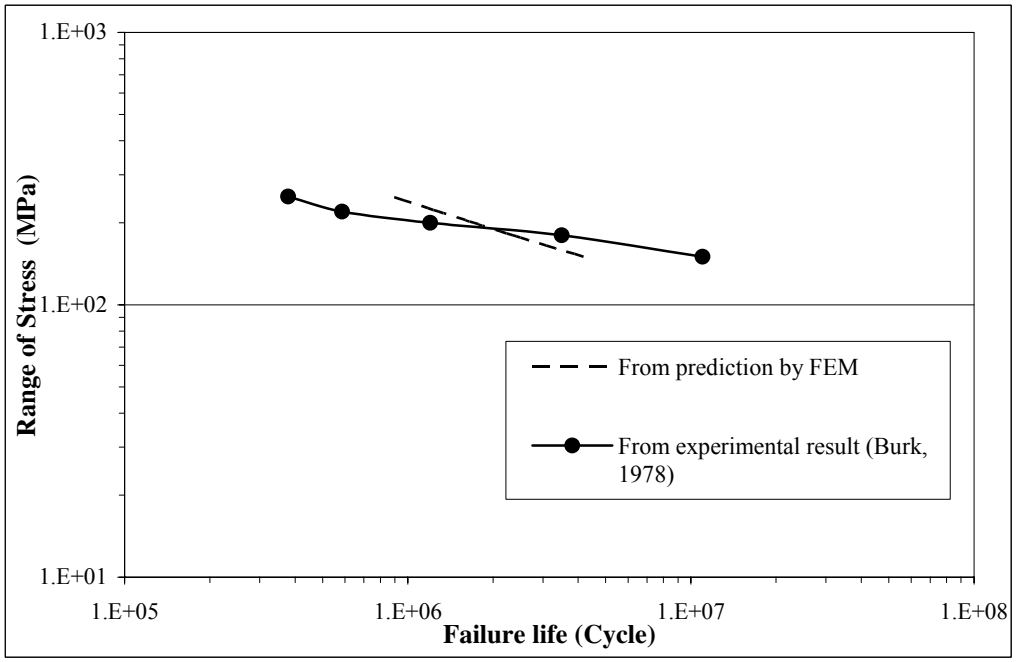

Figure 3.9 Comparison of FEM and experimental results for solidification crack.

Furthermore, the prediction obtained from this study for a solidification crack has been compared with experimental results available in literature [Burk, 1978] and the comparison is shown in Fig. 3.9. In both cases single-V butt joint are considered and the specimen material and other material properties are similar to those shown in Table 3.1 & Table 3.2). The same solidification initial crack length and the same stress ratio are considered. It is found that both

results compare well. The result obtained in this study is comparable to empirical formulations and experimental results found in the literature [Burk, 1978].

3.9 Conclusions

The weld imperfections significantly reduce the fatigue crack propagation life and fatigue strength of welded joints. Solidification crack and undercut are more serious than embedded porosity. Improvement of weld geometry decreases the stress concentration and increases the fatigue strength. The residual stress, bending stress and dissimilar mechanical properties of base, weld and HAZ metals also decrease the fatigue strength of welded structure. The bi-axial loading and the combined effect of a solidification crack and a circular porosity reduce the fatigue crack propagation life. But when they interact each other, the fatigue life increases comparing to when they are apart.

CHAPTER 4 FATIGUE CRACK PROPAGATION LIFE OF WELDED STRUCTURES

4.1 Finite Element Modeling for Stress Intensity Factor Solutions

Analytical solutions are available in the literature for determination of stress intensity factor (SIF) for through-thickness cracks in single edge notched specimens such as those employed for crack growth measurements in the present study [Broek, 1982]. However these analytical solutions are mainly based on plane stress or plane strain conditions, i.e. in 2-D models, which are applicable to cracks in plane sheet or plate specimens. Since the geometry of welded plates differs from those of the un-welded plates due to the presence of the weld reinforcement profile, traditional relations for stress intensity factor calculation, based on flat plate geometry, may not be valid for welded joints. On the other hand, removing the weld reinforcement completely to make the geometry similar to that of a flat plate may be impractical, uneconomical or even impossible in practical engineering applications. Using flat plate equations for predicting fatigue life for as-welded components may lead to over estimated results. Some recent studies employing 3-D modeling have indeed suggested that fatigue cracks on the weld toe cannot be accurately represented by 2-D models, which ignore the weld profile geometry [Bowness and Lee, 1996]. While the results of these studies are not directly applicable in this case, due to differences in the specimen and weld geometry, the magnitude of error introduced by the 2-D approximation needs to be investigated. Hence, in the present study, a 3-D finite element analysis of the butt weld joint was carried out to compute the stress intensity factor solutions for weld toe cracks. These are then compared to solutions from a 2-D plane strain model as well as those given by analytical solutions in literature. The magnitude of stress intensity factor at the tip of a crack in the weld reinforcement region is also affected by factors other than the weld geometry, such as the presence of residual

stresses and changes to material properties in the heat affected zone. In the present finite element analysis, the influences of these factors are considered.

4.2 Assumption in Finite Element Model

1. The material is homogeneous, isotropic and linearly elastic
2. The crack tip is subjected to mode-I when only axial load is applied and mode II and III when biaxial load is applied.
3. The effects of plasticity ahead of the crack tip and in its wake are ignored.

4.3 Theory of Stress Field at the Crack Tip

There are three types of loading that a crack can experience as shown in figure 4.1. Mode I loading, where the principal load is applied normal to the crack plane, tend to open the crack. Mode II corresponds to in-plane shear loading and tends to slide one crack face with respect to the other. Mode III refers to out-of-plane shear. A cracked body can be loaded in any one of these modes, or a combination of two or three.

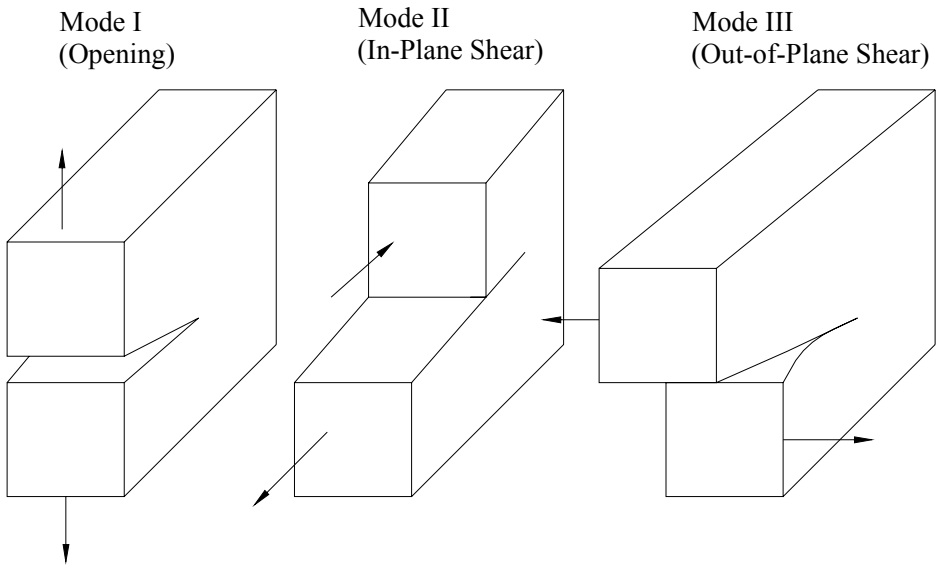

Figure 4.1 The three modes of loading that can be applied to a crack

Figure 4.2 schematically shows an element near the tip of a crack in an elastic material, together with the in-plane stresses on this element. In linear Elastic Fracture Mechanics, the stress field around crack tip can be described by equation 4.1

$$\sigma_{ij} = (\frac{c}{\sqrt{r}})f_{ij}(\theta\theta + \sum_{m=0}^{\infty} A_m r^{m/2} g_{ij}^{(m)}(\theta\theta \quad (4.1)$$

Where σ_{ij} is the stress tensor, r and θ are defined in figure 4.1, A, m, c are constants and, f_{ij} and g_{ij} are dimensionless function of θ.

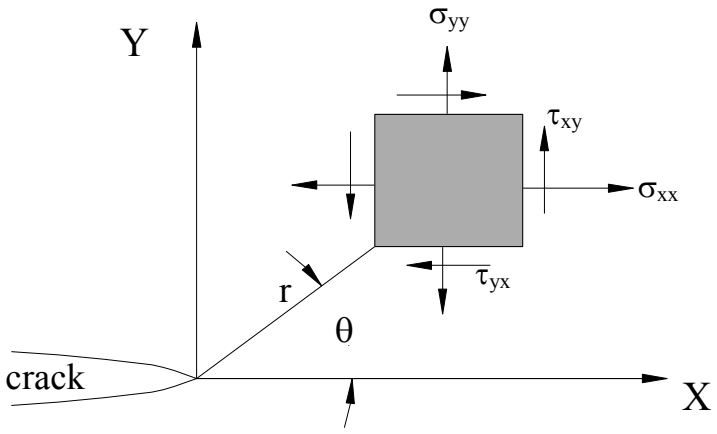

Figure 4.2 Stress field at crack-tip [Anderson, 1995]

In equation 4.1, the higher order terms depend on geometry, but the solution for any given configuration contains a leading term that is proportional to $1/\sqrt{r}$. As $r \to 0$, the leading terms approaches infinity and other terms remain finite or zero. Thus the stresses in the vicinity of the crack tip tend to be infinite large as r approaches zero. This unusual character of stresses at the crack tip is known as crack tip stress singularity. For the different types of loading, the crack tip stress fields can be described [Anderson, 1995] by

$$\sigma_{xx} = \frac{K_I}{\sqrt{2\pi r}} \cos(\frac{\theta}{2})[1 - \sin(\frac{\theta}{2})\sin(\frac{3\theta}{2})] \quad (4.2)$$

$$\sigma_{yy} = \frac{K_I}{\sqrt{2\pi r}} \cos(\frac{\theta}{2})[1 + \sin(\frac{\theta}{2})\sin(\frac{3\theta}{2})] \quad (4.3)$$

$$\sigma_{xx} = \frac{K_{II}}{\sqrt{2\pi r}} \sin(\frac{\theta}{2})[2 + \cos(\frac{\theta}{2}) \cos(\frac{3\theta}{2})] \tag{4.4}$$

$$\sigma_{yy} = \frac{K_{II}}{\sqrt{2\pi r}} \sin(\frac{\theta}{2}) \cos(\frac{\theta}{2}) \cos(\frac{3\theta}{2}) \tag{4.5}$$

$$\tau_{xz} = -\frac{K_{III}}{\sqrt{2\pi r}} \sin(\frac{\theta}{2}) \tag{4.6}$$

$$\tau_{yz} = \frac{K_{III}}{\sqrt{2\pi r}} \cos(\frac{\theta}{2}) \tag{4.7}$$

where σ_{xx}, σ_{yy}, τ_{xz}, τ_{yz} are stresses, $\kappa = 2\text{-}4\nu$ for plane strain and $\kappa = (3-\nu)/(1+\nu)$ for plane stress (ν is Poisson's ratio). K_I, K_{II} and K_{III} are the stress intensity factor is usually given a subscript to denote the mode of loading. Note that each stress component is proportional to a single constant, K_I or K_{II} or K_{III} . If this constant is known, the entire stress distribution at the crack tip can be computed with the equation 4.2-4.7. This constant, which is called the stress intensity factor, completely characterizes the crack tip conditions in a linear elastic material.

Let us consider the mode I singular stress field on the crack plane, where $\theta = 0$. According to equation 4.2 and 4.3, the stresses in the x and y directions are equal:

$$\sigma_{xx} = \sigma_{yy} = \frac{K_I}{\sqrt{2\pi r}} \tag{4.8}$$

It should be noted that equation 4.8 is only valid near the crack tip, where the stress singularity dominates the stress field. Figure 4.2 is a schematic plot of σ_{yy}, the stress normal to the crack plane, as a function of radial distance from the crack tip.

The stress intensity factor (K_I) related to the stress in Y direction at crack tip singularity zone can be described by the relation:

$$K_I = \lim_{r \to 0} \left[\sigma_{yy} \sqrt{2\pi r} \right] ; \ (\theta = 0) \tag{4.9}$$

By finite element modeling, the stresses in the region of the crack tip singularity zone can be estimated. The stress intensity factor can then be determined by plotting the quantity in square brackets in equation 4.9 against distance from the crack tip, and extrapolating it to r $\rightarrow$0.

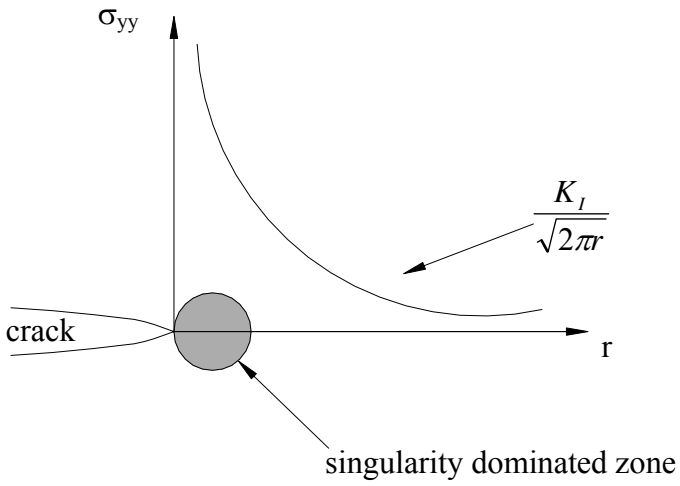

Figure 4.3 Stress normal to crack plane in mode-I loading

Alternatively, K_I can be evaluated from a similar extrapolation of crack opening displacement:

$$K_I = \frac{2\mu}{\kappa+1}\lim_{r\to 0}\left[u_{yy}\sqrt{\frac{2\pi}{r}}\right];\ (\theta = 0) \tag{4.10}$$

Since displacements can be determined with a higher degree of precision than stresses in an FEM model [Anderson, 1995], Equation 4.10 tends to give a more accurate estimation of the stress intensity solution K_I. Hence this approach is employed for estimating stress intensity factors for the cracks in welded joints. The greatest advantage of this method is that it can be used not only for flat plates but also for more complicated shapes and 3-D geometry such as weld reinforcements, as long as the stresses and /or displacement fields near the crack tip can be estimated with reasonable accuracy by FEM. To obtain an acceptable degree of accuracy by this method, singular elements have to be created around the crack tip and elements meshes near the crack tip have to be fine enough so that the condition r$\rightarrow$0 can be met. To pick up the singularity in the strain, the crack

faces should be coincident, and the elements around the crack tip (or crack front) should be quadratic, with the mid-side nodes placed at the quarter points. Such elements are called singular elements.

Stress singularities are not of the real world. Nonetheless, they can be a real fact of a stress analysis. It is essential to take them into account if the analysis is to be of any real use [Sinclair, 2004]. To give an appreciation of a stress singularity's occurrence, there are two options open to the stress analysis if the stress analysis is actually be used. First, it is necessary to try and improve the modeling so that the singularity is removed and physically sensible to stresses result. Second, to try and interpret singularities that persists in a physically meaningful way. To implement an approach using stress intensity factors in a general context, two types of companion analysis are usually required: analytical asymptotic to characterize local singular fields; and numerical analysis to capture participation in global configurations.

4.4 Numerical Analysis: A New Approach for Fatigue Crack Growth Using Interface Element

A new approach for the simulation of fatigue crack growth in two dissimilar elastic materials has been developed in this thesis work and specifically, the concept has been applied to a butt-welded joint. The phenomena of crack propagation and interface debonding can be regarded as the formation of new surface. Thus, it is possible to model these problems by introducing the mechanism of surface formation. In the proposed method, the formation of new surface is represented by an interface element based on the interface potential energy. The properties of this interface element represent the bonding strength of the material. As the cyclic load continues, the bonding strength decreases between the interacting surfaces and the crack propagates slowly. Based on this concept, an ANSYS code has been written for the simulation of crack propagation. Using this code, the fatigue crack growth rate and fatigue crack propagation life of a 2-D FEM

model of a butt-welded joint for different stress ratios have been analyzed and presented in this paper. The variation of the crack opening displacement (COD) over crack lengths and crack tip stress and strain over crack tip stress have also been presented. The trend of fatigue crack growth rate is similar to results found in the literature. For validation, the predictions are compared with experimental results and reasonably good comparisons are found. The method is relatively simple compared to other conventional FEM methods and it eliminates the limitation of crack propagation of one element length per cycle and saves computer time significantly.

4.4.1 Introduction

For assessment of structural integrity of welded structures, it is essential to calculate the fatigue life allowing for cracks or welding defects. Then the fatigue life is generally compared with the required design life and the decision for replacement or onward and continual use of the structure is taken. To determine the fatigue life by the Finite Element Method (FEM) the fatigue crack propagation rate with applied load must be calculated. Unfortunately, in traditional FEM the modeling of crack tip propagation with fatigue load is complicated and requires a numerically expensive program. The cracks do not generally propagate with each cyclic load. Because materials do not remember load history during cyclic load, the properties of materials are not changed after cyclic load. Therefore, in the traditional methods, the crack tip mesh is redefined or the crack tip node is released in each cycle and the crack propagates one element length in each cycle. But in reality, crack advance takes place in very small increments over many cycles. To reduce this limitation, the interface element (a new approach) is used in this analysis. Basically in crack formation and extension, failure is the consequence of new surface formation accompanied by crack extension. Based on this idea, interface elements (nonlinear element) are used between the crack faces, which explicitly model the formation of new crack surfaces (details are given in the subsequent sections and [Alam and Wahab, 2005]).

Using this method, the fatigue crack propagation life of welded and weld-repaired joints can be analyzed appropriately. Thus this research will help to assess the remaining life and structural integrity of large welded and repair-welded structures (i.e. railway, bridges, aircraft, ship, oil and gas pipelines, off-shore structures etc.)

4.4.2 Traditional and New Approach

A crack tip node-release scheme was suggested in [Newman, 1977], in which, a change in the boundary condition was characterized for a crack growth. This was achieved by changing the stiffness of the spring elements connected to boundary nodes of a finite element mesh. Before Newman's work, investigators changed boundary conditions of the crack tip node directly to obtain a free or fixed node. When the crack tip is free, the crack advances by an element length. The approach Newman used to change boundary conditions was to connect two springs to each boundary node [Newman, 1977]. To get a free node, the spring stiffness in terms of modulus of elasticity was set equal to zero, and for the fixed ones it was assigned an extremely large value (about 10^8 GPa (14.5 x10^9 ksi)) which represents a rigid boundary condition. McClung, Sehitoglu and their collaborators have also investigated fatigue crack closure by the finite element method. Their model for the elastic-plastic finite element simulation of fatigue crack growth used a crack closure concept [McClung and Sehitoglu, 1989]. They followed the node-release scheme at the maximum load and assumed that the crack propagates one element length per cycle.

The past use of finite element analyses had certain shortcomings and recent versions have been tremendous improvements and have removed many of these limitations. For example, to avoid numerical instability, schemes such as releasing the crack tip node at the bottom of a loading cycle were adopted in certain studies, e.g. [McClung and Sehitoglu, 1989]. They have not considered element bonding stress and surface energy, which are associated with crack formation and extension. They also did not consider the material properties change during cyclic loads. They

applied symmetric boundary conditions at the crack plane and also assumed that the crack can propagate only in symmetric planes. In this study, a crack can propagate in both symmetric and anti-symmetric planes about the applied load.

4.4.3 Theoretical Formulation

The crack is formed when the applied stress exceeds the critical bonding strength of the material. The bonding strength decreases with cyclic load and progressively becomes weak. Finally the atomic bonds lose its strength and breaks; and the cracks form and extend slowly. The total stiffness of the material decreases with the decreases of bonding strength. As the cyclic load continues, the stiffness decreases and the crack propagate slowly. Therefore, there is a close relationship between the bonding strength and crack propagation. To analyze crack propagation under cyclic load, a method using the interface element, which characterizes the element bonding-strength, has been proposed. In this method, the formation and the propagation of the crack are modeled by using the interface element. The mechanical behavior of the interface element is governed by the interface potential ϕ per unit area of the crack surface. There are wide choices for such a potential. In this analysis, the Lennard-Jones type potential ϕ [Masakazu et. al., 2000] is employed because it explicitly involves the surface energy γ, which is necessary to form a new surface. The surface potential per unit of crack surface area ϕ defined by Lennard-Jones is:

$$\phi(\delta) = 2\gamma\left\{\left(\frac{r_o}{r_o+\delta}\right)^{2n} - 2\left(\frac{r_o}{r_o+\delta}\right)^{n}\right\} \tag{4.11}$$

where γ, r_o n and δ are surface energy per unit area, scale parameter, shape parameter and crack opening displacement, respectively. The surface energy γ, which is required to form the new surface, is a material constant. The values of the surface energy and the other parameters n and r_o are found experimentally. Thus the surface potential ϕ is a continuous function of opening

displacement δ. The derivative of ϕ with respect to crack opening displacement δ gives the bonding stress σ on the crack surface.

$$\sigma = \frac{\partial \phi}{\partial \delta} = \frac{4\gamma n}{r_o}\left\{\left(\frac{r_o}{r_o+\delta}\right)^{n+1} - \left(\frac{r_o}{r_o+\delta}\right)^{2n+1}\right\} \tag{4.12}$$

Further, the bonding strength per unit area becomes a maximum under the following condition.

$$\frac{\delta}{r_o} = \left\{\left(\frac{2n+1}{n+1}\right)^{\frac{1}{n}}\right\} - 1 \tag{4.13}$$

The maximum bonding strength σ_{cr} is given by,

$$\sigma_{cr} = \frac{4\gamma n}{r_o}\left\{\left(\frac{n+1}{2n+1}\right)^{\frac{n+1}{n}} - \left(\frac{n+1}{2n+1}\right)^{\frac{2n+1}{n}}\right\} \tag{4.14}$$

To find the stress intensity factor, K from the crack opening displacement δ, the following expression can be used:

$$\delta = \left(\frac{8\sigma_y a}{\pi E}\right) \ln \sec \frac{\pi \sigma}{2\sigma_y} \tag{4.15}$$

When $\sigma/\sigma_y << 1$

$$\delta = \frac{K^2}{\sigma_y E} \tag{4.16}$$

where a is crack length, σ is remotely applied stress and σ_y is the yield stress.

Further the stress intensity factor can be calculated directly by using the ANSYS code and in this study this approach has been used.

After evaluating the stress intensity factor K, the fatigue crack growth rate can be calculated using the Griffith–Irwin empirical equation [www.utm.edu] that fits the entire crack growth region.

$$\frac{da}{dN} = \frac{C(\Delta K - \Delta K_{th})^m}{(1-R)K_{crit} - \Delta K} \tag{4.17}$$

where R is the stress ratio, equal to $\sigma_{min}/\ \sigma_{max}$, K_{crit} is critical stress intensity factor, m and C are material dependent constants, ΔK_{th} is threshold stress intensity factor. The essential part of this equation (4.17) is to calculate the stress intensity range, ΔK . Since there is no closed form solution of ΔK, an empirical equation of the form $\Delta K = Y\Delta\sigma\sqrt{\pi a}$ is usually assumed to relate the range of stress intensity factor, with the nominal stress range, Δσ and with the crack length, a; Y is a factor related to the specific geometry in question.

In order to appropriately assess fatigue crack propagation in welded joints it is necessary to obtain accurate results for stress intensity factor solution in the crack propagation phase. Generally the stress intensity factor for a crack in a welded joint depends on the global geometry of the joint, which include the weld profile, crack geometry, residual stress condition, the properties of HAZ material and the type of loading. Therefore, the calculation of the stress intensity factor, even for simple types of weldments, requires detailed analysis of several geometric parameters and loading systems. The two approaches that have mostly been used till now for assessing stress intensity factors for crack in weldments are the weight function method [Bueckner, 1970] and the finite element method (FEM).

The FEM enables the analysis of complicated weld geometry due to its great versatility. It is able to use elastic-plastic elements to include crack tip plasticity. In FEM the stress intensity factor can be calculated directly from the stress field or from the displacement field around the crack tip. In this study FEM has been used for calculation of stress intensity factor using the concept of debonding.

After integrating the above expression, the fatigue crack propagation life N_p is obtained by the following equation

$$N_p = \int_{a_o}^{a_f} \frac{(1-R)K_{crit}-\Delta K}{C(\Delta K-\Delta K_{th})^m} da \tag{4.18}$$

The debonding model and the fracture mechanics crack growth model are essentially the same. The debonding model is used for the calculation of range of stress intensity factor ΔK in equation (4.17) and using equation (4.17) and (4.18) fatigue crack growth rate and propagation life is calculated. All other values in Equation (4.17) are known or assumed. This equation (4.17) is applicable for the entire three regions of the crack growth curve. Crack initiation growth rate or initiation life has not been modeled in this analysis. This model is being used for the calculation of crack propagation life taken just after the range of the threshold stress intensity factor.

4.4.4 Interface Element and Its Properties

The interface elements employed in this study (Fig. 4.3) are the distributed nonlinear truss elements existing between surfaces forming the crack surfaces. They are assumed to have zero mass and zero volume. Figure 4.4 represents a model of two linearly connected elements. The top element represents an elastic-plastic continuum, which represents the plastic zone near the crack tip. The non-linear truss element represents a potential failure surface. The relation between the bonding stress and crack opening displacement is shown in Fig. 4.5.

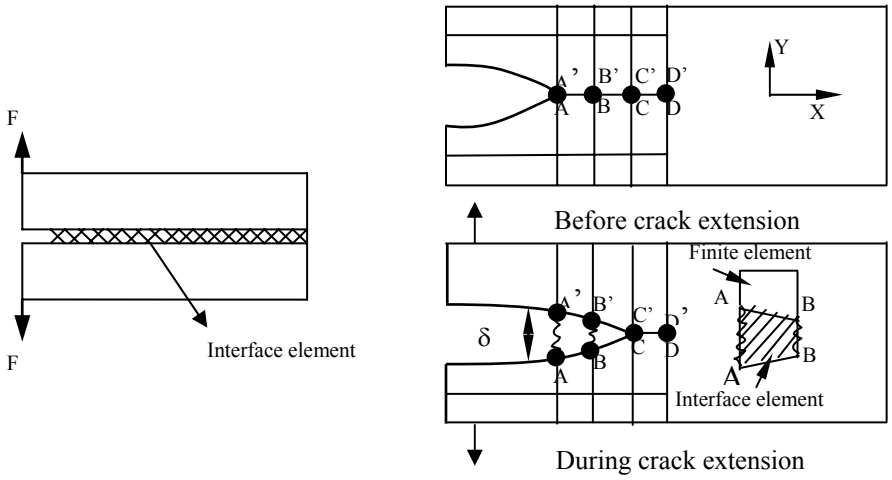

Figure 4.4 Interface element between crack faces

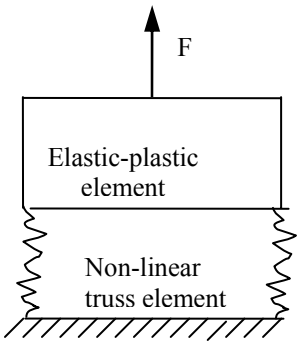

Figure 4.5 Interface element as a combination of non-linear truss and elastic-plastic elements.

When the opening displacement is small, the bonding between the two surfaces is maintained. As the opening displacement increases, the bonding stress increases until it reaches a maximum value σ_{cr}. With further increase of δ, the bonding strength is rapidly lost and the surfaces are completely separated.

The mechanical properties of these two non-linear elements are characterized by the following sets of parameters, (γ, r_o) and (E, σ_y, h_t), respectively. The parameter γ and r_o are the surface energy and the scale parameter of the interface. The parameters E, σ_y, and h_t are Young's modulus, the yield stress and the tangent modulus (slope of plastic portion of stress-strain curve) for a multi-linear or bilinear material. The mechanical behavior of the idealized elastic-plastic continuum can be represented by Figure 4.6.

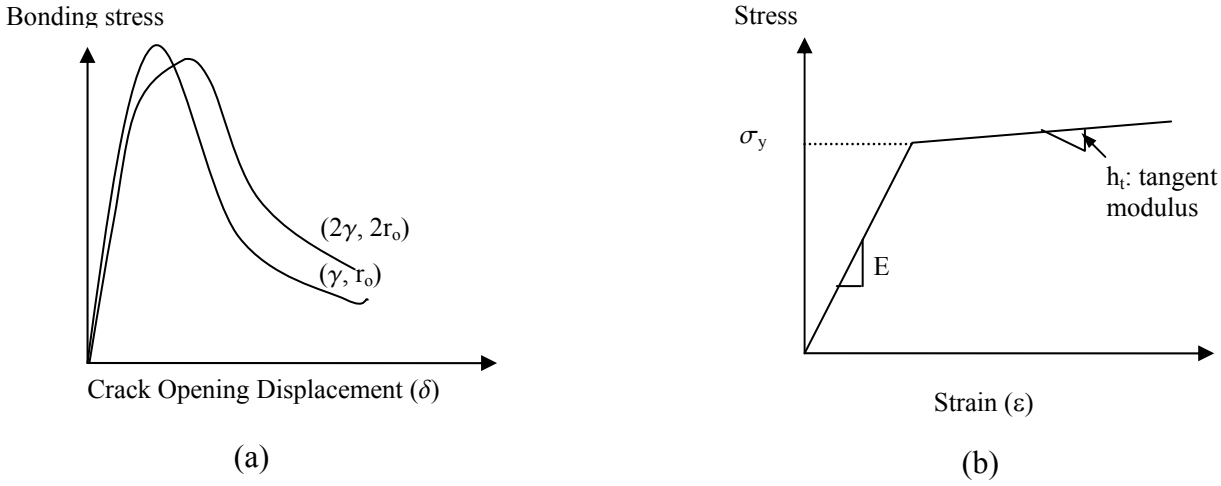

Figure 4.6 (a) Mechanical properties of interface (non-linear truss) element (b) Mechanical properties of elastic-plastic continuum

4.4.5 Equilibrium Equation of the System

For simplicity, the outline of the mathematical formulation is presented for crack propagation in an elastic solid. When the material is elastic, the equilibrium equation can be derived based on the principle of minimum potential energy. The total energy Π of the elastic body with a propagating crack can be described [Hidekazu and Wu, 1999] as the sum of the strain energy U, the potential of external load W and the interface energy of the newly formed surface during crack propagation U_s, i.e.

$$\Pi = U + U_s + W \tag{4.19}$$

In the finite element method, the elastic body to be analyzed is subdivided into small elements and the displacements in each element are interpolated by nodal displacement u_o. The total energy is described as

$$\Pi = \Pi(u_o) = U(u_o) + U_s(u_o) + W(u_o), \tag{4.20}$$

Further, $U(u_o)$, $U_s(u_o)$, $W(u_o)$ can be represented as the sum of the contributions from each element $U_e(u^e_o)$, $U^e_s(u^e_o)$, $W(u^e_o)$, i.e.

$$\Pi(u_o) = \Sigma \{U^e(u^e_o) + U^e_s(u^e_o) + W(u^e_o)\}, \tag{4.21}$$

where u^e_o is the nodal displacement vector for each element extracted from the nodal displacement vector of the whole system u_o.

Once the total energy Π is given as in Eq. (4.21), the equilibrium equation in incremental form can be derived in the following manner. Denoting the nodal displacement at the present step and its increment to the next step as u_o and Δu_o, the total energy Π can be described as a function of $u_o + \Delta u_o$ and can be expanded in a Taylor's series, i.e.

$$\begin{aligned}\Pi(u_o + \Delta u_o) &= \Pi(u_o) + \Delta^1\Pi(\Delta u_o) + \Delta^2\Pi(\Delta u_o) \\ &= \Pi(u_o) - \{\Delta u_o\}^T\{f\} + \tfrac{1}{2}\{\Delta u_o\}^T[k]\{\Delta u_o\}\end{aligned} \tag{4.22}$$

where $\Delta^1\Pi$ and $\Delta^2\Pi$ are the first and second terms in Δu_o, i.e.

$$\Delta^1\Pi(\Delta u_o) = -\{\Delta u_o\}^T\{f\} \tag{4.23}$$

$$\Delta^2\Pi(\Delta u_o) = \tfrac{1}{2}\{\Delta u_o\}^T[k]\{\Delta u_o\} \tag{4.24}$$

Further, the equilibrium equation can be derived as the stationary condition of $\Pi(u_o + \Delta u_o)$ with respect to Δu_o,

$$\partial\Pi(u_o + \Delta u_o)/\partial\Delta u_o = -\{f\} + [k]\{\Delta u_o\}$$

$$\text{or,} \quad [k]\{\Delta u_o\} = \{f\}. \tag{4.25}$$

where [k] and {f} are the tangent stiffness matrix and the load vector, respectively.

4.4.6 Stiffness Matrix and Force Vector of Interface Element

The stiffness matrix and the load vector of the interface element can be derived in basically the same manner as that for the whole system. The two surfaces separate when the load is applied. The opening displacement is denoted by δ, the surface area of the interface element is S^e and the interface energy for an element $U^e_s(u^e_o)$ is given by the following equation [Hidekazu and Wu, 1999].

$$U^s{}_e(u^e{}_o) = \int \phi(\delta) dS^e \tag{4.26}$$

where δ is the crack opening displacement at an arbitrary point on the surface that can be interpolated using an interpolation function $N_i(\xi,\eta)$, i.e.

$$\delta(\xi,\eta) = \Sigma N_i(\xi,\eta)(w_{i+4} - w_i), \tag{4.27}$$

where

$N_1(\xi,\eta)= 0.25\ (1+\xi)(1-\eta)$, $N_2(\xi,\eta)= 0.25\ (1+\xi)(1+\eta)$, $N_3(\xi,\eta)= 0.25\ (1-\xi)(1+\eta)$, $N_4(\xi,\eta)= 0.25\ (1-\xi)(1-\eta)$

and w_i is the nodal displacement normal to the surface. These interpolations are for a 3D model where the interface elements are 2D. But for a 2D model the interface element is 1D and the shape functions are given by: $N_1(\xi)= 0.5\xi(\xi-1)$, $N_2(\xi)= -(\xi+1)(\xi-1)$, $N_3(\xi)= 0.5\xi(\xi+1)$.

Finally, the tangent stiffness matrix $[k^e]$ and the load vector $\{f^e\}$ of the interface element can be derived by expanding $U^e_s(u^e_o+ \Delta u^e_o)$ with respect to Δu^e_o in the following manner.

$$U^e_s(u^e_o+ \Delta u^e_o) = \int \phi(\delta + \Delta\delta) ds^e$$

$$= \int \phi(\delta) ds^e + \int \frac{d\phi(\delta)}{d\delta} \frac{\partial\delta}{\partial u_o e} \Delta u^e_o ds^e + \frac{1}{2}\int \frac{d^2\phi(\delta)}{d\delta^2} (\frac{\partial\delta}{\partial u^e_o} \Delta u^e_o)^2 ds^e + \text{higher order terms} \quad (4.28)$$

where
$$\int \frac{d\phi(\delta)}{d\delta} \frac{\partial\delta}{\partial u_o{}^e} \Delta u^e_o ds^e = -\{f^e\}^T \{\Delta u^e_o\} \quad (4.29)$$

$$\frac{1}{2}\int \frac{d^2\phi(\delta)}{d\delta^2} (\frac{\partial\delta}{\partial u^e_o} \Delta u^e_o)^2 ds^2 = \tfrac{1}{2} \{\Delta u^e_o\}^T [k^e] \{\Delta u^e_o\} \quad (4.30)$$

Since the interface element has no volume or mass, the same formulation can be applied to both static and dynamic problems. By arranging the interface elements along the crack extension path in the simple model, crack propagation problems can be analyzed.

4.4.7 FEM Simulation of Fatigue Crack Growth

A new approach for crack propagation by killing or "death" elements (deactivate the element properties) is introduced in this analysis (birth and death option in Ansys 7.1). A bundle of non-linear truss elements as shown in Fig. 4.7, each having different material properties (modulus of elasticity, yield stress and tangent modulus) is used to connect to each boundary node ahead of the initial crack tip. These values are lower to higher order from the crack tip to the other end.

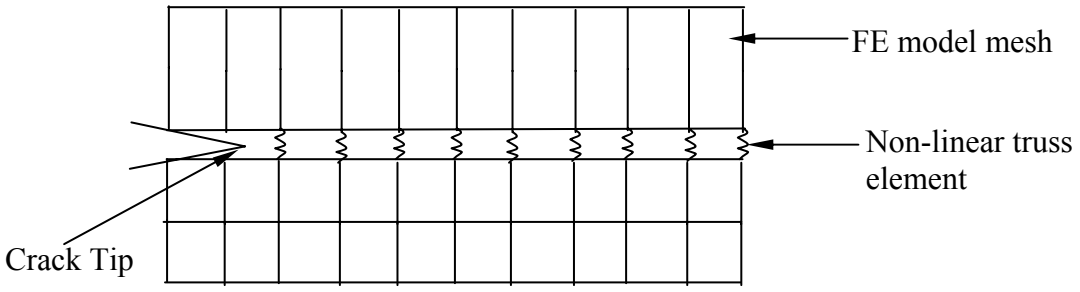

Figure 4.7 A schematic views of truss elements connected between two surfaces of two mild steel plates.

These elements have the same cross-sectional area and have capabilities to take both tension and compression loads. The stiffness of each truss element in terms of modulus of elasticity has different values from an extremely large value (210GPa) (other end from the crack tip) to a value near the yield stress (280MPa) (near crack tip). The other interface elements' modulii of elasticity are determined by linear interpolation of those values. During each cycle of loading and unloading, the stiffness of each truss element is decreased by a certain amount (depends on total number of interface elements) using the MPCHG (ANSYS command to change properties) command. After each cycle of loading and unloading, the elemental axial stress is calculated. When any element's stress exceeds the critical bonding stress that element is killed (deactivated material property) by using EKILL command. At the same time the element material properties from the crack tip to the other end is moved (changed) successively. Thus, when one element is killed the next element's stress increased. Since the next element has higher stiffness, its stress will be little less than the broken element. Because the next element will elongate less and accordingly, the cross-section of the next element will decrease or change slowly. Similarly, after ten cycles, the final crack length is observed and the stress intensity factor at the crack tip (next to the killed element) is calculated by defining the crack path and using the KCALC command. From the stress

intensity factor, the crack growth rate is calculated using equation (4.17) and the crack propagation life using equation (4.18).

This method has several advantages compared to other methods. The node release by killing elements can be performed at any time during a cyclic loading process irrespective of the magnitude of the deformation caused by the release of the nodes. Furthermore, several elements can be killed simultaneously, e.g. during a single overload cycle (which is higher than the yield strength of the material). This method overcomes the limitation of crack propagation of one element length during each cycle of loading. In this method, the crack propagates automatically when the element's stress exceeds the bonding stress of the element. Here a crack can propagate in more than one direction but a limitation is that the possible directions have to be determined earlier depending on the physical crack configuration, loading and material homogeneity. For bi-axial (multi load) loading where the crack directions are not obvious, this method may be suitable.

4.4.8 Overall Methodology for Fatigue Life Calculation

1. The critical stress intensity factor for short-term fracture K_{crit}, material constants C and m, and the threshold stress intensity factor range $\Delta K_{th}(R)$ as a function of R for the material to be analyzed is determined or collected from literature ($\Delta K_{th}(R)$ as a function of R could be found [Anderson, 1995]).
2. The values of the surface energy per area γ, the scale parameter r_o, and the shape parameter, n for the material are determined experimentally or collected from literature.
3. The Finite Element model is created and the interface elements are introduced in the possible crack propagation directions (maximum stress concentration, weld defect, etc). The critical bonding stress, σ_{cr} of the interface elements is determined using the equation (4.12). The plastic zone radius is calculated using the standard equation and the elastic-plastic material properties are applied to the elements within the plastic zone.

4. The cyclic load for a particular stress ratio is applied to the model and after each cycle of loading the interface element-stress is calculated. When any element stress exceeds the critical bonding strength, (which was calculated using equation (4.14)), that element is killed. Thus after some cycles (10 to 20 or more) the crack propagation is viewed (only the active elements are viewed and killed elements are kept hidden) and the final crack length is determined. For the same crack length and stress conditions, the stress intensity factor range, ΔK is calculated using ANSYS.
5. The fatigue crack growth rate and the fatigue life are calculated using equation (4.17) and (4.18).

4.4.9 Case Studies

4.4.9.1 Butt Welded Plate

4.4.9.1.1 Finite Element Model and Analysis

A 2-D finite element model of a butt-welded joint as shown in Fig. 4.8 is created and interface elements as described above are applied in the crack faces. The left side of the model is fixed in all degrees of freedom and a cyclic load is applied at the right side. The constant amplitude cyclic load shown in Fig. 4.9 is applied to the model. The model is created and analyzed by writing code in ANSYS 7.1 as mentioned in Section 4.4.7.

The mechanical properties of base, weld and heat-affected-zone (HAZ) materials as shown in Table 3.2 are applied to the model. The Paris' crack growth rate constants for steel are assumed as: $C = 3 \times 10^{-11}$, $m = 4$. The ΔK_{th} values were taken as 4, 5, 6 $MN/m^{3/2}$ for stress ratios of 0.3, 0.2 and 0.1 respectively, from Fig.10.9 in [Anderson, 1995] for this particular weld. In this study the positive stress ratios are considered because the negative stress ratios have less or no significant effect on fatigue crack propagation life [Anderson, 1995]. The critical stress intensity factor K_{crit} is taken as 150 $MN/m^{3/2}$ which is an average value of the critical stress intensity factor for mild steel.

The value of the critical stress intensity factor for mild steel are reported to be in the range from 100 to 200 MN/m$^{3/2}$. Therefore, it is reasonable to take an average value of 150 MN/m$^{3/2}$. In addition, the residual stresses of different magnitudes at different depth/thickness are applied. The residual stress values varied from 120 MPa (17.4 ksi) to -120 MPa.

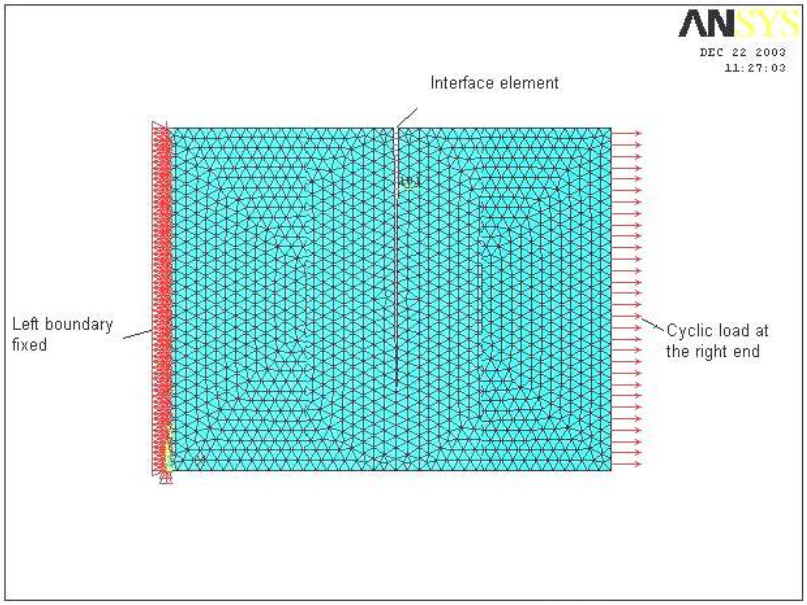

Figure 4.8 A 2-D FEM model of butt-welded plate

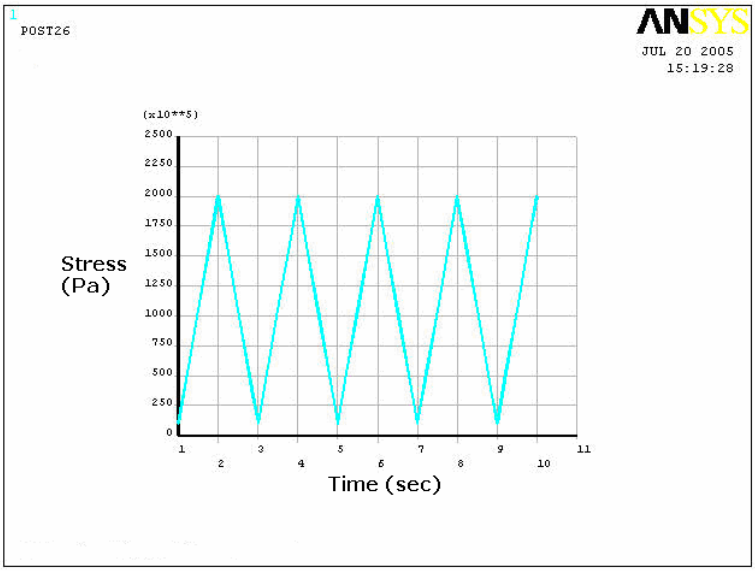

Figure 4.9 A typical constant amplitude axial cyclic load

It is assumed that for this welded joint the crack initiation phase is very short and insignificant due to the presence of welding defects. Initial crack length has been assumed to be 0.2 times width as suggested in ASTM-E647 [1995]. An axial cyclic load near the yield strength of the material is applied for various cycles, and the corresponding stress intensity factor and crack opening displacement are calculated from the FEM analysis. Then using equation (4.17) and (4.18), the fatigue crack growth rate and fatigue crack propagation life are calculated.

4.4.9.1.2 Results and Discussions

For the 2-D model, the fatigue crack growth rates for different stress ratios, R are calculated and are shown in the Fig. 4.10. As the stress ratio decreases, the crack growth rate increases. For constant amplitude loading when the stress ratio is increased, both the maximum and the minimum stresses are increased and hence the crack growth rate increases. Again, the threshold stress intensity factor range, ΔK_{th} decreases with increase of stress ratio [Anderson, 1995]. The ΔK_{th} values were taken as 4, 5, 6 $MN/m^{3/2}$ for stress ratios of 0.3, 0.2 and 0.1 respectively, from Fig.10.9 in [Anderson, 1995] for this weld. According to the equation (4.17), the crack growth rate decreases with increase of ΔK_{th} .The results shown in Fig. 4.10 confirm this trend and give a good indication of the effectiveness of this method. The critical stress intensity factor, K_{crit} for mild steel generally falls within the range of (100-200) $MN/m^{3/2}$ and from the results shown in Fig. 4.10, it is found that the graph starts changing its slope near a value of 100 $MN/m^{3/2}$. Although this is not the final fracture but due to the limitations in computing in FEM it is only possible to get the near-final K_{crit} value. At the start of the fast fracture the material loses its full stiffness rapidly, and the program convergence is very slow. For this reason, only the starting point of the fast fracture has been calculated in this program. Since the materials used in this study is not pure mild steel rather a weld, the start of the fast fracture which is close to 100 $MN/m^{3/2}$ is reasonable. Further, the

difference in the crack growth rate for different stress ratios at high range of stress intensity factor is smaller than that at the low range of stress intensity factor. This may be due to the effect of the threshold stress intensity factor. At low stress levels the rate of crack propagation is low and the rate of stress intensity factor is also low.

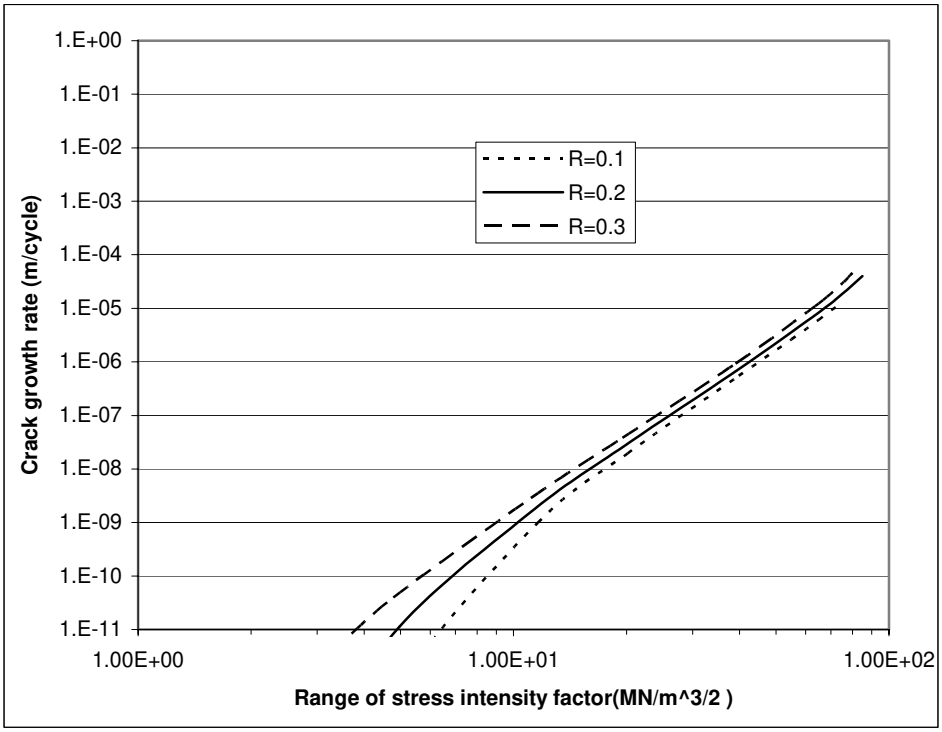

Figure 4.10 Variation of fatigue crack growth rate with range of stress intensity factor.

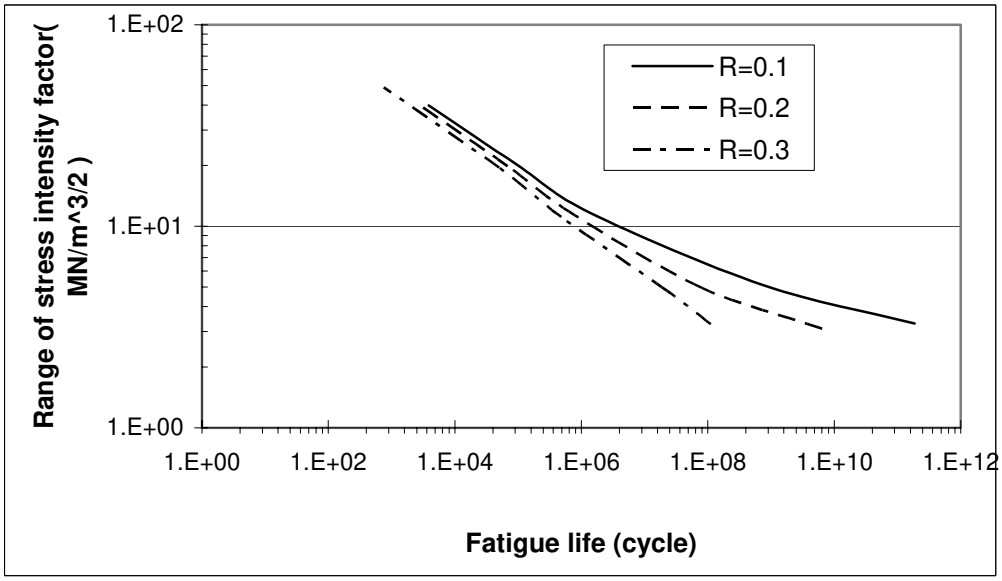

Figure 4.11 Variation of fatigue life with range of stress intensity factor

At this low range of stress intensity factor; the effect of the threshold stress intensity factor on crack growth rate is more pronounced than at high stress levels or at higher rate of crack propagation.

The variation of fatigue life with range of stress intensity factor for three stress ratios is shown in Fig.4.11. The fatigue life increases at low stress intensity factor and the trend is for life to become infinite below the threshold stress intensity factor. On the other hand, the fatigue life decreases with increase of stress intensity factor range. At low stress ratio, the fatigue life increases and at high stress ratio, the life decreases. For a particular range of stress intensity factor of 10, the fatigue life decreases about 25% at a stress ratio of 0.2 and 55% at a stress ratio of 0.3 compared to that at a stress ratio of 0.1.

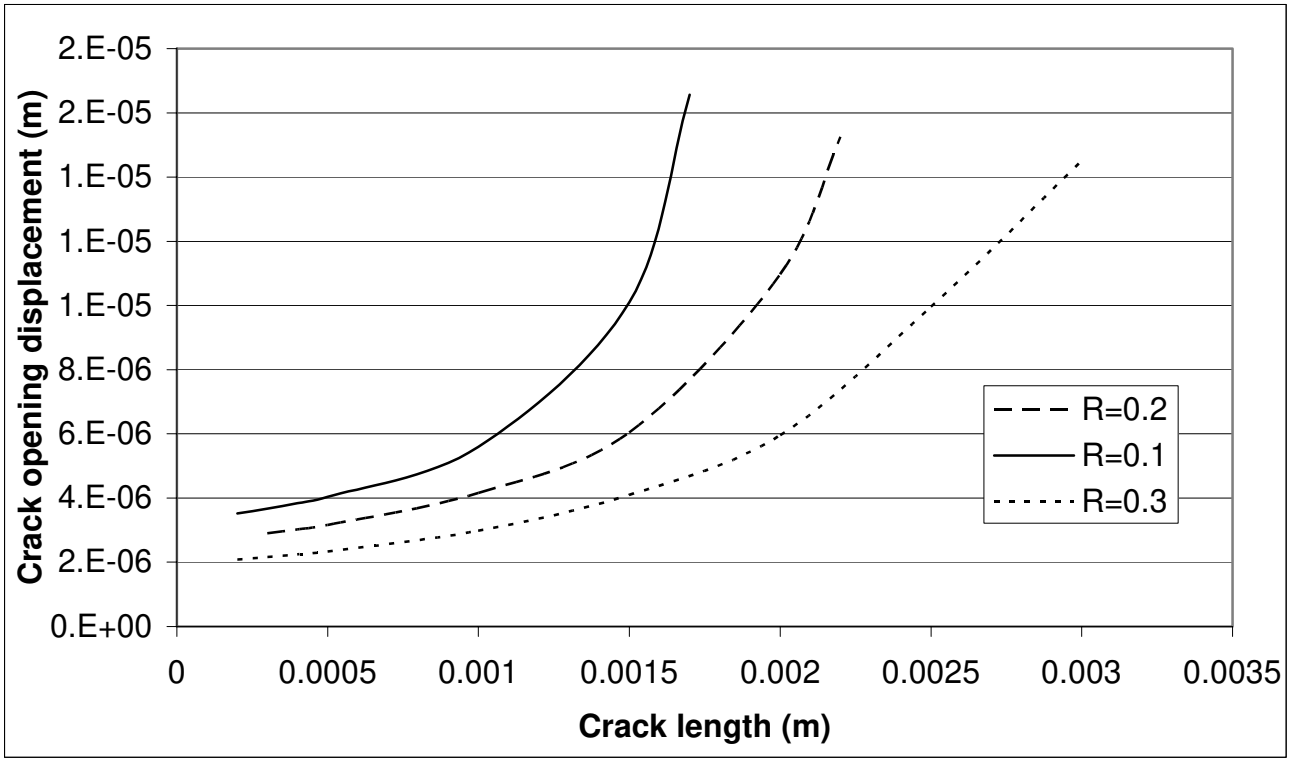

Figure 4.12 Variation of crack opening displacement with crack length

The variation of crack opening displacement with crack length is shown in Fig. 4.12. The crack opening displacement (COD) increases with crack length. For a particular crack length, the COD decreases with increase of stress ratios. In this case, changing the maximum stress and keeping the minimum stress constant, the stress ratios have been changed. Therefore, the stress ratio decreases with increase of maximum stress. For this reason, the COD increases with decrease of stress ratio.

The variation of strain at the crack tip and the COD with crack tip stress are shown in Fig. 4.13. The strain increases with crack tip stress. At the starting point of fast fracture, the strain increases rapidly. Similarly the COD increases with crack tip stress and at the start of fast fracture, the COD increases rapidly. At high crack- tip stress, the strain is greater and hence COD increases rapidly.

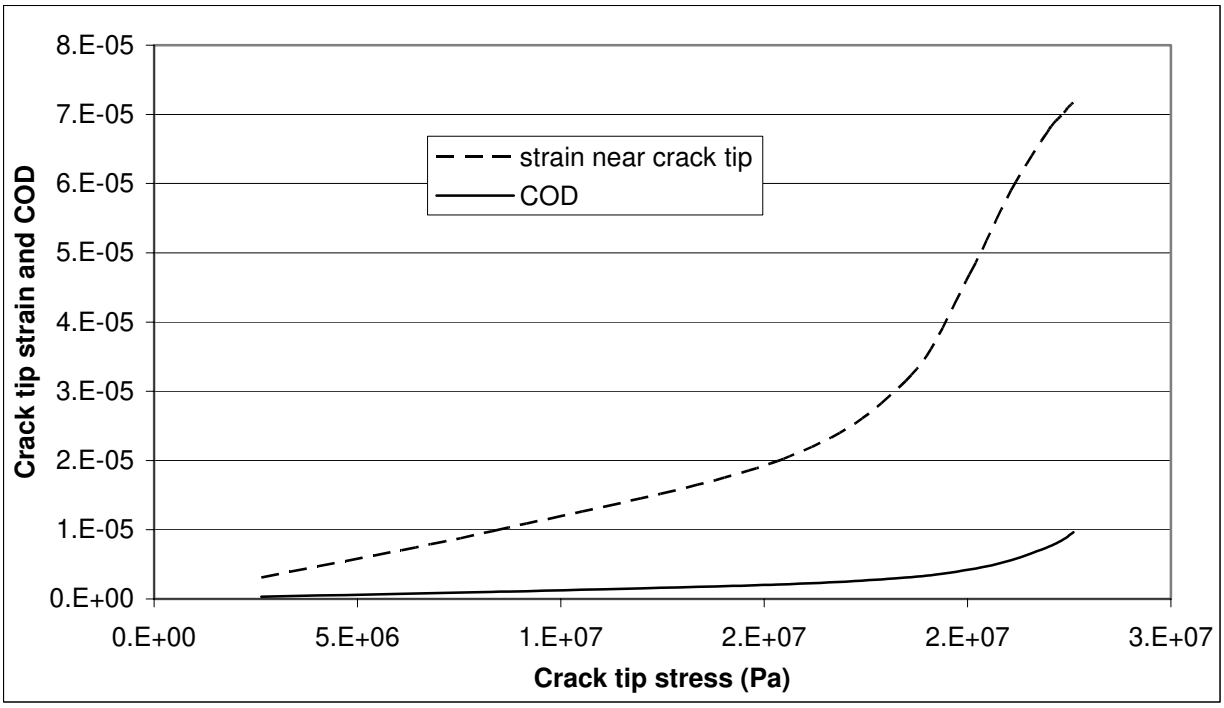

Figure 4.13 Variation of strain near crack-tip and crack-tip opening displacement (COD) with crack-tip stress

4.4.9.2 Welded Tubular Joints

4.4.9.2.1 Finite Element Model and Analysis

A 2-D finite element model as shown in Fig.4.14 of tubular joint is created and in the crack faces, interface elements as described above are applied. Symmetric boundary conditions are applied at the left side of the model. Two load cases are considered as shown in Fig. 4.15(a) and 4.15(b). In case (a) cyclic pressure load is applied at the outer surface and in case (b) cyclic pressure load is applied at the nodes between 45 and 90 degrees (similar to wave load on offshore structures). The same constant amplitude cyclic loads are applied to the model for both cases. The model is created and analyzed by writing code in ANSYS 7.1.

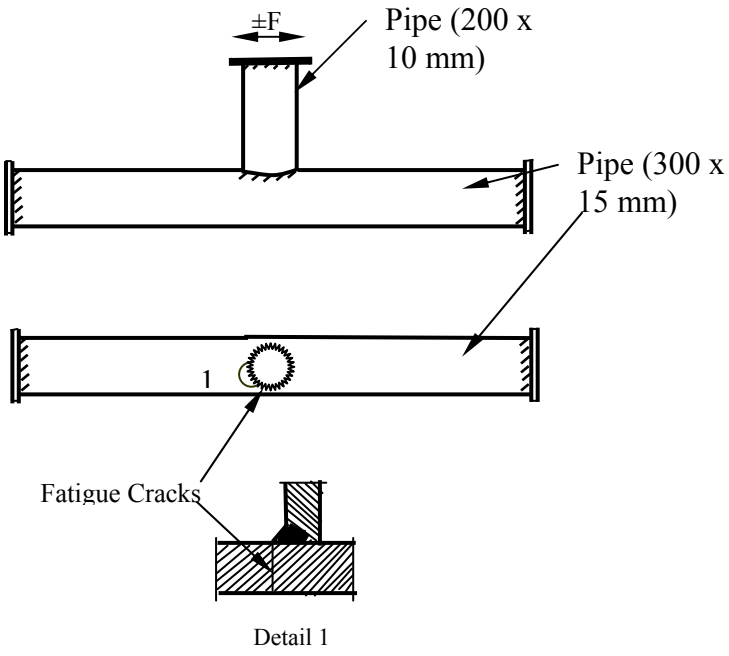

Figure 4.14 A schematic view of T- joint offshore structure under cyclic loading

The same mechanical properties of base, weld and heat-affected-zone (HAZ) material as shown in Table 3.1 are applied to the model. The Paris' crack growth rate constants and the other properties same as case (a) are also applied to the model. The axial cyclic load near the yield strength of material is applied for various cycles, and the corresponding stress intensity factor and crack

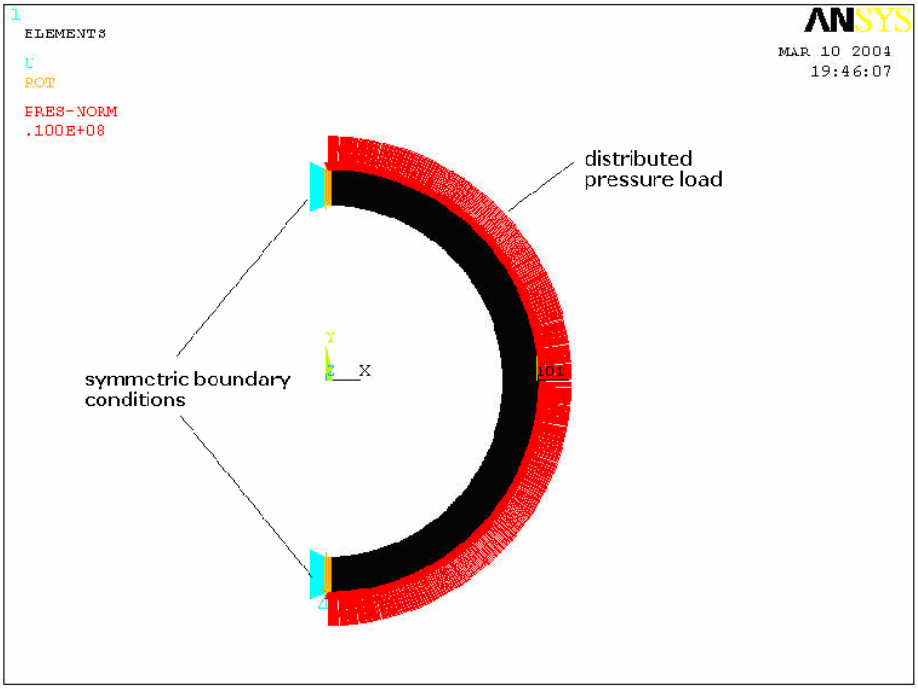

Figure 4.15 (a) A 2-D FEM model of a tubular welded joint (compressive pressure load at the outer surface)

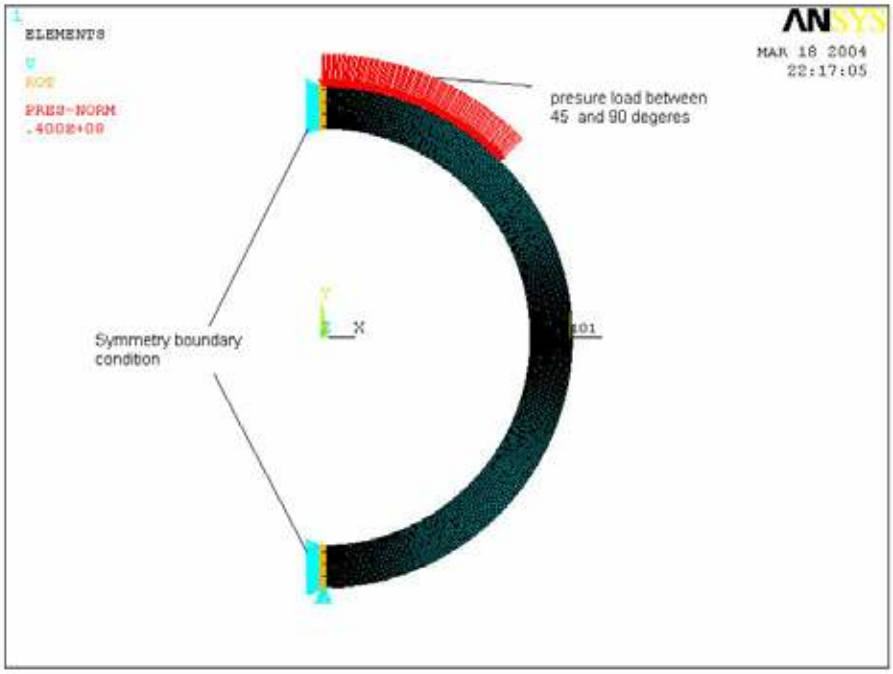

Figure 4.15 (b) A 2-D FEM model of a tubular welded joint (compressive pressure load at intermediate location between 45 and 90 degrees)

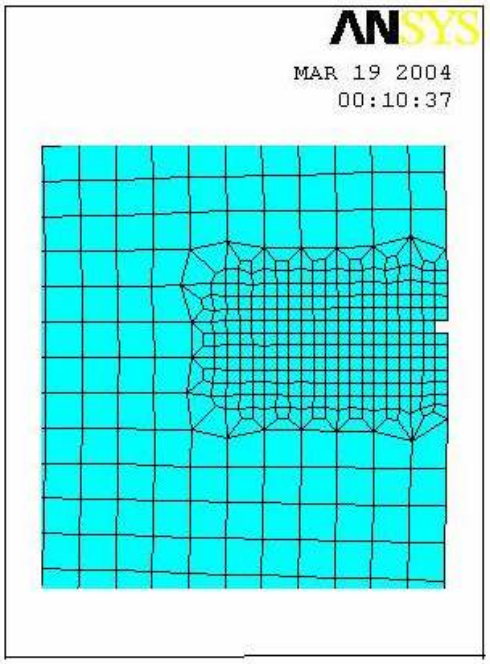

Figure 4.15 (c) Denser mesh at the crack-tip

opening displacement are calculated from the FEM analysis. Then using subsequent equation (4.17) and (4.18), the fatigue crack growth rate and fatigue crack propagation life are calculated.

4.4.9.2.2 Results and Discussions

For load case (a), the fatigue crack growth rates for different stress ratios, R are calculated and shown in fig. 4.16. As the stress ratio decreases, the crack growth rate increases. When the stress ratio increases, the range of stress increases and hence the crack growth rate increases. Again, generally the range of threshold stress intensity factor decreases with increase of stress ratio. According to equation (4.17), the crack growth rate decreases with increases of ΔK_{th} .The results of Fig. 4.16 indicates this trend. Further, the difference in crack growth rate for different stress ratios at high range of stress intensity factor is smaller than that at low range of stress intensity factor. This may be due to the effect of threshold stress intensity factor. At low stress level i.e. low range of stress intensity factor; the effect of threshold stress intensity factor over crack growth rate is more than at high stress level. Furthermore, after the range of stress intensity value about 8, the

crack growth rate becomes constant for all stress ratios. This may also be for threshold stress intensity factor. For this type of mild steel, the threshold stress intensity factor is less than 8 $MN/m^{3/2}$. Therefore, there is less effect of threshold stress intensity factor on fatigue crack growth rate after 8 $MN/m^{3/2}$. The variation of fatigue life with range of stress intensity factor for three stress ratios is shown in Fig.4.17. The fatigue life increases at low stress intensity factor and the trend is to become infinity below threshold stress intensity factor. Because at low stress level the accumulation of fatigue crack growth is very low and the fatigue life increases to infinity. On the other hand, the fatigue life decreases with the increase of stress intensity factor. For a particular range of stress intensity factor 10, the fatigue life decreases about 25% at stress ratio 0.2 and 52% at stress ratio 0.3 comparing to that at stress ratio 0.1.

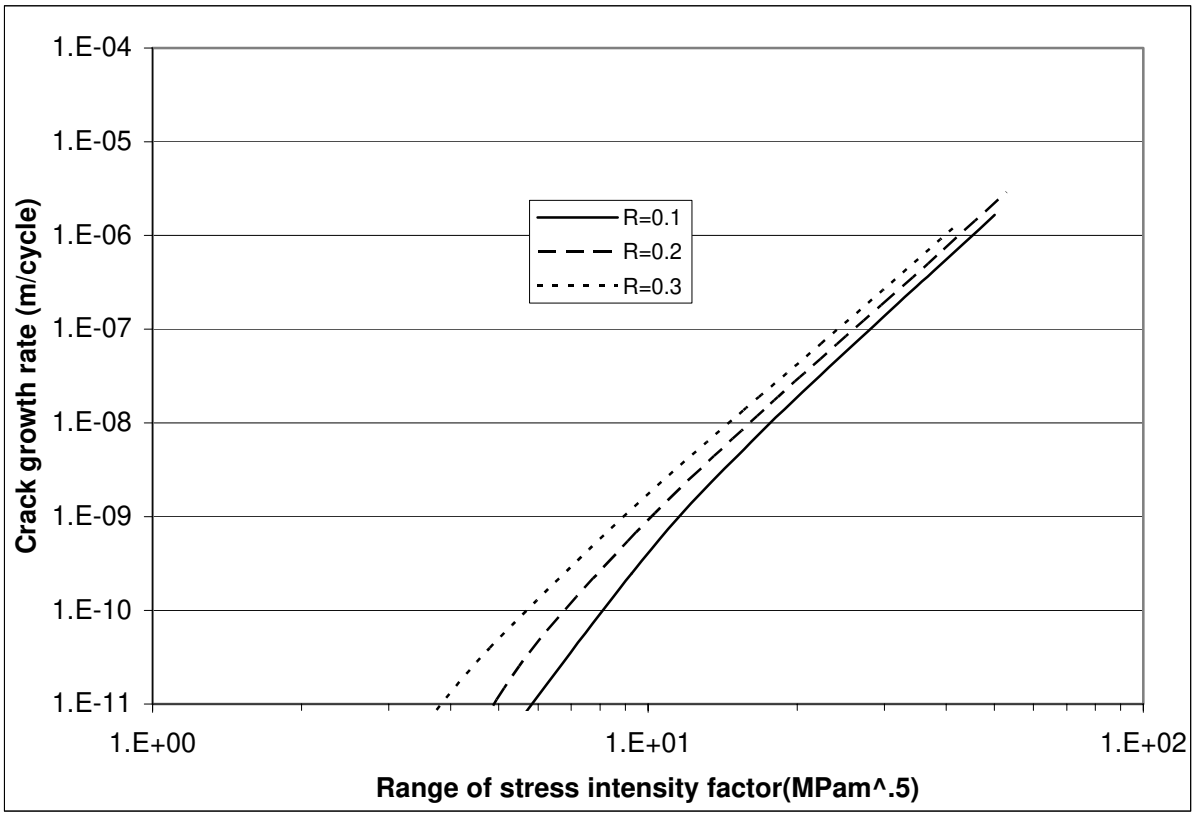

Figure 4.16 Fatigue crack growth rate with the range of stress intensity factor

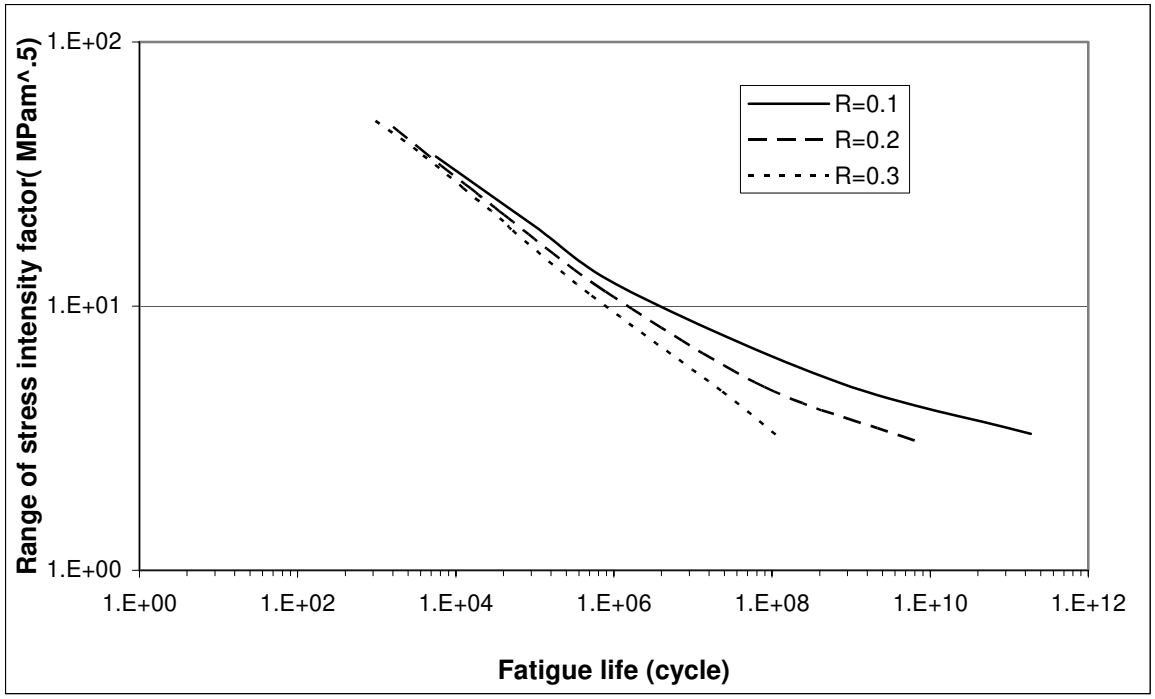

Figure 4.17 Variation of fatigue life with range of stress intensity factor

The variation of crack opening displacement with crack tip stress is shown in Fig. 4.18. The crack opening displacement (COD) increases with crack tip stress. For a particular crack tip stress, the COD increase with increases of stress ratios. In this case, load amplitude was constant; increasing both minimum and maximum load has changed the stress ratios. Therefore, the stress ratio increases with the increases of maximum stress. The results shown here are for the maximum load only. For this reason, the COD increases with the increase of stress ratio. Further at low stress, the variation of COD is less comparing to high stress level. The crack tip stress increases with the increases of crack length. So the COD increases with the increases of crack tip stress. The variation of strain in the y direction at the crack tip with crack tip stress is shown in Fig. 4.19. The strain increases with crack tip stress. At low crack tip stress, the change in strain for different stress ratios is less comparing to that in high crack tip stress. The crack tip stress increases with increases of crack length. As the crack length increases, the material stiffness decreases and crack tip stress increases, and hence the strain increases.

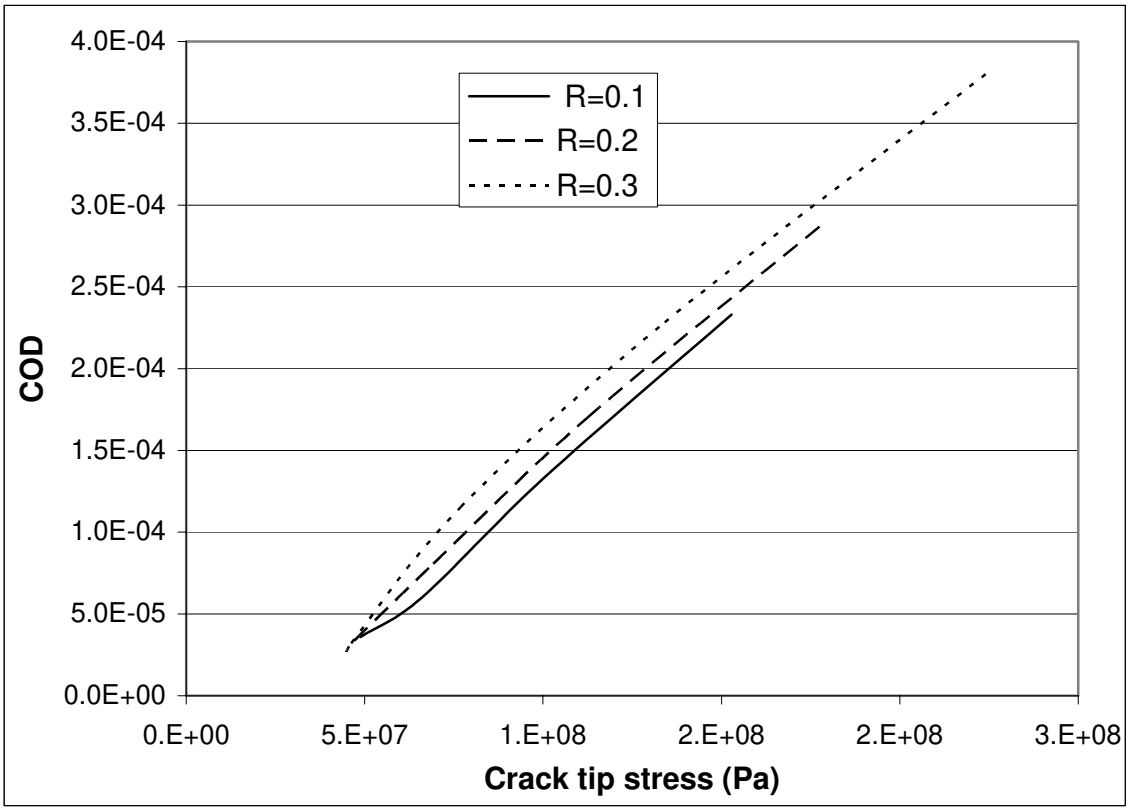

Figure 4.18 Variation of crack-tip opening displacement (COD) with crack-tip stress

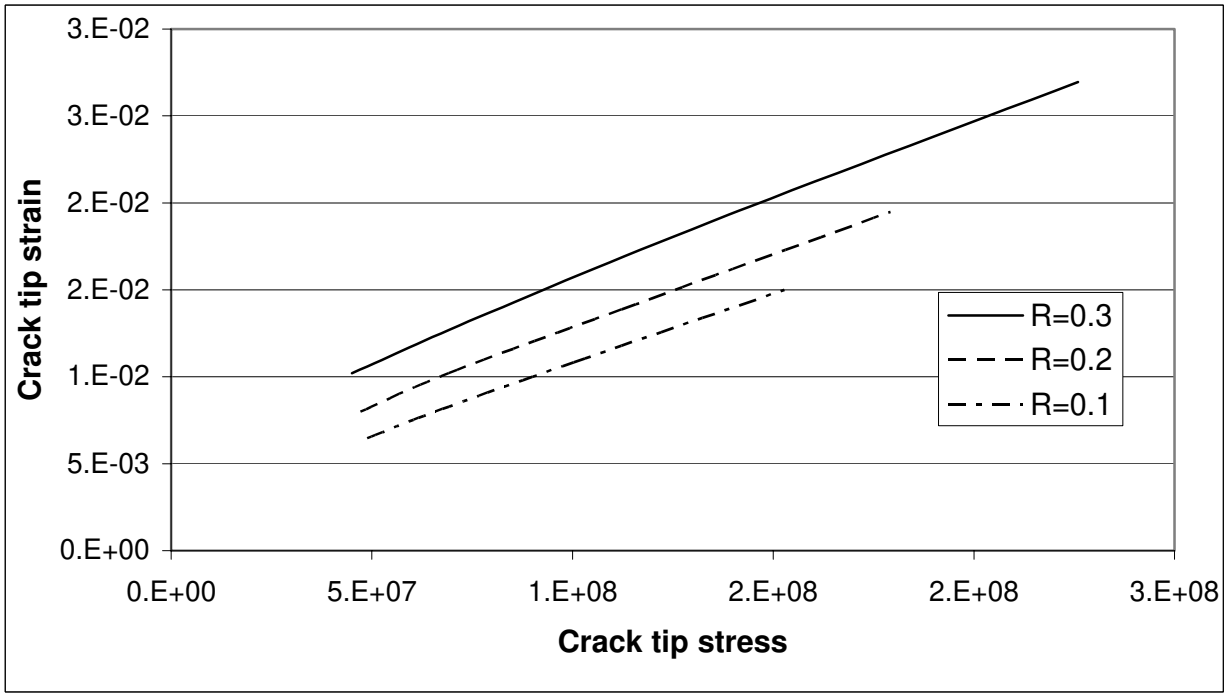

Figure 4.19 Variation of strain at crack-tip with crack-tip stress.

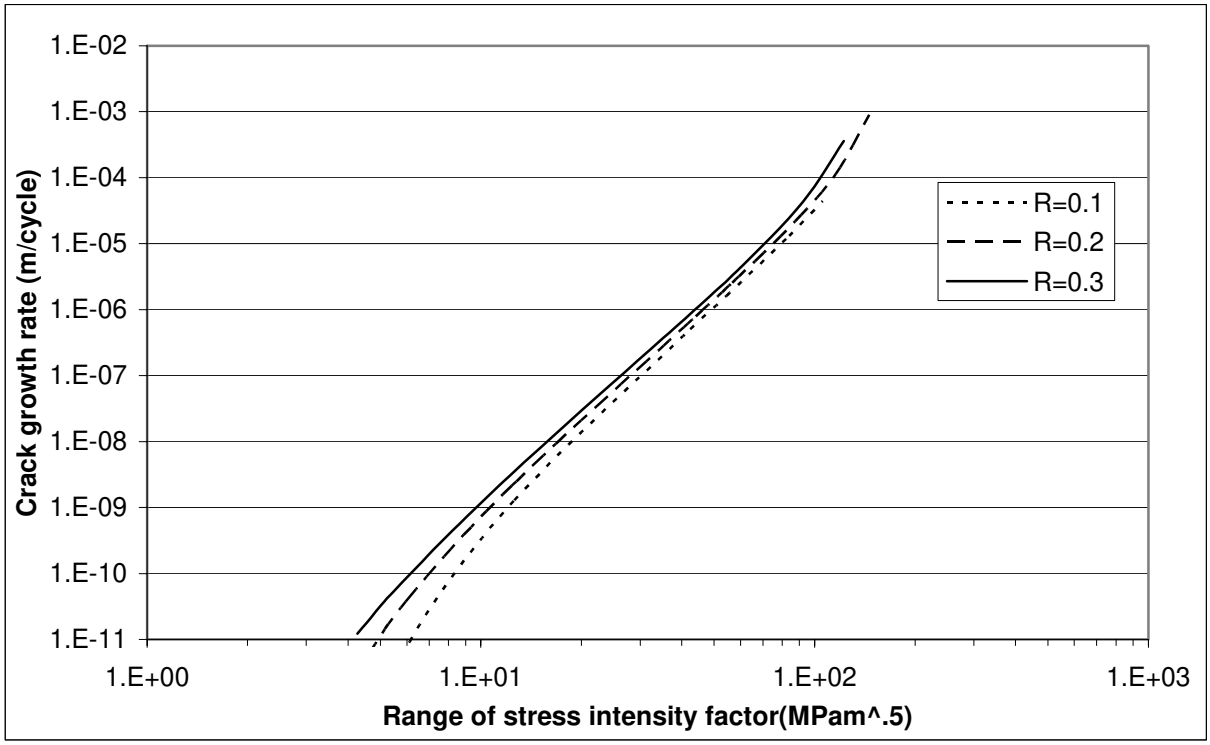

Figure 4.20 Fatigue crack growth rate with the range of stress intensity factor (for case b).

For case (b), the fatigue crack growth rate for different stress ratios, R is shown in fig. 4.20. For case (b), the crack growth rate is higher than that in case (a). Because in case (a), the compressive pressure load above and below the crack faces neutralizes some tensile load at the crack tip. Further compressive pressure load near the crack tip decelerated crack growth rate. The crack growth rate increases rapidly above the starting point of the fast fracture. At the fast fracture, the material losses stiffness and stability and the crack growth rate increases rapidly.

The variation of fatigue life with range of stress intensity factor for case (b) is shown in Fig.4.21. For the same reason i.e. the compressive pressure load above and below the crack faces neutralizes some tensile force at the crack tip; in case (a) the fatigue crack growth rate is less comparing to that in case (b). Therefore the fatigue life increases in case (a) comparing to case (b).

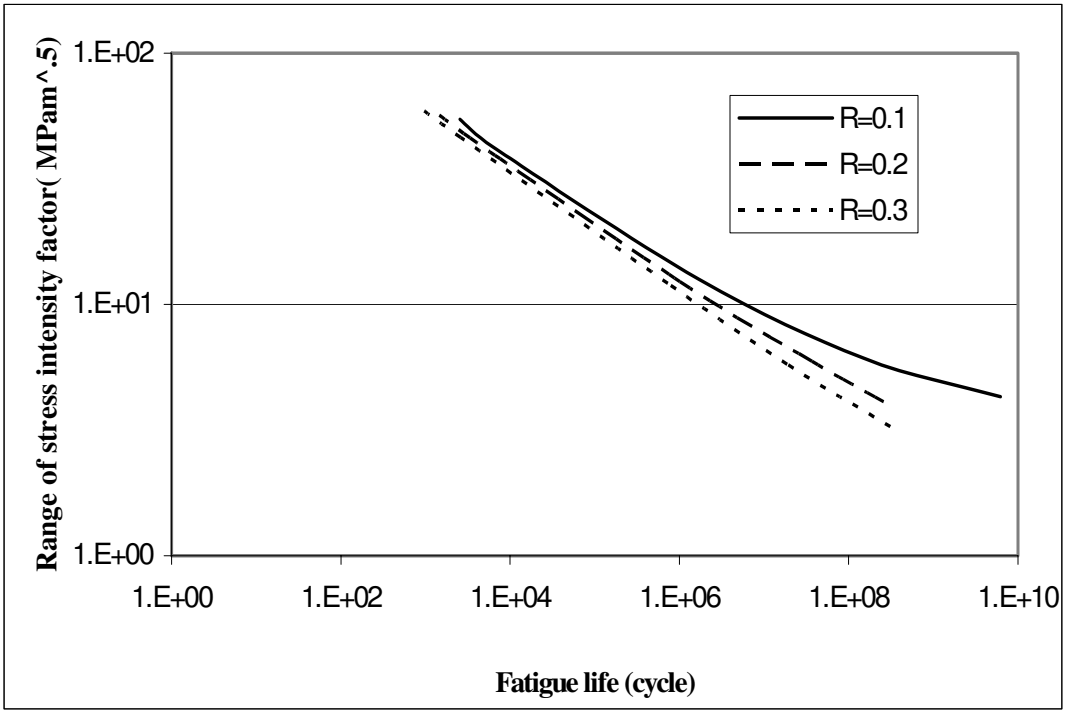

Figure 4.21 Variation of fatigue life with range of stress intensity factor (case b)

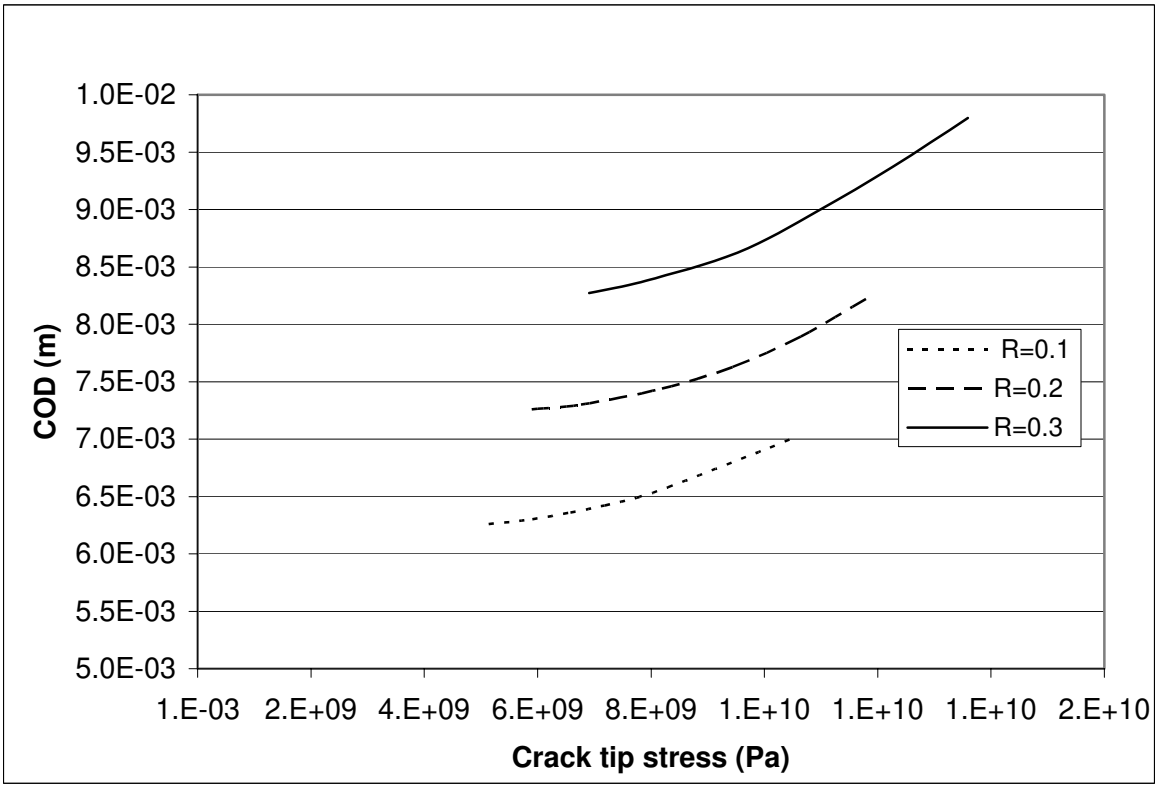

Figure 4.22 Variation of crack-tip opening displacement (COD) with crack-tip stress (case b)

At low range of stress intensity factor the fatigue life increases rapidly and its trend is toward infinity. At low stress level, the accumulation of fatigue crack growth is very low and the fatigue life increases toward infinity.

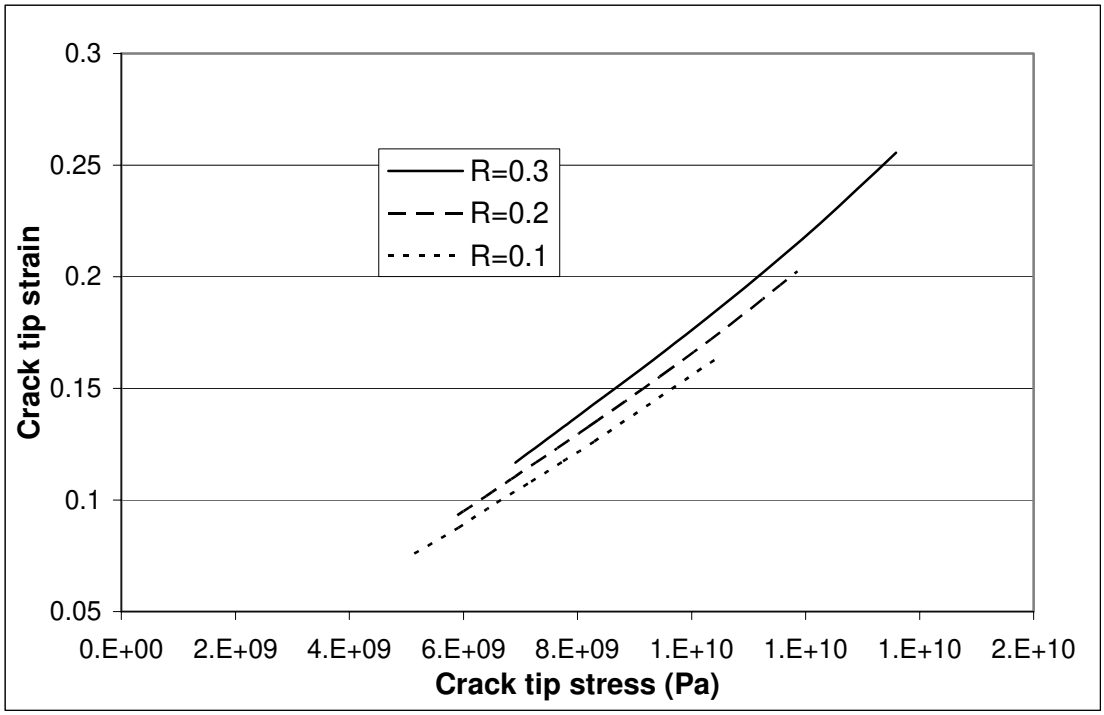

Figure 4.23 Variation of strain at crack-tip with crack tip-stress (case b)

The variation of crack opening displacement with crack tip stress for case (b) is shown in Fig. 4.22. The crack opening displacement (COD) increases with the increases of crack tip stress. Since in case (a), the compressive pressure load above and below the crack faces neutralizes some tensile force at the crack tip and fatigue crack growth rate is less, the COD in case (a) decreases comparing to that in case (b). The variation of strain at the crack tip with crack tip stress for case (b) is shown in Fig. 4.23. The strain increases with crack tip stress. At low crack tip stress, the change in strain for different stress ratios is less comparing to that in high crack tip stress. The crack tip stress increases with increases of crack length. As the crack length increases, the material stiffness decreases and hence the strain increases. Further in case (a), the compressive pressure

load above and below the crack faces neutralizes some tensile force at the crack tip and fatigue crack growth rate is less, the strain in case (a) decreases comparing to that in case (b).

4.4.10 Traditional FEM Model for Fatigue Crack Propagation

Traditional FEM model for an edge-cracked plate is shown Fig. 4.24. In the lower edge of the plate fixed boundary condition is applied and in the upper edge cyclic stress loading is applied. In traditional FEM, the crack tip propagation with fatigue load is considered to be linear. One crack tip node (from left side) is released (degrees of freedom is deleted) after each cycle and the crack propagates one element length in each cycle of the fatigue load.

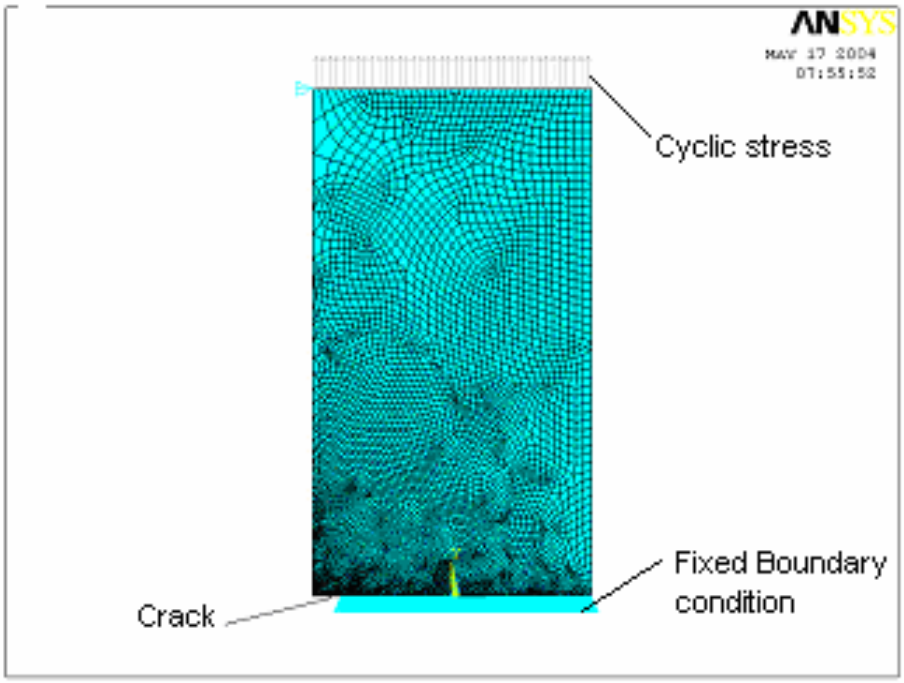

Figure 4.24 Traditional FEM model for fatigue crack propagation of a center cracked plate

The comparison of fatigue crack propagation life between new (Interface Model) and traditional FEM model is shown in Fig. 4.25. It is found that in the traditional method, the fatigue crack propagation life is less (i.e. more conservative) comparing to that in the new proposed method. Since in the traditional method the crack propagation rate is more (one element length in each

cycle in a linearly fashion), therefore, the fatigue crack propagation life is lesser than the new method. Furthermore, the difference in fatigue life at low stress range is more than in the high stress range, because at higher stress cycles, crack initiation occurs much faster.

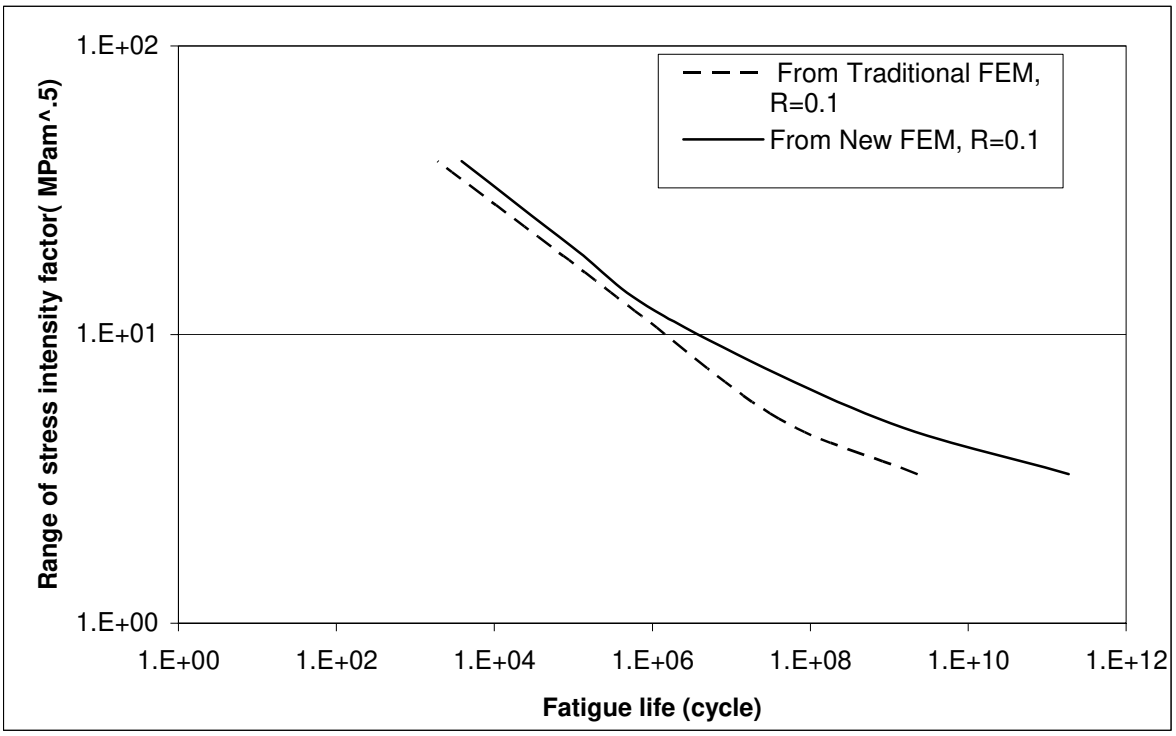

Figure 4.25 Comparison of fatigue crack propagation life from new and traditional FEM model

4.4.11 Validation

For validation, the predictions have been compared with the experimental data collected from the literature [Anderson, 1995]. The experimental results are for a single-V butt weld joint of the dimensions (356 x 98 x 16 mm). The mechanical properties of the weld material are the same as shown in Table 4.1. Similar model (same geometric and mechanical properties) has been analyzed using the authors' computer program and ANSYS code. The stress ratios for both the cases (experimental and prediction) are the same (R = 0) and the maximum loads are also the same (150, 180, 200, 220, 250 MPa respectively). The initial crack lengths for both the cases are considered to be the same (0.2 times width). It has been found that the prediction compares well with the

experimental results, and the comparison is shown in Fig 4.26. At low stress range, the trend of both the results is slightly different but at high stress range, both are close to each other.

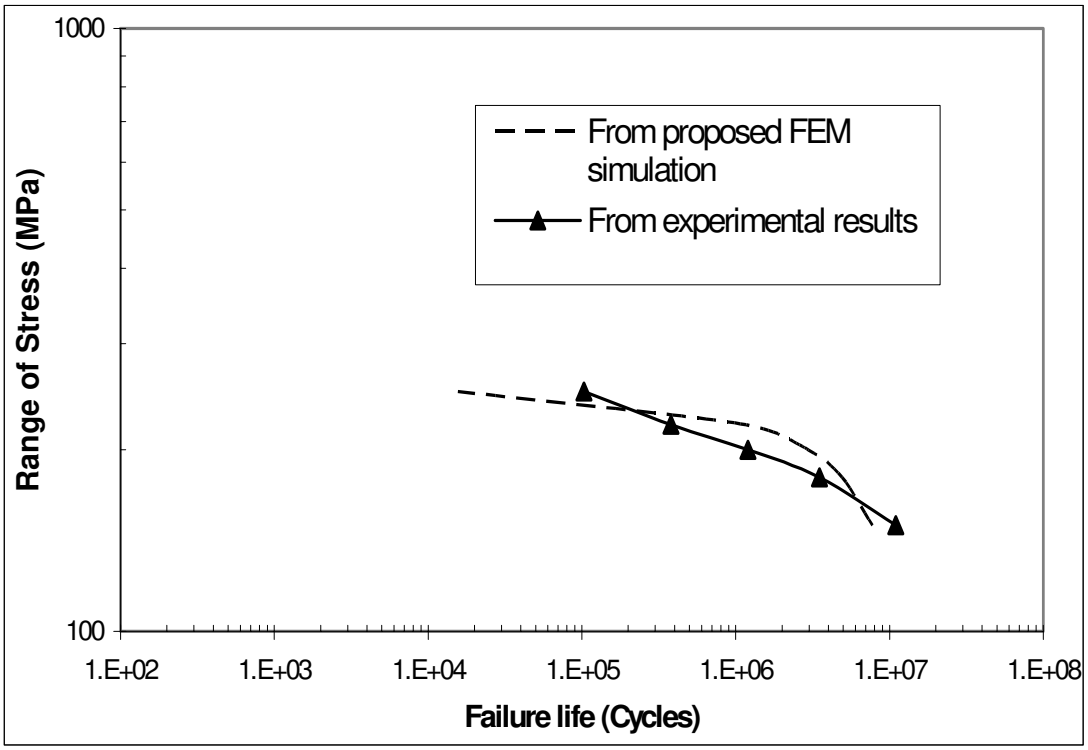

Figure 4.26 Comparison of prediction and experimental results [Burk, 1978]

At 2x 10^6 cycle, the percentage change in the stress range is about 6. This difference may be due to a different threshold stress intensity factor. The threshold stress intensity factor used in this analysis is collected from the literature [Anderson, 1995] available in the field and an average value dependent on stress ratio was assigned. In the experiment, threshold stress intensity factor need not to be considered separately and it is counted automatically. Another reason for this slight deviation may be the effect of residual stress. The residual stresses used in the prediction model are in the range from –120 MPa to 120 MPa (17.4 ksi) but in the experiment these values may be slightly different. The same model is also analyzed using the traditional FEM and the results are shown in Fig 4.25 for comparison.

4.4.12 Conclusions

The proposed simulation of fatigue crack propagation using an interface element is simple in formulation, effective in practice, and numerically less intensive. The method can be applied for symmetric and anti-symmetric planes under cyclic load and also for biaxial loading. This method overcomes the limitation of crack growth at a rate of one element length per cycle. In this method the crack propagates only when the applied load reaches the critical bonding strength. The method can also be applied in tubular welded joint.

CHAPTER 5 FINITE ELEMENT MODELING OF GAS METAL ARC WELDING (GMAW)

5.1 General

The GMA welding process has been widely studied, whether on researching a mathematical model to describe the complex physical phenomena arising from the technological process, or carrying out numerous experimental tests, and the resulting experimentation, together with experience gained in the field, are the most efficient means of determining optimum process parameters.

The greatest limitations to the empirical approach are nevertheless, the financial burden and length of time spent. However, theoretical study has encountered enormous obstacles, essentially due to the strongly non-linear nature of the problem and the scarce knowledge of physical and thermal parameters of metal at very high temperature. The advent of the electronic computer has opened up new horizons in the theoretical study of welding. The numerical technique of finite element method is the most frequently used methods of calculation.

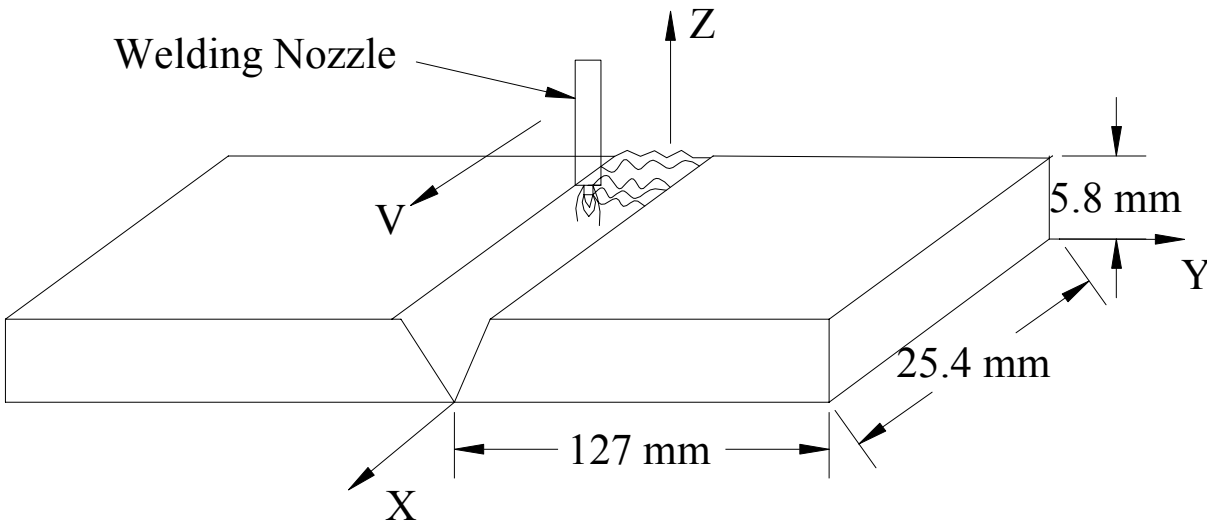

Figure 5.1 Gas metal arc welding process

5.2 GMA Welding Process

Figure 5.1 shows the GMAW process in which a constant supply of the consumable electrode is maintained through the centre of the welding nozzle. When the electrode comes close to the work piece, an arc is produced, which cause the electrode tip to melt and join the V-groove between the two plates. A constant supply of the shielding gas (98% argon and 2% oxygen) is also maintained through the annulus around the feed wire inside the nozzle, protecting the weld from atmospheric contamination.

Regarding to modelling the process, the following may be noted:

(1) A part of the heat supplied by the arc is consumed to melt the welding wire continuously

(2) A part of the heat is lost to the surroundings before it is received by the plates.

(3) The heat of the arc and the molten metal joining the work piece induces heat flow in all three dimensions in the work piece. Consequently, complex metallurgical changes are caused in the fusion zone or the melt-pool zone (MPZ) due to the severe thermal cycle the metal undergoes. Adjacent to the MPZ, the metal is heated to below the melting point that causes significant changes in the microstructures. This region is called heat-affected zone.

(4) In the heat transfer process heat is lost from the surfaces in the form of convection and radiation.

(5) The drift of the shielding gas causes enhanced convective heat loss from a part of the surface.

5.3 Energy Equation

The governing energy equation of heat conduction is:

$$\rho c \frac{\partial T}{\partial t} = k\left(\frac{\partial^2 T}{\partial x^2} + \frac{\partial^2 T}{\partial y^2} + \frac{\partial^2 T}{\partial z^2}\right) + \frac{\partial k}{\partial T}\left[\left(\frac{\partial T}{\partial x}\right)^2 + \left(\frac{\partial T}{\partial y}\right)^2 + \left(\frac{\partial T}{\partial z}\right)^2\right] \tag{5.1}$$

Where ρ is the density, c is the specific heat, k is the thermal conductivity, and T is the temperature. The mathematical analysis of heat flow in a solid is a solution of equation (5.1) using

a set of initial and boundary conditions, such as initial temperature distribution, shape and size of the heat source, geometry of the base plate, and temperature gradients on surfaces of the base plate.

If we assume that the thermal properties (ρ, c, k, T) are constant with temperature and a = k/ρc, the equation (5.1) is reduced to:

$$\frac{\partial T}{a\partial t} = \left(\frac{\partial^2 T}{\partial x^2} + \frac{\partial^2 T}{\partial y^2} + \frac{\partial^2 T}{\partial z^2}\right) \tag{5.2}$$

It has been noted [Nguyen, 2004] that equation (5.2) is satisfied by

$$T(x, y, z, t) = \frac{Q}{(4\pi at)^{3/2}} \exp\left(-\frac{(x - x')^2 + (y - y')^2 + (z - z')^2}{4at}\right) \tag{5.3}$$

This means that T(x, y, z, t) is the solution of the general heat-conduction equation (5.2) that represents the temperature distribution in an infinite body due to a particular heat source located at point (x' , y', z'). Convection heat losses are evaluated using following equation.

$$q = h\,(T - T_o) \tag{5.4}$$

Where q is heat losses, h is convective heat transfer coefficient; T is plate temperature and T_o is ambient temperature. Radiation heat losses are accounted by using the equation (5.5).

$$q = \varepsilon\,\sigma\,(T^4 - T^4_o) \tag{5.5}$$

Where ε is emissivity of body surface, σ is Stefan Bolzman constant.

5.4 Model of Heat Input to the Work Piece

The thermal power transferred by the electric arc Q may be written as:

$$Q = \eta VI = Q_{ind} + Q_{dir} \tag{5.6}$$

where Q_{ind} is the power necessary to melt and raise the filler metal to droplet temperature, while Q_{dir} is the part of the heat flux transferred directly from the arc to the joint.

Droplet temperature may be calculated according to current magnitude and wire diameter. In this case it is assumed to be equal to 2027 ^oC, (3680 ^oF) in accordance with [Barberis and Rebora,

1996]. Once the droplet temperature is fixed and wire feed speed noted, it is possible to calculate the indirect equation [Barberis and Rebora, 1996].

$$Q_{ind} = (\rho v_f \pi d^2/4)\left[\int_{T_o}^{T_S} c_p d\theta + \int_{T_S}^{T_L} (L/\Delta L/\Delta T + \int_{T_L}^{T_g} c_p d\theta\right] \quad (5.7)$$

$$Q_{dir} = Q - Q_{ind} \quad (5.8)$$

where ρ = filler metal density

C_p = specific heat of filler metal

L = latent fusion heat of filler metal

ΔT= temperature interval of phase change

T_o = ambient temperature

T_s = solidus temperature

T_L = liquidus temperature

T_g = droplet temperature

m = mass of filler metal

Now Q_{dir} is assumed to be received by the work piece surface in a radially symmetric Gaussian profile. The direct heat flux Q_{dir} is assumed to be heat flux per unit volume per unit time generated inside the elements which fall instantaneously under the electric arc. In this study the Gaussian distribution on the double ellipsoid is reduced to constant distribution. It is mention in [Barberis and Rebora, 1996] that the main results of the calculation are not significantly influenced by this approximation.

5.5 Surface Heat Losses

Natural convective heat transfer occurs on all surfaces of the plates except the plane of symmetry (y = 0). But the area directly beneath the nozzle of the torch experience forced convection due to the flow of the shielding gas. Based on previous models [Tekriwal and

Mazumder, 1988], h = 10 W/m^2 ^oC (0.2582 $Btu/min/in^2/^oF$) is used for all the surfaces not influenced by the shielding gas. The heat exchange coefficient for forced convection is evaluated using the correlation proposed in [Sten, 1976]:

$$h_g = 13 Re^{1/2} Pr^{1/3} K_{gas}/NPD \tag{5.9}$$

Reynold's number, $Re = \frac{v_{gas}\rho_{gas}D}{\mu_{gas}}$

Prandtl number, $Pr = \frac{\mu_{gas}Cp_{gas}}{K_{gas}}$

where:

v_{gas} = gas outflow speed

ρ_{gas} = gas density

μ_{gas} = dynamic viscosity of gas

K_{gas} = heat conductivity of gas

Cp_{gas} = specific heat of gas

D = nozzle diameter

NPD = nozzle to plate distance

The other researcher [Tekriwal and Mozumder, 1988], however, asserted that the forced convection flux is below 5% of the total heat exchange and a more accurate representation of h_g will not produce any difference in overall results. For this reason, in this study, a constant value of h_g is used for every point under the nozzle. The radiation emission factor is considered as 0.5 in this study.

5.6 Finite Element Modeling of GMAW

A 3-D FEM model of a single-V butt-weld joint (Figure 5.1) in a steel specimen has been created using author's written Ansys code. Due to symmetry of heat flux and geometry on plane

YZ, only half the joint is modelled (Figure 5.2). In the FE model "Solid-5" (3-D 8-nodes element) elements are used which have the capability of treating both conduction and convection.

It is assumed that only the convection occurs on the surface of the specimen and conduction occurs within the specimen. Convection describes the effect of temperature gradients between the post-weld plate surfaces and the room temperature of the surrounding air (assumed 15^{o}C (59 ^{o}F) from the literature [Runnemalm, 1999]). In this case it has been assumed that the plate surface-temperature changes due to the combined effects of (i) conduction within the specimen and (ii) convection from the specimen surface-temperature to the surrounding-air temperature and (iii) radiation. The temperature within the specimen changes from weld pool to the location away from the weld pool due to conduction.

The temperature-dependent material properties (i.e. modulus of elasticity, thermal conductivity, coefficient of specific heat, modulus of thermal expansion, Poisson's ratio, yield stress, tangent modulus etc.) of base and weld materials were collected from the work of Runnemalm [1999] for various temperature conditions and have been applied to the model. A moving heat flux method is used in the transient heat transfer analysis. The magnitude of the heat flux is determined from the heat input, welding speed and thickness of the plate. For a set of welding parameters (i.e. voltage 23 V, current 232 Amps, welding speed 5 mm/sec, arc efficiency 93.7%, and plate thickness of 10 mm) the magnitude of heat flux is calculated as 100E6 Joule/m^2 (voltage x current x arc efficiency/(weld speed x thickness). This heat flux is applied as a surface elemental-load from one end of the plate to the other, using a "do-loop" command. After finishing one increment of the "do-loop", the previous heat flux is deleted and another heat flux (the same amount) is applied to the next element. The temperature constraints from the elements of the base material and weld materials are removed, which will allow the base metal to contract or expand freely. In the FE model "Solid-5" elements are used which have the capability of treating both conduction and

convection conditions. The natural convection heat transfer coefficient for all external surfaces was assumed to be 10 $W/m^2/ {}^oC$ (0.2582 Btu/ $min/in^2/{}^oF$) and the temperature of the surrounding air was 15 ^OC (59 ^OF) [Takriwal and Mazumder, 1988]. The forced heat transfer coefficient h_g (119 $W/m^2/ {}^oC$) is calculated using equation (5.7) and is applied only in the weld elements (y = 0 plane). In transient analysis the convective heat transfer is applied as a surface-load using authors' written Ansys code. The Ansys command "SF" is used for applying surface load and "CONV" is used to represent type of surface load. The convective heat transfer coefficient and the ambient temperature are also mentioned in the same command line.

A convenient way to model radiation between a surface and a point is to use surface effect elements superimposed on surfaces that emit or receive radiation. ANSYS provides such elements: SURF151 for 2-D models and SURF152 for 3-D models. The element option KEYOPT(9) activates radiation for these elements. The form factor can be specified as a real constant (defaults to 1) using KEYOPT(9) = 1, from the basic element orientation and the extra node location. In this analysis SURF152 is used for surface effects element and a space node has been defined where energy is radiated from the surface. The surface emission factor is considered as 0.5 and Boltzeman constant is considered as 5.667E-8. The radiation is considered only from the top of the surface.

Thus for a particular weld speed, the bead deposition is completed by a particular time and the analysis proceeds until time t = 60 sec to include at least the most significant part of the heat transfer. Following welding parameters are used in this analysis [Tekriwal and Mazumder, 1988]:

Ambient temperature = 15 ^oC

Filler metal temperature = 2027 ^oC

Solidius temperature = 1427 ^oC

Liquidus temperature = 1482 ^oC

Latent heat of fusion = 273790 J/kg

Density of mild steel = 7870 kg/m^3

Welding voltage = 28 V

Welding current = 380 A

Arc efficiency = 0.67

Welding speed = 5.08 mm/s

Filler wire diameter = 1.6 mm

Filler wire feed speed = 55.5 mm/s

Nozzle to plate distance = 19.05 mm

Nozzle diameter = 19.05 mm

Nozzle angle with the vertical = 0 deg

Shielding gas data (98 % Ar + 2% O_2)

Flow rate = 0.3933 L/s

Thermal conductivity =0.0178 W/m K

Specific heat = 518.816 J/kg K

Dynamic viscosity = 2.247 x 10^{-5} kg/m sec

Density = 1.73337 kg/m^3

5.7 Distortion and Residual Stress in Gas Metal Arc Welding

The development of welding technology to its present state is one of the most significant manufacturing achievements in this century. Power plants, super tankers, pipelines and ground vehicles are just a few examples of structures that are critically dependent on welding operations. Post-weld distortion, residual stresses and altered microstructures are all undesirable effects of welding operations that cost industry millions of dollars each year to prevent or to correct [Bachorski et al., 1999 and Smith, 1994]. There has been international effort to find suitable

solutions to this post-weld distortion that is the change in shape experienced by structure as a result of the fusion welding process. The distorted shape is the combination of transverse, longitudinal and angular distortions. In fusion welding process local expansion, contraction and volume change from phase transformation lead to non-homogeneous plastic deformation and the generation of residual stress field [Wohlfart and Zhang, 1994, Goglio and Gola, 1993].

A common concern in welding simulation is to account for the interaction between welding process parameters, the evolution of the material microstructure, temperature, and deformation. The resultant material structure and deformation may be needed in order to, in combination with in-service loads, predict life time and performance of a component. Therefore, research in this field requires the collaborative effort of experts in welding methods, welding metallurgy, material behaviour, computational mechanics, and crack propagation, for example. It is important to observe that uncertain material properties and net heat input make the success of simulations to a large extent dependent on experimental results [Lindgren, 2001].

The objectives of this research is to develop time efficient numerical model capable of predicting the post-weld distortion in a butt-welded joint, which results from the Gas Metal Arc Welding (GMAW) operation and measure the residual stresses and restraining forces in plates while welding (some of this research has been published in [Alam and Wahab, 2004]).

5.7.1 Finite Element Model and Analysis

A 3-D FEM model (figure 5.2) of a single V butt weld joint of dimension (254x25x6 mm) has been created using Ansys code. The same material properties and the same procedure as explained in section 5.5 are also applied in this model. After transient analysis for a particular time (60 sec), the angular, longitudinal and transverse distortion and the residual stresses for a particular location at different directions are calculated and presented in the work. The included angle of V-joint has

been changed to 30, 45, 60, 75, 90 degrees and the corresponding distortions and residual stresses are also calculated.

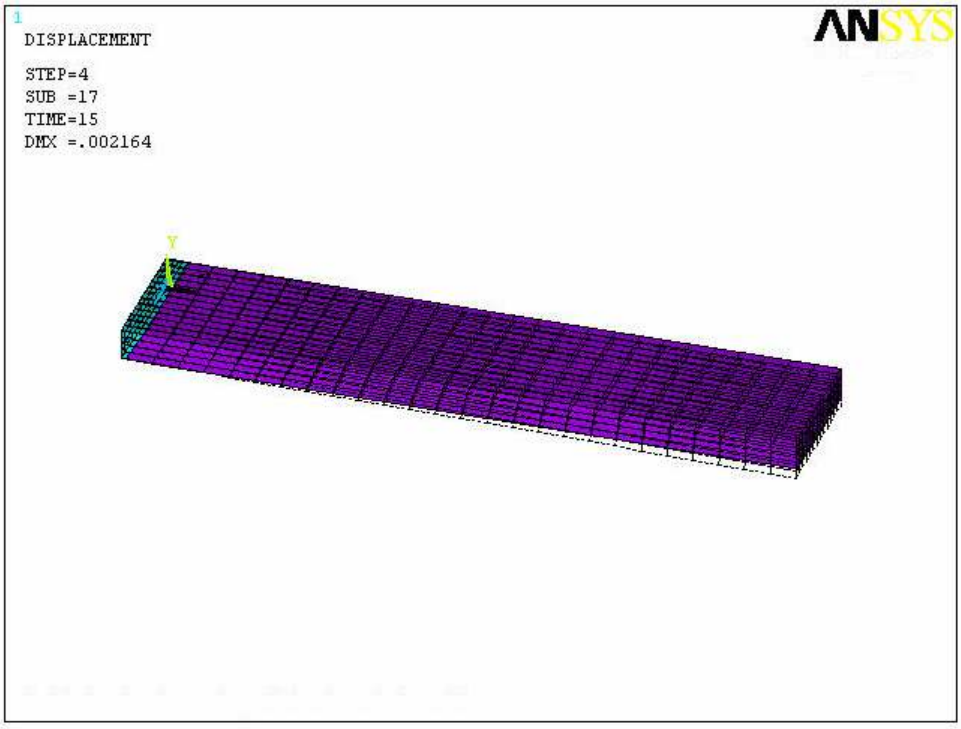

Figure 5.2 A symmetric 3-D FEM model (254 x 25 x 6 mm) of figure 5.1 after distortion

5.7.2 Results and Discussions

The temperature distribution at point 10 mm from centre of weld after 60 sec is shown in Fig. 5.3. The temperature at the first 5 sec increased sharply and then it decreases slowly. This is obvious case in welding. The variation of angular distortion with included angle is given in Fig. 5.4. The angular distortion increases linearly up to 60 degrees but thereafter sharply. The volume of filler material increases with increase of included angles. The expansion or contraction of the filler material also increased with the increasing of filler material. These expansion and contraction forces act on the weld metal and on the base metal. As the weld metal solidifies and fuses with the base metal, it is in its maximum expanded from. On cooling, it attempts to contract to the volume it would normally occupy at the lower temperature, but it is restrained from doing so by the adjacent

base metal. Because of this, stresses develop within the weld and the adjacent base metal. At this point, the weld stretches (or yields) and thins out, thus adjusting to the volume requirements of the

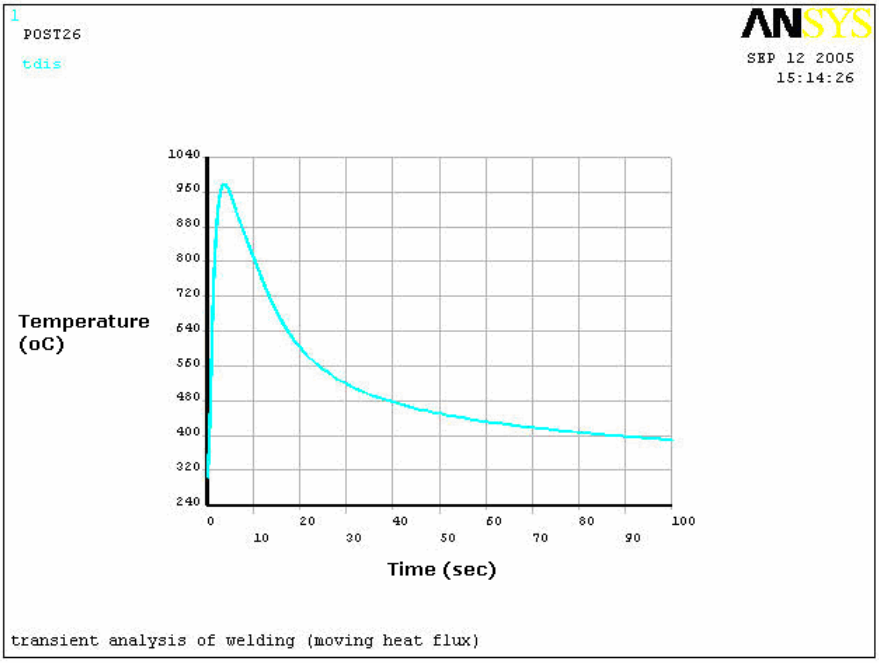

Figure 5.3 Temperature distribution after 60 sec at a distance of 10 mm from centre of weld

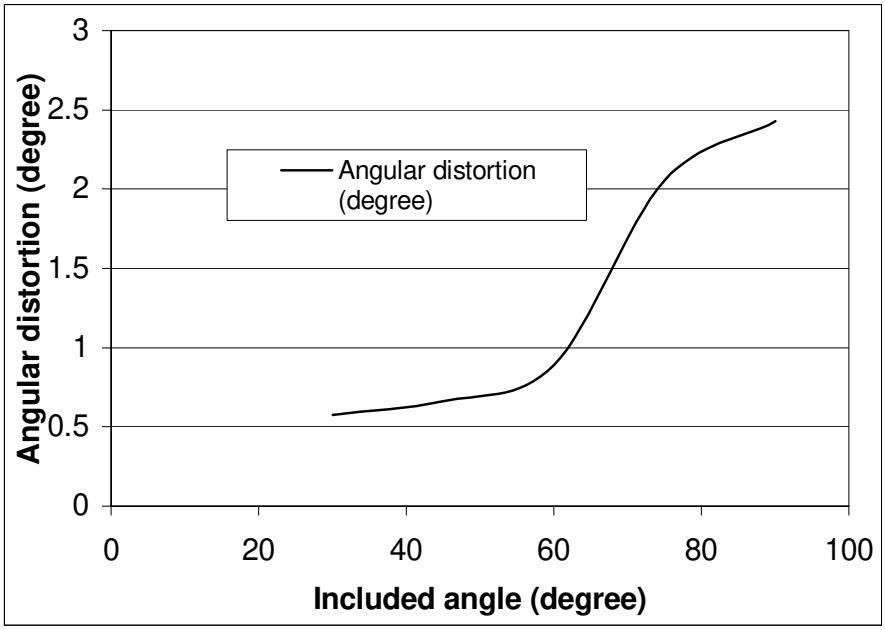

Figure 5.4 Angular distortion with included angle

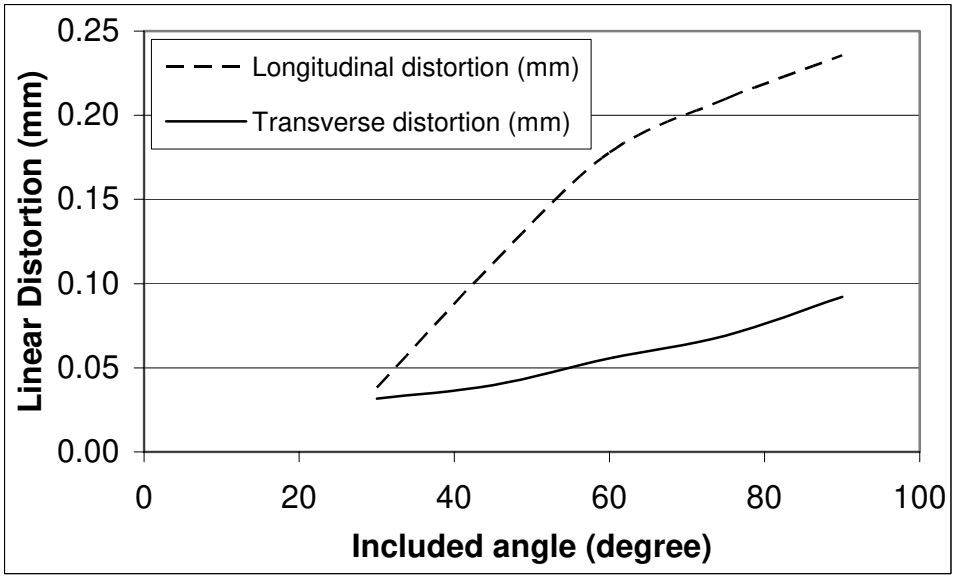

Figure 5.5 Longitudinal and transverse distortion

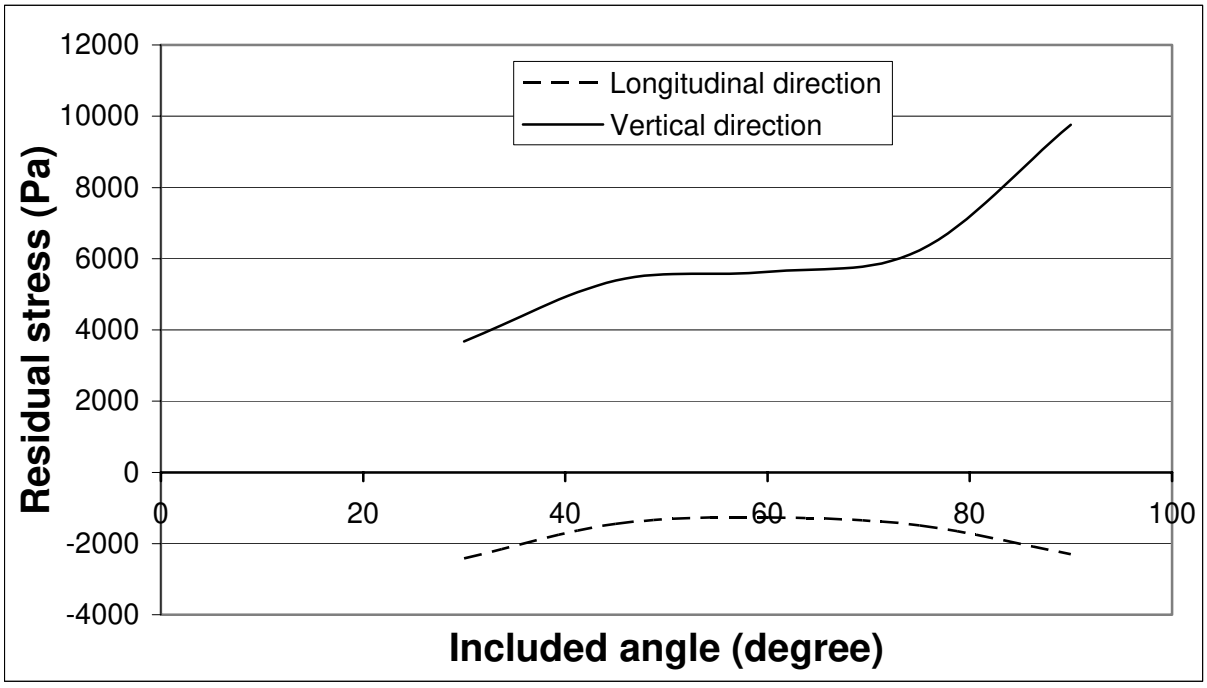

Figure 5.6 Residual stress over included angle in longitudinal and transverse direction

lower temperature. But only those stresses that exceed the yield strength of the weld metal are relieved by this straining. By the time the weld reaches room temperature - assuming complete restraint of the base metal so that it cannot move - the weld will contain locked-in tensile stresses approximately equal to the yield strength of the metal. If the restraints (clamps that hold the work

piece or an opposing shrinkage force) are removed, the residual stresses are partially relieved as they cause the base metal to move, thus distorting the weldment. If the volume of filler material increases, the residual force increases and hence the distortion increases with increase of included angle.

The variation in longitudinal and transverse distortions is shown in Fig. 5.5. The variation in longitudinal distortion is more than that in transverse distortion. This happens due to the fact that the restraint forces from the base plate in longitudinal directions are more than that in transverse directions (length is larger than width in this model). The variation of residual stress versus included angle at a particular point (25 mm from centre line of weld) in longitudinal and vertical direction is shown in Fig. 5.6. Residual stresses are tensile in transverse direction but compressive in longitudinal direction. It is mentioned that restraint forces from base plate in longitudinal directions are more than that in transverse directions. So the residual stress in longitudinal direction is compressive.

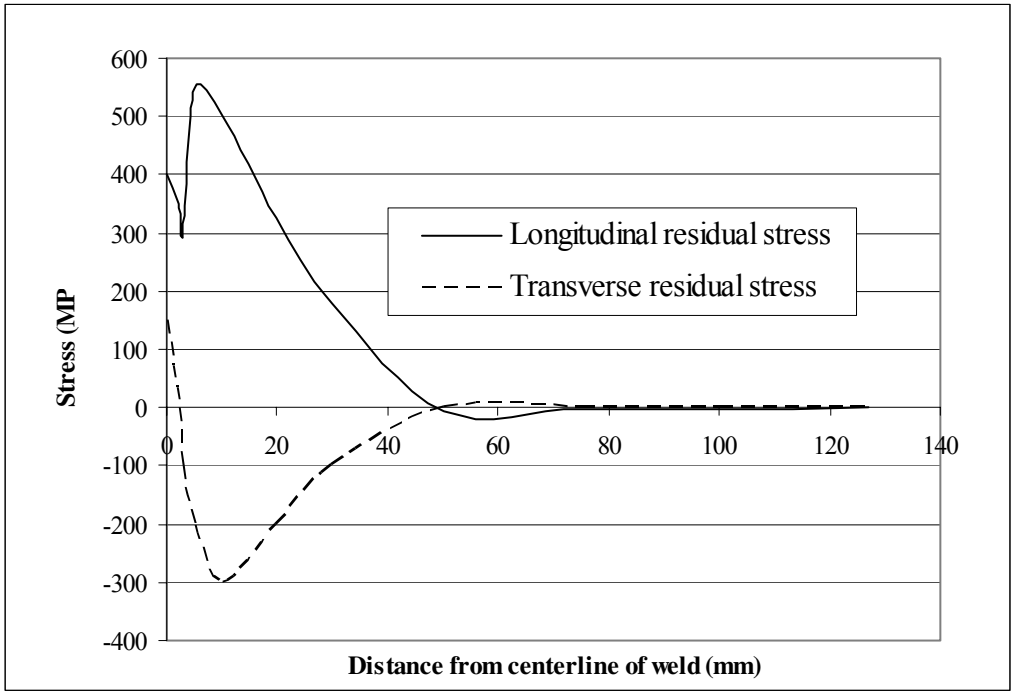

Figure 5.7 Residual stresses over distance in longitudinal and transverse direction

Residual stresses in longitudinal (welding direction) and transverse directions at different distance are shown in figure 5.7. Both residual stresses are tensile at the centerline of weld and then longitudinal is tensile and transverse is compressive. But at far away from weld line both are compressive. During the weld thermal cycle, material mechanical properties change drastically, especially when material approaches melting temperature. The initial expansion of material due to the temperature increase is constrained by material placed away from the heat source, therefore generating compressive stress. At a temperature higher than material critical temperature, the material starts exhibiting thermal softening where heating results in decrease of flow stress. As phase change occurs deviatory stress becomes zero and considerable plastic deformation occurs in the weld metal and the base metal regions near the weld. As temperature decreases during the cooling phase, the stress in the solidifying material increases, and becomes tensile due to the positive temperature gradient.

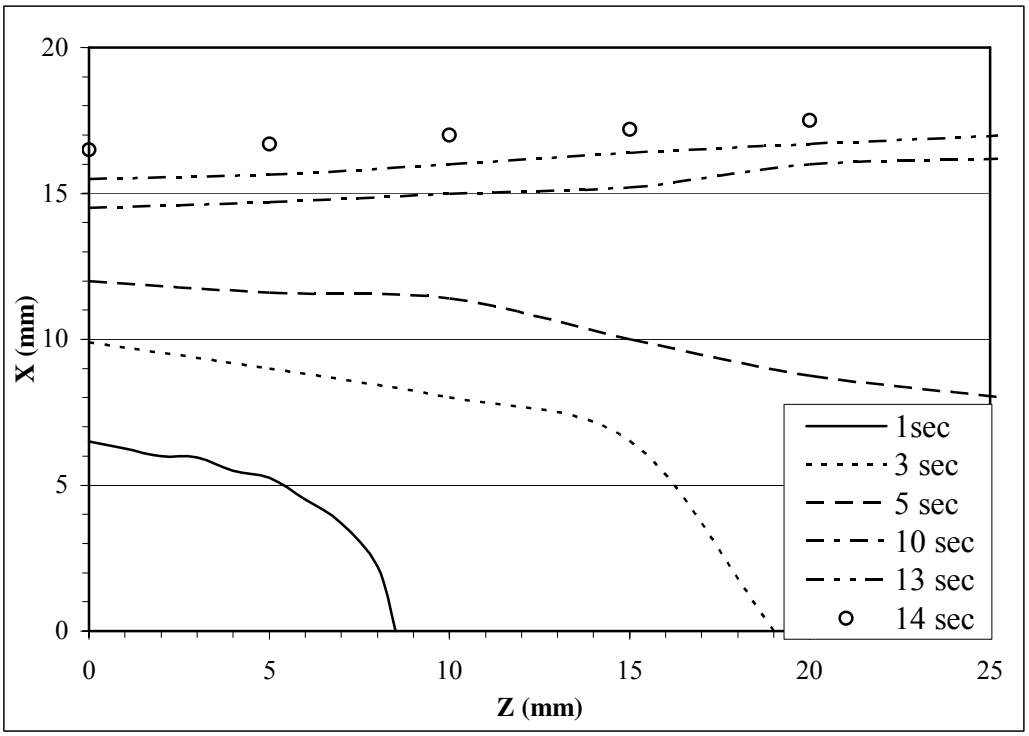

Figure 5.8 Isothermal line of the heat-affected-zone (727 ^{o}C)

The region placed away from the weld line, will therefore, be in compression since the resultant force and the resultant moment induced by residual stress evaluated in any plane section must satisfy translation and rotational equilibrium. The maximum residual stress is about 550 MPa (80 ksi) which is higher than yield stress of 350 MPa (51 ksi)). This may be due to the boundary constraints used in the model. To avoid rigid body motion, in addition to symmetric boundary condition two simple supports were used near the weld line.

The isothermal (constant temperature 727 ^{0}C) lines for different times are shown in figure 5.8. The maximum heat-affected-zone is found in 14 sec and is about 18 mm. For comparison, similar model was analyzed by Barbaris and Rebora [1996] and they found the heat-affected-zone 15.85 mm in 15 sec. The Takriwal and Mazumder [1987] got the zone 16 mm in 20 sec. The isothermal lines for fusion zone is shown in figure 5.9. The maximum fusion zone is found

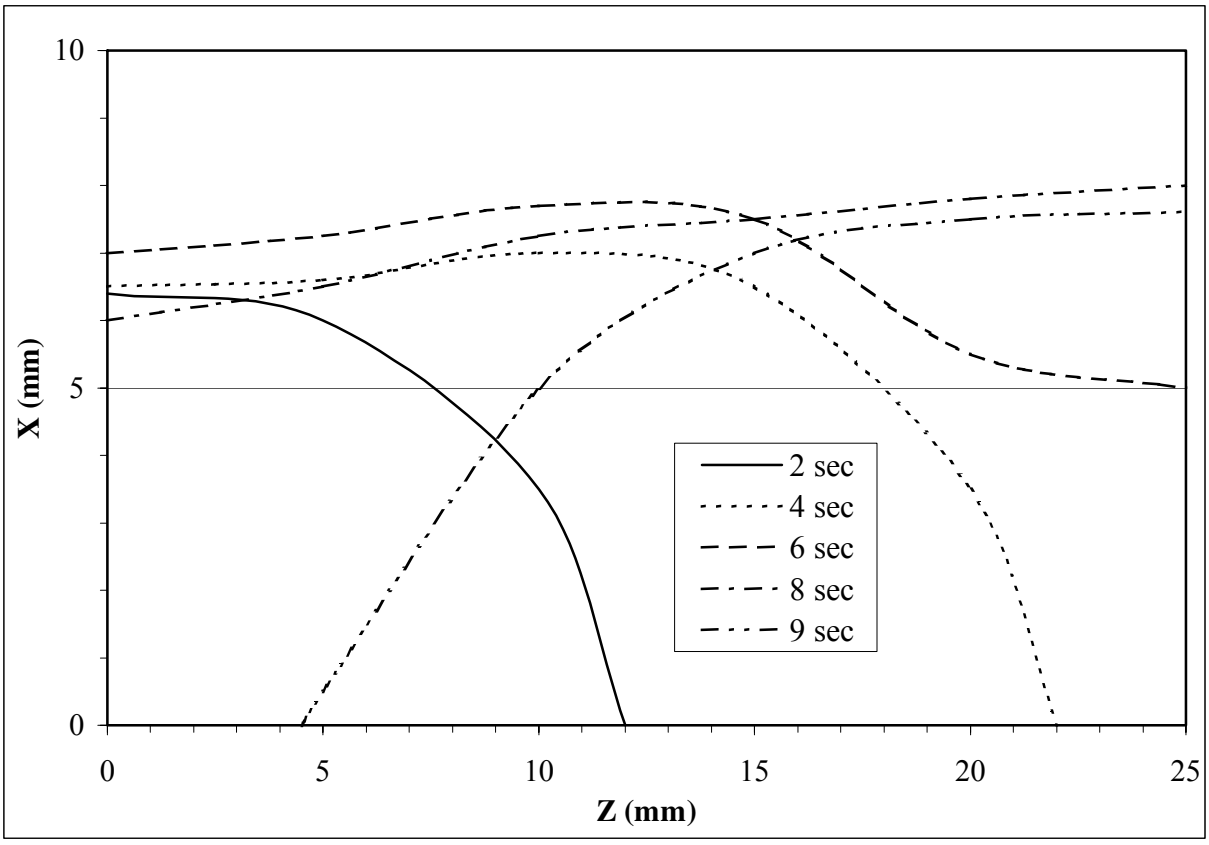

Figure 5.9 Isothermal lines of fused zone (1480 ^{o}C)

about 7 mm in 6 sec. Barbaris and Rebora [1996] found the fusion zone 8.6 mm in 7 sec. The Takriwal and Mazumder [1987] got the zone 7.7 mm.

5.7.3 Conclusions

The finite element simulation of the thermal process involved in the GMAW technique has been performed by means of ANSYS 8.1 codes. The temperature history with time, the heat- affected-zone, fusion zone, distortion, residual stress and restraining forces have been computed. Some results are compared with experimental and other similar results available in literature. Good agreement has been achieved between those results.

The included angle has influence on all distortions and residual stresses. As the included angle increases, all distortions increase. The angular distortion increases linearly up to 60 degrees and then increases rapidly. Residual stress in vertical direction increases up to 60 degrees and then decreases.

5.8 Restraining Forces in Gas Metal Arc Welded Joint

5.8.1 Introduction

Restraining forces arise from the non-uniform thermal field generated by welding. In this study restraining force exerted during welding process is calculated both numerically and experimentally. In numerical analysis Finite Element software (ANSYS 8.1) has been used. In experimental analysis, a jig was designed and built which uses load cells to measure the force required to restrain two steel plates while they are being welded by an automatically controlled welding-robot. After checking for reliability, tests were carried out to determine the effects of various welding speeds and heat inputs on the restraining forces. The results showed that welding speed has little effects on the restraining force but by increasing heat input, restraining forces increases significantly. The edge preparation has significant effect on the restraining force as well. The most relevant and useful information on the effects of the welding conditions is derived from

the slope of the graph of the force versus the distance traveled in time. The Finite Element predictions of restraining force due to various welding conditions produce similar trends and the slopes as the experimental results. The major objective of this current research is to simulate the retraining force of Gas Metal Arc Welded plate both experimentally and numerically and interesting new results have been observed from this investigation.

5.8.2 Mathematical Relation of Restraining Forces

In the welding process, the heat input around a weld joint causes a non-uniform temperature distribution and thermal stress. As a result, the plastic strain remains around the weld bead and permanent deformation occurs after welding. The plastic strain that causes the welding deformation is defined as the inherent strain [Jang and Lee, 2003]. In general, the inherent strain caused by welding has six components according to their directions. However, in the case where a plate has a large length/thickness ratio, only two components ε^*_{px} and ε^*_{py} are dominant, where ε^*_{px} and ε^*_{py} are inherent plastic strain in x and y directions respectively.

The inherent strain distribution and the restraining force can be formulated using a simplified thermal elastic-plastic analysis model as shown in Figure 5.10. The welding region, where the inherent strain occurs, can be modeled as a bar and a spring. The bar element has stiffness K_B, modulus of elasticity E, cross sectional area A and length L. The spring element has stiffness K_s.

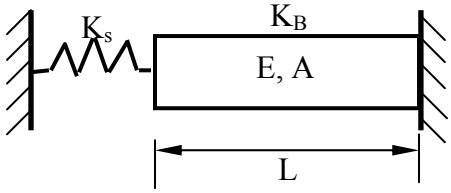

Figure 5.10 A simple elastic-plastic model of welding

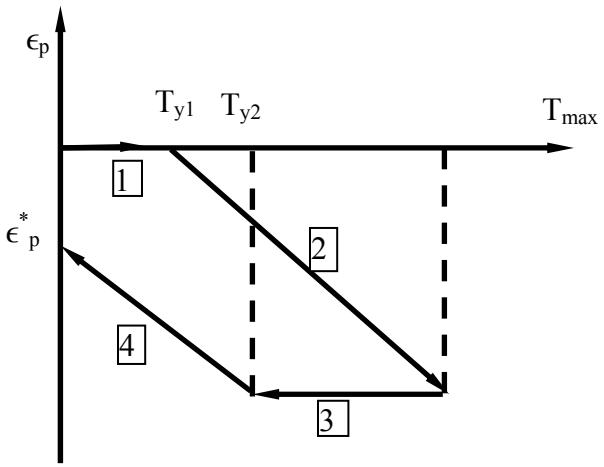

Figure 5.11 Thermal history of plastic strain

The thermal history of the inherent strain according to the temperature change of the bar can be divided into four steps, as shown in Figure 5.11. After all the thermal history the compressive plastic strain remains as an amount of ε^*_p. The magnitude of residual plastic strain can be calculated from the totals strain, the stress-strain relation and the equilibrium equation of a bar-spring system.

$$\text{Total strain} \qquad \varepsilon = \varepsilon_{ther} + \varepsilon_e + \varepsilon_p \tag{5.10}$$

$$\text{Stress-strain relation} \qquad \sigma = E\varepsilon_e \tag{5.11}$$

$$\text{Equilibrium equation} \qquad F_B = F_S \tag{5.12}$$

$$\text{The restraining force} \qquad Fs = K_S\, \varepsilon^*_p L \tag{5.13}$$

where ε total strain, ε_{ther} thermal strain, ε_e elastic strain and ε_p plastic strain, σ stress, E modulus of elasticity, F_B internal force of the bar element, F_S internal force of the spring. In Finite Element model, the equivalent restraint forces can be obtained by using the inherent strain. All types of equivalent loads are shown in Figure 5.12. The restraining force f_{yi} and f_{xi} can be found using equation (5.14) and (5.15)

$$f_{yi} = \frac{AE}{l} \sum_{j=1}^{N_i} \varepsilon^*_{pyj} l_j \tag{5.14}$$

$$f_{xi} = \frac{AE}{l} \sum_{j=1}^{N_i} \varepsilon^*_{pxj} l_j \tag{5.15}$$

The total equivalent transverse and longitudinal forces can be calculated using equation (5.16) and (5.17) respectively.

$$f_y = \sum_{i=1}^{N} f_{yi} \tag{5.16}$$

$$f_x = \sum_{i=1}^{N} f_{xi} \tag{5.17}$$

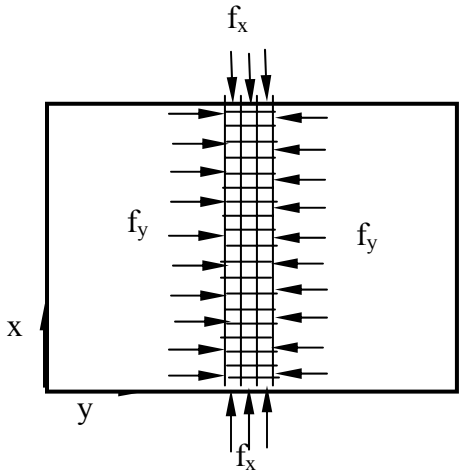

Figure 5.12 Equivalent loads of inherent strain

5.8.3 Experimental Procedure

5.8.3.1 Design

To generate the experimental data, a jig was designed and built. The aim of the jig was to hold two steel plates in position while being butt-welded and measure the restraining forces in position. The jig was designed to comply with the following constraints:

(i) To hold two hot rolled mild steel plates, 10mm x 100mm x 500mm (0.4 in x 4 in x20 in) ;

(ii) To allow measurement of restraining forces typically in the vertical and horizontal directions during simple butt-welding;

(iii) To allow access to Gas Metal Arc Welding torch;

(iv) To allow flexible placement of the restraint positions.

To measure the restraining forces, it was necessary to use some suitable force-measuring device. The two types of force measuring device available are strain gauge and load cell. For ease of interpretation of output and simplicity of design load cells were selected. As a result of thermal expansion and the restraints, the welded steel plates will shrink in the direction perpendicular to the direction of the weld. The jig was designed to measure only in compression, which includes the restraining forces for expansion and contraction down to zero loads (0.0 kN).

5.8.3.2 Configuration

The aim of the design of the jig (figure 5.13 and 5.14) is to hold the load cells against the plates so that they can prevent the plates from distorting and measure the restraining forces.

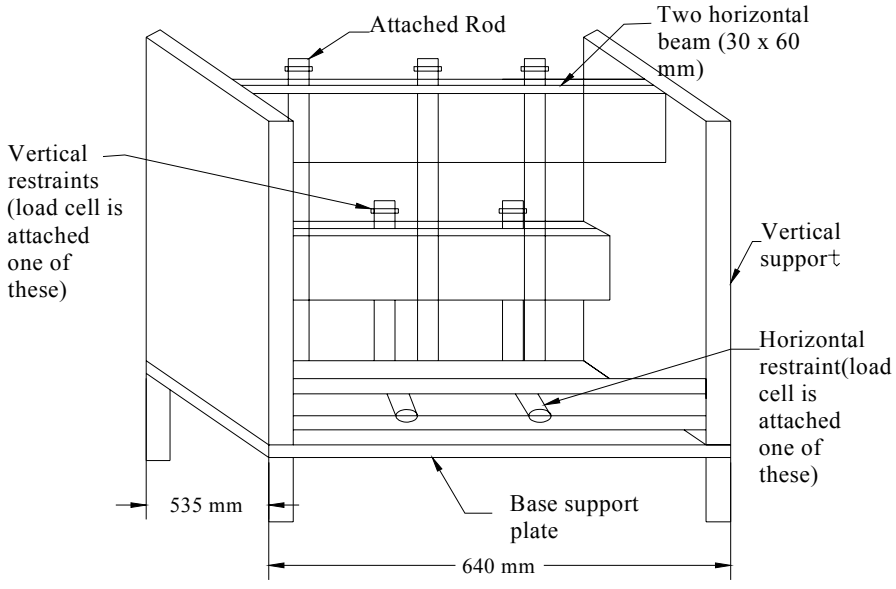

Figure 5.13 CAD drawing of the jig

The load cells are attached to studs, which tighten against slotted beams above and to the side of the plates. An important part of the design of the jig was making sure that the bed and restraint

supports were stiff enough. If either the bed or restraint supports deflected significantly, the results would become inaccurate. The layout of the jig consists of two end plates with the bed and restraint support between them. Because the two plates being welded were identical, the restraining forces for both are the same. For this reason, the jig is designed to only restrain one plate with load cells. The plate restrained with load cells will be referred to as the measured plate. An important part of the design of the restraint supports was to make them versatile enough to restraint the plates with any number of restraints in any position. This was achieved by the slots in the beams, which allow the studs to slide to any position.

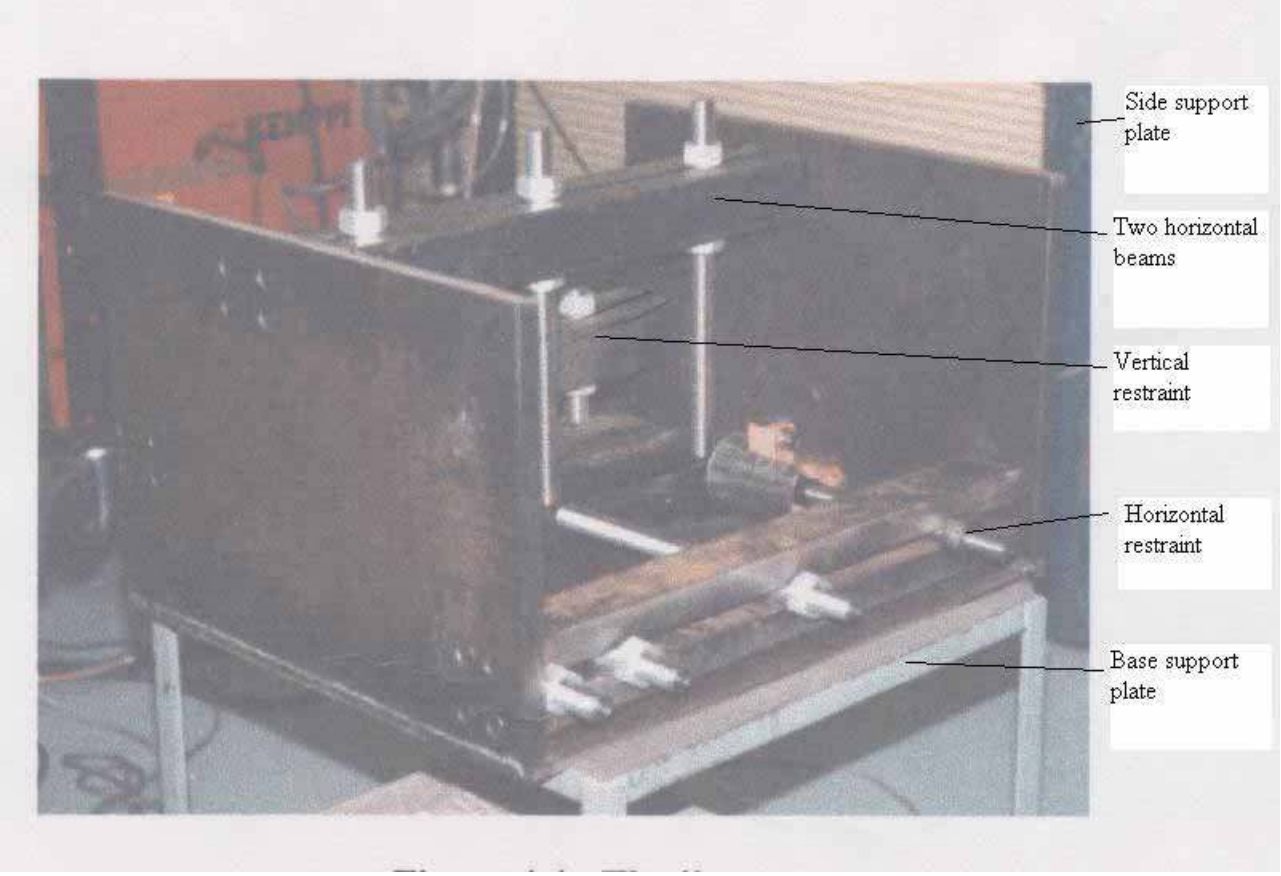

Figure 5.14 Photo of the jig

5.8.3.3 Instrumentation and Testing

The data was collected with two load cells connected to a load cell amplifier with the output to a data logger. A 20 kN (4496 lb_f) load cell was used in low force position on the jig. The 100 kN (2248 lb_f) load cells (Tokyo Sokki Kenkyujo CLP 10B) were calibrated by compressing them in an MTS testing machine and charting the output voltage from the amplifier against the measured load on the MTS. The restraints can be tightened against the plate with a compressive force, called preloading. The effects of preloading had to be determined to find the best experimental procedure and ensure that the experiments could be reliably repeated. A large pre-load greatly decreased the restraining force before and after the peak force value. This can be explained by the restrained expansion and free contraction model described by Cornu [1988]. When the yield stress of the base metal is exceeded in the high temperature region near the weld, the restraining force is relieved by plastic deformation. In the case of a large pre-load, the pre-load is also relieved by plastic deformation. This result in greater shrinkage and the restraining force drops. For the force values taken from the side positions to be true, there must be no sideway force resisted by the top restraints. Increasing the force on the top of the plates did not reduce the force measured by a load cell on the side of the plate.

5.8.3.4 Test Procedure

The aim of the experiments is to gain an understanding of what factors influence distortion by undertaking two main sets of experiments, varying one parameter at a time. As this research aim was to look at the overall trends for each parameter rather than calculation of the effects of a small change; only three samples were taken, from the upper, central and lower bounds of what may be used in commercial practice. Two restraints on each of the top and edge of each plate were used. This helps to understand the results better way than those of three restraints tried earlier. This gives

a total of four positions which data will be collected from: Top start, Top End, Side Start and Side End (figure 5.15).

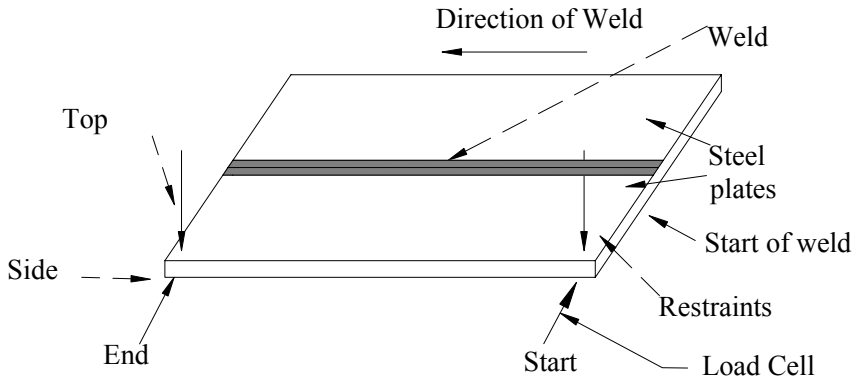

Figure 5.15 Position of load cell for side of plate, end of weld

To conduct an experiment with the jig, the following steps are taken:

1. Two steel plates are placed on the bed and pushed against the end stops.
2. The load cells and other supports are placed in their positions and tightened to about 1 kN.
3. The load cells are connected to the amplifier and the amplifier is set to the appropriate gain setting.
4. The amplifier is connected to the data logger and the appropriate data is entered into the data logger.
5. The robot is programmed according to the desired welding conditions.
6. Data from the data logger can be loaded directly into MS Excel and analysed.

5.8.3.5 Welding Conditions

The first set of experiments was carried out keeping the welding speed constant and changing the heat input. The range in heat inputs covered spans from the minimum to maximum, which could be used on the 10 x 100 mm (0.4 in x 4 in) mild steel. The next sets of experiments examine the effect of applying the same heat input at various speeds. The values for various parameters for

different welding conditions (constant speed, varied speed) are given in Table 5.1, Table 5.2 and Table 5.3.

Table 5.1 Welding conditions for constant speed but varied heat input

Current (Amps)	Voltage (V)	Heat Input (kJ/mm)	Speed (mm/min)
124	20	0.5 (12 Btu/in)	300 (12 in/min)
232	23	1.0 (24 Btu/in)	300 (12 in/min)
278	27	1.5 (36 Btu/in)	300 (12 in/min)

Table 5.2 Welding conditions for constant heat input, varied speed

Current (Amps)	Voltage (V)	Heat Input (kJ/mm)	Speed (mm/min)
228	23	1.5 (36 Btu/in)	200 9 (8 in/min)
278	27	1.5 (36 Btu/in)	300 (12 in/min)
334	31	1.5 (36 Btu/in)	400 (16 in/min)

Table 5.3 Welding parameters

Base plate	Mild steel plate (ASTM A-36), yield strength 280 MPa
Filler Wire	Auto craft LW1 (yield strength 390 MPa) type filler wire of 1.2 mm (0.05 in) diameter
Gas	Argon with 1.5% Oxygen
Air Temperature	18-25 degrees Celsius

5.8.3.6 Edge Preparation

A square butt was selected for the above experiments because it allows greater flexibility in welding conditions. The jig was designed to be used for single pass and the influence of the weld

bead shape on the restraining forces is more visible in a square butt because depth of penetration and width of weld bead depend directly on the welding conditions.

5.8.4 Experimental Results and Discussions

5.8.4.1 Side, End of Weld

The variation of restraining force over weld speed is shown in figure 5.16. It is seen that as the speed increases, the peak occurs earlier and at a higher force. The reason for the peak occurring earlier is because as the speed increases, the weld finishes earlier. The peaks occur at the finish of the weld in all cases and this is shown by the black line, which is drawn where the welding current drops to 0.0 for each weld.

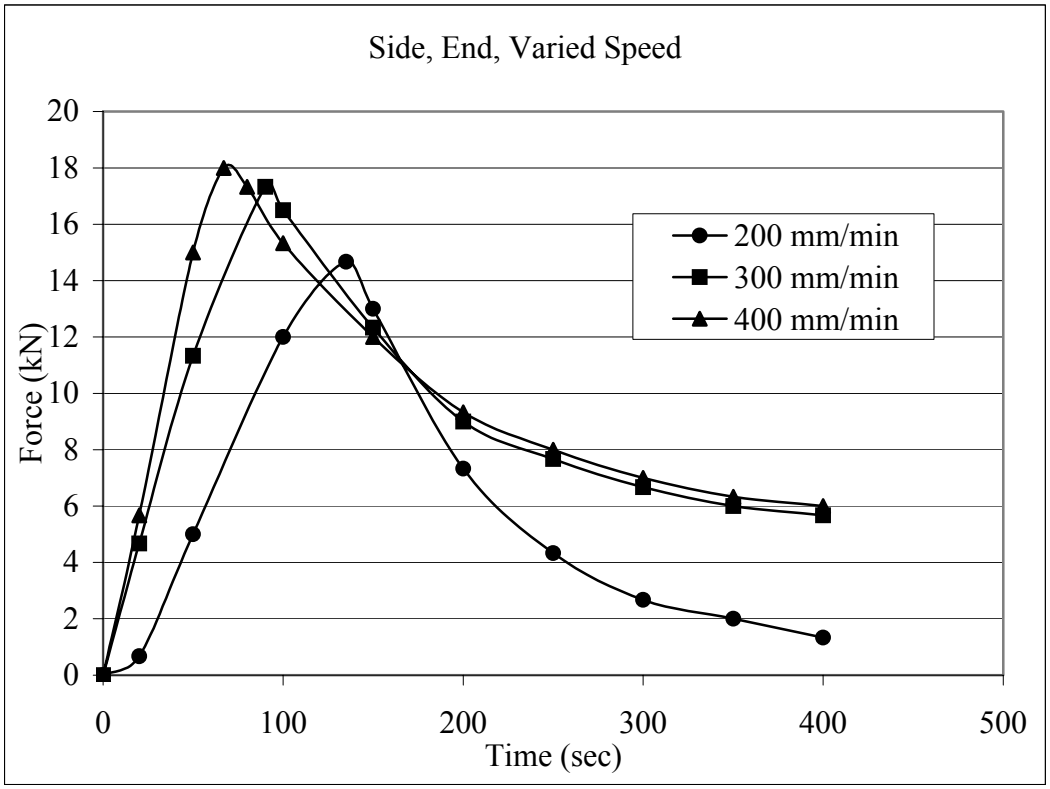

Figure 5.16 Variation of restraining forces with weld speed

Further the linear rise in force starts at the same position for all of the welding speeds. The delayed start is because the weld metal is initially liquid and after solidification, it takes time to cool. An easier way to understand graph uses a distance scale rather than a time scale (figure 5.17).

This has all of the welds starting and ending at the same position on the x-axis and only shows the force while welding is happening. This plot shows that the restraining force is independent of speed for most of the graphs and only gains a dependence on speed in the region close to the restraint. As the weld gets closer to the restraint, the graphs loose linearity with the slowest weld losing linearity first and the fastest last. This indicates that a certain welding speed, the graph will be linear and any further increase in speed will have not effect on the restraining force at this position.

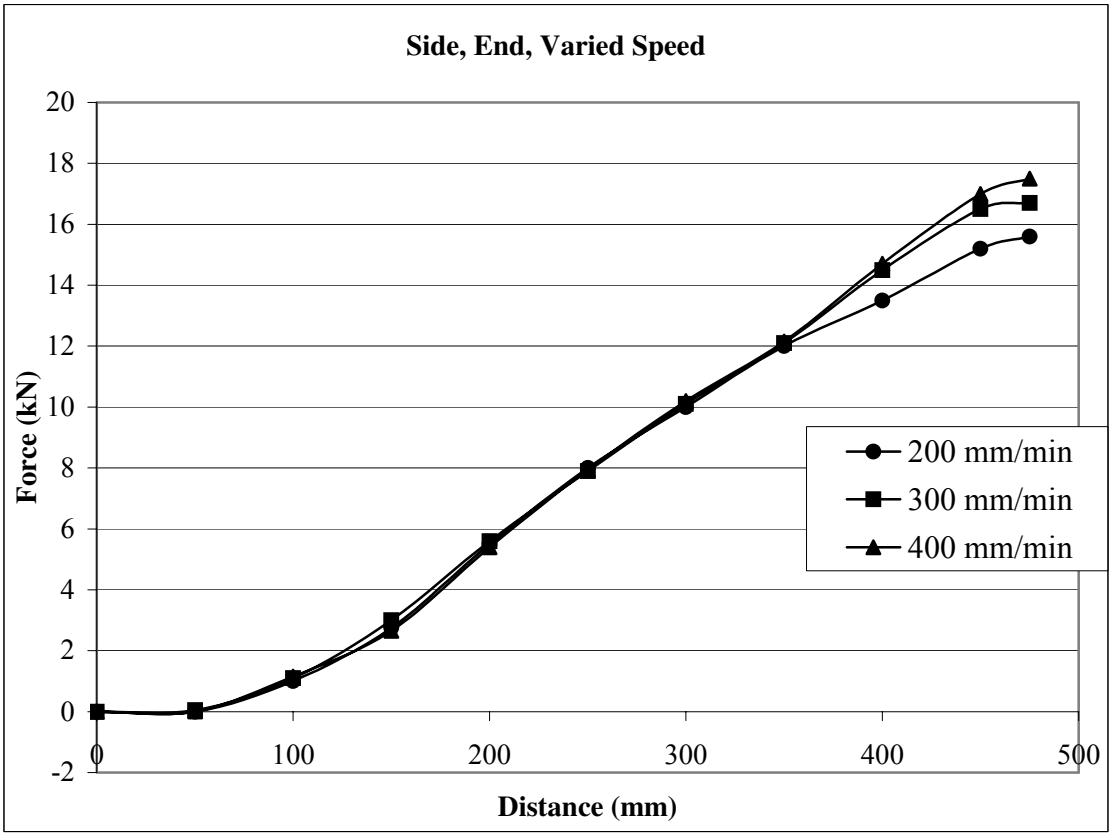

Figure 5.17 Variation of restraining forces with distance (1 kN = 224.81 lb_f)

The linear rise in restraining force with distance indicates that the maximum force reached is a linear function of the length of the welded plates, so as a means of comparing two alternative welding processes; the slope of the linear part of the graph would be more useful.

Figure 5.18 shows the restraining forces for varied heat input but constant speed. As a mean of comparing figure 5.18 with figure 5.16, the graph for 1.5 kJ/mm (36.2 Btu/in) and 300 mm/min (12 in/min) is the same on both graphs. Figure 5.18 has four distinct sections which will be considered separately. These are: a flat heating time, a linear rise, a non-linear rise and force relaxation. To make the first three sections easier, figure 5.19 is plotted for the time from the start to the end of the weld and figure 5.20 is plotted for force relaxation. On this graph the flat heating time is clearly visible. The heating time is the same for all three heat inputs indicating that it is independent of heat input. The linear rise starts at the end of the heating zone and extends to the non-linear zone near the end restraint. This is the most important part of the graph because the slope of the linear section gives a direct means of comparison of the effect of different heat inputs. For a clear comparison of the effects of heat input on restraining force, figure 5.21 shows the slope of the force-time curve plotted against heat input.

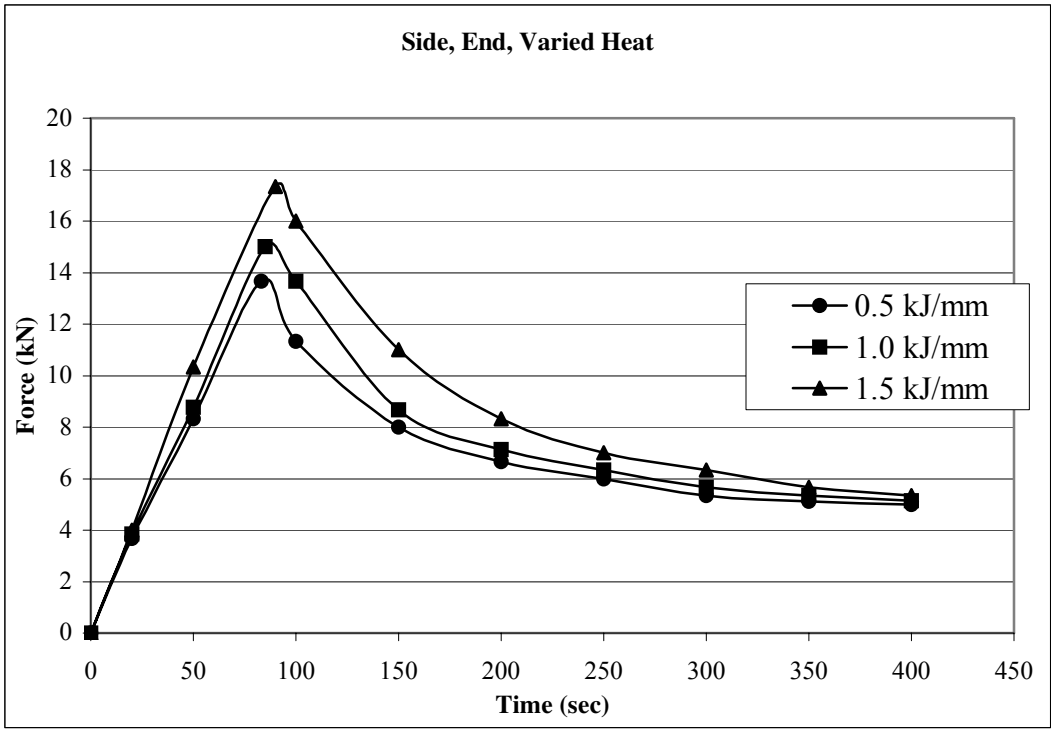

Figure 5.18 Variation of restraining forces with heat input (1kJ = 0.95 Btu)

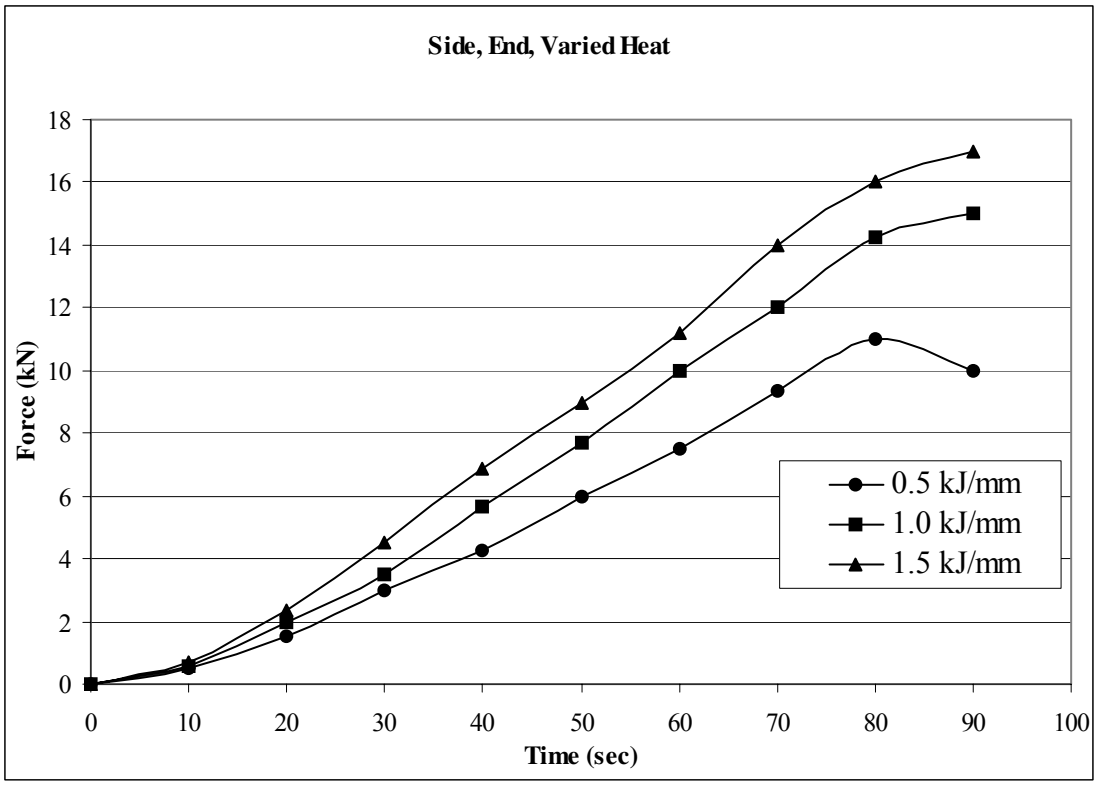

Figure 5.19 Detail of force rise while welding (1kJ = 0.95 Btu)

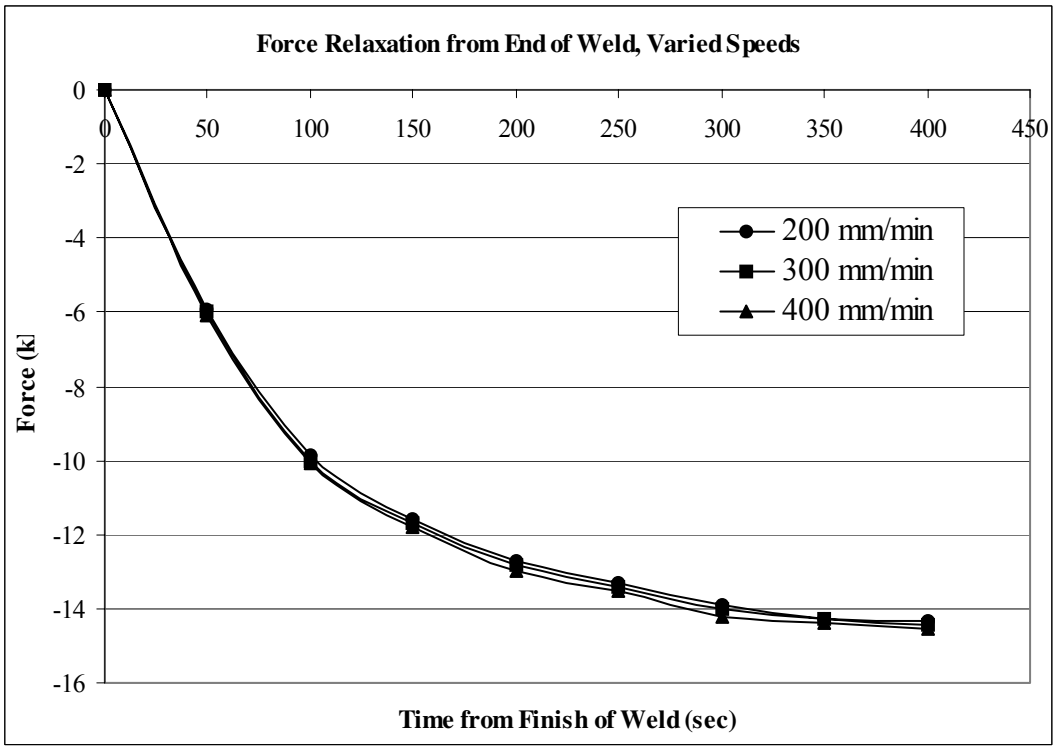

Figure 5.20 Force relaxation versus time

This graph shows that the relationship is certainly non-linear but only has three data points so it cannot be conclusive at this stage. This graph can be used as a rough guide as to what the slope of the linear part of the force-time graph will be. It should be mentioned once again that the slope of the force-time graph is independent on the shape and size of the two plates being welded and therefore the numbers presented in this study can not be applied directly to other sized plates and other methods of welding and other then Gas Metal Arc Welding without further investigating.

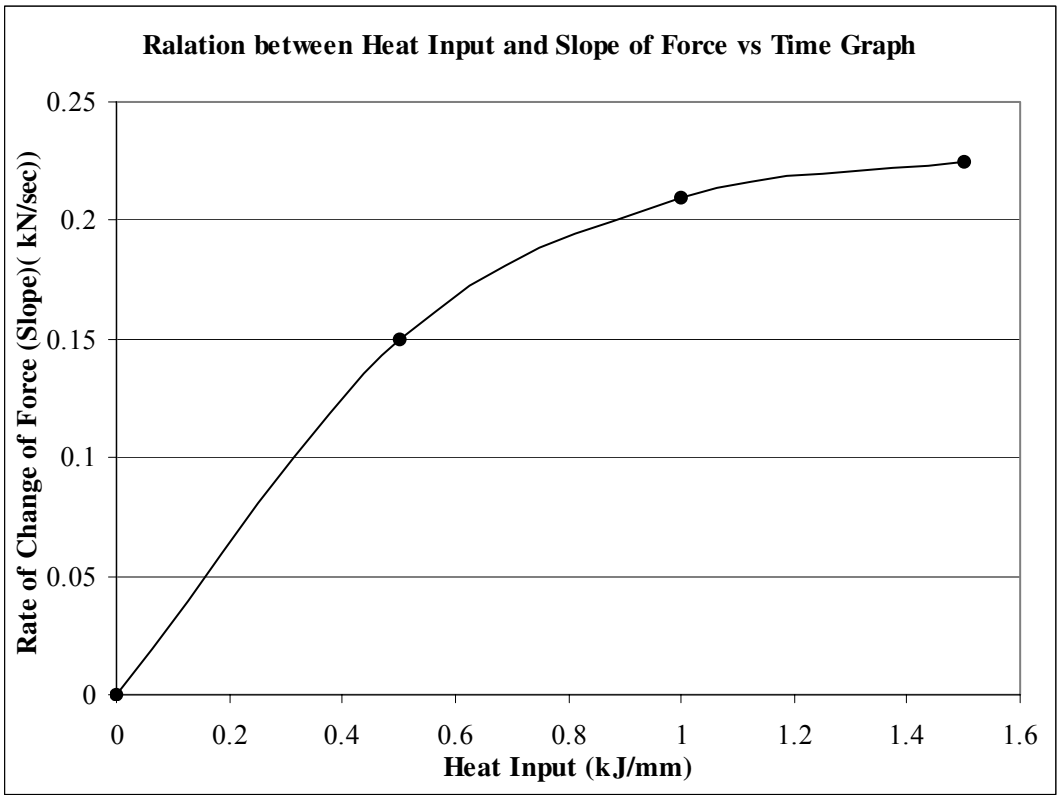

Figure 5.21 Heat input and slope of force vs. time graph

5.8.4.2 Side, Start of Weld

The load cell position at the start of the weld (figure 5.22) shows the restraining force required to restrain against thermal expansion only. Because the weld starts at this restraint, there is no opening force against the restraint. The first noticeable feature of this graph is that the restraining force rises from the instant the arc is struck, unlike the restraining force at the end of the plate.

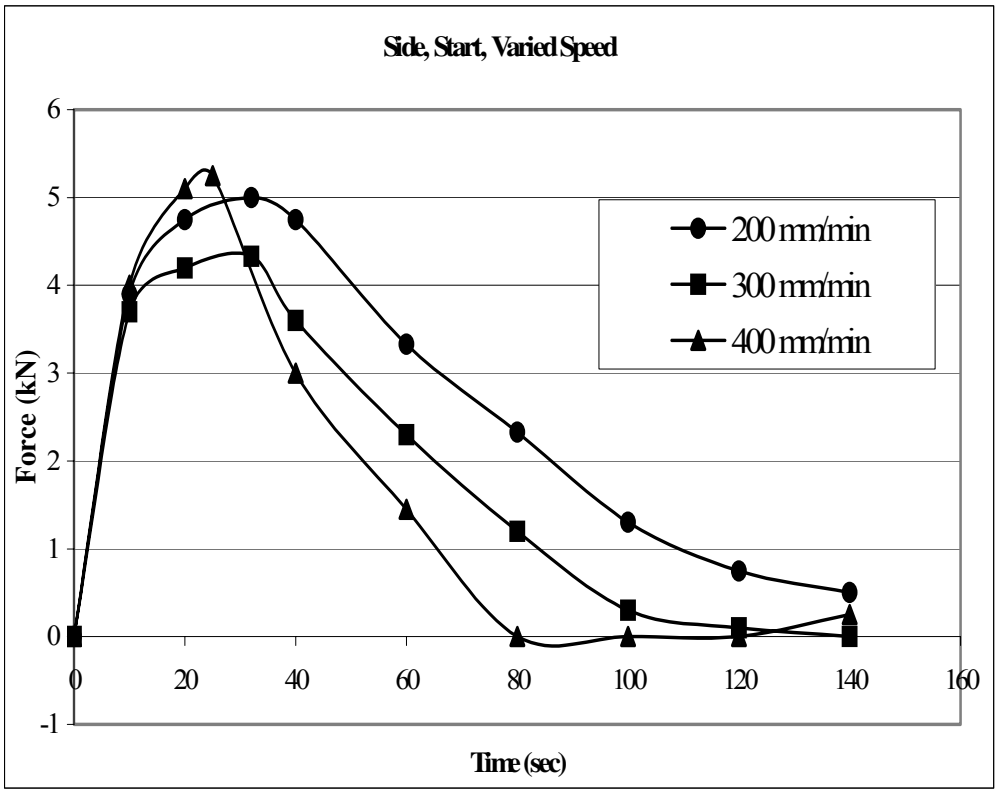

Figure 5.22 Variation of restraining forces with speed (1 kN = 224.81 lb_f)

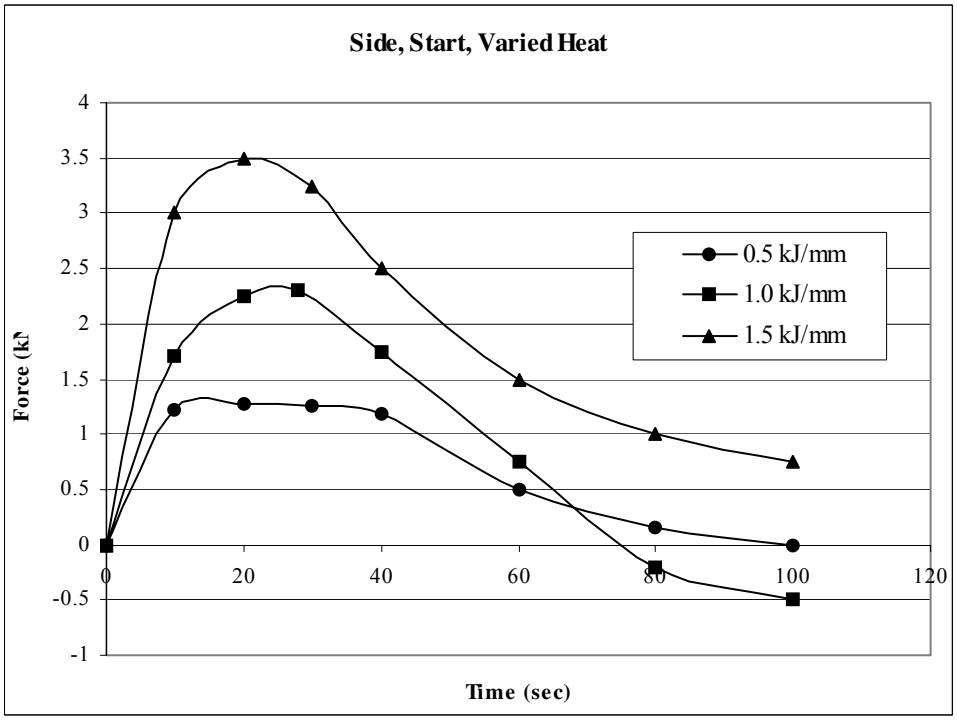

Figure 5.23 Variation of restraining force with heat input (1 kN = 224.81 lb_f)

While the graphs are rising, they have approximately the same shape and peak at the same place. This is because the heat input is the same and because the weld is deposited instantly, regardless of speed, the rate of increase of force in the first few second is independent of time. The variation of restraining force over varied heat is shown in figure 5.23. When the heat input is increased, the restraining force at the start of the weld is increased. Because of the poor resolution of the data logger for this set of data, an earlier set is shown on the graph, which was recorded with the x-y plotter. The weld for this graph was about 50 mm (2 in) shorter than the welds discussed above but this should have no effect on the restraining force near the start of the weld. The graph shows clearly the rise in restraining force with increased heat. For all heat inputs, the peak occurs in about the same place and by the end of the weld; the restraining force has decreased to about 0.0 kN.

5.8.4.3 Top, Start of Weld

There was little variation of the maximum force measured at the start and end of the weld for the same welding conditions and therefore the discussion will concentrate at the start of the weld. This differs from the side of the plate where the restraining force is about three times larger at the end than the start. The variation of restraining force for top of plate, start of weld at varied speed is shown in figure 5.24. There are two effects on the restraining force from welding speed. Firstly, the force increases at a greater rate with increased welding speed, and secondly, the maximum restraining force increases with increasing welding speed. The steeper slope of the graph with increased force is because the faster weld finishes earlier. The first few seconds of the weld show instability because the restraining force varies between positive and negative with no clear pattern. This is especially evident on the graph for 200 mm/min (8 in /min). An interesting result is that the force for the 400 mm/min (16 in /min) graph starts to decrease before the weld is finished (63 sec)

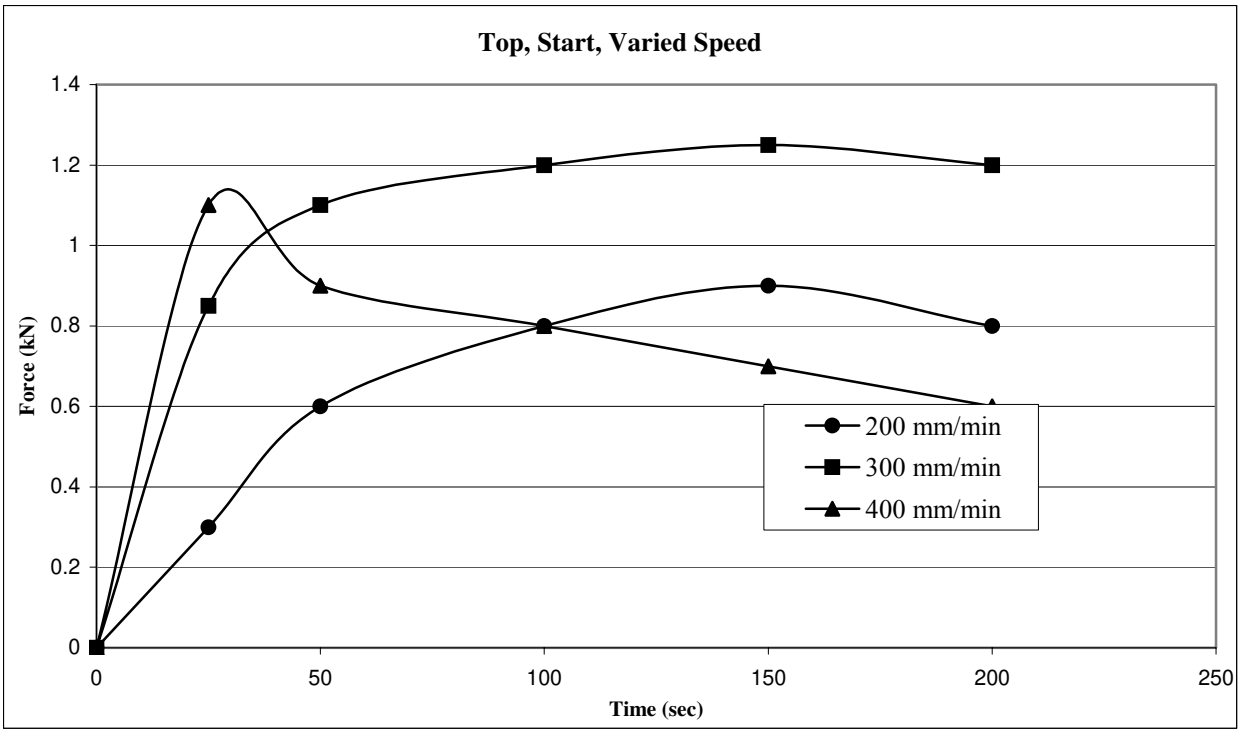

Figure 5.24 Variation of restraining force with weld speed (1 kN = 224.81 lb_f)

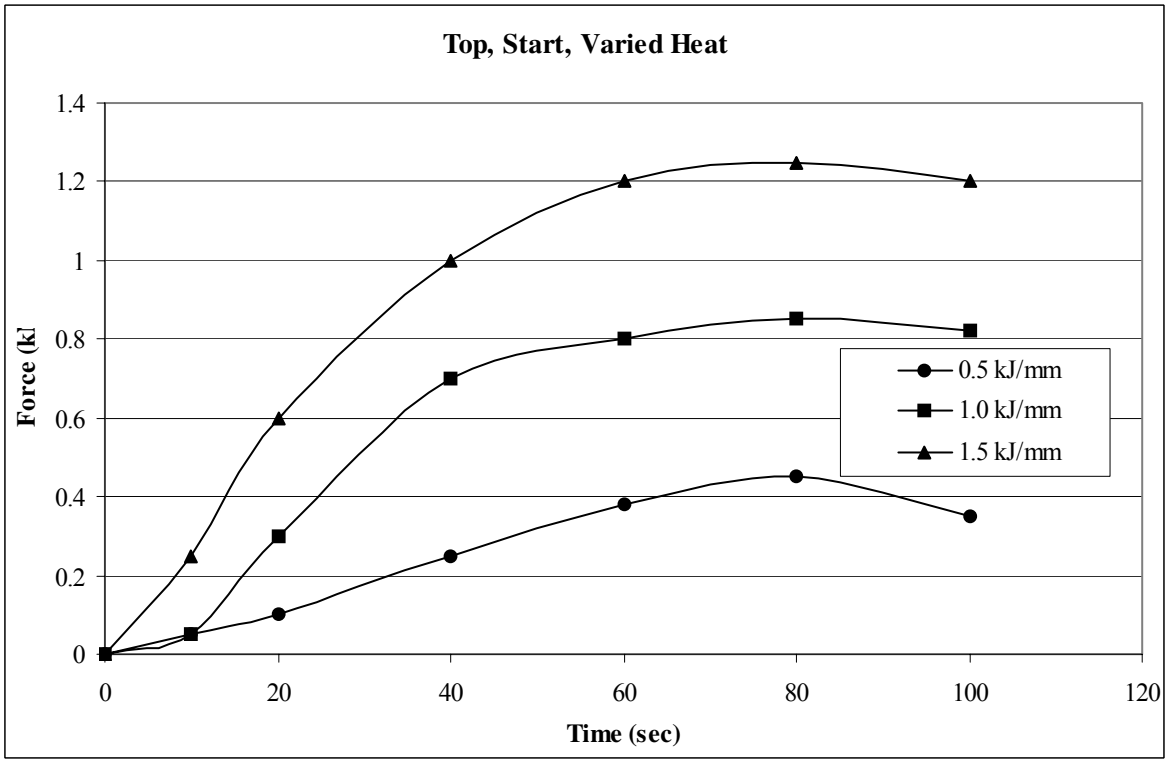

Figure 5.25 Variation of restraining forces with heat input

while the 300 (12 in/ min) and 200 mm/min (8 in /min) welds increase slowly until the weld finishes (90 and 135 sec respectively).

The variation of restraining force for the top of plate, start of weld at varied heat is shown in figure 5.25. The graph shows that increasing the heat input increases the restraining force. Both the slope of the graph and the maximum force reached increase as heat input increases. The relationship between heat input and restraining force is approximately linear which means doubling the heat will double the peak restraining force. Because the fusion area increases with increase of heat input and the restraining force increases. The instability of the first few seconds of the weld increases with the decreasing welding speed.

5.8.5 Finite Element Model (FEM) and Analysis

A 3-D FEM model (figure 5.26) of a square butt-welded joint in a steel specimen of dimensions (500x100x10 mm) has been created using authors' written Ansys code. For symmetry only half-part of the specimen has been considered for modeling and analysis. It is assumed that only the convection occurs on the surface of the specimen and conduction occurs within the specimen. Convection describes the effect of temperature gradients between the post-weld plate surfaces and the room temperature of the surrounding air (assumed 15^{o}C from the literature [Runnemalm, 1999]). In this case it has been assumed that the plate surface-temperature changes due to the combined effects of (i) conduction within the specimen and (ii) convection from the specimen surface-temperature to the surrounding-air temperature and (iii) radiation. The temperature within the specimen changes from weld pool to the location away from the weld pool due to conduction.

The temperature-dependent material properties (i.e. modulus of elasticity, thermal conductivity, coefficient of specific heat, modulus of thermal expansion, Poisson's ratio, yield stress, tangent modulus etc.) of base and weld materials were collected from the work of Runnemalm [1999] for various temperature conditions and have been applied to the model. A

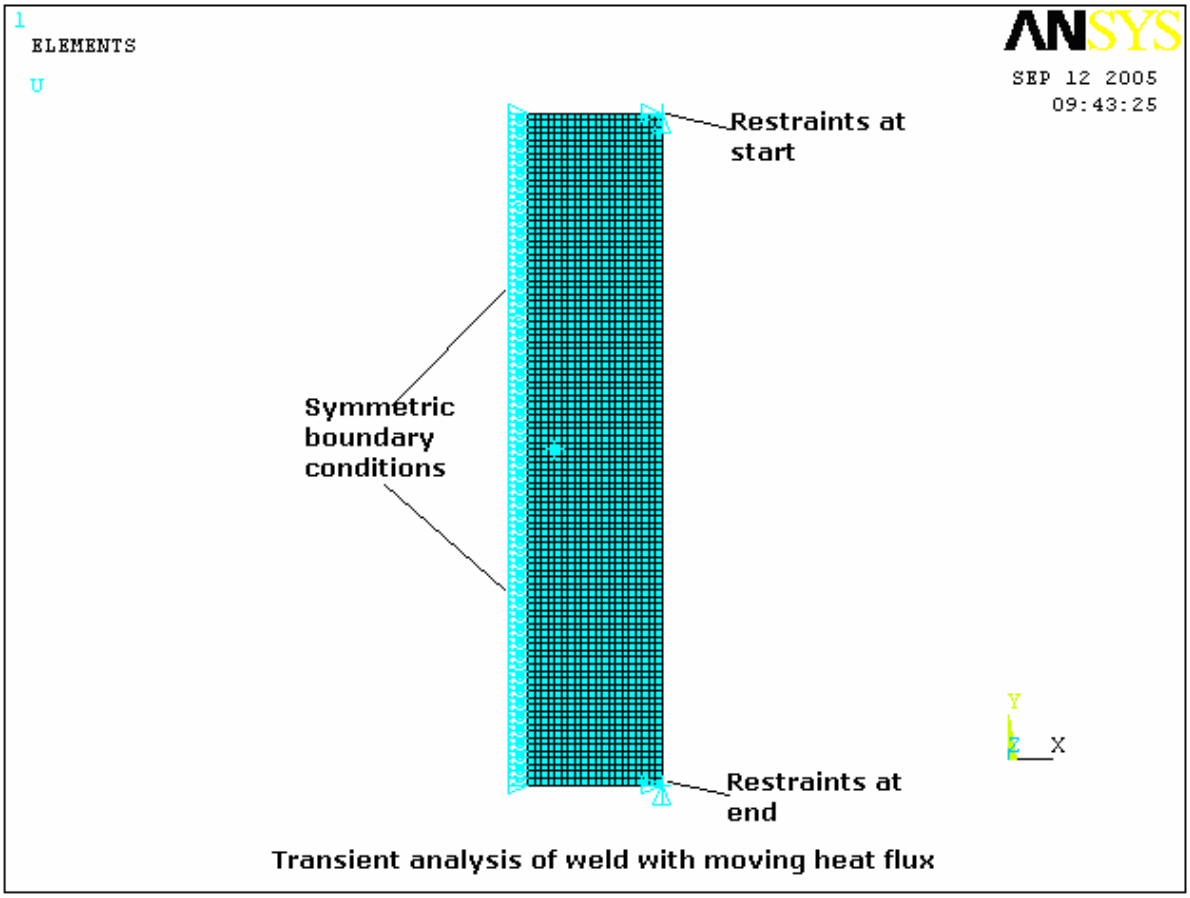

Figure 5.26 A 3-D FEM weld model (symmetric part only) with mesh and boundary condition (500x100x10 mm)

moving heat flux method is used in the transient heat transfer analysis (figure 5.27). The magnitude of the heat flux is determined from the heat input, welding speed and thickness of the plate. For a set of welding parameters (i.e. voltage 23 V, current 232 Amps, welding speed 5 mm/sec, arc efficiency 93.7%, and plate thickness of 10 mm) the magnitude of heat flux is calculated as 100E6 Joule/m^2 (voltage x current x arc efficiency/(weld speed x thickness).

This heat flux is applied as a surface elemental-load from one end of the plate to the other, using a "do-loop" command. After finishing one increment of the "do-loop", the previous heat flux is deleted and another heat flux (the same amount) is applied to the next element. The temperature constraints from the elements of the base material and weld materials are removed, which will

allow the base metal to contract or expand freely. In the FE model "Solid-5" elements are used which have the capability of treating both conduction and convection conditions. The convection heat transfer coefficient for all external surfaces was assumed to be 100 $W/m^2/^oC$ and the temperature of the surrounding air was 15^oC (59^oF) and these values are assumed from the work of Runnemalm [1999]. In transient analysis the convective heat transfer is applied as a surface-load using authors' written Ansys code. The Ansys command "SF" is used for applying surface load and "CONV" is used to represent type of surface load. The convective heat transfer coefficient and the ambient temperature are also mentioned in the same command line. The restraining force is found from fixing the edge nodes at the start and end positions and the reaction forces of the fixed nodes give the restraining forces.

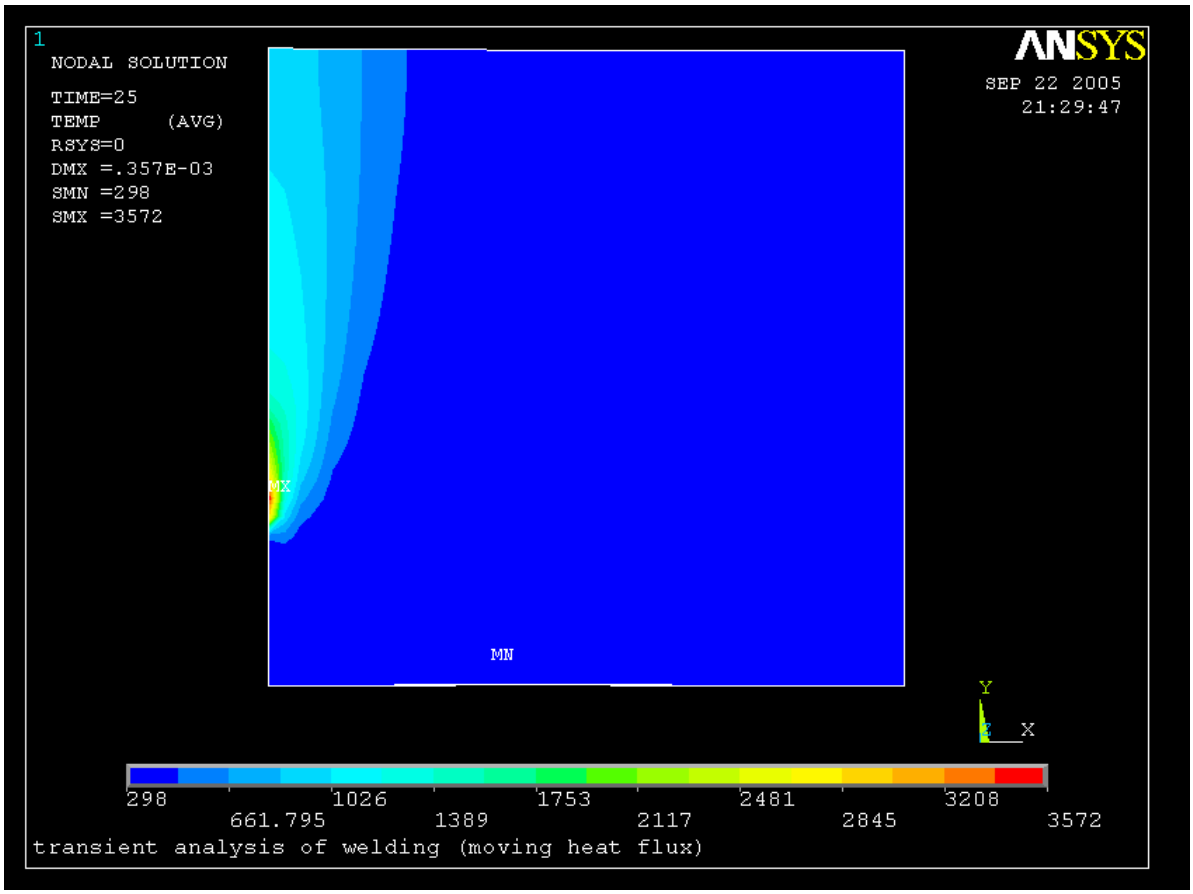

Figure 5.27 Finite element model showing moving heat flux

5.8.6 FEM Results and Discussions

The restraining force for side and start position found in ANSYS analysis is shown in figure 5.28. The restraining forces increase with increase of time. Due to thermal expansion the volume of welds metal increases. Hence the restraining forces due to the expansion of weld metal increases with time; but when welding has been completed, the metal contracted due to the conduction and convection and consequently, the restraining force decreases.

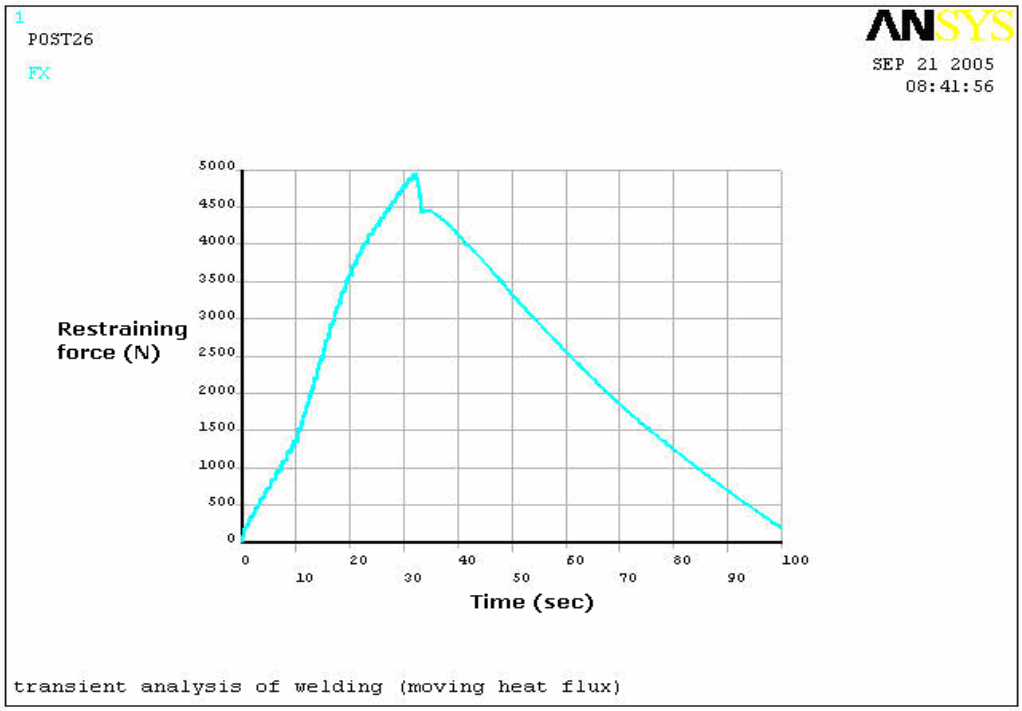

Figure 5.28 Restraining force found from ANSYS post processing for side, start position with weld speed 300mm/min and heat put 1kJ/mm.

For validation the prediction has been compared with the experimental results shown in figure 5.29 for the side and at the start of the plate condition. The location and the magnitude of the maximum force for both experimentally obtained values and numerical results occur very close to each other and only slight variation occurs in the magnitudes. This slight variation (7%) in the magnitude of the peak force may be due to the change in actual material properties for both cases (experimental and prediction). Furthermore, the convective heat transfer coefficient that has been

used in the numerical modelling may be slightly different from the actual experimental case and accordingly, it can be concluded that the predicted results are within the acceptable ranges.

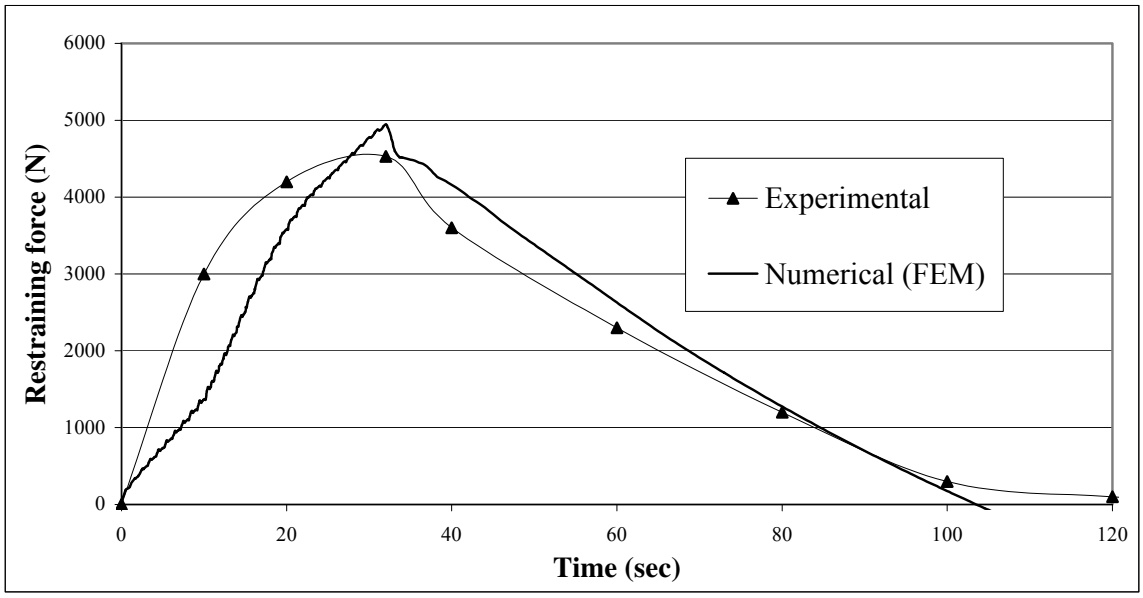

Figure 5.29 Comparison of predictions with experimental result (weld speed 400 mm/sec, heat input 1 kJ/mm).

5.8.7 Conclusions

1. For a given heat input, the restraining force will be the same as a function of distance except close to the end of the plate while it is being welded, regardless of welding speed.
2. For a given heat input, the force relaxation after welding will have the same shape regardless of welding speed and maximum restraining forced reached.
3. Decreasing welding speed makes the force versus distance graph depart from linearity earlier.
4. Increasing the heat input increases the slope of the force versus time graph and the maximum restraining force.
5. The slope of the force versus time graph gives a better indication of the effects of the welding conditions than maximum restraining force.
6. The restraining force for the top of the plate increases with increased welding speed.
7. The restraining force for the top of the plate increases with increased heat input.

CHAPTER 6 FATIGUE IN WELD-REPAIRED JOINTS

6.1 Repair Techniques of Welded Joints

The strength of long life weld structures normally deteriorates with time due to fatigue, corrosion and corrosion fatigue or stress corrosion cracking. A survey conducted by the Underwater Engineering Group [UEG, 1982] reported that in the case of welded offshore platform structures in the North Sea of UK, 60% damage were due to fatigue cracks caused by the harsh climate and cyclic wave loads. Similar environment assisted fatigue problems may occur in other welded structures such as bridges, aircrafts, railways, automobiles, boats aircraft, steam turbine casing, high pressure generator rotor, nuclear power plant, etc. When large defects or fatigue cracks are discovered in welded components, the best method is to replace them with new components. Unfortunately, in most cases it is impossible to do so because of the time involved and or economic reasons. Crack-repairs thus have become principal techniques for the extension of fatigue life or rehabilitation of cracked welded structures.

A weld repair of high pressure generator rotor for Commonwealth Edison Co. Joliet station #29 was carried out by Holby and Galanes [1995]. A 550 MW, high pressure (HP) generator field developed a circumferential crack in the transition formed between the main rotor body (1016 mm diameter) and shaft extension (584.2 mm diameter) at the collector ring end after 20 years of service. Metallurgical investigation of a sample from the HP rotor revealed that the crack initiated from low cycle fatigue in the thin ligament section formed between the edge of the pole slot and the edge of a 16 mm diameter bolt hole. It was determined that the crack initiated at the OD surface of the generator shaft and propagated to a radial depth of 78.74 mm. The repair consisted of machining the crack to removal using a narrow groove (approximate groove angle of 2 degrees per side) extending 360 degrees around the circumference of the rotor. The narrow groove was weld repaired using the automatic gas tungsten arc welding process. The repaired shaft was

subjected to a post weld hydrogen bake at 260 ^{o}C and final post weld heat treatment at 663 ^{o}C for 4 hours. By performing this repair, Common-Wealth-Edison Co. saved approximately $ 1.5 million in generator field replacement costs and avoided 12 to 18 months of lost generation while waiting for the replacement HP generator field. Thus weld repaired is economically beneficial over replacement of certain structures.

Fatigue crack repair techniques can be categorized [Fisher and Dexter, 1994] as (1) weld-toe surface crack repair; (2) repair of small through-thickness cracks; and (3) altering the stiffness of the connection to reduce the cause of cracking. These repair techniques were developed to repair and extend the fatigue lives of cracked welded steel bridge. Many of these applications have successfully withstood considerable subsequent traffic loadings. These repair techniques are applicable to a wide variety of dynamically-loaded welded structures such as ships, cranes, and large vehicles. However, any method used to repair fatigue damaged details is case specific and is generally dependent on the size and location of the crack at the time of repair [Fisher et al., 1979].

Methods that generally have been used for the repairs of welded structures include:

- weld repair
- grinding
- hole drilling
- hammer peening
- TIG (Tungsten Inert Gas) dressing
- Mechanical (bolted) clamps
- Use of cover-plates

Among these methods, the technique of weld repair combined with grinding, mechanical peening and other post-weld treatment techniques has been effectively applied in some practical engineering cases such as the welded structures of North Sea offshore platform in UK [Haagensen,

1994], fatigue damaged parts of Boeing 747 engine [Water, 1983], Aluminum structures in marine applications [Solsteel, 1993] and some mining facilities [Higgins, 1986].

Since weld repair may led to loss of mechanical properties, microstructure change in HAZ and redistribution of weld residual stresses in weldments, the fatigue crack growth behavior can vary significantly compared with as welded structures. As of now, the effects of weld repair techniques on the variation of fatigue crack growth behavior still remain unclear although these effects are critical for fatigue life evaluation of weld repaired structures. In order to evaluate the improvement in fatigue life of weld-repaired structures, fatigue crack propagation data should be determined first. Unfortunately at this time limited work has been reported in this field. Crack growth data of weld-repaired structures under fatigue loads is necessary for the application of fracture mechanics methods to evaluate the effects of weld repair and calculate residual life of weld repaired structures. Therefore, the investigation of fatigue crack growth behavior of weld-repaired structures is of significant importance.

6.2 Weld Repair on Welded Joints with Crack

For the weld repaired specimens, 1 mm wide and up 25 mm long through thickness saw cut was made at the toe of the initial weld to simulate pre-existing crack (the weld toe, the intersection between the reinforcement bead and the parent metal surface, the most vulnerable spot and the location of fatigue crack initiation in all preliminary trials). To repair the crack, a V-groove was first machined along the simulated crack up to a length of about 30 mm to ensure that the crack is fully covered (figure 6.1). For single side repair the V-groove was machined only on one side, while for the double-sided repair the V-groove was made on both sides of the specimen. The crack was repaired using manual metal arc (MIG) weld process.

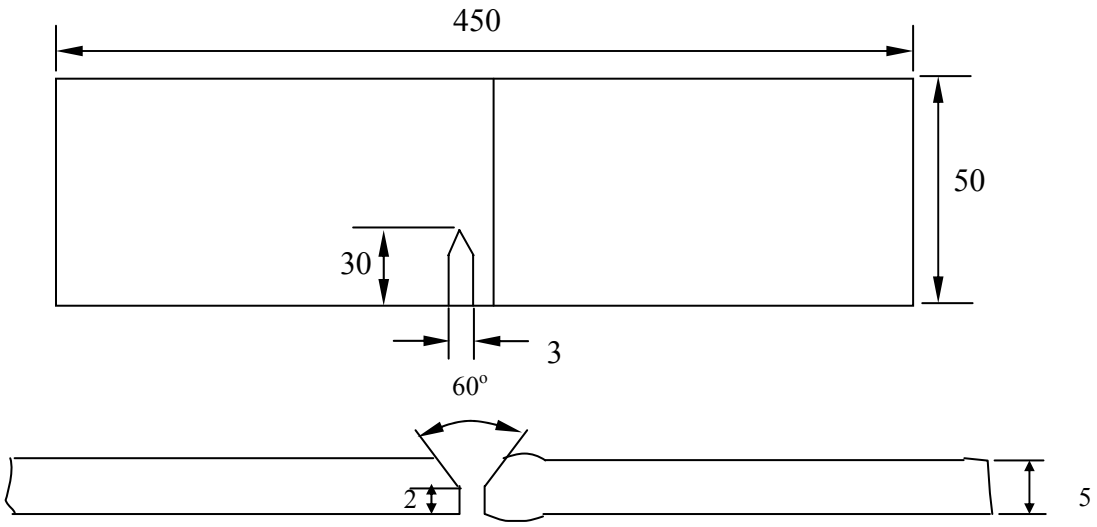

Figure 6.1 Weld design for single side weld repair (all dimensions in mm)

6.3 Fatigue Crack Failure Test Specimens

The crack growth tests on the un-welded parent material were conducted according to ASTM standard E-647 [ASTM, 1995]. It is however, to be noted that there are no established standards for fatigue crack growth tests in welded and weld-repaired material. In general ASTM E-647 recommends the use of either middle tension (MT) specimens or Single Edge Notched specimens (SENT) for fatigue crack growth tests. In this study, the Single Edge Notched specimen geometry was used for all tests and crack propagated in the direction of weld pass (-pro) in the welded and weld repaired materials. For the un-welded specimens as well as the weld-repaired specimens with reinforcement beads removed, notches were introduced on one edge at the mid-section of the test specimens. The notch dimension and the geometry of these specimens are given in figure 6.2.

On some of the as-welded specimens, the notch was introduced at the starting point of the weld pass, so that the crack propagation would be in the same direction as the weld pass, while in other specimens the notch were introduced at the end point of the weld pass, so that the crack grew in the direction opposite to that of the weld pass. The dimensions of the specimen for single side repair are shown in figures 6.3 and 6.4.

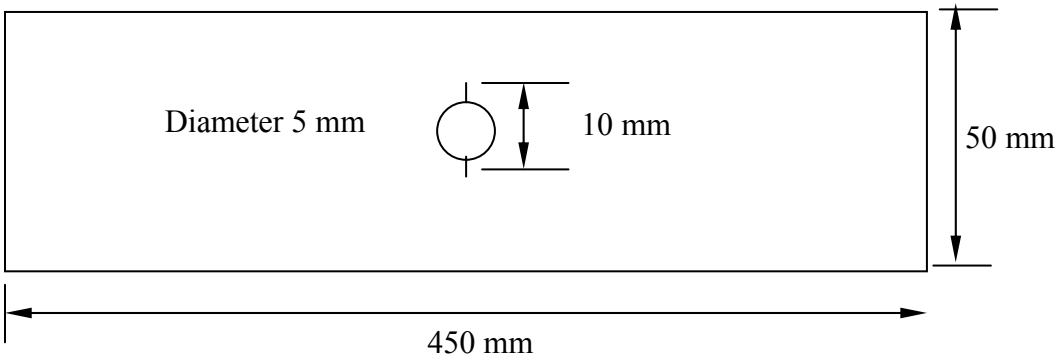

Figure 6.2 Fatigue crack test specimen geometry un-welded and weld-repaired specimens

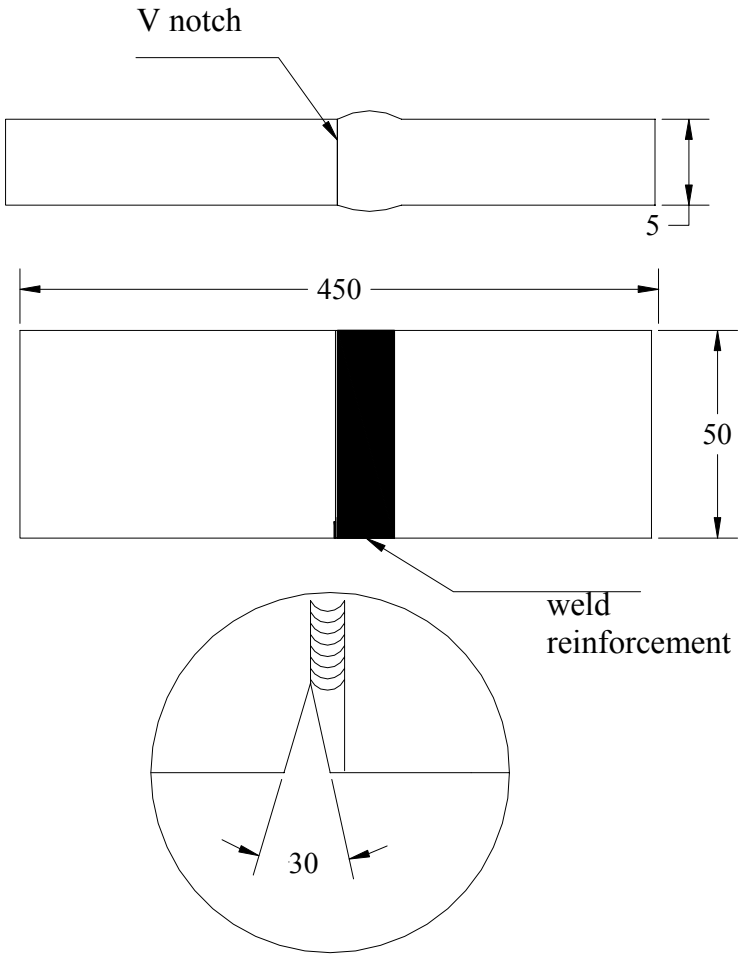

Figure 6.3 Fatigue crack test specimen for welded specimens (-pro)

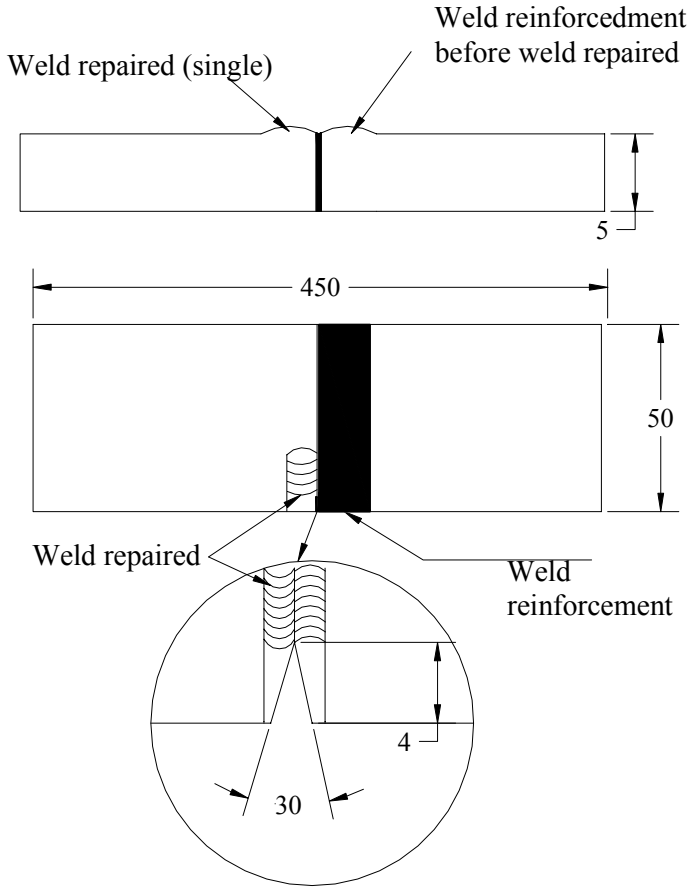

Figure 6.4 Fatigue crack test specimen for single side weld-repaired specimens

6.4 Fatigue Crack Failure Life Experiments

The fatigue tests for failure life measurements on the un-welded, welded and weld-repaired specimens were conducted on a MTS universal testing machine. The parameters used during test are shown in table 6.1. Before crack growth measurement can be performed, an initial crack (center crack) was produced on each of the un-welded, welded and weld-repaired specimens by fatigue pre-cracking using saw of thickness 1.0 mm, with the length of 10 mm (the pre-crack no less than 2.0 mm as recommended by ASTM-E647). The specimens were tested on constant amplitude fatigue at stress ratios R from 0.1 to 0.3. Only positive stress ratios are considered because it is found that negative stress has very less effect on fatigue crack growth rate [Anderson, 1995]. The test plans for the fatigue and crack growth experiments is shown in Table 6.2.

Table 6.1 Test parameters

	Un-welded	Welded	Weld-Repaired
Maximum stress (MPa)	125	50	50
Stress ratio	0.1-0.3	0.1-0.3	0.1-0.3
Frequency	0.5	0.5	0.5

Table 6.2 Test plan

Specimen	Crack growth direction	Initial crack position	No. of specimens	Type of test
Un-welded	Pro-weld pass	center	9	Fatigue failure
welded	Pro-weld pass	center	9	Fatigue failure
Weld- repaired (pro-weld pass)	Single side repair	center	9	Fatigue failure

6.5 Comparison of Fatigue Crack Failure Life among Un-welded, Welded and Weld-Repaired Specimens.

The fatigue crack failure lives over range of stress intensity factor of un-welded, welded and weld-repaired plate for different stress ratios are shown in figures 6.5-6.7. The fatigue life of welded and weld repaired specimens decreased comparing to un-welded specimens. This may be due to change of microstructure attributed to the large amount of heat input during the welding and weld repaired process. Further, much larger defects generated by the second weld process (weld-repair) employed to repair the cracks in the HAZ of the initial weld. The fatigue strength decrease about 32% due to weld-repaired comparing to welded plates at a fatigue life of 30,000 cycles and at a same stress ratio 0.1.

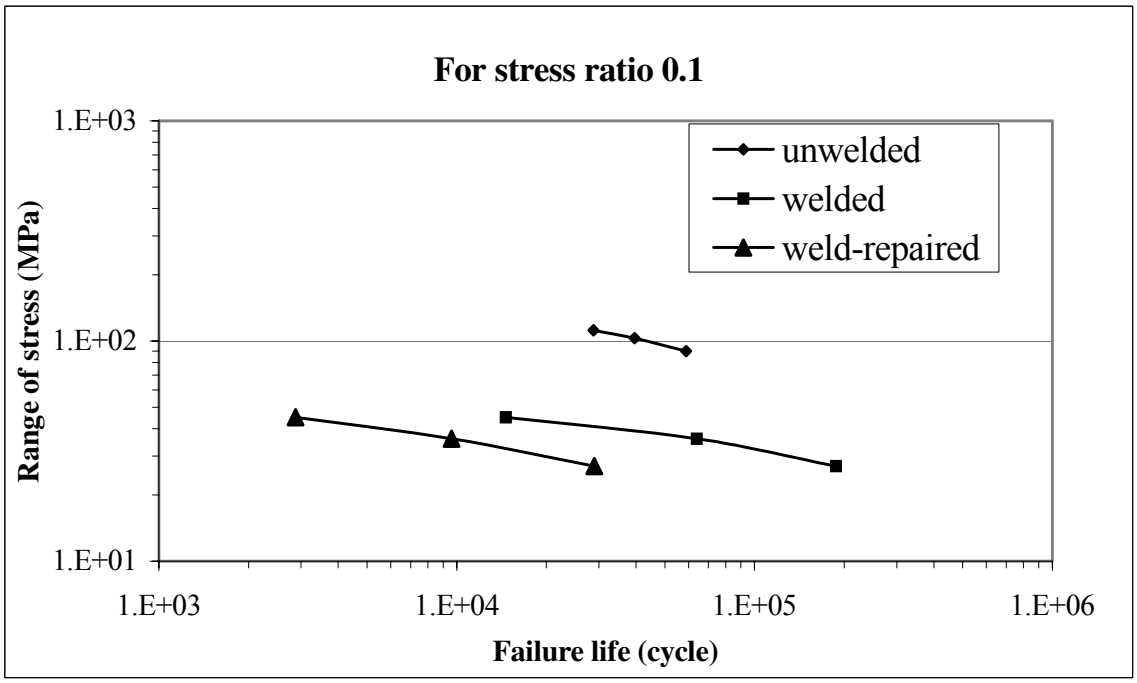

Figure 6.5 Variation of failure life with range of stress of un-welded, welded and weld-repaired joints at stress ratio 0.1

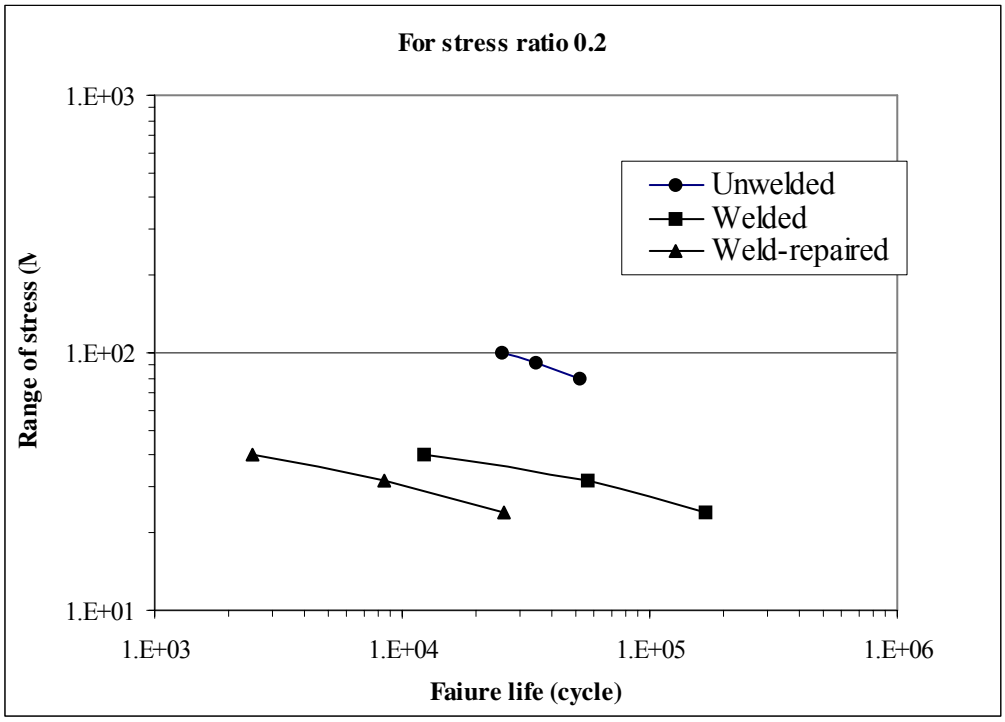

Figure 6.6 Variation of failure life with range of stress of un-welded, welded and weld-repaired joints at stress ratio 0.2.

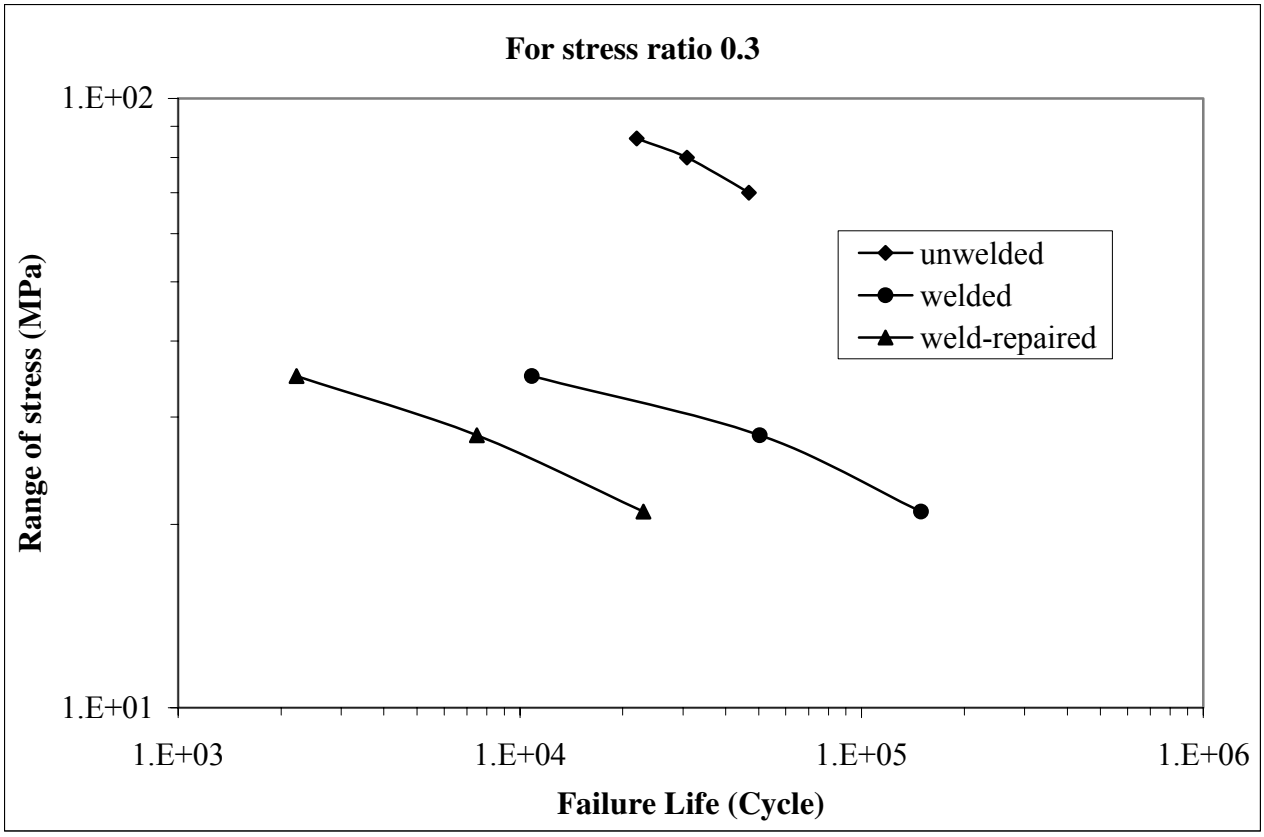

Figure 6.7 Variation of failure life with range of stress of un-welded, welded and weld-repaired joints at stress ratio 0.3

The variation of failure life with range of stress for different stress ratios of un-welded, welded and weld-repaired plates are shown in figures 6.8-6.10. The failure life decreases with increase of stress ratio for a particular range of stress. This is due to the fact that as the stress ratio increases the threshold stress intensity factor decreases and fatigue crack growth rate increases. Further, in this study the stress ratios are increased keeping maximum stress constant and increasing minimum stress. Therefore, as the stress ratio increases the crack remain open for more length in time and there is less crack closure effect.

The fatigue strength decreases about 12% at stress ratio 0.2 and about 26% at stress ratio 0.3 comparing to that at stress ratio 0.1 for unwelded plate. The fatigue strength decreases about 13% at stress ratio 0.2 and about 27% at stress ratio 0.3 comparing to that at stress ratio 0.1 for welded plate.

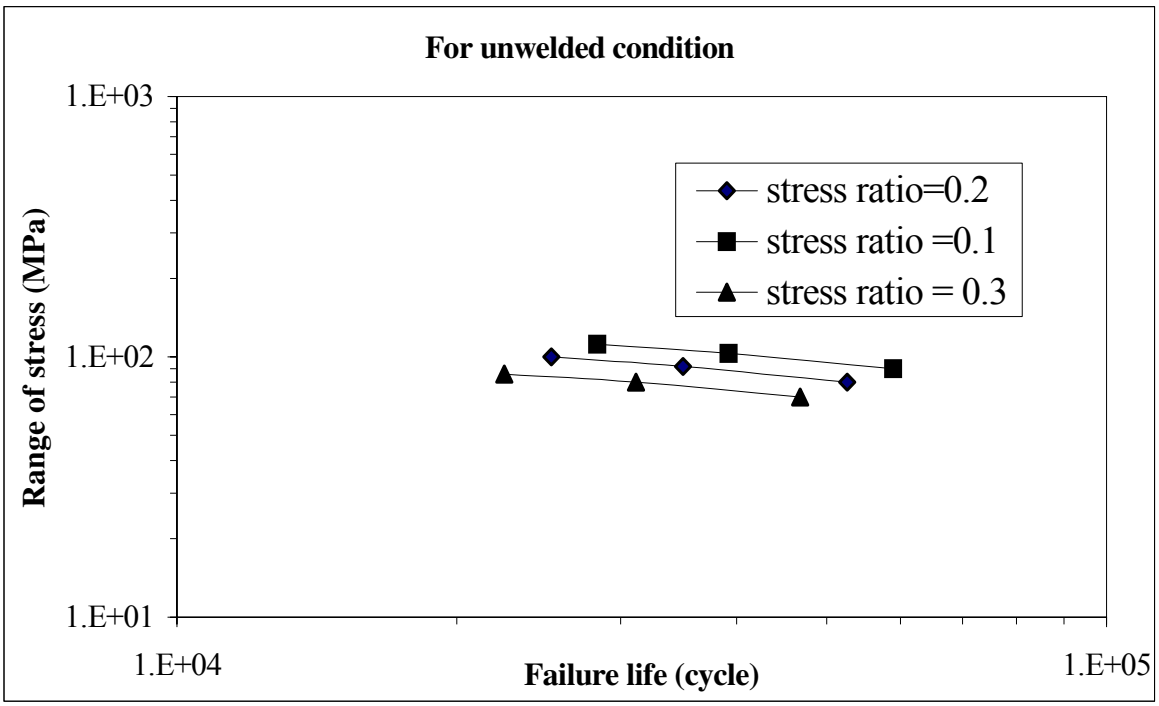

Figure 6.8 Failure life with range of stress of un-welded joints at various stress ratios

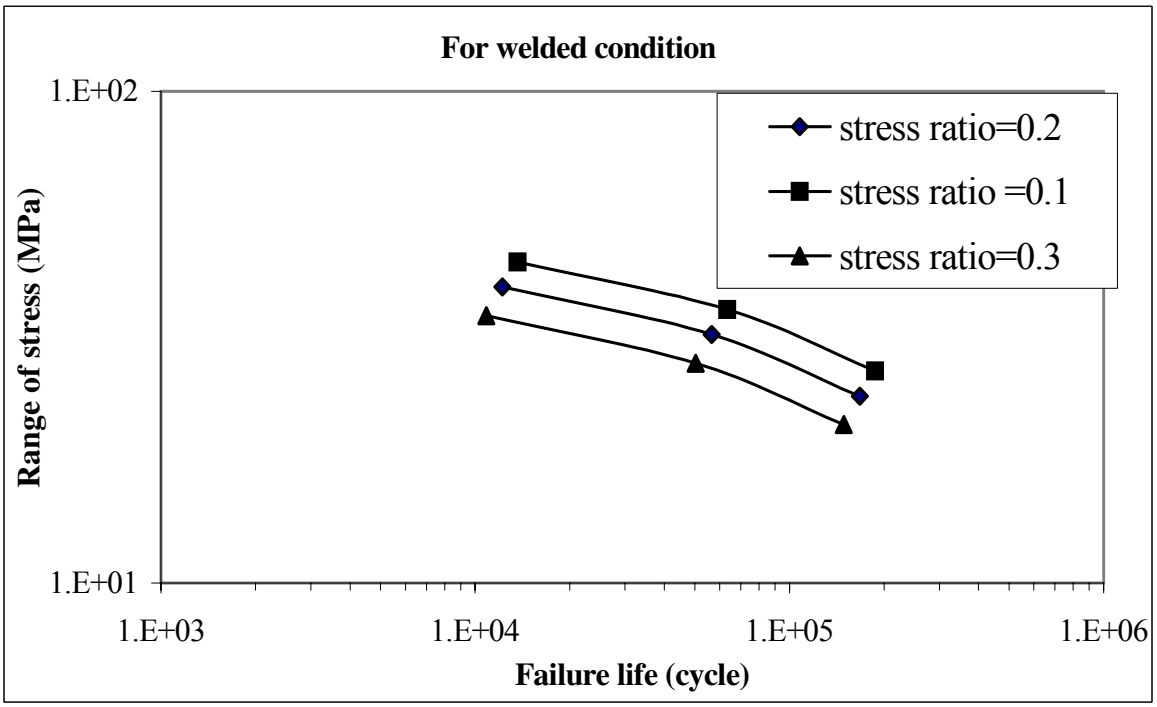

Figure 6.9 Failure life versus range of stress of welded joints at various stress ratios

The fatigue strength decreases about 14% at stress ratio 0.2 and about 29% at stress ratio 0.3 comparing to that at stress ratio 0.1 for un-welded plate. Therefore, it may be said that fatigue strength decreases with increase of stress ratio. Further fatigue strength decreases for welded and weld-repaired joints comparing to un-welded joint.

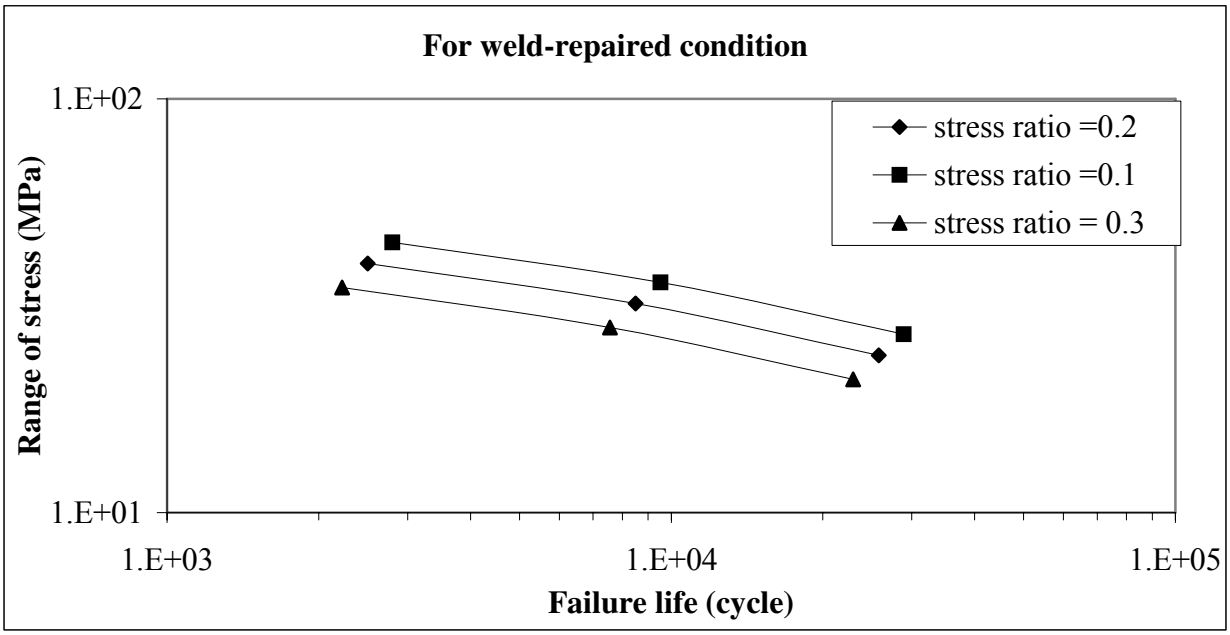

Figure 6.10 Failure life versus range of stress of weld-repaired joints at various stress ratios

6.6 Microscopic Examination and Micro-Characterization of Un-Welded, Welded and Weld-Repaired Joints

At the end of fatigue test, samples were cut from the fracture surfaces of typical un-welded, welded and weld-repaired specimens and were examined with Scanning Electronic Microscope (SEM). Fatigue crack initiation, stable propagation and fast growth areas of un-welded, welded and weld-repaired specimens are scanned. Different characteristics features are shown in figures 6.11-6.20. The sections were cut transverse to the weld bead. The un-welded sample exhibit an elongated fine grain structure resulting from the appreciable amount of cold working (strained-hardening) employed in the manufacturing process. Welded specimens have partially recrystallised structure with fine and equiaxed grains (figures 6.14-6.18) as a consequence of heat-input during

the weld process. Comparing with the unwelded and as-welded samples, the weld-repaired microstructure exhibits abnormally coarse grains and weld porosities (figure 6.19-6.20), which may be attributed to the large amount of heat input during the weld repair processes. In addition, more voids and porosities were found located along grain boundaries of the weld-repaired plates. These welding defects tend to connect each other and subsequently form large cracks as shown in figures 6.19-6.20, when subjected to external fatigue loads. This indicates the high fatigue crack growth rates and low fatigue lives of the weld-repaired specimens.

The fracture in the un-welded and welded plates appeared uniform and flat, indicating crack initiation and stable propagation with lower crack growth rate. Weld-repaired plates generally show fairly rough surface and coarse grain representing unstable crack growth phase with higher fatigue crack growth rate. It appears that in this case the maximum stress approached the material yield strength because of distinctive softening effects of the weld repair process of aluminum plates. In addition, from figures 6.19-6.20, it can be seen that in the weld-repaired specimens; the coarse grains were pulled out during cyclic fatigue loading, which is most likely caused by the grain boundary separation due to the voids and porosities in the second heat-affected-zone (HAZ). This indicates the significant role played by weld defects in accelerating the fatigue crack growth. The grain boundaries are the weakest regions in the material, so the crack grows along the grain boundaries. This is called inter-granular fracture. Inter-granular fatigue cracking occurred in case of brittle fracture. The cleavage feature of brittle fracture is characterized by the dimpled rupture. These features are created during fast fracture. A typical mode of ductile fracture is by void growth. Ductile fracture is normally trans-granular. Void coalescence is the final stage in void-controlled ductile fracture. Plasticity is localized between voids.

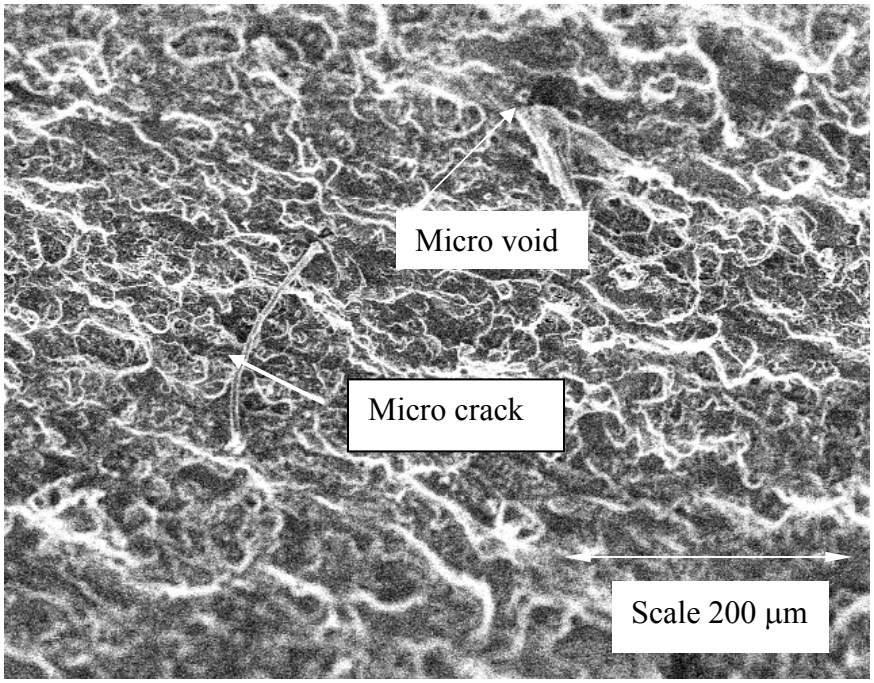

Figure 6.11 SEM photograph of fracture surface of failed un-welded specimen (tested at stress ratio = 0.2, stress range = 80, MPa, frequency = 0.5 Hz)

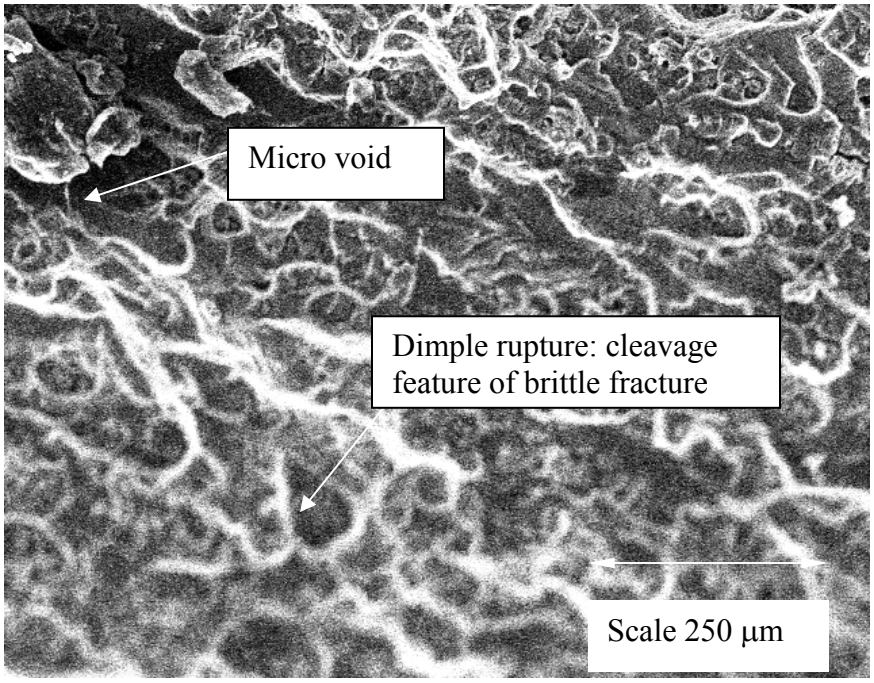

Figure 6.12 SEM photograph of fracture surface of failed un-welded specimen (tested at stress ratio = 0.2, stress range = 100 MPa, frequency = 0.5 Hz)

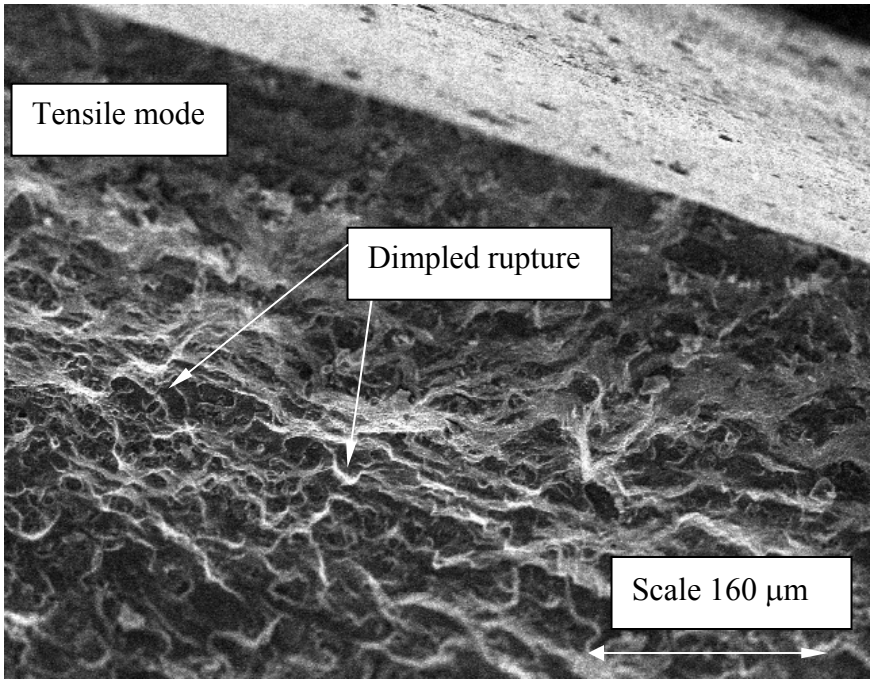

Figure 6.13 SEM photograph of fracture surface of failed un-welded specimen (tested at stress ratio = 0.2, stress range = 92 MPa, frequency = 0.5 Hz)

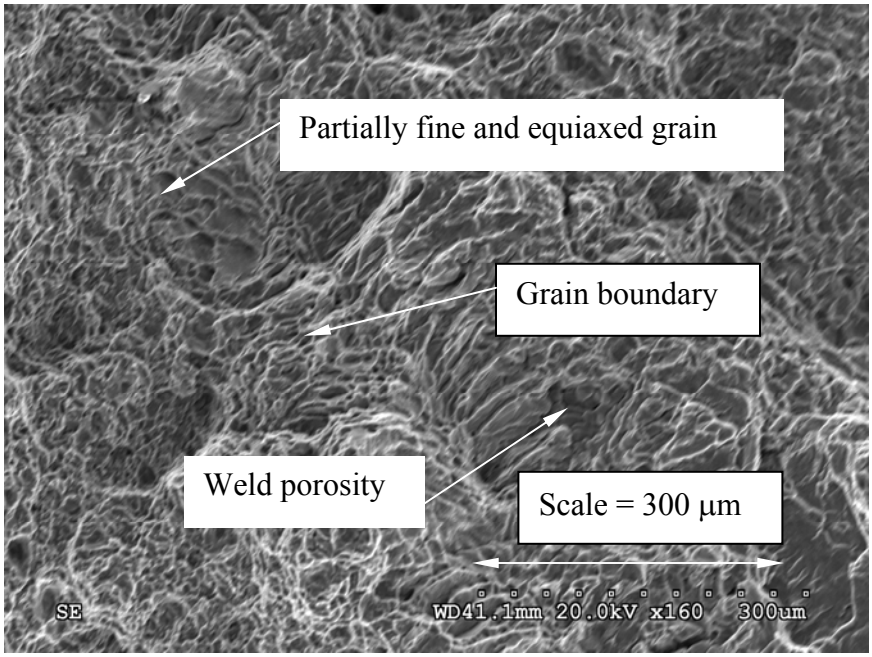

Figure 6.14 SEM photograph of fracture surface of failed welded specimen (tested at stress ratio = 0.2, stress range = 48 MPa, frequency = 0.5 Hz)

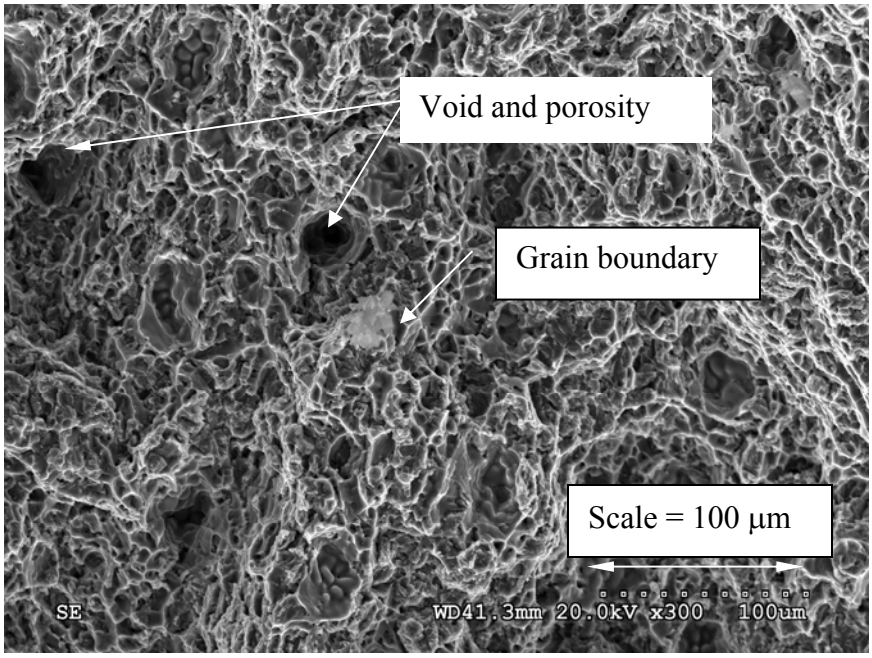

Figure 6.15 SEM photograph of fracture surface of failed welded specimen (tested at stress ratio = 0.2, stress range= 48 MPa, frequency = 0.5 Hz)

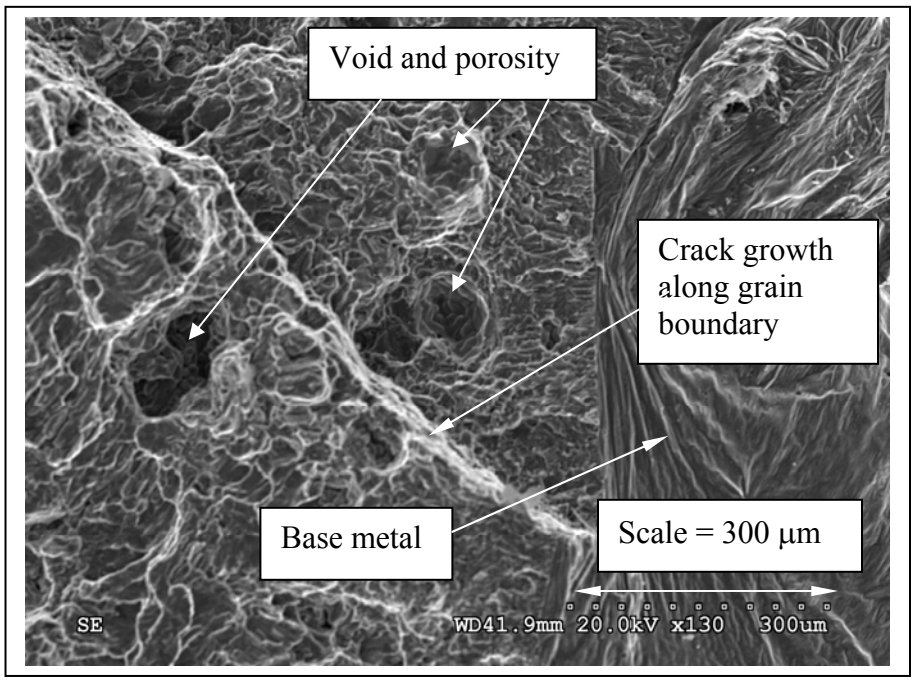

Figure 6.16 SEM photograph of fracture surface of failed welded specimen (tested at stress ratio = 0.2, stress range = 48 MPa, frequency = 0.5 Hz)

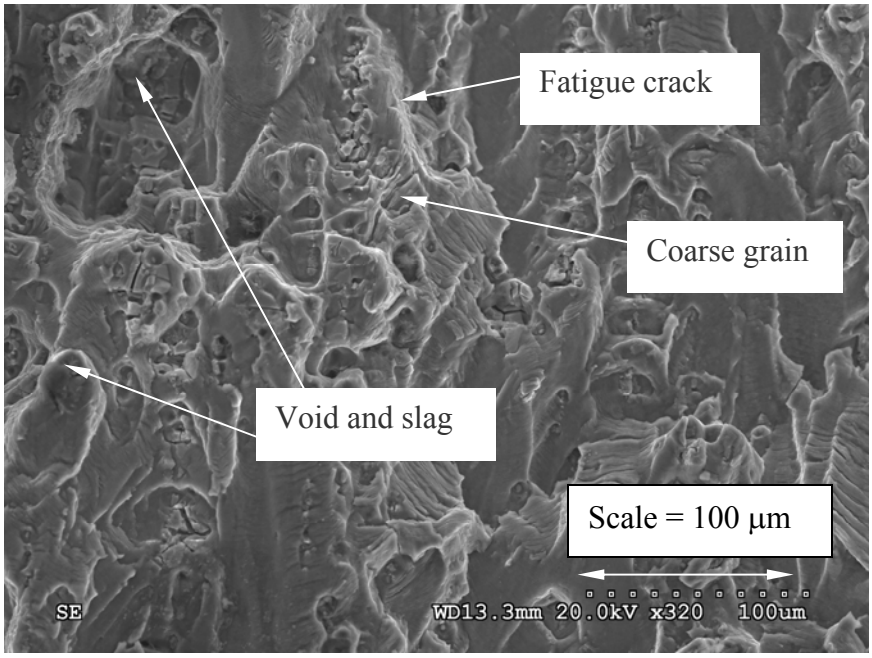

Figure 6.17 SEM photograph of fracture surface of failed welded specimen (tested at stress ratio = 0.2, stress range = 40 MPa, frequency = 0.5 Hz)

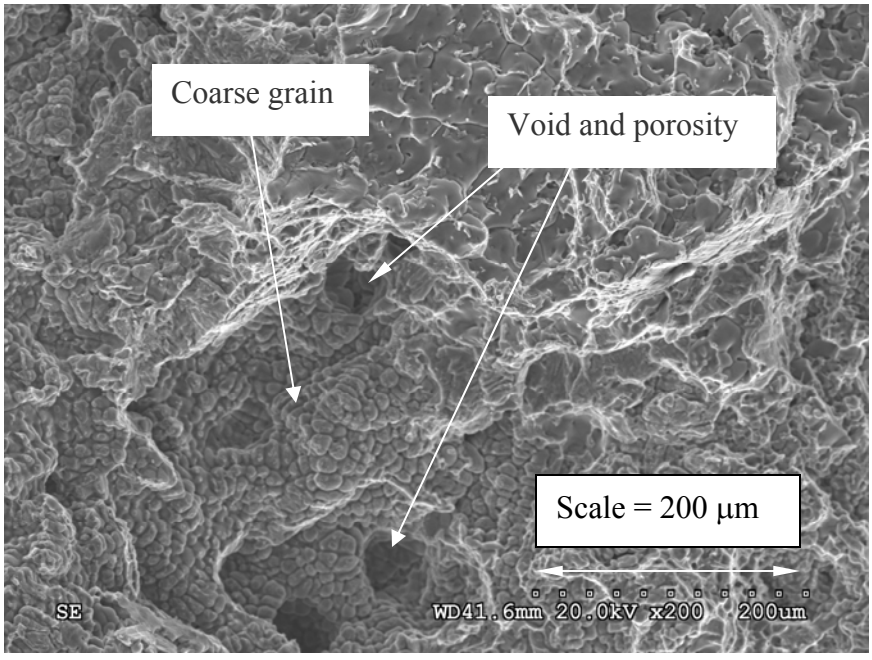

Figure 6.18 SEM photograph of fracture surface of failed welded specimen (tested at stress ratio = 0.2, stress range = 24 MPa, frequency = 0.5 Hz)

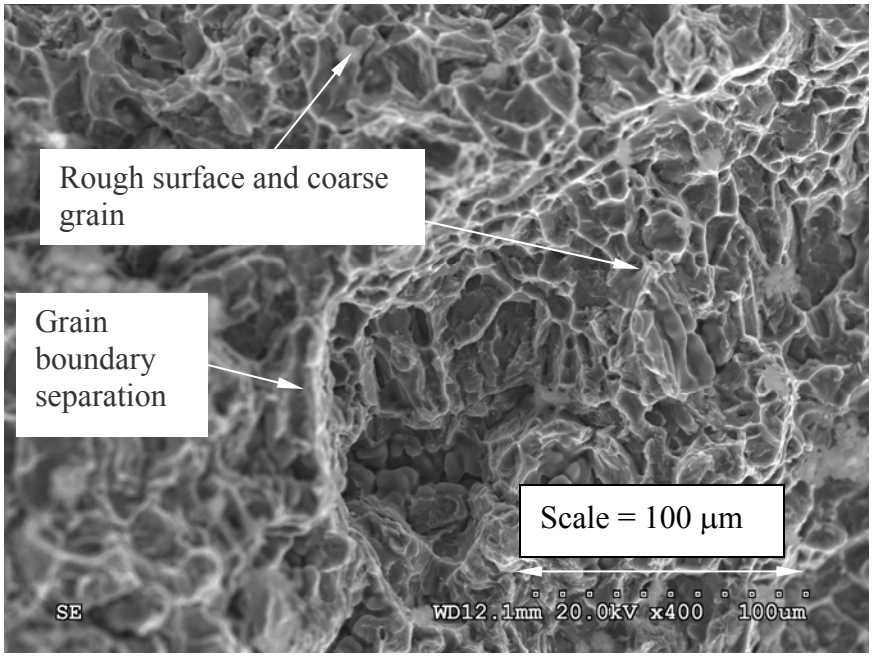

Figure 6.19 SEM photograph of fracture surface of failed weld-repaired specimen (tested at stress ratio = 0.2, stress range = 24 MPa, frequency = 0.5 Hz)

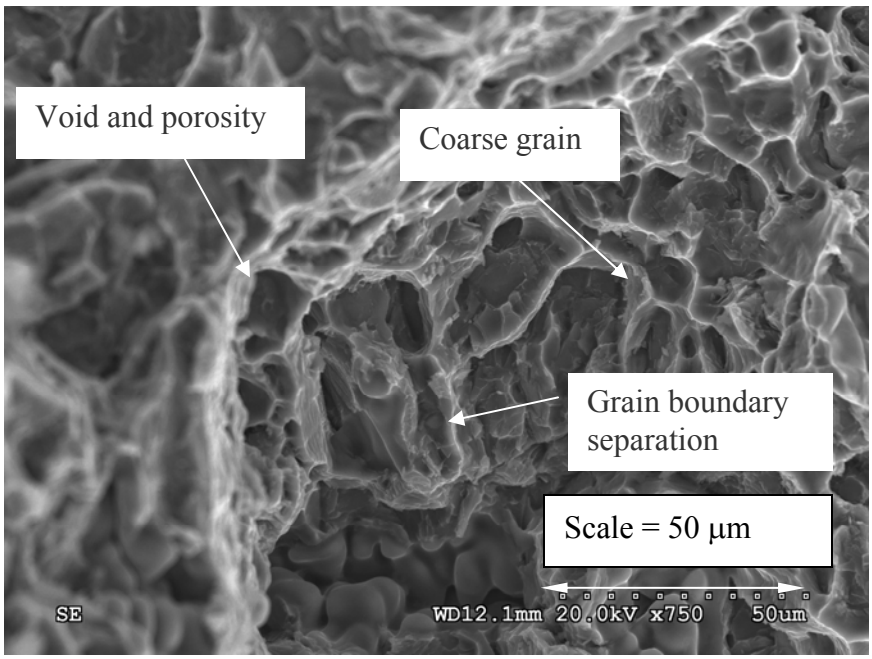

Figure 6.20 SEM photograph of fracture surface of failed weld-repaired specimen (tested at stress ratio = 0.2, stress range = 40 MPa, frequency = 0.5 Hz)

This localized deformation leads to final coalescence of voids and complete failure. These three sequential steps for fracture by voids is one of the major features of ductile fracture. Figure 6.13, shows micro-void coalescence that is indicative of the ductile fracture. Tear dimples and micro-voids are found on the crack surface. Dimpled rupture that is indicative of the cleavage feature of brittle fracture is found partly on the surface. Tear dimples result from non-uniform applied stresses. A gradual transition in failure mode from tensile mode (ductile) to brittle mode is observed on the crack surface by SEM photography. This observation show that a ductile failure mode is prominent as the crack grows transgranularly through the material.

6.7 Conclusions

The welded and weld-repaired plates have lower fatigue life than unwelded plates. The weld-repaired plates exhibited significant (32%) lower fatigue life than the as-welded plates. This is attributed to the much larger defects generated by the second weld process (weld-repair) employed to repair the cracks in the HAZ of the initial weld. This indicates repair of cracks in weldments by a second weld does not extend the life of the joint above that of the original welded joints.

Microstructure of un-welded, welded and weld-repaired plated were evaluated by means of scanning electronic microscopy. The un-welded sample exhibited elongated fine grain structure resulting from the appreciable amount of cold working employed in the manufacturing process while welded specimens presented partially recrystallised structure with fine and equiaxed grains as a consequence of the heat-input during welding process. The microstructure of the weld repaired specimens exhibit abnormally coarse grains and weld porosity, which may be attributed to the large amount of heat input during the weld-repair processes. In addition, more voids and porosity were found located along grain boundaries of the weld-repaired plates. This explains the higher fatigue crack growth rates and significantly lower fatigue lives of the weld-repaired specimens.

CHAPTER 7 CONCLUSIONS AND RECOMMENDATIONS FOR FUTURE WORK

7.1 Conclusions

It was found that the weld imperfections significantly reduce the fatigue crack propagation life and fatigue strength of welded joints. Solidification crack and undercut were more severe than embedded porosity. Improvement of weld geometry decreases the stress concentration and increases the fatigue strength. The residual stress, bending stress and dissimilar mechanical properties of base, weld and HAZ metals also decrease the fatigue strength of welded structure. Compressive residual induced on the surface of welded joint by surface peening made limited improvement on fatigue life and fatigue strength of welded joints. The bi-axial loading and the combined effect of a solidification crack and a circular porosity reduce the fatigue crack propagation life. But when they interact each other, the fatigue life increases comparing to when they are apart.

The simulation of fatigue crack propagation using an interface element is effective in practice, and numerically less intensive. The method can be applied for symmetric and anti-symmetric planes under cyclic load and also for biaxial loading. This method overcomes the limitation of crack growth at a rate of one element length per cycle. In this method the crack propagates only when the applied load reaches the critical bonding strength. The traditional finite element analyses had certain shortcomings and recent versions have been an improvement and have removed many of these limitations. In this approach, element bonding stress and surface energy, which are associated with crack formation and extension has been considered. The material properties have been changed during cyclic loads. The method can be applied in straight and curve tubular welded joint.

The finite element simulation of distortion and residual stress arising in gas metal arc welding has been investigated. The predicted results matched well with experimental results. The included

angle has influence on all distortions and residual stresses. As the included angle increases, all distortions increase. The angular distortion increases linearly up to 60 degrees and then increases rapidly. Residual stress in vertical direction increases up to 60 degrees and then decreases.

For a given heat input, the restraining force is the same as a function of distance from the start except at close to the end of the plate while it is being welded, regardless of welding speed. The force relaxation after welding have the same shape regardless of welding speed and maximum restraining forced reached. Decreasing welding speed makes the force versus distance graph depart from linearity earlier. Increasing the heat input increases the slope of the force versus time graph and the maximum restraining force. The slope of the force versus time graph gives a better indication of the effects of the welding conditions than maximum restraining force. The restraining force for the top of the plate increases with increased welding speed and heat input. Restraining force in the side direction is maximum at 90 degree and minimum at 30 degrees of included angle.

The fatigue failure life of unwelded, welded and weld-repaired specimen have been investigated. The welded and weld repaired plates have lower fatigue life than unwelded plates. The weld repaired plates exhibited significant lower fatigue life than the un-welded and as-welded material. This is attributed to the much larger defects generated by the second repair-weld process employed to repair the cracks in the HAZ of the initial weld. This indicates repair of cracks in weldments by a second weld does not extend the life of the joint above that of the welded joints.

Microstructure of un-welded, welded and weld-repaired plated were evaluated by means of scanning electron microscopy (SEM). The un-welded sample exhibited elongated fine grain structure resulting from the appreciable amount of cold working employed in the manufacturing process while welded specimens presented partially recrystallised structure with fine and equiaxed grains as a consequence of the heat-input during welding process. The microstructure of the weld repaired specimens exhibit abnormally coarse grains and weld porosity, which may be attributed to

the large amount of heat input during the weld repair processes. In addition, more voids and porosity were found located along grain boundaries of the weld repaired plates. This explains the higher fatigue crack growth rates and significantly lower fatigue lives of the weld -repaired specimens.

7.2 Recommendations for Future Work

For time constraints some works were not completed and are recommended for future work**.**

1. Fatigue crack growth model using interface element has been used in 2-D model. It can be applied in 3-D models. It can also be applied in multi-axial loading and for various stress ratios and stress ranges.
2. The interface element model is valid for quasi-brittle elastic-plastic material; the work can be extended for complete ductile material.
3. The finite element model for gas metal arc welding was used in butt-weld joint. It can be used for pipe girth weld, fillet weld and multi-pass welding.
4. The weld-repair technique was applied for aluminum-6061 and for certain geometries. The technique can be applied in other materials and other geometries.
5. The weld repair technique can be applied for other stress ratios and stress ranges and fatigue crack growth rate for un-weled, welded and weld-repaired plates can be investigated.

REFERENCES

1. Agerskov H. and Ibso J. B. (1993). Fatigue Life of Repair-Welded Tubular Joints in Offshore Structures. Proc. of the Third Int. Offshore and Polar Engineering Conf., Singapore, June 6-11.

2. Ainsworth RA, Editor. R5 (2003). Assessment Procedure for the High Temperature Response of Structures, Issue 3. British Energy Generation Ltd.

3. Alam M.S. and Wahab M.A. (2005). Modeling of Fatigue Crack Growth and Propagation Life of Joint of Two Elastic Materials Using Interface Elements. International Journal of Pressure Vessel and Piping, 82, pp. 105-113.

4. Alam M.S. and Wahab M.A. (2004). Finite Element Prediction of Distortion and Residual Stress in Gas Metal Arc Welded Joint. Proceeding of 11th International Conference on Composite Engineering, South Carolina, USA.

5. Anderson, T.L. (1995). Fracture Mechanics, Fundamentals and Applications. 2nd Edition, CRC Press.

6. Avram J. B. (2001). MS thesis. Department of Aeronautics and Astronautics, Air Force Institute of Tech.

7. Ansys 5.7 User Manual (1999), 1 – Procedure Manual, Swanson Analysis Systems.

8. ASTM E647 - 95a (1995). Standard Test Method for Measurement of Fatigue Crack Growth Rates. Annual Book of ASTM Standards, Vol. 11.03.

9. Bachorski A., Painter M. J., Smailes A. J. and Wahab M. A. (1999). Finite Element Prediction of Distortion during Gas Metal Arc Welding Using Shrinkage Volume Approach. J. of Mater. Process. Tech., 92-93, pp. 405-409.

10. Barsom J. M. (1994). Fracture Mechanics Analysis of Fatigue Crack Initiation and Growth. The International Conference on Fatigue, Toronto, Ontario Canada, 88-98.

11. Barberis U. and Rebora A. (1996). Finite element analysis of GMA (MIG) welded joints, Welding International, Vol. 10, No. 1, pp. 44-50.

12. Barrenblatt G.I. (1962). The mathematical theory of equilibrium of cracks in brittle fracture. Adv. Apply. Mech., **7**, pp. 55-129.

13. Beg R.G. (1992). Marine Structural Integrity Programs (MSIP). Ship Structural Committee SSC-365, NTIS, Springfield, VA.

14. Bell R., and Vosikovsky O. (1992). A Fatigue Life Prediction Model for Multiple Cracks in Welded Joints for Offshore Structures. OMAE, Vol. III-B, Material Engineering, ASME.

15. Benoit H. L and Truchon M. (1978). A Study of the Propagating of Fatigue Cracks in the Heat-Affected-Zones of Welded Joints in E-36 Steel. European Offshore Steel Research Seminar, Cambridge, UK, pp. 13-1-7.

16. Berkovis, D.W. Kelly and Di S. (1998). Consideration of the Effect of Residual Stresses on Fatigue Welded Aluminum Alloys Structures. Journal of Fatigue & Fracture of Engineering Material and Structure, Vol. 21, pp. 159-170.

17. Bimalendu G. (1993). Effect of Specimen Geometry on Fatigue of Welded Joints. Engineering Fracture Mechanics, Vol. 46, No. 1, pp. 35-39.

18. Boellinghaus T. and Kannengiesser T. (2003). Effect of filler material selection and shrinkage restraint on stress strain build up in component welds. 6th International Trends in Welding Research Conference Proceedings, ASM International, pp. 906-911.

19. Bowness D. and Lee M.M.K. (1996). Stress Intensity Factor Solution for Semi-Elliptical Weld-Toe Cracks in T-Butt Geometry. Fatigue and Fracture of Engineering Materials and Structures, Vol. 19, pp. 787-797.

20. Braid J. E. M., Bell R. and Milirau D.V. (1997). Fatigue Life of As-Welded, Repaired, and Hammer-Peened Joints in High-Strength Structural Steel. Welding in the World, 39 (5), 248-261.

21. Britz, W and Hoffmeister H. (1987). Effect of Hydrogen, Restraint and Welding Conditions on Weld Metal Cold Cracking of HSLA Steels in the IRC Test. Steel Res., Vol. 58, no. 3, pp. 142-147.

22. Broek D. (1982). Elementary Engineering Fracture Mechanics. Third Edition, Martinus Nijhoff Publishers.

23. Bucci R. J. (1981). Effect of Residual Stress on Fatigue Crack Growth Rate Measurement. Fracture Mechanics, ASTM STP 743, pp. 28-47.

24. Bueckner H.F. (1970). A Novel Principle for the Computation of Stress Intensity Factors. Zeitschrift Angewandte Mathematik and Mechanick 50, pp. 129-146.

25. Burk J. D. (1978). Ph. D Thesis. Department of Metallurgy and Mining, University of Illinois, Urbana-Champaign.

26. Burdekin, F.M. and Stone, D.E.W. (1966). The crack opening displacement approach to fracture mechanics in yielding. Journal of Strain Analysis, 1, pp.145-153.

27. Camacho G.T. and Ortiz M. (1996). Computational modeling of impact damage in brittle materials", Int. J. Solids Structures, 33, pp. 2899-2938.

28. Camacho G.T. and Ortiz M. (1997). Adaptive Lagrangian modeling of ballistic penetration of metallic targets. Comput. Meth. Appl. Mech. Engg, 142, 269-301.

29. Chandra U. (1985). Determination of Residual Stresses Due To Girth-Butt Welds Pipes. ASME J. Pressure Vessel Technology, 107, 178-184.

30. Chen H. F and Ponter A.R.S. (2005(1)). Integrity assessment of a 3D tube plate using linear matching method Part 1. Shakedown, reverse plasticity and ratcheting. Int J Pressure Vessels and Piping, 82, pp.85-94.

31. Chen H. F. and Ponter A. R.S. (2005(2)). Integrity assessment of a 3D tube plate using linear matching method Part 2: creep relaxation and reverse plasticity. Int J Pressure Vessels and Piping, 82, pp.95-104.

32. Chen H. F. and Ponter A. R. S. (2003). Application of the linear matching method to the integrity assessment for the high temperature response of structures. ASME Pressure Vessels Piping Division (Publication) PVP; 458, 3–12.

33. Chermahini, R.G., Shivakumar K.N. and Newman Jr, J.C., (1988). Three Dimensional Finite Element Simulations of Fatigue Crack Growth and Closure. ASTM STP 982, Philadelphia, PA, 398-401.

34. Chitoshi M., Tokeshi M. and Tajima J. (1986). Effect of Stress Ratio and Tensile Residual Stress on Near Threshold Fatigue Crack Growth. Structure Engineering, Vol. 1, pp.175-182.

35. Choi J. and Mazumder J. (1995). Numerical and Experimental Analysis for Solidification and Residual Stresses in the GMAW process for AISI 304 Stainless Steel. Proc. of the 4th Int. Conf. on Trends in Welding Research, p.75.

36. Chowdhury S.G, Mukhopadhyay N. K., Das G, Das S.K., and Bhattachrya D.K. (1998). Failure Analysis of a Weld Repaired Steam Turbine Casing. Engineering Failure Analysis, Vol. 5, No. 3, pp. 205-218.

37. Conley, D. S. (1999). Fatigue Response of Repaired Thick Aluminum Panels with Bond line Flaws. MS Thesis, AFIT/GAE/ENY/99M-03. School of Engineering, Air Force Institute of Technology, (AU), Wright-Patterson AFB, 1999.

38. Cornu J. (1988). Advanced Welding System-Fundamentals of Fusion Welding Technology. Bedford, UK. IFS Publication Ltd.

39. Davis D.A. and Czyryca E.J. (1981).Corrosion Fatigue Crack-Growth Behavior of HY-130 Steel and Weldments. Transactions of ASME, Vol. 103, 314-321.

40. Dexter R. (1991). Residual Stress Analysis in Reactor Pressure Vessel Attachments-Review of Available Software. Electrical Power Research Institute, EPRI NP-7469s.

41. Donald J. K. (1988). A Procedure for Standardizing Crack Closure Levels. Mechanics of Fatigue Crack Closure, ASTM STP 982, pp. 222-229.

42. Dong Y., Hong J. K., Tsai C.L. and Dong P. (1997). Finite Element Modeling of Residual Stresses in Austenitic Stainless Steel Pipe Girth Welds. Welding Journal, pp. 442-449.

43. Dong P. Hong J. K., Zhang J. Rogers P., Bynum J. and Shah S. (1998). Effects of Repair Weld Residual Stresses on Wide-Panel Specimens Loaded in Tension. ASME J. Pressure Vessel Technology, Vol. 120, pp. 122-128.

44. Dong P. Hong J. K. and Rogers P. (1998). Analysis of Residual Stresses in Al-Li Repair Weld and Mitigation Techniques. Welding Journal, Nov., pp. 439-445.

45. Dugdale D.S. (1960). Yielding of steel sheets containing slits. Journal of Mechanics and Physics of Solids, 8, pp. 100- 104.

46. Elber W. (1970). Fatigue Crack Growth under Cyclic Tension. Engineering Fracture Mechanics, 2, pp. 37-45.

47. Ferrica J.A. and Branco C.M. (1990). Fatigue Analysis and Prediction in Filled Welded Joints in the Low Thickness Range. Journal of Fatigue & Fracture of Engineering Materials and Structures, Vol. 13, No. 3, pp. 201-212.

48. Fisher J.F. and Dexter R.J. (1994). Field Experience with Repair of Fatigue Cracks. The International Conference on Fatigue, Toronto, Ontario Canada, 45-52.

49. Fisher, J. W., Hausammann, H., Sullivan, M.D. and Pense, A. W. (1979). Detection and Repair of Fatigue Damage in Welded Highway Bridge. NCHRP Report 206, Transportation Research Board.

50. Forman R.G., Kearney V.E., and Engle R. M. (1967). Numerical Analysis of Crack Propagation in a Cyclically Loaded Structure. ASME Trans. J. Basic Eng. 89D, P. 459.

51. Ghose D.J., Nappi N.S. and Wiernecki C.J. (1995). Residual Strength of Damaged Marine Structures. Ship Structural Committee, SSC-381, NTIS, Springfield, VA.

52. Giachino J.W., Week W. and Johnson G.S. (1973). Welding Technology. 2nd Edition, American Technical Publishers, Inc.

53. Gibatein M. and Moe E. T. (1987).Grind Repair. Det Norske Veritias Report No. 873093.

54. Glinka G. (1979). Effect of Residual Stress on Fatigue Crack Growth in Steel Weldments Under Constant and Variable Amplitude Load. Fracture Mechanics, ASTM STP 677, pp. 198-214.

55. Glinka G. (1994). Fatigue Crack Growth and Effects of Residual Stresses. The International Conference on Fatigue, Toronto, Ontario Canada, pp. 99-123.

56. Goglio L and Gola M. M. (1993). Shrinkage in Butt-Welded Joints: Measurements and Predictions. Welding International, 7, 776-787.

57. Gu M. and Goldak J. (1991). Mixing Thermal Shell and Brick Elements in FEA of Welds. Proc. Of 10th Int. Conf. on Offshore Mechanics and Arctic Eng. (OMAE), Vol. III-A Material Eng., p.1.

58. Gu M., Murakawa H., Ueda Y., Okumoto Y. and Ishiyama M. (1997). Simulation of Out-of-plane Deformation in Butt Welding of Large Steel Plate. H. Cerjak (ed.) Mathematical Modeling of Weld Phenomena 3, The Institute of Materials, p. 689.

59. Gurney, T.R. (1979). Fatigue of Welded Structures, 2nd Edition, Cambridge University Press, London.

60. Haagensen P.J. and Slind T. (1993). Life Extension and Repair of Weld Joints by Grinding and Peening. Fifth International Conference on Fatigue and Fatigue Threshold, 3-7 May, Montreal, Canada.

61. Haagensen P. J. (1994). Method for Fatigue Strength Improvement and Repair of Welded Offshore Structures. Proceeding of 13th International Conference on Offshore Mechanics, Vol. 3.

62. Harrison, J. D. (1989). Significance of Weld Defects With Regard to Fatigue Behavior. Proceedings of the International Symposium on the Occasion of Retirement of Prof. Ir. J. Deback; Delft, 1-20.

63. Higgins J. (1986). The Maintenance Repair of Mining Equipment. Australian Welding Journal, Summer, Vol. 31, No. 4.

64. Hidekazu M., Serizawa H. and Wu Z. (2000). Strength Analysis of Joints Between Dissimilar Materials Using Interface Elements. Journal of Welding Research Institute; 29(2), 71-75.

65. Hidekazu M. and Wu Z. (1999). Computer Simulation Method for Crack Growth Using Interface Element Employing Lennard Jones Type Potential Function. Material Science Research International; 5(3), 195-201.

66. Hideyuki S. and Akitake M. (1998). Drawbead Restraining Force When the Sliding Direction of the Sheet is not Normal to the Drawbead Line, A Study on Drawbead Restraining Force in Sheet Metal Forming. Journal of the Japan Society for Technology of Plasticity, 39 (448): pp. 33-44.

67. Hoffmeister H. and Harneshaug S. (1987). Investigation of the conditions for weld metal hydrogen cracking of low carbon offshore steels by the IRC weld ability test. Steel Res., Vol. 58, no. 3, pp. 134-141.

68. Hoffmeister H., Christensen N., Akselsen O. M. (1987). Effect of heat input and preheating on hydrogen assisted weld joint cracking of a 0.13%C, 1.5%Mn, 0.032%Nb high strength steel of 50 mm plate thickness in the IRC test. Steel Res., Vol. 58, no. 12, pp. 570-576.

69. Holby E.R. and Galanes G. (1995). Weld Repair of a High Pressure Generator Rotor for Commonwealth Edison Co. Proceedings of the American Power Conference, vol. 1, 595-599.

70. http://www.Utm.Edu/Departments/Engin/Lemaster/Machine%20Design/Lecture%2012.Pdf

71. Itoh Y. Z., Suruga S. and Kashiwaya (1989). Prediction of Fatigue Crack Growth Rate in Welding Residual Stress Field. Journal of Engineering Fracture Mechanics, Vol. 33, No. 3, pp. 397-407.

72. James M. N. (1998). Engineering Materialism and Structural Integrity**.** Journal of Engineering Design. Vol. 9 No. 4, published by Carfax Publishing Ltd., pp.329-342.

73. James M N and Wei L. (1999), Hail damage to polycarbonate roofing sheets, Proceedings of an International Conference on Case Histories on Integrity and Failures in Industry, Milan, September 1999, (eds. V Bicego et al) EMAS Cradley Heath,West Midlands, 715-724.

74. Jang, C. D. and Lee C. H. (2003). Prediction of Welding Deformation of Ship Hull Blocks. Proceedings of International Workshop on Frontier Technology in Ship and Ocean Engineering, pp. 41-49.

75. Jang, C. D. and Seo, S. I. (1996). A Study on the Automatic Fabrication of Welded Built-Up Beams. Transactions of the Society of Naval Architects of Korea, 33(1), pp. 206-213.

76. Karsson L. (1997). Modeling in Welding, Hot Power Forming and Casting. ASM International.

77. Karlssson R.I. and Josefson B.L. (1990). Three-Dimensional Finite Element Analysis of Temperatures and Stresses in a Single-Pass Butt-Welded Pipe. ASME J. Pressure Vessel Technology, Vol. 112, pp. 76-84.

78. Kang K. J. and Earmme J.H. (1989). Behavior of Fatigue Crack Growth and Closure through Tensile Residual Stress Field under Compressive Applied Loading. Fatigue and Fracture of Engineering Materials and Structure, Vol. 12, pp. 363-376.

79. Kang K. J., Song H. and Young Y. (1990). Fatigue Crack Growth and Closure Behavior through a Compressive Residual Stress Field. Journal of Fatigue and Fracture of Engineering Material and Structures, Vol. 13, No.1, pp. 1-13.

80. Kannengieber T., Bollinghaus T., Florian W., and Herold H. (2001). Effect of weld metal strength and welding conditions on reaction forces and stress distribution of restrained components. Welding in the world, 45 (1/2), pp. 18-26.

81. Kapadia B.M. (1978). Influence of Residual Stresses on Fatigue Crack Propagation in Electro-slag Welds. ASTM STP 648, D.W. Hoeppner, Ed., ASTM, pp. 244-260.

82. Kelly B. A. and Dexter R. J. (1997). Restored Fatigue Life with Repair Welds. Proceeding of the Seventh International Offshore and Polar Engineering Conference, Vol. 4, pp. 572-577.

83. Kosteas D. (1988). Estimating Residual Stress and Their Effect in Welded Aluminum Components in Fatigue. Analytical and Experimental Methods for Residual Stress Effects in Fatigue, ASTM STP 1004, Philadelphia, pp. 122-130.

84. Kumar A., Raj B., Kalyanasundaram. P., Jayakumar T., and Thavasimuthu M. (2002). Structural Integrity Assessment of the Containment Structure of a Pressurized Heavy Water Nuclear Reactor using Impact-Echo Technique. NDT&E International, 35, pp. 213-220

85. Lawrence F.V. Jr., Mattos R.J., Higashida Y. and Burk J.D. (1978). Estimating the Fatigue Crack Initiation Life of Welds, Fatigue Testing of Weldments. ASTM STP 648, D.W. Hoeppner, Ed., ASTM, pp. 134-158.

86. Leggatt R.H. (1991). Computer Modeling of Transverse Residual Stresses in Repair Welds. Welding Research Supplement, November, 299-310.

87. Linda R. (1990). Fatigue Crack Growth of Weldments. Fatigue Fracture Testing of Weldments, ASTM Publ. STP 1058, pp 16-33.

88. Lindgren L. E. (2001). Finite Element Modeling and Simulation of Welding Part 1: Increased Complexity. Journal of Thermal Stress, 24, 141-192.

89. Lindgren L-E. and Karlsson L. (1988). Deformation and Stresses in Welding of Shell Structures. Int. J. for Numerical Methods in Engineering. Vol. 25, pp. 635-655.

90. Maddox S.J. (1994 (1)). Applying Fitness-for Purpose Concepts to the Fatigue Assessment of Welded Joints. The International Conference on Fatigue, Toronto, Ontario Canada, pp 72-81.

91. Maddox S.J. (1994(2)). Tips on Fatigue Design of Weldments. The International Conference On Fatigue, Toronto, Ontario Canada, 19-27.

92. Maddox S.J. (1974). Fatigue Crack Propagation Data Obtained From Parent Plate, Weld Metal and HAZ in Structural Steels. WRI, 4(1), pp. 32-42.

93. Maddox S.J. (1993). Recent Advances in the Fatigue Assessment of Weld Imperfections. Welding Journal, 72 (7), pp. 42-52.

94. Masakazu Shibahara, Hisashi Serizawa and Hidekazu Murakawa (2000). Finite Element Method for Hot Cracking Using Temperature Dependent Interface Element (Report II), Journal of Welding Research Institute; 29 (1), 59-64.

95. Masubuchi K. (1980). Analysis of Welded Structures, Residual Stress, Distortion and Their Consequence. International Series on Material Science and Technology, Vol. 33, Pergamon Press.

96. McClung R.C. and Sehitoglu H. (1989). On The Finite Element Analysis of Fatigue Crack Closure-I, Basic Modeling Issue. Journal of Engineering Fracture Mechanics; 3, 237-252.

97. McDill J. M. J., Oddy A. S., Goldak J.A. and Bennison S. (1990). Finite Element Analysis of Weld Distortion in Carbon and Stainless Steels. J. of Strain Analysis for Engineering Design, Vol. 25, No. 1, pp. 51-53.

98. Michaleris P., Feng Z. and Campbell G. (1997). Evaluation of 2-D and 3-D FEA models for predicting residual stresses and distortion. Proc. of ASME Pressure Vessels and Piping Conf., Approximate Methods in the Design and Analysis of Pressure Vessels and Piping Components, PVP-Vol. 347, p. 91.

99. Michaleris P. and DeBiccari A. (1997). Prediction of Welding Distortion. Welding Journal, Vol. 76, No. 4, pp.172-181.

100. Miki and H. Takenouchi (1989). Repair of Fatigue Damage in Cross Bracing Connection in Steel Girder Bridges. Journal of Structural Engineering/ Earthquake Engineering, Vol. 6 No. 1, April, pp. 31-39.

101. Murakawa, H., Luo, Y., and Ueda, Y. (1997). Prediction of Welding Deformation and Residual Stress By Elastic FEM Based on Inherent Strain. Journal of the Society of Naval Architects of Japan 180, pp. 739-751.

102. Murthy R.D.S., Gandhi P. and Madhava Rao A.G. (1994). A Model for Fatigue Prediction of Offshore Welded Stiffened Steel Tubular Joints Using FM Approach. International Journal of Offshore and Polar Engineering, 4(3), 241-247.

103. Nasstrom M., Wikander L., Karlsson L, Lindgren L-E. and Goldak J. (1992). Combined 3D and Shell Modeling of Welding, IUTAM Symposium on the Mechanical Effects of Welding, p.197.

104. Nelson F.G. (1961). Effects of Repeated Repair Welding of Two Aluminum Alloys. Welding Journal, April.

105. Newman J.C. Jr. and Harry A. Jr. (1975). Elastic-Plastic Analysis of a Propagating Crack under Cyclic Loading. Journal of AIAA; 13,1017-2023.

106. Newman J.C. Jr. (1977). Finite-Element Analysis of Crack Growth under Monotonic and Cyclic Loading. ASTM STP 637, Philadelphia, PA, 56-80.

107. Newman J.C. and Raju I.S. (1986). Stress Intensity Factors Equations for Cracks in Three Dimensional Finite Bodies Subjected to Tension and Bending Loads. Computational

Methods in the Mechanics of Fracture (Edited By S.N. Atluri), North-Holland, Amsterdam, pp. 311-334.

108. Nguyen N.T. (2004). Thermal Analysis of Welds. WIT press, Ashurst Lodge, South Hampton, UK.

109. Nguyen O., Repetto E.A., Ortiz M., and Radovitzky R.A. (2001). A cohesive model of fatigue crack growth. International Journal of Fracture 110, pp. 351–369.

110. Nguyen N.T. and Wahab M.A. (1995). The Effect of Residual Stresses and Weld Geometry on the Improvement of Fatigue Life. Journal of Material Processing Technology, Vol. 48, pp. 583-588.

111. Nguyen N.T. and Wahab M.A. (1993). The Effect of Butt Weld Geometry Parameters on Stress Intensity Factor and Fatigue Life. Computational Mechanics, Valliappan, Pulmano & Tin-Loi (Eds), Rotterdam, pp. 883-888.

112. Niu X.and Glinka G. (1987).The Weld Profile Effects on Stress Intensity Factors in Weldments. International Journal of Fracture, Vol. 35, pp 3-20.

113. Nordmark G.E., Herbein W.C. and Dickerson P.B. (1987). Effect of Weld Discontinuities on Fatigue of Aluminum Butt Joints. Journal of Welding, 66(6), 162-173.

114. Nordmark G.E., Mueller L. N., and Kelsey R. A. (1989). Effect of Residual Stresses on Fatigue Crack Growth Rate in Weldments of Aluminum Alloy 5456b Plate. Residual Stress Effects in Fatigue ASTM STPT 776, pp 45-62.

115. Ohji K., Kubo S., Tsuji M, Ogawa H. and Sakurada K. (1987). Method of Predicting Fatigue Crack Growth Lives in Residual Stress Fields. Transactions, Japan Society of Mechanical Engineers, 53, 1516-1523.

116. Ohta, T. Mawari and N. Suzuki (1990). Evaluation of Effect of Plate Thickness on Fatigue Strength of Butt Welded Joints By A Test Maintaining Maximum Stress At Yield Strength. Engineering Fracture Mechanics, Vol. 37, No. 5, pp. 987-993.

117. Paris P., and Erdogan F. (1963). A Critical Analysis of Crack Propagation Law. J. of Basic Engineering, Vol. 85, pp. 528-534.

118. Park J.H. (2004). Effect of Corrosion Prevention Compounds and Overloads on Fatigue Life in Aluminum Alloy. MS Thesis, Louisiana State University, USA.

119. Pandolfi A., Krysl P. and Ortiz M. (1999). Finite element simulation of ring expansion and fragmentation: the capturing of length and time scales through cohesive models of fracture. Int. J. Fracture, 95, pp. 279-297.

120. Pandolfi A., Guduru P.R., Ortiz M. and Rosakis A.J. (2000). Three-dimensional cohesive-elements of dynamic fracture in C300 steel. Int. J. Solids Structures, 37, pp. 3733- 3760.

121. Potente H., Schneiders J., Herrmann K.P., Ferber F. and Linnenbrock K. (2001). Investigations concerning the development of inherent stresses during welding by using the drilled-hole method as well as the finite element method. Welding in the World, 45 (1/2), pp. 9-17.

122. Radaj D. (1992). Heat Effect of Welding, Temperature Field, Residual Stress and Distortion. Published By Springer-Verlag.

123. Ravichandran G. Raghupathy V.P., Ganesan N. and Krisnakumar R. (1996). Analysis of Transient Longitudinal Distortion in Fillet Welded T-Beam using FEM with Degenerated Shell Element. Int. J. for the Joining of Materials, Vol. 8, No. 4, pp. 170-179.

124. Ravichandran G. Raghupathy V.P., Ganesan N. and Krisnakumar R. (1997). Prediction of Axis Shift Distortion during Circumferential Welding of Thin Pipes Using the Finite Element Method. Welding Journal, January, pp. 39-55.

125. Rice J.R. (1968). A Path Independent Integral and the Approximate Analysis of Strain Concentration by Notches and Cracks. Journal of Applied Mechanics, Vol. 35, 379-386.

126. Rodriguez J.E., Brennan F. P. and Dover W.D. (1998). Minimization of Stress Concentration Factors in Fatigue Crack Repairs. International Journal of Fatigue, Vol. 20, No. 10, pp. 719-725.

127. Rogers P. R. and Bynum J. E. (1998). Wide Panel Testing Technique for Evaluating Repair Weld Strengths. Pressure Vessel and Piping, ASME, Vol. 373, pp. 411-420.

128. Runnemalm H. (1999). Efficient Finite Element Modelling and Simulation of Welding. Phd Dissertation, Lulea University of Technology, Sweden.

129. Ruiz G., Ortiz M.and Pandolfi A. (2001). Three dimensional cohesive modeling of dynamic mixed-mode Fracture. Int. J. Numer. Meth. Engg, 52, pp. 97-120.

130. Sanders W.W. and Gannon S.M. (1974). Fatigue Behavior of Aluminum 5083 Butt Welds. WRC Bulletin 199, Welding Research Council, New York.

131. Sanders W. W. Jr. and Lawrence F.V., Jr. (1977). Fatigue Behavior of Aluminum Alloy Weldments. Fatigue Testing of Weldments, ASTM STP 648.

132. Seo, S. I. and Jang, C. D. (1999). A Study on the Prediction of Deformations of Welded Ship Structures. Journal of Ship Production 15(2), pp. 73-81.

133. Sinclair G. B. (2004). Stress singularities in classical elasticity-I: Removal, interpretation, and analysis. Appl Mech Rev 57 (4), pp. 251-297.

134. Sinha P. P., Arumugham S. and Nagarajan K.V. (1993). Influence of Repair Welding of Aged 18Ni 250 Maraging Steel Weldments on Tensile and Fracture Properties. Welding Research Supplement, August, 1993, pp. 391-396.

135. Smith S. D. (1992). A Review of Numerical Modeling of Fusion Welding for the Prediction of Residual Stresses and Distortion. TWI Journal, 3 (4), 440-503.

136. Solsteel, Pty Ltd (1993). Aluminum and Sea. Technical Publication, Solsteel Pty Ltd, pp.62-69.

137. Steen W.M. (1976). Ph. D Thesis. Imperial College, London, England.

138. Taylor N. (2002). Current Practice for Design Against Fatigue in Pressure Equipment. EPERC Bulletin 6, European Commission, Petten, Netherlands.

139. Tekriwal, P. (1989). Three-Dimensional Transient Thermo-Elasto-Plastic Modeling of Gas Metal Arc Welding Using the Finite Element Method. Ph. D. Dissertation, Urbana, Ill., U.S.A., U. of Illinois at Urbana-Champaign.

140. Tekriwal P. and Mazumder J. (1988). Finite Element Analysis of Three- Dimensional Transient Heat Transfer in GMA Welding, Welding Research Supplement, July, pp. 150-156.

141. Tubby P.J. (1989). Fatigue Performance of Repaired Tubular Joints. Offshore Technology Report (OHT) 89 307.

142. Tsai C. L., Park S. C. and Cheng W. T. (1999). Welding Distortion of a Thin-Plate Panel Structure, Welding Research Supplement, May, pp. 156-165.

143. UEG, Underwater Engineering Group (UEG) (1982). Review of Repairs of Offshore Installations. Pennwell Publishing Company, UR21.

144. Ueda Y., Murakawa H., Nakacho K. and Ma N.X. (1995). Establishment of Computational Weld Mechanics. Journal of Welding Research Institute, 13(2), 165-174.

145. Ueda, Y., and Ma, N. X. (1995). Measuring Methods of Three-Dimensional Residual Stresses with Aid of Distribution Function of Inherent Strains (Report 3). Transactions of Japanese Welding Research Institute, 24(2), pp.123-130.

146. Xu X. P. and Needleman A. (1994). Numerical simulations of fast crack growth in brittle solids. J. Mech. Phys. Solids, 42, pp. 1397-1434.

147. Xu X. P. and Needleman A. (1995). Numerical simulations of dynamic interfacial crack growth allowing for crack growth away from the bond line. Int. J. Fracture, 74**,** pp. 253-275.

148. Xu X. P. and Needleman A. (1996). Numerical simulations of dynamic crack growth along an interface. Int. J. Fracture, 74**,** pp. 289-324.

149. Yurioka N. and Koseki T. (1997). Modeling Activities in Japan. In H. Cerjak (Ed.), Mathematical Modeling of Weld Phenomena 3, The Institute of Materials, pp. 33-52.

150. Wahab M.A. and Alam M.S. (2004). The Significance of Weld Imperfection and Surface peening on Fatigue Crack Propagation Life of Butt Welded Joints. Journal of Material Processing Technology, 153-154, pp.931-937.

151. Wahab M.A. and Alam M. S. (2003). The Effect of Torsional Interaction of a Circular Porosity and a Solidification Crack on Fatigue Crack Propagation Life of Butt Welded Joints. Proceeding of 10th International Conference of Composite Engineering, New Orleans, pp.753-754.

152. Water V. D. (1983). The Role of Welding in Qantas Operations. Australian Welding Journal, Autumn, Vol. 38, No. 1.

153. Wohlfart H. and Zhang F. (1994). Experimental Evaluation and Calculation of Transverse Distortions Due to Welding in Butt-Joints and T-Joints. Welding in the World/ Soudage Dans Le Monde, 34, 397-406.

154. Wu J. and Ellyin F. (1996). A Study of Fatigue Crack Closure by Elastic-Plastic Finite Element Analysis for Constant-Amplitude Loading. International Journal of Fracture; 82, 43-65.

155. Wu W. (2002). MS Thesis. Department of Mechanical Engineering, University of New South Wales, Australia.

156. Wu A., Ma N-X, Murakawa H. and Ueda Y. (1996). Effects of Welding Procedures on Residual Stresses in T-Joints. JWRI, Vol. 25, No. 4, pp.81-89.

157. Williams J.R. and Ma S.Y. (1993). A New Repair and Strengthening Technique for Steel Offshore Structures. The Proc. of the 25th Annual Offshore Technology Conference in Houston, 155-164.

158. Wernicke R. and Pohl R. (1998). Underwater Wet Repair Welding and Strength Testing on Pipe-Patch Joints. Journal of Offshore Mechanics and Arctic Engineering, Vol. 120, No. 4, pp. 237-242.

159. Weisman C. (1976). Welding Handbook. Vol. 1 Fundamental of Welding, Seven Edition, American Welding Society, Miami, Florida.

160. Webster P.J. (1992). Welding Application of Neutron Strain Scanning. International Trends in Welding Science and Technology, Ed S.A. David and J.M Vitek, ASM.

161. Zhang J., Dong P. and Brust F. W. (1997). A 3-D Composite Shell Element Model for Residual Stress Analysis of Multi-pass Welds. 14th Int. Conf. on Structural Mechanics in Reactor Technology (SMIRT 14), p.335.

162. Zhang J., Dong P. (1998). 3-D Residual Stress Characteristics in Pipe Repair Welds. Proc. Of the 5th Int. Conf. on Trends in Welding Research, p. 949.

163. Zhai J. and Zhou M. (2000). Finite element analysis of micro-mechanical failure modes in a heterogeneous ceramic material system. Int. J. Fracture, 101, pp.161-180.

164. Zavattieri P.D. and Espinosa H.D.(2001). Grain level analysis of crack initiation and propagation in brittle materials. Acta. Mater. 49, pp. 4291-4311.

165. Zhou F., Molinari J-F. and Li Y.(2004). Three-dimensional numerical simulation of dynamic fracture in silicon carbide reinforced aluminum. Engineering. Fracture Mechanics, 71, 1357-1378.

166. Zhou F., and Molinari J-F., (2004). Stochastic fracture of ceramics under dynamic tensile loading. Int. J. Solids and Structures, in press.

APPENDIX A: LIST OF PUBLICATIONS FROM THIS RESEARCH

Published or Accepted

1. Alam M.S. and Wahab M.A. (2005). Modeling of Fatigue Crack Growth and Propagation Life of Joint of Two Elastic Materials Using Interface Elements. International Journal of Pressure Vessel and Piping, 82, pp. 105-113.

2. Wahab M.A. and Alam M.S. (2004). The Significance of Weld Imperfection and Surface peening on Fatigue Crack Propagation Life of Butt Welded Joints. Journal of Material Processing Technology, 153-154, pp.931-937.

3. Wahab M.A., Alam M.S., Painter M.J and Stafford P.E. (2005). Experimental and Numerical Simulation of Restraining Forces in Gas Metal Arc Welded Joint. Journal of Welding Research Supplement(American Welding Journal) (accepted).

4. Alam M.S. and Wahab M.A. (2005). Finite Element Modeling of Fatigue Crack Growth in Curved-Welded Joints Using Interface Elements. Journal of Structural Integrity & Durability (accepted).

5. Wahab M.A. and Alam M.S. (2003). The Effect of Torsional Interaction of a Circular Porosity and a Solidification Crack on Fatigue Crack Propagation Life of Butt Welded Joints. Proceeding of 10th International Conference of Composite Engineering, New Orleans, pp. 753-754.

6. Wahab M.A. and Alam M.S. (2003). The Significance of Weld Imperfection and Surface peening on Fatigue Crack Propagation Life of Butt Welded Joints. Proceeding of the International Conference on Advanced in Material and Processing Technology, Dublin, Ireland, pp.990-993.

7. Alam M.S. and Wahab M.A. (2004). Finite Element Prediction of Distortion and Residual Stress in Gas Metal Arc Welded Joint. Proceeding of 11th International Conference on Composite Engineering, South Carolina, USA.

8. Alam M.S. and Wahab M.A. (2005). A New Technique for Modeling of Fatigue Crack Growth in Welded Tubular Joints and Structures. Proceeding of the International Mechanical Engineering Congress and Exposition , Florida, USA.

Submitted and Under Review Process

1. Wahab M.A. and Alam M.S. (2004). Bi-axial Interaction and the Influence of Welding defects on Fatigue Life of Welded Joints. International Journal of Structural Engineering and Mechanics (in review).

2. Wahab M.A., Alam M.S., Painter M.J and Stafford P..E. (2005). A Study of Restraining Forces in Gas Metal Arc Welded Joint. Journal of European Welding (in review).

APPENDIX B: LIST OF ANSYS COMMAND

```
! This program will simulate gas metal arc welding using moving heat flux and calculate restraint force,

 ! temperature distribution

/TITLE, TRANSIENT ANALYSIS OF WELDING (MOVING HEAT FLUX)

/FILNAM, TRANSIENT WELD

/UNITS, SI                ! UNITS: SI  (KG-M-SEC-KELVIN)

/CONFIG, NRES, 100000  !NUMBER OF RESULT SETS

/PREP7

ET, 1, SOLID5, 0, , ! ELEMENT 1 SOLID5

ET, 2, SURF152, , , ,1,1      !ELEMENT 2 IS  3-D THERMAL SURFACE EFFECT ELEMENTS !FOR RADIATION

KEYOPT, 2, 9, 1           ! RADIATION OPTION

R, 2, 1, 5.667E-8         ! FORM FACTOR = 1, STEFAN BOLTZMANN CONSTANT =5.667E-8

MP, EMIS, 2,0 .5           ! RADIATION EMISSION FACTOR 0.5

K=273                     ! A PARAMETER

MP,REFT,1, 25+K  !  MAT DEPEND REF TEMP

TREF, 15+K

MPTEMP,1,15+K,100+K,200+K,300+K,400+K,500+K    !    TEMPERATURE    DEPENDENT !MATERIAL PROPERTIES
```

```
MPDATA,EX,1,1,210E9,200E9,190E9,185E9,180E9,130E9

MPDATA,KXX,1,1,15,15.5,16.5,18,20,21

MPDATA,C,1,1,477,480,528,544,565,649

MPDATA,PRXY,1,1,.28,.285,.288,.29,.295,.305

MPDATA,ALPX,1,1,11.9E-6,11.9E-6,12.7E-6,13.3E-6,13.9E-6,14.3E-6

MPTEMP,7,600+K,700+K,800+K,900+K,1000+K,1100+K

MPDATA,EX,1,7,70E9,20E9,5E9,2E9,0,0

MPDATA,KXX,1,7,22,23,24,25.5,26,26.2

MPDATA,C,1,7,741,831,1449,833,550,600

MPDATA,PRXY,1,7,.31,.315,.315,.315,.315,.315

MPDATA,ALPX,1,7,14.6E-6,14.7E-6,14.7E-6,14.95E-6,15.20E-6,15.4E-6,

!MPDATA,THSX,1,7,.0065,.007,.008,0.01,.011,.0125

MPTEMP,13,1200+K,1300+K,1400+K,1500+K,2500+K, 3500+K

MPDATA,EX,1,13,0,0,0,0,0,0

MPDATA,KXX,1,13,26.3,26.5,26.8,27,28, 30

MPDATA,C,1,13,675,700,710,4076,4000,800

MPDAT,PRXY,1,13,.315,.315,.315,.315,.315,.315

MPDATA,ALPX,1,13,15.7E-6,15.90E-6,16.15E-6,16.35E-6,16.5E-6,17E-6

!MPDATA,THSX,1,13,.015,.017,.02,.025

MPPLOT, EX, 1, 0, 1500, 0,210E9
```

```
MPPLOT,KXX,1,0,1500,0,100

MPPLOT,C,1,0,1500,450,1400

MPPLOT,ALPX,1,0,1500,0,.025

MP,MURX,1,1

MP,MURX,2,1

MP,MURX,3,1

MP,RSVX,1,1

MP,RSVX,2,1

MP,RSVX,3,1

MP,DENS,1,7850

! GEOMETRY OF THE MODEL (100X500X5 MM)

K,1,0,.250

K,2,.005,.25

K,3,.1,.25

K,4,.1,-.25

K,5,.005,-.25

K,6,0,-.25

A,1,2,5,6

A,2,3,4,5

AGLUE, ALL
```

```
VEXT,1,2,1,0,0,.005

VSEL,S,VOLU,,1,1

TYPE,1

MAT,1

ESIZE,.003,    !WELD ELEMENT SIZE = 0.003 M

MSHAPE,0,3D

MSHKEY,1

VMESH,1

VSEL,S,VOLU,,2,2

TYPE,1

MAT,1

ESIZE,.005,

MSHAPE,0,3D            !BASE PLATE ELEMENT SIZE = 0.005 M

MSHKEY,1

!MOPT,AORDER,ON

VMESH,2

!BOUNDARY CONDITIONS

NSEL,S,NODE,,981,981,

D,ALL,UX,0

D,ALL,UZ,0
```

```
D,ALL,UY,0

NSEL,S,NODE,,1000,1000,

D,ALL,UX,0

D,ALL,UZ,0

D,ALL,UY,0

NSEL,S,LOC,X,0

DSYM, SYMM, X, ! SYMMETRIC BOUNDARY CONDITION

NSEL,S,LOC,Z,0.0

NSEL,R,LOC,X,0.02

NSEL,R,LOC,Y,0

D,ALL,UZ,0

NSEL,ALL

TYPE, 2

REAL, 2

MAT, 2

N, 5000, .0, .0, .1          ! EXTRA "SPACE" NODE FOR RADIATION

ESURF, 5000              ! GENERATE SURF152 ELEMENTS

FINISH

/SOLU

ANTYPE,TRANS ! START TRIANSIENT ANALYSIS
```

```
NLGEOM,ON     ! NONLINEAR GEOMETRY IS ON

TRNOPT,FULL

NROPT,AUTO, ,

EQSLV,

SOLCONTROL,ON

NEQIT,100

AUTOTS,ON

KBC,1                         !APPLY FULL LOAD IN A STEP

OUTRES,ALL,ALL,

   !LOAD STEP 1, INITIAL CONDITIONS  15 C

TIME,.01

DELTIM,.01,.01,.01

TUNIF,15+K,

SOLVE

!LOAD STEP 2..... , APPLY MOVING HEAT FLUX

J=1

EN=102

*DO, I, 69,102,1

  TIME, J

  DELTIM,.04,.04,.04,
```

```
  SFEDELE,I-1,2,HFLUX      !DELETE HEAT FLUX OF PREVIOUS STEP
NSEL,ALL
DDELE,ALL,TEMP,
NSEL,ALL
SFE,I,2,HFLUX, ,100E6, , ,       !APPLY HEAT FLUX, FACE 2 ,
  SOLVE
  J=J+1
*ENDDO
TIME, 34.001
DELTIM,.001,.001,0.001
SFEDELE,EN,2,HFLUX  !DELETE HEAT FLUX FROM THE LAST ELEMENT
NSEL,ALL
SOLVE
TIME,140
DELTIM,.5,.5,.5
NSEL,ALL
SF, ALL, CONV, 130, 15+K,  ! APPLY CONVECTION
SOLVE
FINISH
/POST1
```

/EFACE,1

SET,LAST

/POST26

X=1395 ! ELEMENT NUMBER OF CONSTRAINT NODE

Y=1428 !ELEMENT NUMBER OF 2ND CONSTRAINT NODE

A=981 ! NODE NUMBER OF CONSTRAINT

B=1000 ! NODE NUMBER OF 2ND CONSTRAINT

ESOL, 2, X, A, F, X

ESOL, 3, Y, B, F, X

ESOL,4, X, A, F, Z

ESOL,5,Y, B, F, Z

NSOL,6,10,TEMP,,TDIS ! TEMPERATURE DISTRIBUTION AT DIFFERENT NODES

NSOL,7,2461,TEMP,,TDIS1

NSOL,7,207,TEMP,,TDIS1

NSOL,8,25,TEMP,,TDIS2

PRVAR, 2, 3, 4, 5, 6, 7, 8

SAVE

FINISH

VITA

Mohammad Shah Alam was born in Shariatpur, Bangladesh, on October 16, 1969. He received his bachelor's degree in naval architecture and marine engineering from Bangladesh University of Engineering and Technology (BUET), Dhaka, Bangladesh, in October 1993, with first class third position. He was also awarded talent pool scholarship for both elementary and secondary school education, and also was awarded merit scholarship for both higher secondary school education and undergraduate degree in engineering at BUET.

After graduation he enrolled for a Master of Science degree in naval architecture and marine engineering at BUET. After completing course work, he joined Chittagong Dry Dock Ltd., a government organization in Bangladesh, as an Assistant Naval Architect in 1994. Later he joined BUET as a lecturer in October, 1997 and promoted to a rank of Assistant Professor in 1999. He earned his Master of Science degree in 1998 from BUET. Later he moved to the United States of America and obtained a Master of Science in Mechanical Engineering degree from South Dakota School of Mines and Technology, South Dakota, USA in May, 2002.

Alam became a graduate student in the Department of Mechanical Engineering at Louisiana State University for pursuing a doctoral degree in August 2002 and since then he has been working on this degree in mechanical engineering till December 2005. To date, he has authored seven journal publications and eight conferences proceeding publications, and contributed to five conference presentations.